Thèse n° 8692

Wireless soft microscale actuators and robotic devices to study mechanobiology

Présentée le 5 novembre 2021

Faculté des sciences et techniques de l'ingénieur
Laboratoire de Systèmes MicroBioRobotiques
Programme doctoral en biotechnologie et génie biologique

pour l'obtention du grade de Docteur ès Sciences

par

Raquel Filipa PENACHO PARREIRA

Acceptée sur proposition du jury

Prof. B. E. Ferreira De Sousa Correia, président du jury
Prof. M. S. Sakar, directeur de thèse
Dr M. Mastrangeli , rapporteur
Dr B. Trappmann, rapporteuse
Prof. S. Pané Vidal, rapporteur

École
polytechnique
fédérale
de Lausanne

2021

Abstract

Tissues morphogenesis and homeostasis involve the spatiotemporal regulation of mechanics at multiple scales. Characterization of mechanical properties of biological systems as well as investigating the effects of mechanical forces on biological function are instrumental. However, existing biomanipulation systems are bulky and invasive, therefore, they do not allow application of forces within native tissues or biomimetic platforms. Investigation done with cells cultured on planar substrates provide limited information on multicellular organization and the interactions between cells and the surrounding extracellular matrix (ECM). Recent work has introduced biochemically and mechanically tunable synthetic matrices, with which the mechanics of the cellular microenvironment can be engineered. What has been missing is an actuated polymer system that can be freely shaped at microscale, and be seamlessly interfaced with living systems. Considering the small size of the actuators, the power must be transmitted wirelessly. Application of physiologically relevant forces using physiologically acceptable energy input requires an efficient transduction mechanism. This thesis is built upon two important nanoscale phenomena. Gold nanoparticles efficiently transduce visible light into localized heat due to plasmon resonance, and certain class of polymers display powerful contractions in the course of microseconds by going through a thermally-induced hydrophilic to hydrophobic transition. The thesis exploits these two phenomena on the same platform using nanotechnology and chemical synthesis, and introduces a series of microengineering techniques that would transform the active nanomaterial into microscale soft actuators and machines. To this end, the thesis explores a number of bottom-up engineering approaches including droplet microfluidics, magnetic and hydrodynamic interactions, and thermocapillary effects. The deformation generated by the actuators is transformed into a desired set of mechanical operations using rationally designed hydrogel mechanisms.

The use of wirelessly-powered microactuators for mechanobiology research is demonstrated at two different levels. First, a high-throughput microscale compression device is built for bulk mechanical loading of three-dimensional (3D) culture models such as spheroids and organoids. Second, the chemical crosslinking of microactuators to collagen fibers is achieved to apply local forces to cells residing within reconstituted collagen I gels. The materials and methods are not restricted to the cell types and ECM components that are explored in this thesis, therefore, the technology can be applied to study almost any mechanobiology process in vitro. As a benchmark to estimate stress and strain that must be applied by wireless actuators in order to initiate a biological response, we performed a detailed study on the mechanical loading of mammary acini inside collagen matrices using a tethered robotic micromanipulator. The results of the study show that externally applied mechanical tension facilitate transition to an invasive phenotype, which involves long-distance force transmission, activation of mechanotransduction pathways, and plasticity of collagen. These conventional micromanipulation techniques are complementary to the presented novel wireless actuation scheme, together pushing the boundaries of our understanding of living systems.

Keywords : Gold nanorods, active matter, wireless actuation, hydrogels, microfabrication, soft robotics, 3D tissue constructs, mechanobiology, mechanotransduction, extracellular matrix.

Résumé

La morphogenèse tissulaire et l'homéostasie impliquent la régulation spatio-temporelle des propriétés mécaniques à des échelles différentes. La caractérisation des propriétés mécaniques des systèmes biologiques ainsi que l'étude des effets des forces mécaniques sur les fonctions biologiques sont déterminantes. Cependant, les systèmes de biomanipulation existants sont encombrants et invasifs, par conséquent, ils ne permettent pas l'application de forces dans les tissus natifs ou les plateformes biomimétiques. Les recherches effectuées sur des cellules cultivées sur des substrats planaires fournissent des informations limitées sur l'organisation multicellulaire et les interactions entre les cellules et la matrice extracellulaire environnante (MEC). Des travaux récents ont introduit des matrices synthétiques compatible biochimiquement et mécaniquement, avec lesquelles la mécanique du microenvironnement cellulaire peut être conçue. Pour cela, un système polymérique à actionnement qui peut être modelé librement à l'échelle microscopique et qui peut être connecté facilement avec les systèmes vivants est nécessaire. En raison de la petite taille des actionneurs, l'énergie doit être transmise à distance. L'application de forces physiologiquement pertinentes en utilisant un apport d'énergie physiologiquement acceptable nécessite un mécanisme de transduction efficace. Cette thèse s'appuie sur deux phénomènes importants à l'échelle du nanomètre. Les nanoparticules d'or transduisent efficacement la lumière visible en chaleur localisée en raison de la résonance plasmonique, et certaines classes de polymères affichent de puissantes contractions en quelques microsecondes en passant par une transition hydrophile à hydrophobe induite thermiquement. Cette thèse exploite simultanément ces deux phénomènes en utilisant la nanotechnologie et la synthèse chimique. Elle présente une série de techniques de micro-ingénierie qui peuvent transformée le nanomatériau actif en actionneurs et en machines souples à l'échelle microscopique. Pour cela, la thèse explore plusieurs approches d'ingénierie ascendantes, notamment la microfluidique de gouttes, les interactions magnétiques et hydrodynamiques et les effets thermocapillaires. La déformation générée par les actionneurs est transformée en un ensemble d'opérations mécaniques utilisant des mécanismes d'hydrogel rationnellement conçus.

L'utilisation de microactionneurs sans fil pour la recherche mécanobiologique est démontrée à deux niveaux différents. Tout d'abord, un dispositif de compression à haut débit à l'échelle microscopique est conçu pour le chargement mécanique de culture tridimensionnels (3D) tels que les sphéroïdes et les organoïdes. Deuxièmement, la réticulation chimique des microactionneurs aux fibres de collagène est réalisée pour appliquer des forces locales aux cellules résidant dans les gels de collagène I reconstitués. Les matériaux et les méthodes ne se limitent pas aux types de cellules et aux composants de la MEC qui sont explorés dans cette thèse. Par conséquent, la technologie peut être appliquée pour étudier presque tous les processus de mécanobiologie in vitro. Dans le but d'estimer le stress et la contrainte qui doivent être appliqués par des actionneurs sans fil afin d'initier une réponse biologique, nous avons réalisé une étude détaillée sur la charge mécanique des acini mammaires à l'intérieur des matrices de collagène à l'aide d'un micromanipulateur robotique filaire. Les résultats de l'étude montrent que la tension mécanique externe facilite la transition vers un phénotype invasif, qui implique une transmission de force à longue distance, l'activation des voies de mécanotransduction et la plasticité du collagène. Ces techniques de micromanipulation conventionnelles sont complémentaires au nouveau schéma d'actionnement sans fil présenté dans cette thèse, permettant de repousser les limites de la compréhension des systèmes vivants.

Mots-clés : Nanotiges d'or, matière active, actionnement sans fils, hydrogel, microfabrication, robotique molle, construction de tissue 3D, mécanobiologie, transduction mécanique, matrice extracellulaire

Acknowledgements

Queria começar por agradecer à minha família, especialmente aos meus pais, pois sem eles a minha vinda para a Suíça não teria sido possível. Também queria agradecer todo o apoio que eles e os meus avós me deram durante estes 5 anos. Obrigado por terem tido toda a paciência do mundo, mesmo quando eu não estava no meu melhor.

I would like to thank my boyfriend, Aurélien Willauer, for being there for me in the good and bad moments of the PhD. Thank you for your support and embracing my craziness. Without you, COVID period and especially quarantine wouldn't have been easy, I'm grateful for that and for having you by my side.

I would like to thank my thesis advisor, Prof. Sakar, for giving me the opportunity of being part of his very multidisciplinary laboratory, where I faced intellectual challenges all the way of my PhD. Thank you for pushing me in the different fields, which kept me motivated to pursue the work. This PhD not only made me grow professionally but also personally.

I would like to thank all the previous and current members of MICROBS lab. Berna Ozkale, who taught me how to do nanoparticle chemistry and mentored me during the first 6 months. Erik Mailand, for all the support handling the lab, all the help regarding biology and for our lunch and coffee breaks together. Murat Kaynak, for all the fruitful intellectual discussions and help with microfluidics. Ece Özelçi my number one co-worker in all the papers we submitted together. Thank you for all the mechanical engineering input and all the simulations. Haiyan Huang, I loved to have you as an office mate and colleague. Thank you for all the help regarding materials science and for bringing me a bit of the Chinese culture, especially the delicious food! Lucio Pancaldi, Matthias Rüegg, Fazil Uslu, Amit Dolev, thank you for your intellectual help in the fields that I do not master.

This thesis wouldn't be as complete as it is if I didn't have the help of my students. I would like to thank my semester project and master thesis students. Specifically, I would like to thank Claire Amadio, Daniel Reichmuth, Selma Attia, Vitaly Pustovalov, Guillaume Girod, Nina Wahler and Alaa Rushdy, with whom I also learned a lot with and made some friendships.

I would also like to thank Ahmet Bekdemir from SuNMiL lab for the immense help with materials science during my first 2 years.

When I came to Switzerland I found a new family, with whom I grew up and had the most amazing moments of my stay here. I would like to thank Cornel Fink, Martha Zoumpoulaki and Dmitry Vasilyev. Martha stayed only 6 months in Switzerland but we kept in touch and did so many trips together. Thank you for listening me when I needed a shoulder. Cornel and Dmitry, I really miss our Tuesday evenings board games and hikes. You really made my stay in Switzerland very pleasant. Cornel you were my best friend here and like a big brother, really missed you when you left. I had to learn how to survive alone when I lost my keys or something else got stolen :). With you, I starting road cycling, an hobby I continued, and you always made sure I was not lazy ahah Thank you for helping me setting my chemical hood and teaching me a few essentials in the chemistry lab. Thanks to the 3 of you, I hope we will have many more adventures together.

Gostaria de agradecer às minhas amigas algarvias Eliana Rodrigues e Joana Colaço pelo apoio e amizade à distância. Sempre foi uma amizade mais sazonal, mas com uma ligação forte. Apesar de termos emigrado para países diferentes conseguimos ver-nos pelo menos uma vez por ano, o que é excelente. Obrigado por todo o apoio que me deram e por me ouvirem quando mais precisava durante estes 5 anos.

E por último, mas não menos importantes, gostaria de gradecer às minhas meninas, ex-colegas universitárias, Ariana Peredo, Ana Margarida Carregosa, Marta Rodrigues, Lídia Jesus, Magda Costa e Mariana Anastácio por todo o apoio que me deram, não só durante o doutoramento mas também durante os nossos estudos. Seguimos caminhos diferentes, mas continuamos em contacto assíduo, o que é excelente para sentirmos o quentinho acolhedor de Portugal e para partilharmos os bons momentos do dia a dia ou desabafar os nosso males. Espero que depois da pandemia nos consigamos encontrar todas juntas novamente, mas até lá manteremos o nosso contacto virtual :).

Table of Contents

Abstract iii

Résumé v

Acknowledgements viii

Figures xv

Tables xvii

Bibliographic Note xix

1 Introduction 1
- 1.1 Problem Statement 2
- 1.2 Background 2
  - 1.2.1 3D culture models and mechanobiology 2
  - 1.2.2 Wireless Microactuators 3
  - 1.2.3 Nanotechnology 4
- 1.3 General Objectives and Methodology 5
- 1.4 Thesis Outline 6

2 Chemical Synthesis of Optomechanical Nanoactuators 9
- 2.1 Introduction 10
- 2.2 Synthesis of gold nanorods 11
  - 2.2.1 Seed solution 11
  - 2.2.2 Growth solution 11
- 2.3 Exploring the design space 13
  - 2.3.1 The influence of pH 13
  - 2.3.2 The influence of the ascorbic acid concentration 15
  - 2.3.3 The influence of the seed concentration 16
  - 2.3.4 The influence of the silver nitrate concentration 16
  - 2.3.5 Combinatorial analysis 17
- 2.4 Toward automation of nanorod synthesis 19
- 2.5 Thermoresponsive polymer coating 22
- 2.6 Synthesis of gold nanorods with magnetic and catalytic properties 23
- 2.7 Detailed protocols 25
  - 2.7.1 Materials 25
  - 2.7.2 Gold nanorod synthesis 25
  - 2.7.3 Polymer coating 27
  - 2.7.4 Magnetization 28
  - 2.7.5 Particles characterization 29
  - 2.7.6 Sample preparation for TEM imaging 30

3 Top-down and bottom-up assembly of microactuators from optomechanical nanoactuators 32
- 3.1 Introduction 33
- 3.2 Template-assisted assembly of microactuators 34

3.2.1 Characterization of contraction and relaxation kinetics 35
3.2.2 Fluorescent labelling of microactuators 38
3.2.2.1 Formation of colloidosomes 38
3.2.3 Conclusions 40
3.2.4 Detailed protocols 40
3.2.4.1 Materials 40
3.2.4.2 Fabrication of microfluidic channels 40
3.2.4.3 Fabrication of microactuators 41
3.2.4.4 Characterization of microactuators 42
3.2.4.5 Fluorescent labelling 42
3.2.5 Experimental set-up and video processing 43
3.3 Casting and printing of nanocomposite microactuators 44
3.3.1 Extrusion of fiber microactuators 44
3.3.1.1 Characterization of fiber microactuators 44
3.3.2 Casting of actuated polymer substrates 46
3.3.3 Conclusions 48
3.3.4 Detailed protocols 48
3.3.4.1 Materials 48
3.3.4.2 Synthesis of alginate-composite fibers 48
3.3.4.3 Synthesis of Polyacrylamide-composite films 48
3.3.4.4 Synthesis of alginate-composite films 49
3.3.4.5 Synthesis of Polyacrylamide-alginate-composite films . . . 49
3.3.4.6 Experimental set-up 49
3.4 In situ-self-assembly of microactuators 50
3.4.1 Photothermal and magnetic assembly of mNAs 51
3.4.2 Controlled in situ self-assembly and characterization of mNAs . . . 51
3.4.3 Understanding the mechanism of permanent colloidal assembly . . . 54
3.4.4 Experimental set-up 55
3.4.5 Conclusions 57
3.4.6 Detailed protocols 58
3.4.6.1 Materials 58
3.4.6.2 Synthesis of nanoactuators 58
3.4.6.3 Characterization of Nanoactuators and microactuators . . 58
3.4.6.4 Sample Preparation for Cryo-SEM imaging 58
3.4.6.5 Image processing 59
3.4.6.6 Calculation of energy density absorbed by the artificial μmuscle 59

4 Development of soft robotic microdevices using projection lithography 61
4.1 Introduction 62
4.2 Design, production and characterization of compliant hydrogel mechanisms 64
4.3 Development and characterization of soft robotic microgrippers 68
4.4 Investigating tissue mechanics *in vitro* using untethered soft robotic microdevices 72
4.4.1 Design and computational analysis of the compressor microdevice . 73
4.4.2 Heat transfer during device operation 75
4.4.3 Calibration of poly-acrylamide sensing probes 79
4.4.4 Biomechanical characterization 82
4.4.5 Integration with microfluidic systems 82

4.5 Design and in-situ production of antagonistic mechanism 85
4.6 Controlled *in-situ* self-assembly and characterization of soft micromachines 87
4.7 Conclusions 89
4.8 Detailed protocols 90
  4.8.1 Materials 90
  4.8.2 Synthesis of microactuators 90
  4.8.3 Fabrication of hydrogel mechanisms : Digital maslkless lithography 90
  4.8.4 Laser actuation 90
  4.8.5 Mechanical characterization of hydrogel mechanisms : MEMs force sensor measurements 91
  4.8.6 Synthesis of polyacrylamide beads 91
  4.8.7 Formation of spheroids 91
  4.8.8 Viability assay 91
  4.8.9 Simulations : Finite element models 92

5 Tensile loading transmitted through collagen matrix drives mammary acini toward invasive phenotype 94
5.1 Introduction 95
5.2 Background on 3D mammary organoids 95
5.3 The in vitro culture system 96
5.4 Optomechanical actuation to stimulate cells 98
5.5 Micromanipulation platform 99
  5.5.1 Characterization of the invasive phenotype 99
  5.5.2 Tensile loading and matrix remodelling 100
  5.5.3 Tensile loading and intracellular mechanics 104
5.6 Discussion 107
5.7 Detailed Protocols 108
  5.7.1 2D cell culture 108
  5.7.2 3D cell culture : MCF10A acini formation 108
  5.7.3 Experimental set-up : MCF10A acini sandwich and pin set-up . . . 109
  5.7.4 Immunohistology 109
  5.7.5 Image acquisition and data analysis 110
  5.7.6 mOMAs integration in collagen 110

6 Conclusions and outlook 112
6.1 Actuators and mechanical systems 113
6.2 Mechanobiology 114
6.3 Bioinspired programmable active matter 115

Bibliography 120

Curriculum Vitae 138

Figures

1.1 Schematic illustration of an organoid embedded inside a fibrous matrix. . . 6
1.2 Schematic summary of the methodologies developed and applications of this thesis. 7
2.1 AuNRs final reaction suspension. 13
2.2 AuNRs characterization. 14
2.3 AuNRs characterization under different synthesis conditions, with change in hydrochloric acid (HCL) concentration. 14
2.4 AuNRs characterization under different synthesis conditions, with change in ascorbic acid (AA) concentration. 15
2.5 AuNRs characterization under different synthesis conditions, with change in seed concentration. 16
2.6 AuNRs characterization under different synthesis conditions, with change in silver nitrate ($AgNO_3$) concentration. 17
2.7 AuNRs characterization under different synthesis conditions, with change of two parameters at a time. 18
2.8 Characterization of the optomechanical nanoactuators (nOMAs). 23
2.9 Characterization of the multifuncitonal nanoactuators (mNAs). 24
2.10 STEM-EDX characterization of the multifunctional nanoactuators (mNAs). . 25
2.11 pNIPMAM coating of AuNRs set-up. 28
3.1 Overview of the microacturators' assembly techniques explored in this work. 33
3.2 Colloidal assembly. 34
3.3 Microfluidic assisted colloidal assembly. 35
3.4 Second version of Microfluidic assisted colloidal assembly. 35
3.5 Characterization of the contraction and relaxation kinetics. 37
3.6 Characterization of the contraction and relaxation kinetics of the larger μOMAs. 38
3.7 Surface functionalization of the actuators with fluorophores. 39
3.8 Colloidosomes. 40
3.9 Extrusion of alginate composite fibers. 45
3.10 Alginate fibers actuation. 45
3.11 Photothermal and magnetic assembly of mNAs. 51
3.12 Controlled self-assembly and characterization of artificial μmuscle. 53
3.13 Discovering the mechanism of permanent colloidal assembly. 54
3.14 Experimental set-up 56
4.1 Inspiration, concept, and realization of bioinspired soft robotic actuators and microdevices. 63
4.2 Concept of *in situ* development of bioinspired soft robotic actuators and microdevices. 63
4.3 *In situ* fabrication of hydrogel mechanisms 64
4.4 *In situ* fabrication of hydrogel lever systems 65
4.5 *In situ* fabrication of hydrogel compliant mechanisms with multiple mechanical elements. 66
4.6 Cantilever system and characterization of bending modulus 67
4.7 Development of soft robotic microprototypes to study locomotion 67
4.8 Development of soft robotic microgrippers actuated by μOMAs 68
4.9 FEM simulations and performance characterization of parallel jaw μgrippers. 69

4.10 Development of flextensional mechanisms 70
4.11 Development of inverted soft robotic microgrippers actuated by μOMAs . . 71
4.12 *In situ* fabrication of the compressor components 74
4.13 Design, operation, and computational analysis of the compressors. 75
4.14 Rapid prototyping of compression devices using projection lithography. . . . 76
4.15 Testing of the soft robotic compressor microdevice performance. 77
4.16 Finite element simulations of the heat transfer during actuation. 78
4.17 Long-term actuation of a μOMA. 79
4.18 Fabrication of pAAm beads and calibration of the sensing probe. 80
4.19 Compressor microdevices fabricated from TPETA polymer. 81
4.20 Biomechanical characterization of 3D tissue samples. 83
4.21 Live/dead assay on the cell-seeded compression microdevice. 84
4.22 Assembly of devices inside microfluidic systems. 84
4.23 Development of soft robotic microdevices actuated by μOMA fibers 86
4.24 Controlled self-assembly and characterization of soft micromachines actuated by artificial μmuscle. 88
5.1 MCF10A epithelial organoids growth methodology and characterization. . . 97
5.2 mOMAs fucntionalization for collagen integration. 98
5.3 mOMAs factuation in 3D-collagen I. 99
5.4 Platform development for mechanical manipulation of MCF10A acini. 101
5.5 Mechanically stress-induced invasive cell phenotype. 102
5.6 Collagen deformation characterization 103
5.7 Investigating the role of myosin II in the invasive phenotype. 105
5.8 Investigating cellular processes involved in the epithelial invasive phenotype. 106

Tables

1 AuNRs optical and morphological characterization when HCl concentration is changed in the growth solution. 15

2 AuNRs optical and morphological characterization when ascorbic acid concentration is changed in the growth solution. 15

3 AuNRs optical and morphological characterization when seed concentration is changed in the growth solution. 16

4 AuNRs optical and morphological characterization when $AgNO_3$ concentration is changed in the growth solution. 17

5 AuNRs optical and morphological characterization when 2 different parameters were changed in the initial protocol. 18

6 Comparison between 2 modalities of automated reactors. 19

7 Determination of the best automated system ; evaluation scale from 1 to 5 where 1 = very bad, 2 = bad, 3 = neutral, 4 = good and 5 = very good. . . 21

8 Summary of all the conditions tested for pAAM-based composites polymerization. 47

9 Parameters used in the FEM analysis of solid deformation 92

Bibliographic Note

This thesis is a compilation of non-published work and the following publications :

•Berna Özkale, **Raquel Parreira**, Ahmet Bekdemir, Lucio Pancaldi, Ece Özelçi, Claire Amadio, Murat Kaynak, Francesco Stellacci, David J. Mooney, and Mahmut SelmanSakar. Modular soft robotic microdevices for dexterous biomanipulation.*Lab on a Chip*, 19(5) :778–788, 2019.

Contribution : B. O., **R. P.**, A. B. together developed the nanoparticle synthesis protocol. **R. P.** developed methods for assembling nanoparticles using microfluidics, designing soft robotic machines, polymerizing mechanisms using projection lithography. **R. P.** characterized the performance of the actuators and did the cell culture work.

•**Raquel Parreira**, Ece Özelçi, and Mahmut Selman Sakar. Remotely Controlled Colloidal Assembly of Soft Microrobotic Artificial Muscle. *Advanced Intelligent Systems*, 2(7) :2000062, 2020.

Contribution : **R.P.** led the study, performed all the experiments, and analyzed the data. E.O developed the computational models.

•**Raquel Parreira**, Ece Özelçi, and Mahmut Selman Sakar. Investigating Tissue Mechanics *in vitro* Using Untethered Soft Robotic Microdevices. *Frontiers in Robotics and AI*, 8(March) :1–12, 2021

Contribution : **R.P.** led the study, performed all the experiments, and analyzed the data. E.O developed the computational models.

•**Raquel Parreira**, Alaa Rushdy, and Mahmut Selman Sakar. Tensile loading transmitted through collagen matrix drives mammary acini toward invasive phenotype. **Under preparation**

Contribution : **R.P.** performed the experiments and analysed the data with the help of A.R. (Master's student supervised by **R.P.**).

1 Introduction

1.1 Problem Statement

Much of the understanding of the biological mechanisms that underlie cellular functions has been garnered from studying cells cultured on two-dimensional (2D) substrates. However, *in vivo*, cells primarily exist embedded within an information-rich three dimensional (3D) microenvironment that contains multiple extracellular matrix (ECM) components. The microscale architecture of these fibrous networks constrains spatially where cells can form adhesions and imparts complex mechanical characteristics due to viscoelastic response to loading and fiber alignment. Beyond serving as a mechanical support and mechanical communication network for cells, the spatial presentation of diffusible factors is dictated by the structure and porosity of the surrounding ECM.

Given these numerous intricacies, making sense of the dynamic communication among cells connected through a structurally complex fiber network requires a rigorous engineering analysis. To achieve this task, it is essential to develop technologies that can probe the dynamics of multicellular interactions in their social context at multiple length and time scales.

The most common approach to identify the physical mechanisms that drive 3D tissue formation and remodeling is to disrupt the system with physical (e.g. laser ablation), pharmacological, or genetic perturbations, and observe the motion of cells or tissue markers to determine the forces qualitatively. The tracking of the marker positions as they move over time enables the creation of velocity profiles and deformation maps. Recent technological advancements based on visualization of calibrated probes such as traction force microscopy and fluorescence force spectroscopy (e.g. FRET sensors, DNA probes, oil microdroplets) have made it possible to quantitatively measure some of these mechanical stresses and strains inside living tissues. Optogenetic approaches offer a versatile toolbox for the precise spatiotemporal control of signaling pathways in mammalian cells. With this technique, cytoskeletal activities regulated by RhoGTPases, kinesin and myosin are put under the control of optical stimulation by genetically encoding light activated proteins. While these techniques are proven to be instrumental, one cannot simply knock out a mechanical process in the same way as one knocks out a gene, and there is no direct mapping between gene circuits and the mechanical events under their control. It is clear that manipulating the activity of a few genes or proteins will not reveal the whole picture.

1.2 Background

1.2.1 3D culture models and mechanobiology

Cell aggregates, in the form of spheroids and organoids, better recapitulate the microenvironment of native tissues and organs compared to cells cultured on plastic substrates. There are a number of techniques to engineer these tissues, each addressing a different organ-specific requirement [1, 2]. Scaffold-free methods include hanging drops, non-adherent substrates, microfabricated wells, rotating bioreactors while certain tissues are formed within scaffolds using molding or microfluidic chips [1, 2].

In the context of this thesis, here, I highlight the importance of characterizing and manipulating tissue mechanics for better mimicking in vivo conditions and to discover novel treatments. Seminal work has shown that stem cell differentiation depends on the stiffness of the surrounding substrate [3]. The mechanical properties of the ECM ideal for the growth of organoids significantly differ from the conditions required for proper differentiation and self-organization during maturation stages [4]. One way to address this need is to engineer materials with photo-switchable crosslinkers and ligands. Changing the structure of the matrix allows dynamic tuning of matrix stiffness [5]. It has been shown that softening of the ECM promoted crypt formation of intestinal organoids while the original stiff matrix favored the organoid growth [6].

Complimentary to the intrinsic mechanical properties of tissues, cells are continuously subjected to dynamic or sustained mechanical loads that trigger mechanoregulatory signaling [5]. Mechanical forces, such as compression and shear stress, play important roles in the development of organisms and progression of diseases. The translation of mechanical cues into biological responses is called mechanotransduction. Mechanotransduction is involved in cell differentiation, migration, ECM remodeling, and phenotypic transition such as epithelial to mesenchymal transition. The formation of the blastocyst is a representative example. While cells proliferate in the blastula, they are subjected to compression forces that activates several biological pathways, leading to proper differentiation. As a result, multiple layers (i.e., ectoderm, mesoderm and endoderm) are formed that later give rise to different types of tissues and organs. Having a closer look at the single cell level, each individual cell senses the compaction forces and stiffness of the ECM through integrins and cadherins. This information is transmitted to the nucleus through the involvelment of several intracellular proteins, triggering responses at the genome or proteome level [5, 7]. Another textbook example occurs during the early stages of carcinogenesis. Uncontrolled cell proliferation leads to tensile and compressive stresses. Cells remodel their microenvironment as a response, stiffening the matrix and aligning the fibers. The remodeled matrix provides a highway for the cells to first invade the matrix and, later, intravase into the bloodstream. Here, they are subjected to shear stress due to blood flow, which plays an important role in the tumor cell extravasation [8].

The take home messages from these briefly summarized examples is that mechanotransduction is a mechanochemical cellular response to mechanical signals. These signals are transmitted by the ECM and are sensed by transmembrane receptors and adhesion molecules [9, 10]. Two recognized integrin-mediated pathways are the hippo signalling pathway, regulated by the transcriptional co-activator Yap/TAZ (Yes-associated protein/transcriptional co-activator with PDZ binding motif) and the MAPK pathway (mitogen-activated protein kinase) pathway, regulated by three protein families including ERK (extracellular signal-regulated kinase) [5, 9, 10, 11, 12, 13, 14, 15]. Other pathways can be activated or inhibited by the involvement of mehcanosensitive ion channels [5, 9]. Some signaling molecules that have been shown to be activated by mechanical stresses via intergins are the small GTPases (Rho, Rac), protein tyrosine kinases (FAK, src), Shc, β-catenin, ERK1/2, protein kinase C and PI-2-kinase [9, 15, 16, 17].

1.2.2 Wireless Microactuators

The main argument of this thesis is that application of controlled forces within tissue is instrumental to study mechanotransduction and tissue mechanics. In this section, existing tools are summarized. Traditionally, mechanical characterization of solid tissues has been done using MEMS devices or cantilever based measurement instruments (e.g., Atomic Force Microscope). Alternatively, various bulk compression and stretching devices are used for long-term mechanical stimulation [18, 19, 20, 21, 22]. More relevant to our approach, deformable actuated materials with known mechanical properties are used to characterize the local mechanical properties of tissues *in situ.* Seminal work has shown that ferrofluid droplets can be used as wireless microactuators [23]. These droplets consist of fluorinated oils and magnetic nanoparticles. Application of a uniform magnetic field deforms the droplet according to the mechanical properties of the surrounding tissue. Visual evaluation of the 3D deformation gives quantitative information about the stiffness of the matrix. A disadvantage of these droplets is the fact that they are incompressible and non-stretchable, hence, it is not possible to directly measure or apply isotropic forces. To overcome this issue, microgels made of alginate [24] and pAAm [25, 26, 27] have been developed.

As an alternative approach, a magnetic tweezer could be used to pull injected nanoparticles and apply localized forces to embryonic tissues [28]. Same technique was later used for temporal biomechanical characterization of the the blastocyst-stage mouse embryos [29]. This technique is quite invasive because the tip of the electromagnetic must be held very close to the sample, and it can only actuate one area at a time. To address some of these limitations, a more advanced magnetic manipulation system has been recently introduced [30].

The most relevant literature to our work involves the use of thermoresponsive pNIPAM microbeads [31]. These beads are injected into cells aggregates (*in vitro*) or tissues (*in vivo*). Living tissues are kept at 37°C, above the Lower critical solution temperature (LCST) of NIPAM. At this temperature, the polymer shrinks. By lowering the temperature, the bead is made to swell. The differences in size and shape between the original and the regained configuration were used to quantify the stiffness of the matrix.

Although there is the progress in the modulation of active stresses within living tissues, the solutions are either cumbersome to apply or provide very specific options. We converged to the same solution with another group [32], and once they published their results, we decided to follow their footsteps. In this article, nanoparticles that translate optical energy into mechanical work were introduced. This thesis expands the potential of those actuators in two distinct ways. First, we introduce a repertoire of techniques to bring those nanoactuators together to assemble microactuators and integrate them into tissues (see sections 3-5). This is important considering the level of forces required to transmit forces and deform matrices inside living tissues. Second, by synthesizing nanoparticles with not only optomechanical properties but also catalytic and electromagentic features (see Section 2). The microactuators are compatible with target tissues, in the sense that they have a comparable stiffness in the kPa range. They can generate forces from nN to μN range, they can provide strains up to 0.5, and it is possible to engineer their surface biochemistry for adhesion and transmission of forces.

1.2.3 Nanotechnology

The success of our approach depended on harnessing nanotechnology. More specifically, the proper and efficient synthesis and chemical functionalization of structures at the nanoscale has been instrumental for the success of our approach [33]. It is important to note that the governing physics at the macro scale (from milimeter up) may not apply to nanoscale. An important concept is the surface energy. The surface energy increases with decrease of the diameter of a particle, a consequence of the increase of the density of atoms on the surface. This is not only dependent on the size but also the surface roughness and curvature. Nature has the tendency to lower surface energy. One can take advantage of this tendency to perform a diversity of chemical reactions including catalysis. Furthermore, nanoscale materials have relatively high surface area, in the range of 100-1000$m^2.g^{-1}$. Consequently, reactions with these materials will have higher throughput and efficiency than with the equivalent macroscale materials [33]. Concave surfaces are less soluble than convex surfaces because removing a layer from a concave surface would increase the surface area and consequently the surface energy. On the other hand, removing a layer from a convex surface would decrease surface area, thus decrease surface energy, which is favorable. This concept is very important when synthesizing hollow structures, nanotubes and nanoporous materials [33].

1.3 General Objectives and Methodology

The objective of this thesis is to develop novel wireless soft microactuators that can be seamlessly integrated with high-throughput bioengineering platforms and produce physiologically relevant mechanical forces to establish an active dialogue with the cells living within tissues and study the cell-ECM organization. We postulate that the ability to join the cellular communication network and interfere with the biological processes in 3D will lead to a better understanding of morphogenesis and regeneration, and can aid in developing treatments that ensures a microenvironment with a distribution of signals that minimizes disease progression, particularly in cancer.

I primarily focused on the following scenario. The 3D cell cluster is embedded inside a fibrous collagen matrix (Figure 1.1). We would like to apply forces at a distance from the cells so that we can study the transmission of forces, signaling pathways, remodeling of the matrix as a response, and how the mechanical stimulation changes as a result of matrix remodeling. We can envision that the matrix could be rationally designed in a certain way (i.e., fiber are aligned) to perform a combinatorial study. To this end, optomechanical nanoactuators could be harnessed in two different ways. First strategy is based on the direct use of nanoactuators. The nanoactuators could be incorporated into the matrix before the polymerization takes place, or injected later into the target space. The second strategy involves the assembly of microactuators from the nanoactuators. Considering the size, it is preferable to incorporate microactuators before the polymerization of the matrix as injection of microparticles may disrupt the integrity of the culture system. Nevertheless, I developed a material system that is compatible with all these strategies. Figure 1.2 summarizes the different techniques used throughout the thesis. The nanomaterial is syntesized in a way that (i) they can be assembled using bottom-up and top-down manufacturing techniques, (ii) they adhere to extracellular matrix proteins, and (iii) they display multiple functionalities in an efficient way including plasmon resonance based heating, magnetism, and catalytic activity. The rest of the methodology involves effective use of engineering including projection lithography, microfluidics, and robotic micromanipulation. Proof-of-concept demonstrations with biological samples provide evidence to support the argument that this work will have long-term impact on mechanobiology research.

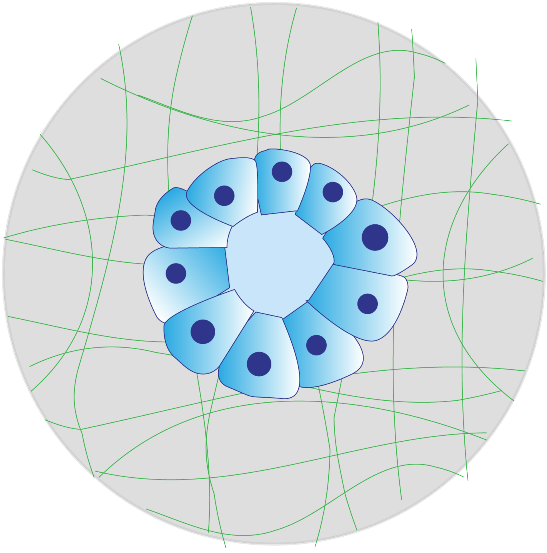

Figure 1.1 – Schematic illustration of an organoid embedded inside a fibrous matrix.

I suggested alternative solutions for the mechanical loading of organoids suspended in fluids. This type of manipulation requires loading of the samples in a chamber and compression through the movement of an indentation apparatus. I show that these hydrogel devices can be fabricated within microfluidic chambers, enabling the creation of a high-throughput testing platform.

1.4 Thesis Outline

The thesis gradually builds up the complexity of the material system. Chapter 2 describes the synthesis of the nanoactuators and the factors that are important for the optimization of their performance. Chapters 3 and 4 describe the development of wirelessly powered microactuators and soft robotic devices. The mechanical and phsyical properties of the structures are extensively characterized to aid the development of future solutions in this domain and compare the presented approach with the alternative solutions. The work presented in Chapter 5 has not been completed yet. So far, we have shown that externally applied mechanical stress has a clear impact on the biomechanical interactions among mammary gland organoids within collagen matrices. Future work will close the loop and connect the work presented in Chapters 2-4 with the biomechanics problem introduced in Chapter 5. Chapter 6 provides a perspective on the future potential of the presented materials and devices.

The detailed protocols are presented at the end of each chapter. This way, I intend to improve the dissemination of the techniques to the community without making it difficult to follow the results. Hopefully, a number of other groups will be able to replicate our work and make discoveries in a number of bioengineered model systems.

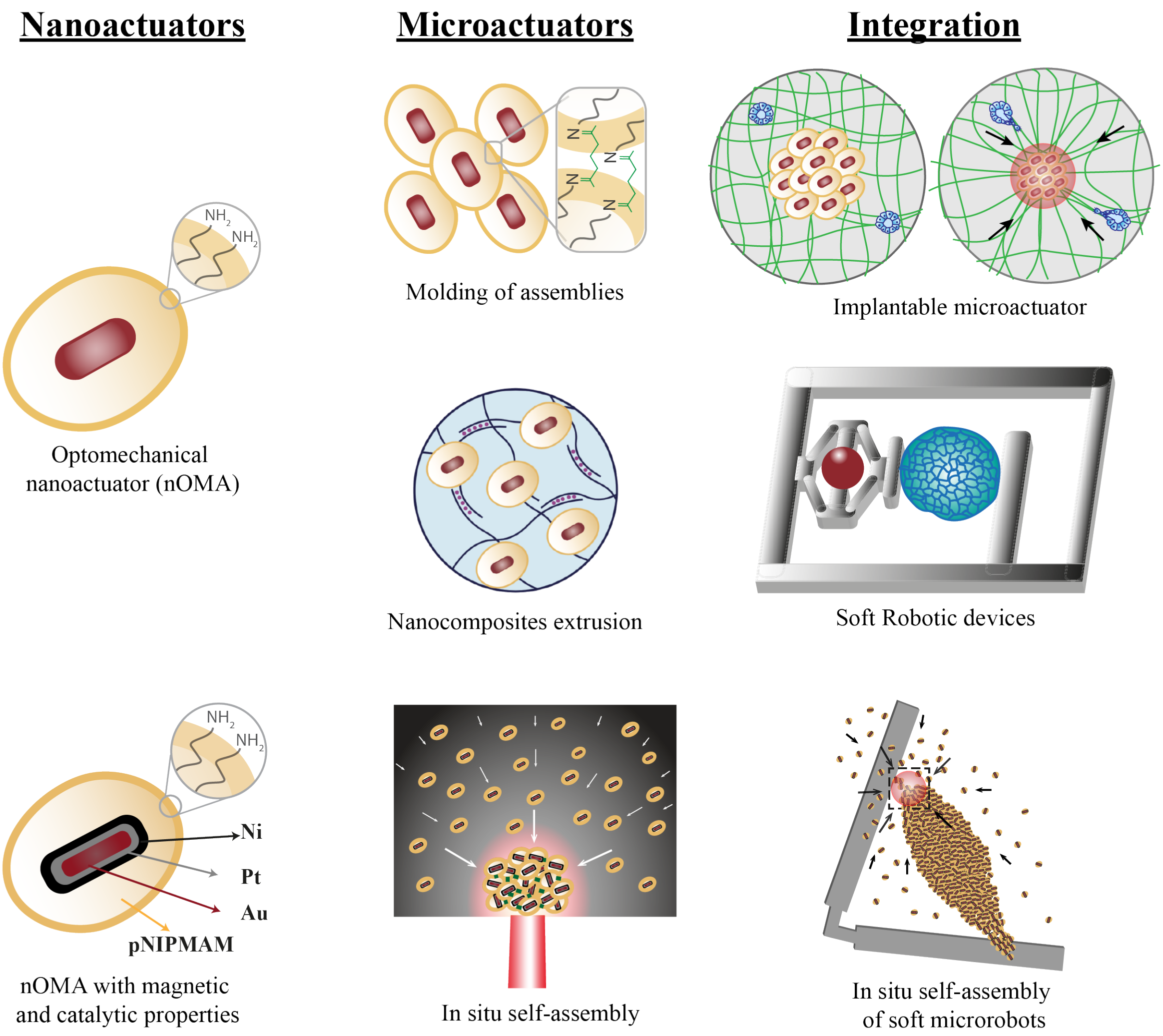
Nanoactuators
Microactuators
Integration
NH$_2$
NH$_2$
Optomechanical nanoactuator (nOMA)
Molding of assemblies
Implantable microactuator
Nanocomposites extrusion
Soft Robotic devices
Ni
Pt
Au
pNIPMAM
nOMA with magnetic and catalytic properties
In situ self-assembly
In situ self-assembly of soft microrobots

FIGURE 1.2 – Schematic summary of the methodologies developed and applications of this thesis. The optomechanical nanoactuator (nOMA) can provide forces in range of the picoNewtons. Gold nanoparticles can efficiently transduce optical light into heat that drives a rapid and powerful collapse of the coating thermoresponsive hydrogel. In order to scale up the forces applied, from pN up to μN, and the size range, these nOMAs are used as building unit of more complex and active micromachines. Several methods are shown to build up higher order structures from molding with microfluidics and casting with biopolymers as nanocomposites. These micromachines can be seen as micromuscles, that can be integrated in biological systems, to apply forces and drive mechanotransduction responses, or can be integrated into soft robotic devices with multiple functionalities. By adding magnetic and catalytic properties to the nOMA, it was discovered a new methodology to bring and click the particles together wirelessly, that can be used to build multifunctional micromachines *in situ* and wirelessly, mimicking out-of-equilibrium assembly processes found in nature.

2 Chemical Synthesis of Optomechanical Nanoactuators

2.1 Introduction

Gold is a noble metal represented by the symbol Au (from the Latin word *Aurum*). Gold structures are stable towards corrosion and oxidation even at high temperatures [34], and inert to acids and bases. Gold reacts with thiol groups, -SH, due to its affinity to sulfur at room temperature and atmospheric pressure. If the temperature is raised above 80^{o}C, thiol groups can be removed or exchanged easily, since they adsorb to the gold surface by van der Waals interactions [33]. Nevertheless, gold surfaces can be oxidized under special conditions, having several oxidation states ranging from -1 to $+5$, the most common and stable states being Au(I) (Au^{+1}) and Au(III) (Au^{+3}) [35].

Metals are good conductors as the electrons can freely move on their surfaces. Notably, exposing gold nanoparticles to electromagnetic fields provokes the migration of free electrons, generating a dipole that will oscillate at a certain frequency. The oscillation of free electrons on the surface of a conductor is called the plasmon effect, and the plasmon resonance of a particle is the natural frequency at which its free electrons oscillate at the highest amplitude. The resonance frequency is where the material absorbs most energy compared to other frequencies. Accordingly, the distinctive color of gold nanoparticle suspensions is a result of this phenomenon [33].

The number of plasmon resonance frequencies (PRFs) depends on the size and shape (aspect ratio) of the nanoparticle [36]. Spherical gold nanoparticles have a single PRF that can be tuned from 510 nm to 540 nm by playing with the diameter of the particle. The aqueous suspension of spherical gold nanoparticles has a ruby red color as a result of the selective absoption of green light [37, 38]. Nanorods have two different resonant peaks depending on which axis the electrons oscillate ; along the short axis (transversal) or along the long axis (longitudinal). Longitudinal surface plasmon resonance (LSPR) is observed at a lower frequency than the transversal surface plasmon resonance (TSPR), hence at higher wavelength, due to the larger distance the electrons must travel.

When the particles are excited (i.e, the particles are exposed to light) at their PRF, the plasmons will enter in resonance state and start absorbing light. They remain in the excited state for a few femtoseconds, and when they return to their initial state they release energy in the form of heat [33, 39]. The heat generated is directly related to the intensity of the incident light and the absorption cross-section of the particles. Our actuation paradigm is based on this physical phenomenon.

We encapsulated the gold nanorods inside a thermoresponsive polymer. The polymer-nanorod assembly is referred to as the optomechanical nanoactuator (nOMA). The nanoactuator transforms optical energy first into heat and subsequently into mechanical work due to the polymer collapse [33]. To be able to excite the particles, the light must go through the biological specimen with minimal damage to the cells and ECM. There is a biological window or water window in the near-infrared (NIR) spectrum where the absorbance of light by the aqueous tissues is relatively small, making NIR the ideal choice for excitation of the actuators. To this end, the geometry of the nanorods are designed to set their LSPR in the NIR spectrum [33, 39].

2.2 Synthesis of gold nanorods

Gold nanorods can be synthesized using either the one-step method or the two-step method. The key concept is to carefully control the parameters for the thermodynamic and kinetic reactions because they may have conflicting outcomes. The thermodynamic control focuses on the energy of products and reagents. In our synthesis reaction, it is responsible for the stabilization of crystallographic facets. The kinetic control focuses on the pathway from reactants to products, therefore, it is responsible for the anisotropic growth of the nanorods. Parameters such as concentration, temperature and mass transport will determine the properties of the final products [36]. In the two-step method, these two reaction controls are separated and done step-wise, allowing a homogeneous nucleation or seed formation that is followed by the growth of the seeds into rods under completely different conditions. This strategy results in high monodispersity, quality and reproducibility [40, 41, 42]. In this thesis, the two-step gold nanorod synthesis protocol was used, where we prepare a seed solution and then a growth solution.

2.2.1 Seed solution

The seed solution is the equivalent of a nucleation step, where the seeds that are typically smaller than 5nm in diameter are formed. The reaction is controlled thermodynamically. The reaction is very fast, taking only 2 min to complete. In order to ensure the production of a monodisperse suspension, we add a strong reducing agent such as sodium borohydride, $NaBH_4$.

For the nucleation to happen, the ingredients must include a reducing agent, a gold precursor, and a surfactant. The surface energy of growing nanoparticles is reduced by ligand-capping that is initiated by the surfactant. This way, we alleviate the tendency of the particles to aggregate and stabilize their size within the prescribed range [33]. The most commonly used surfactant is CTAB (Hexadecyltrimethylammonium bromide), and the most widely used gold precursor is tetrachloroauric acid, $HAuCl_4$. Due to the higher ionic strength of bromide ions ($Br^- > Cl^-$), chloride ligands will be replaced by bromide anions as shown below.

$$[AuCl_4]^- \rightleftarrows [AuCl_3Br]^- \rightleftarrows [AuCl_2Br_2]^- \rightleftarrows [AuClBr_3]^- \rightleftarrows [AuBr_4]^-$$

Here on, $AuBr_4^-$ forms complexes with -CTA, which increases the oxidation potential of gold. In the presence of $NaBH_4$, gold will go from the third oxidation state, Au(III), to zero oxidation state, Au(0), and form the particles.

2.2.2 Growth solution

The anisotropic growth is governed by a kinetic control and it is a relatively slow process. Identical to the seed solution, the precursor agent for the gold is $HAuCl_4$ and the surfactant is CTAB in the growth solution. The micelles formed by the cations of the surfactant serve as a mold for directed growth of the particles, which implies that its concentration is an important factor to determine the size of nanorods. Higher concentrations of CTAB lead to smaller rods, which is a consequence of the adsorption of higher concentration micelles. Unlike in the seed solution, here we use a weak reducing agent to ensure that the reduction is not complete and nucleation is not allowed as shown below. In other words, Au(III) is reduced to Au(I) and never to Au(0).

$$Au^{3+} + 2Au^{0} \rightleftharpoons 3Au^{+}$$

The most commonly used reducing agent is ascorbic acid, AA. The activity of AA is highly dependent on the pH of the solution. We prefer a lower reducing potential to modulate the growth rate of the rods and at the same time preventing secondary nucleations. To this end, the reaction is performed at acidic pH. The pH of the suspension is regulated with hydrochloric acid, HCl.

Another important agent that influences the shape of the gold nanorods is silver ions, Ag^+, which is added to the solution as silver nitrate, $AgNO_3$. Silver ions are responsible for higher reduction selectivity at the tip of the rods, and they stabilize the lateral (longitudinal) facets. As a rule of thumb, the higher the Ag^+ concentration is the higher the aspect ratio and yield. To increase the range of aspect ratios without losing efficiency, additives like sodium oleate, NaOL, can be added. In the absence of AA, NaOL double bond reduces slowly $HAuCl_4$. It was shown that the optimal molar ratio between Au(III) and AA is around 3 :1 when both surfactants, NaOL and CTAB, are present [43].

Once the growth solution is ready, the seed solution is added. Determining the right concentration of the solutions is crucial for the intended purpose. Increasing the seed concentration will lead to smaller rods with higher aspect ratios. Another important parameter is the temperature of the reactor. The reaction rate is lower at lower temperatures, favoring the anisotropic growth of nanorods.

It is important to mention that the surfactants used in this thesis are not exclusive. For instance, one can replace NaOL by KOL and may obtain similar results. That is to say, the cations Na^+ and K^+ do not directly affect the reaction. On the other hand, if a surfactant with unsaturated long-chain such as sodium linoleate is used, there might be changes in the sizes of the rods due to the presence of two double bonds in the fatty acid chain instead of one [43, 44].

The final suspension first goes from a yellow color to a colorless solution due to the reduction of Au(III) by the AA. Later, the color changes to dark red due to the chosen aspect ratio of the nanorods (Figure 2.1).

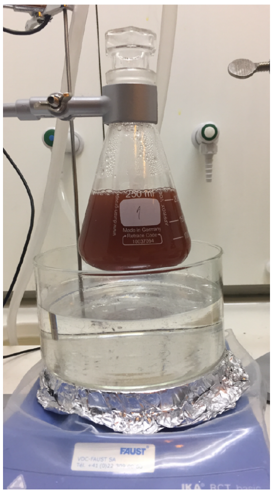

FIGURE 2.1 – AuNRs final reaction suspension. Picture of the final reaction suspension of the AuNRs. The AuNRs produced under these conditions have an LSPR peak at 780 nm and, in average, 95 nm length and 30 nm diameter.

2.3 Exploring the design space

As mentioned before, the synthesis of gold nanorods is a very delicate process because a number of parameters affect the overall size, shape, and stability of the product. At the end of the first step of synthesis, small spherical gold nanoparticles (ranging from 1 nm to 5 nm in diameter) are formed as precursors. The aspect ratio of the final product in the form of nanorods can be finely tuned by playing with experimental conditions. Keeping the intended biological applications in mind, we adjusted the experimental conditions to synthesize particles that respond to NIR. Apart from deep penetration in tissues, this decision complies with fluorescence imaging of proteins using commercially available dyes in the visible light spectrum.

The detailed protocols for synthesis and characterization of the gold nanorods can be found in the subsection 2.7. We confirmed that the nanorods synthesized following the optimized protocol exhibited two different plasmon resonance bands, transverse and longitudinal, as represented in the absorbance spectrum shown in Figure 2.2a. The TSPR was found to be at 530 nm while the LSPR was at 780 nm. We measured the average size of the particles from the transmission electron microscopy (TEM) images (Figure 2.2b.). The nanorods were on average 95 ± 6 nm long and 30 ± 2 nm wide, having an aspect ratio of 3.2 ± 0.8 [45, 46].

In the following sections, I describe the protocols to synthesize gold nanorods with different LSPR. As discussed before, there are 4 main parameters that have a direct impact on the morphology of the nanorods : seed concentration, pH, ascorbic acid concentration, and silver nitrate concentration. Each one of these parameters was tuned in isolation or combination in pairs to produce monodisperse suspension of gold nanorods with desired aspect ratios.

2.3.1 The influence of pH

Decreasing the concentration of HCl by a factor of 2 lead to a blue shift of the LSPR by 80 nm and an increase of the width at half maximum of the gaussian curve (2.3),

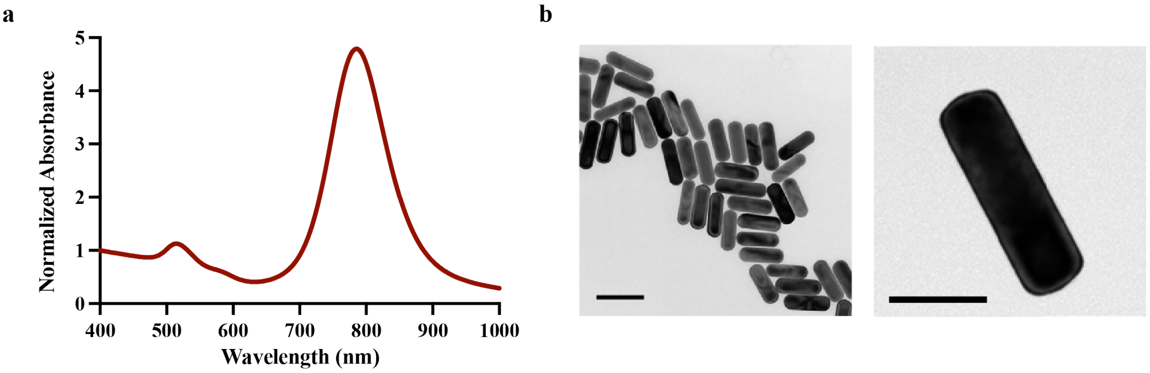

FIGURE 2.2 – AuNRs characterization. a. Representative UV/Vis spectrum of a batch of AuNRs. b. Representative TEM images of AuNRs. Scale bars : 50nm

indicating a decrease in the aspect ratio and monodispersity, respectively. Decreasing HCl concentration further (augmentation of pH) led to a more pronounced decrease in aspect ratio and yield. Table 1 shows how the aspect ratio of the particles change with the increase of pH. Notably, TSPR barely changed (5-10 nm shift in the spectrum) since the seeding conditions were kept constant.

At higher pH, the reducing potential of ascorbic acid is higher, which lead to a rapid non-homogeneous growth of the nanorods and to a complete reduction of Au(III). As a consequence, both length and diameter of the rods are affected. The main conclusion of this study is changing the kinetics without regulating the stoichiometry of the reaction leads to a decrease in yield and monodispersity.

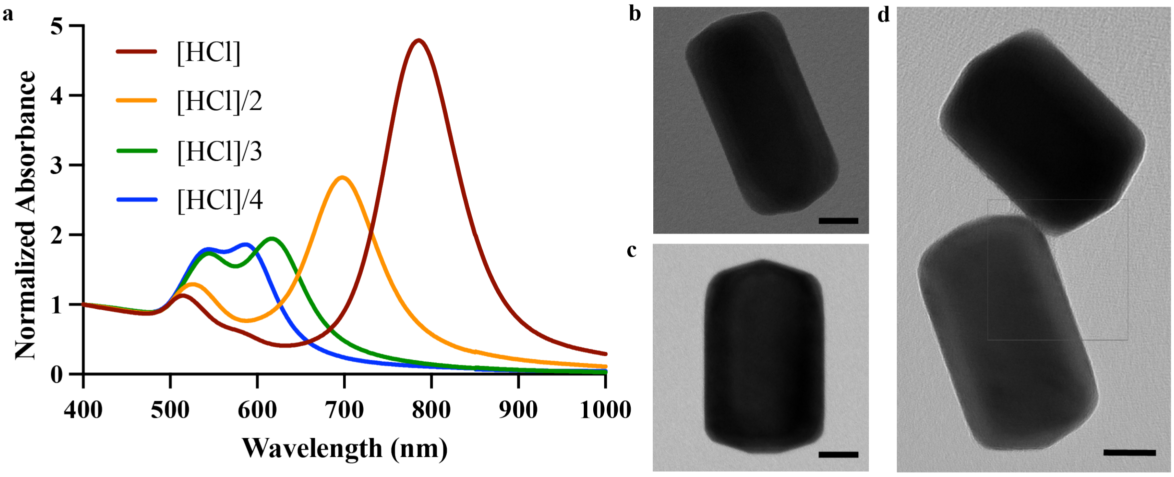

FIGURE 2.3 – AuNRs characterization under different synthesis conditions, with change in hydrochloric acid (HCL) concentration. a. Representative UV/Vis spectrum of the different batches of AuNRs. Red : standard synthesis conditions ; yellow : [HCl]/2 ; green : [HCl]/3 and blue : [HCl]/4. b-d. Representative TEM images of AuNRs under the different synthesis conditions. b. [HCl]/2 c. [HCl]/3 d. [HCL]/4 Scale bars : 20nm [47]

Parameter change	Length [nm]	Diameter [nm]	Aspect ratio	LSPR [nm]
[HCl]	95 ± 6	30 ± 2	3.2 ± 0.8	780
[HCl]/2	100 ± 16	49 ± 4	2.0 ± 0.4	700
[HCl]/3	94 ± 7	65 ± 4	1.4 ± 0.1	615
[HCl]/4	73 ± 7	53 ± 6	1.37 ± 0.2	585

TABLE 1 – AuNRs optical and morphological characterization when HCl concentration is changed in the growth solution. The length and diameter were obtained from TEM images and the aspect ratio was calculated from those. The LSPR was obtained from the absorbance spectra [47].

2.3.2 The influence of the ascorbic acid concentration

Increasing AA concentration led to a blue shift in the LSPR (Figure 2.4a) as a manifestation of a decrease in the aspect ratio of the particles (see Table 2 and Figure 2.4). The width of the curve remained approximately the same, indicating that the yield and monodispersity did not change. The increase of AA concentration led to a faster reduction of the Au (III), resulting in shorter rods. The diameter of rods remained constant because the reduction potential of AA was not affected, therefore, secondary nucleations and complete reduction of gold were avoided.

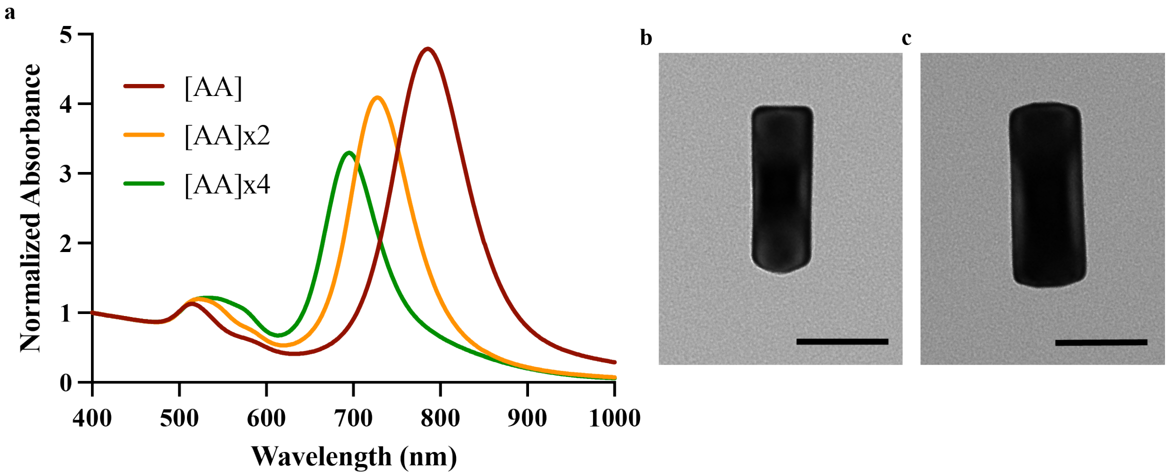

FIGURE 2.4 – AuNRs characterization under different synthesis conditions, with change in ascorbic acid (AA) concentration. a. Representative UV/Vis spectrum of the different batches of AuNRs. Red : standard synthesis conditions ; yellow : [AA]x2 and green : [AA]x4. b-c. Representative TEM images of AuNRs under the different synthesis conditions. b.[AA]x2. c. [AA]x4. Scale bars : 50nm [47].

Parameter change	Length [nm]	Diameter [nm]	Aspect ratio	LSPR [nm]
[AA]	95 ± 6	30 ± 2	3.2 ± 0.8	780
[AA]x2	92 ± 7	36 ± 2	2.6 ± 0.3	725
[AA]x4	74 ± 12	33 ± 6	2.2 ± 0.5	700

TABLE 2 – AuNRs optical and morphological characterization when ascorbic acid concentration is changed in the growth solution. The length and diameter were obtained from TEM images and the aspect ratio was calculated from those. The LSPR was obtained from the absorbance spectra [47].

2.3.3 The influence of the seed concentration

As shown in the absorbance spectrum in Figure 2.5 and Table 3, increasing the seed concentration resulted in thinner rods. The aspect ratio increased in the process, which manifested in the higher LSPR (red shift). Decreasing the seed solution resulted in thicker rods. Larger bandwidth indicates a decrease in monodispersity.

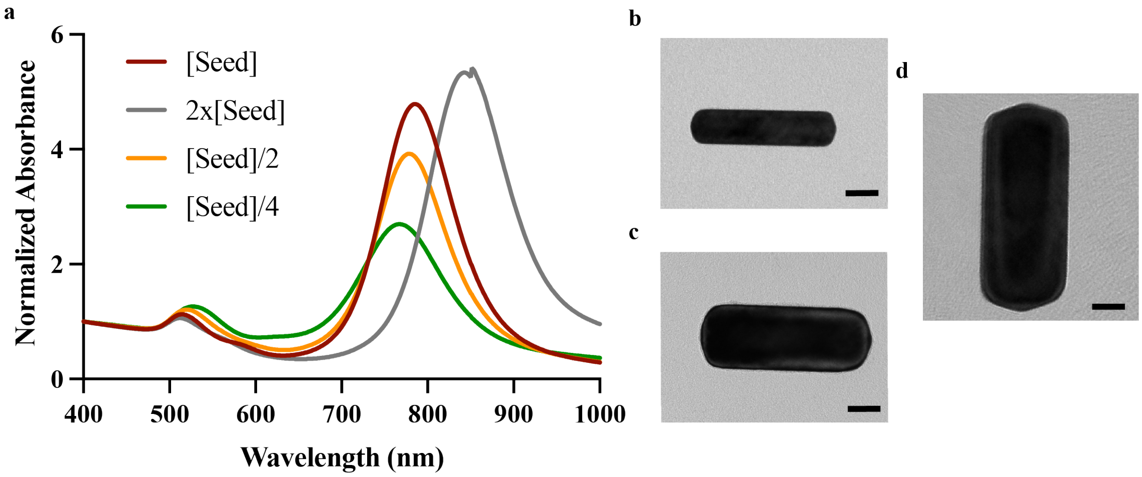

FIGURE 2.5 – AuNRs characterization under different synthesis conditions, with change in seed concentration. a. Representative UV/Vis spectrum of the different batches of AuNRs. Red : standard synthesis conditions ; grey : [seed]x2 ; orange : [seed]/2 and green : [seed]/4. b-c. Representative TEM images of AuNRs under the different synthesis conditions. b.[seed]x2. c. [seed]/2. d.[seed]/4. Scale bars : 20nm [47].

Parameter change	Length [nm]	Diameter [nm]	Aspect ratio	LSPR [nm]
[Seed]	95 ± 6	30 ± 2	3.2 ± 0.8	780
[Seed]x2	86 ± 16	23 ± 4	3.7 ± 0.9	845
[Seed]/2	107 ± 7	35 ± 3	2.9 ± 0.3	765
[Seed]/4	133 ± 7	51 ± 2	2.6 ± 0.2	765

TABLE 3 – AuNRs optical and morphological characterization when seed concentration is changed in the growth solution. The length and diameter were obtained from TEM images and the aspect ratio was calculated from those. The LSPR was obtained from the absorbance spectra [47].

2.3.4 The influence of the silver nitrate concentration

Higher concentrations of silver ions is expected to promote the anisotropic growth of the rods. We lowered the concentration to reduce the aspect ratio, and consequently the LSPR. As expected, decreasing Ag^+ concentration led to a blue shift in the LSPR and an increase of the bandwidth (Figure 2.6). The length of the nanorods decreased significantly with the first two dilutions while the diameter remained constant (TABLE 4). This result is consistent with the theory that silver cations promote selective gold reduction at the tips by stabilizing the lateral facets. However, with further decrease in the concentration of silver nitrate, the diameter increased. This counter intuitive result could be an indication that concentration of Ag^+ was too low to stabilize the longitudinal facets. Nevertheless, aspect ratio decreased with every dilution.

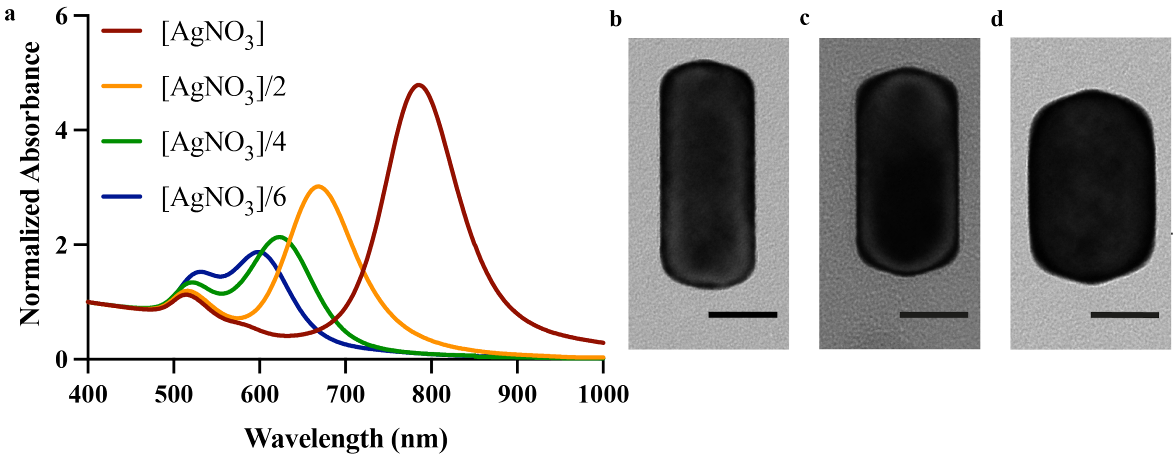

FIGURE 2.6 – AuNRs characterization under different synthesis conditions, with change in silver nitrate ($AgNO_3$) concentration. a. Representative UV/Vis spectrum of the different batches of AuNRs. Red : standard synthesis conditions ; yellow : $[AgNO_3]/2$; green : $[AgNO_3]/4$ and blue : $[AgNO_3]/6$. b-c. Representative TEM images of AuNRs under the different synthesis conditions. b.$[AgNO_3]/2$. c. $[AgNO_3]/4$. d.$[AgNO_3]/6$. Scale bars : 20nm [47].

Parameter change	Length [nm]	Diameter [nm]	Aspect ratio	LSPR [nm]
$[AgNO_3]$	95 ± 6	30 ± 2	3.2 ± 0.8	780
$[AgNO_3]/2$	61 ± 7	26 ± 3	2.3 ± 0.4	670
$[AgNO_3]/4$	53 ± 8	27 ± 4	2.0 ± 0.4	625
$[AgNO_3]/6$	67 ± 8	44 ± 4	1.5 ± 0.2	600

TABLE 4 – AuNRs optical and morphological characterization when $AgNO_3$ concentration is changed in the growth solution. The length and diameter were obtained from TEM images and the aspect ratio was calculated from those. The LSPR was obtained from the absorbance spectra [47].

2.3.5 Combinatorial analysis

The components may have a synergistic or antagonistic effects on the monodispersity and yield of the reaction. I studied the combined effects of the concentration of the seed (as the major factor) and the three other parameters. The resulting absorbance spectra are shown in Figure 2.7 and the TEM data analysis in TABLE 5.

I made manipulations that would create a blue shift in the LSPR. In the first scenario, seed concentration was doubled and HCl concentration was reduced 3 times. The spectrum showed a nice Gaussian curve with the LSPR located at 645 nm. Compared to the results where only HCl was changed by the same amount (Figure 2.3 and Table 1), simultaneous increase in the seed concentration resulted in a spectrum with better resolved peaks and higher absorbance value at the LSPR, which together indicated higher yield.

In the second scenario, both seed and AA concentrations were doubled. We did not observe a significant change in the LSPR wavelength. Nevertheless, the signal was dampened around the LSPR. Notably, there were two TSPR peaks, indicating that the sample was polydisperse. The length and diameter were smaller, and the aspect ratio slightly increased, which is consistent with the change in the absorbance spectrum.

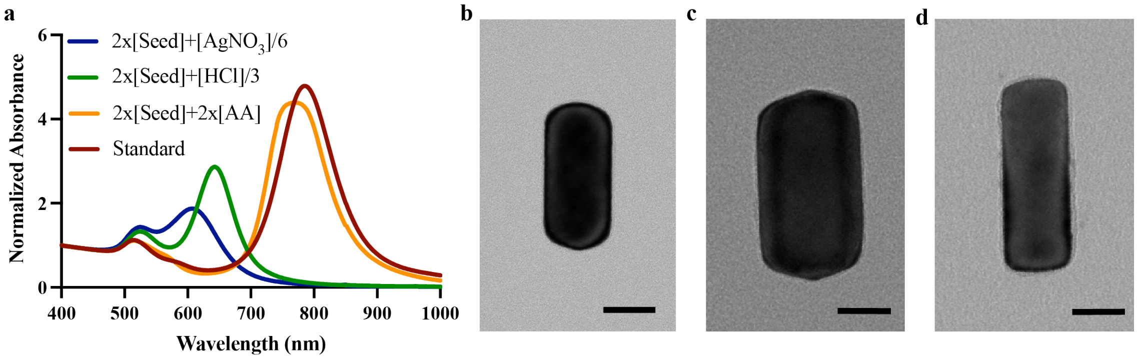

Figure 2.7 – AuNRs characterization under different synthesis conditions, with change of two parameters at a time. a. Representative UV/Vis spectrum of the different batches of AuNRs. Red : standard synthesis conditions ; yellow : [Seed]x2 + [AA]x2 ; green : [Seed]x2 + [HCl]/3 and blue : [Seed]x2 + [$AgNO_3$]/6. b-c. Representative TEM images of AuNRs under the different synthesis conditions. b.[Seed]x2 + [$AgNO_3$]/6. c. [Seed]x2 + [HCl]/3. d.[Seed]x2 + [AA]x2. Scale bars : 20nm [47].

Finally, we increased the seed concentration while decreasing Ag concentration. There was a considerable blue shift in the LSPR, going from 780 nm to 610 nm.

Parameter change	Length [nm]	Diameter [nm]	Aspect ratio	LSPR [nm]
Standard protocol	95 ± 6	30 ± 2	3.2 ± 0.8	780
2*[Seed] and [HCl]/3	75 ± 5	41 ± 4	1.9 ± 0.2	645
2*[Seed] and 2*[AA]	75 ± 5	23 ± 2	3.3 ± 0.3	765
2*[Seed] and [Ag]/6	57 ± 5	31 ± 4	1.8 ± 0.3	610
6*[Seed] and [Ag]/6	37 ± 6	20 ± 4	1.9 ± 0.5	590

Table 5 – AuNRs optical and morphological characterization when 2 different parameters were changed in the initial protocol. The length and diameter were obtained from TEM images and the aspect ratio was calculated from those. The LSPR was obtained from the absorbance spectra [47].

2.4 Toward automation of nanorod synthesis

Gold nanorods synthesis is a very delicate process with many parameters that must be continuously monitored. Furthermore, scaling up the synthesis is not straightforward because increasing the concentrations of reagents and reaction volumes would influence mass and heat transfer, compromising the reaction homogeneity. An automated reactor would address both issues. Automated systems improve reproducibilty, provide finer control over mass transport and mixing, enable real-time monitoring of key variables, and reduce time [48].

There are three types of chemical reactors : batch reactors, continuous stirred-tank reactors (CSTR), and plug flow reactors (PFR), where the last two are categorized as continuous reactors. In a discontinuous stirred-tank reactor, known as batch stirred tank reactor (BSTR), the reagents are added in the beginning of the reaction and mechanically mixed. As the name indicates, it is a discontinuous process and operates in a cyclic manner. Each cycle comprise a production period, a discharge period, a washing period and a loading period. During the reaction period, the concentrations of reagents and products are modulated continuously. There is also a semi-continuous modality, where the reagents are added at different time points depending on the kinetics of the reaction. In a continuous reactor, the reagents are added continuously and products are discharged continuously. Depending on the configuration, the reagents are mixed with a mechanical stirrer or mixed at the junction of different tubes. At the laboratory scale, a PFR can be a microfluidic device or a milifluidic reactor. The comparative advantages and disadvantages of each reactor are listed in the Table 6.

TABLE 6 – Comparison between 2 modalities of automated reactors.

BSTR	PFR
• Easier to handle and to scale up • Easier maintenance • Smaller amounts produced	• Difficult to scale up but with its continuous modality, one can produce higher quantities avoiding the hurdles that come with the scale up of batch systems.
• Lower investment costs	• Higher investment costs
• Higher operation costs	• Low operation costs
• Flexible in terms of conditions and different products production	• Lower flexibility. Specific for one product.
• Lower homogeneity	• Higher homogeneity • Requires higher degree of specialization • More complicated designs • Excellent heat transfer and accurate temperature control • In the case of microfluidic and milifluidic devices, the mixing geometries and reaction channel sizes allow a fine control over the reagent addition timing on top of the thermal diffusion.

In a research laboratory setting, where multiple reactions are performed and they are continuously modified for different projects, a batch system is favorable. A market evaluation is shown in Table 7. Several criteria were taken into consideration :

- Reactor tank size. The tank should be big enough to scale up the reaction volume to 1L or more.
- Size of the system. The whole system must be small enough to fit inside the fume hood.
- Multiple reactors. We would like to run multiple reactions with different conditions for optimization.
- Multiple sensors. Detailed characterization of reaction kinetics.
- Cost. Lab budget is limited.

The most promising automated reactor for the intended purposes is Mya 4 Reaction station, which could perform several reactions in parallel with different type of tank reactors. It contains several controls and sensors, and the price was reasonable. Unfortunately, we could not arrange a demonstration in our laboratory and decided to pursue this direction later. I completed my studies using the reactor that I built myself.

Table 7 – Determination of the best automated system; evaluation scale from 1 to 5 where 1 = very bad, 2 = bad, 3 = neutral, 4 = good and 5 = very good. FTIR stands for Fourier-transform infrared spectroscopy and FBRM for Focused Beam Reflectance Measurement [49, 50, 51, 52, 53].

Critera	**Syrris Atlas HD**		**OptiMax 1001 Termostat**		**FlexyCUBE**		**Mya 4 Reaction Station**		**AutoLab**	
Reactor Size	6 volumes from 100mL to 2L (possible to scale up up to 50L)	5	3 volumes fro 250mL to 1L	4	4 volumes from 70 to 400 mL	4	5 volumes from 50 to 400mL	4	6 volumes from 100mL to 2 L	5
Platform dimension (w, d, h in cm)	54x47x127	3	38.8x41.4x78	4	20x49x33	5	60x36x37	5	48x60x67	4
Number of reactions on series	1	2	1	2	2-6	5	4	5	1	2
Controls and sensors	T, pH, Turbidity, In-Situ FTIR, FBRM	5	T, pH, pressure, FBRM	4	TR, TH, pH, pressure, gas flow	5	pH, balances, gas flow controllers, pressure	5	T, dosing, pH	4
Userfriendly software	Atlas PC Software1	4	PC software iControlTM + touchscreen control pad	5	FlexySys application software	4	Mya Control Software + touchscreen control pad	5	PC Control Software	4
Adequate stirring device	Different geometries and materials available	5	3 types : Pitchblade, Anchor, Half-moon	4	Different geometries and materials available	5	4 different types	4	Different geometries and materials available	5
Price (chf)	30 000- 35 000	4	70 000 - 75 000	2	40 000 – 45 000	3	30 000 – 36 000	4	70 000 – 75 000	2
Sum		28		25		31		32		26
Rank based on the criteasecond		3		5		2		1		4

2.5 Thermoresponsive polymer coating

Thermoresponsive polymers, such as poly-n-isopropylacrylamide (pNIPAM) and poly-n-isopropyl- -methacrylamide (pNIPMAM), exhibit a phase transition when the ambient temperature is higher than their Lower Critical Solution Temperature (LCST). In the case of pNIPAM and pNIPMAM, the material switches from a hydrphilic to a hydrophobic phase at 32^{o}C and 42^{o}C, respectively. This transition contracts the material due to the rupture of hydrogen bonds. These stimuli-responsive polymers also respond to changes in ionic strength and pH of the solution [32, 54, 55, 56, 57, 58, 59].

Seminal work has shown the feasibility of heating and collapsing thermoresponsive gels using gold nanoparticle. In one work, gold nanoparticles were adsorbed on pNIPAM microparticles [58]. In another article, Contreras et. al. reported a method to coat spherical gold nanoparticles with NIPAM through a two-step reaction [57]. First, a polysterene shell was grown on the gold nanoparticle, which was followed by the precipitation polymerization of pNIPAM . As an alternative strategy, instead of coating the surface of the gold nanoparticles with polystyrene, they were functionalized with thiol groups [60]. The methodology that is most relevant for our approach was reported by Khalid etal.[32]. In this work, instead of using pNIPAM as the polymer, they developed a protocol to coat gold nanorods with pNIPMAM—a polymer that is more suitable for biological experiments.

Gold nanorods were coated with pNIPMAM using an *in situ* free radical precipitation polymerization reaction. To initiate the synthesis, the surfaces of the nanorods were functionalized with thiol groups. Allylamine was added to the reaction to decorate the polymer chains with amine groups, which served for two different purposes. Amine groups not only initialized the self-assembly reaction but also enabled subsequent surface functionalization of actuators. Propargyl was also used to functionalize the pNIPMAM coating with alkyl groups in order to harness the benefits of click chemistry[32].

Several techniques were used to characterize the morphology, structure, and optical response of the final product, nOMAs. TEM accurately reports the size of the rods (Figure 2.8a). However, the images are unreliable to measure the thickness of the polymer coating since the particles must be dried prior to imaging (Figure 2.8b). In situ TEM may address this limitation but we did not have access to this imaging modality. To estimate the thickness of the hydrogel coating, dynamic light scattering (DLS) technique was used. This technique also reports the dispersity of the suspension (Figure 2.8c). UV-Vis spectra indirectly inform about the diameter and aspect ratio of the rods from the absorbance peaks. Performed with a thermal cycle, it is possible to validate the presence of a thermoresponsive polymer using the UV-Vis spectra. As mentioned before, when the LCST is reached, the polymer changes conformation. The refractive index of the polymer shell increases with decreasing size, which leads to a shift in the absorbance peak (around 20nm) towards longer wavelengths (Figure 2.8 d). Likewise, it is possible to couple a heating cycle to the DLS measurements. With increasing temperature the diameter of the particles decreased, as expected (Figure 2.8e). The process is completely reversible and follows the same trend without showing hysteresis.

The pNIPMAm coated gold nanorods were approximately 400 nm in diameter. The hydrodynamic diameter of the polymer coating can be adjusted by regulating the ni-

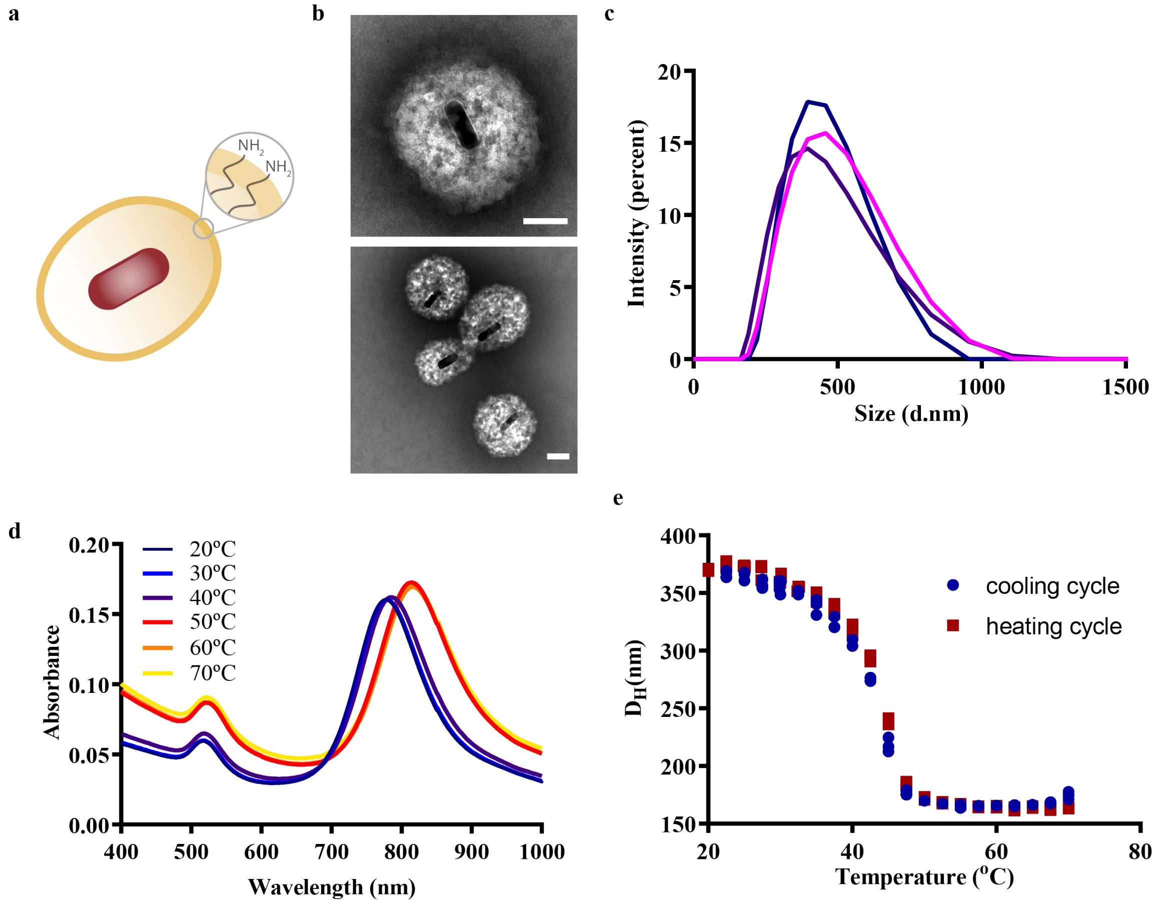

FIGURE 2.8 – Characterization of the optomechanical nanoactuators (nOMAs). a. Schematic representation of the nOMA. b. TEM images showing the pNIPMAM coating aroung the gold nanorod. Scale bars : 100nm. e) DLS spectra showing monodisperse samples with a hydrodynamic diameter around 400nm. d) UV/Vis-NIR absorption spectra of nOMAs with a temperature cycle from 20 to 70^{o}C. The shift in the NIR peak is very clear when the LCST (42^{o}C) is reached. e) The DLS with heating cycle shows a thermal response of the polymer coating.

trogen flow, which changes the turbidity of the suspension. We tested this idea and by decreasing the nitrogen flow we could produce nOMAs with diameters up to 2000 nm. We have also observed that the hydrodynamic diameter of the polymer coating doubled when we reduced the crosslinking monomer concentration (N,N'- methylenebisacrylamide, BIS) by 50%. Further experiments are required to rigourously study the influence of different parameters. Based on previous work [61] we can speculate that increasing pNIPMAM monomer concentration would lead to an increase in the coating diameter. However, changing BIS or pNIPMAM concentration may lead to polydispersity. To overcome this issue, the concentration of the surfactant may be increased.

2.6 Synthesis of gold nanorods with magnetic and catalytic properties

It is possible to add a catalytic and a magnetic layer on the Au surface without altering the optomechancial properties of the nanoactuator. These extra properties were instrumental during self-assembly studies presented in the next chapter. To this end, we followed a previously published protocol [62]. The details of the protocol can be found in

Section 2.7.4).

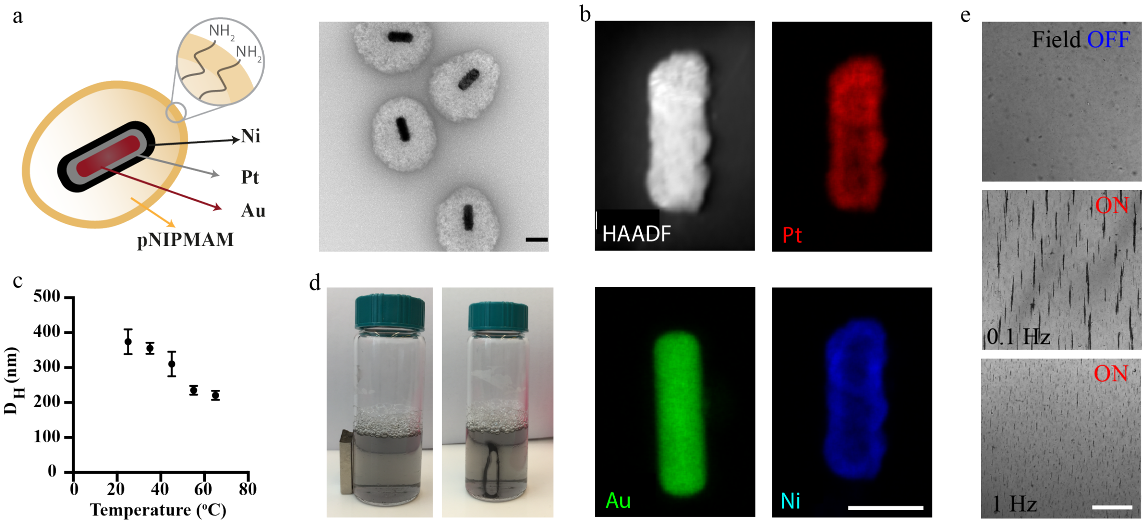

FIGURE 2.9 – Characterization of the multifuncitonal nanoactuators (mNAs). a. Schematic representation of the multifunctional nanoactuator, mNA, along with the TEM image showing the thermoresponsive polymer encapsulating the multilayered nanorod. Scale bar, 100 nm. b. STEM-EDX images showing the elemental content of the nanorods. High-angle annular dark field (HAADF) shows the overall morphology and different metal layers. Scale bar, 50 nm. c. Hydrodynamic diameter, DH, of the mNAs measured at different temperatures. DH is calculated from the measured value of the translation diffusion coefficient using the Stokes–Einstein equation. d. Magnetic concentration of mNAs in a suspension. A permanent magnet was kept next to the mNA suspension for 5 min (left). After the removal of the magnet, an agglomerate of mNAs with a shape that followed the magnetic field lines was visible (right). e. Reversible assembly of mNAs under uniform rotating magnetic fields at different frequencies. Scale bar, 100 nm [46].

The magnetization of the nOMAs was done through controlled growth of a nickel film on the encapsulated nanorods (Figure 2.9a). Prior to the growth of the Ni layer, the Au core was covered with a small amount of Pt, which served as a catalyst for the decomposition of a Ni–hydrazine complex. Elemental analysis using energy dispersive X-ray (EDX) spectroscopy confirmed the existence of a Pt–Ni shell, whereas Au was the predominant element at the particle center (Figure 2.9b). Line scanning microanalysis across a single nanoactuator showed that the thickness of the Ni layer was on the order of 10nm (Figure 2.10). We checked whether the magnetic coating influenced the thermoresponsive behavior of the pNIPMAM nanogel using dynamic light scattering (DLS) measurements (Figure 2.9c). The resulting multifunctional nanoactuators exhibited a drastic decrease in hydrodynamic size above the LCST of 42 ^{o}C, from 400 nm to 300 nm, and reached a steady-state value of 220 nm at 65 ^{o}C. Despite the small volume of magnetic material, the magnetic particles readily responded to externally applied magnetic field gradients at room temperature by accumulating in the vicinity of a permanent magnet that was placed next to the glass vial (Figure 2.9d). Furthermore, application of a homogeneous rotating magnetic fields led to the formation of particle chains (Figure 2.9e), whose size depend on the particle concentration, magnetic field strength and frequency of rotation. The chains broke up and particles formed smaller clusters at higher frequencies (at B = 40 mT, transition frequency was 1 Hz) due to hydrodynamic effects [46, 63].

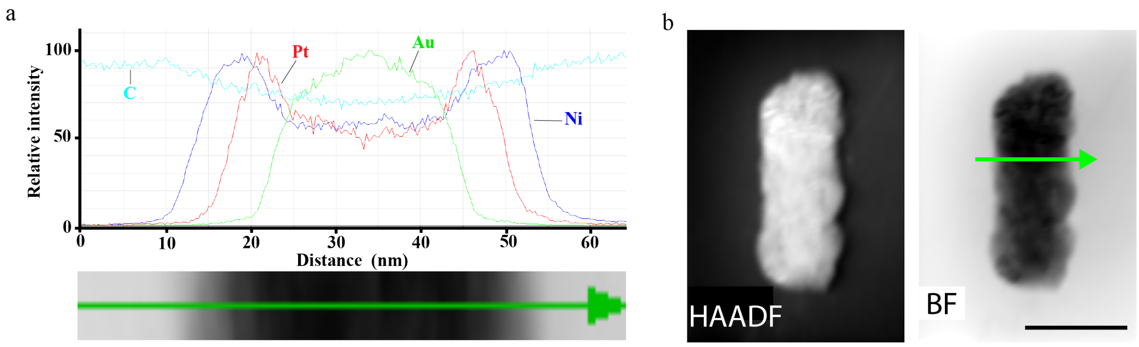

FIGURE 2.10 – STEM-EDX characterization of the multifunctional nanoactuators (mNAs). a.Representative STEM-EDX line scan obtained for the Au/Pt/Ni+pNIPMAM nanoparticle shown in Figure 2.9. Au (green), Pt (red) and Ni (dark blue). Carbon (cyan) was added as a control. b.HAADF (High-angle annular dark-field) image showing the different layers of metals (left), and bright-field image showing the direction of the line scan. Scale bar, 50 nm [46].

2.7 Detailed protocols

2.7.1 Materials

All reagents were purchased from Sigma Aldrich and used as received, unless otherwise stated : Gold(III) chloride trihydrate (HAuCl4, 99.99%), hexadecyltrimethylammonium bromide (CTAB, 98%), sodium borohydride ($NaBH_4$, 99.99%), sodium oleate (NaOL, 95%), silver nitrate ($AgNO_3$, 99.0%), hydrochloric acid (HCl, 37%), L-ascorbic acid (AA, 99.9%), N-isopropylmethacrylamide (NIPMAM), N,N'-methylenebisacrylamide (BIS), 2,2' azobis(2-methylpropionamidine) dihydrochloride (AAPH), allylamine (98%), potassium tetrachloroplatinate (II) (K_2PtCl_4, 99.9%), nickel (II) chloride ($NiCl_2$, 98%), hydrazinemonohydrate (98%). N,N' -bis(acryloyl) cystamine was acquired from Alfa Aesar.

2.7.2 Gold nanorod synthesis

This protocol was adapted from a procedure reported [32] to obtain AuNPs of approximately 95nm length and 30nm diameter. As mentioned before, it follows the 2-step preparation method :

Seed solution preparation :

Note : Seed solution should be prepared in the last 40 min of step 4 of the growth solution preparation to ensure the right aging time for the seed solution.

1. Prepare a 5 ml solution of 0.2 M CTAB in milli-Q-water in a glass vial and sonicate for 15 – 30 minutes until completely dissolved.
2. In a separate glass vial, prepare a 5 ml solution of 0.5 mM $HAuCl_4$.
3. Add the CTAB solution to the HAuCl4 solution and start stirring vigorously (maximum speed available at the Topolino small magnetic stirrer).
4. Prepare a fresh 0.01M $NaBH_4$ and dilute 0.6 ml in milli-Q-water making a final volume of 1mL. Add the 1 ml solution directly into the seed solution during vigorous

stirring. This is a critical step, to avoid different shapes of the Au nanoparticles, dip in the pipette tip and add the solution in one go.

5. Continue stirring for 2 minutes, stop stirring, and leave undisturbed for aging at room temperature for 30 minutes (not more, more we wait larger the particles). The resulting seed solution should have a brownish/purple color. (Ideally, leave the solution in a water-bath at 25ºC to avoid CTAB precipitation.)

Growth solution

1. Prepare solution with 3.6 g CTAB and 0.4936 g NaOL in 100 ml milli-Q water (in 250 ml Erlenmeyer flask) and mix until completely dissolved at 50 °C with 700 rpm stirring rate (3 cm stirring bar). To endure an homogeneous temperature, use an oil bath with a stirring bar in it.
2. Cool solution down to 30 °C and let it stir for 30 minutes in order to ensure a thermally homogeneous solution.
3. Add 8.5 ml of 4 mM $AgNO_3$ in mili-Q-Water and leave undisturbed (no stirring) for 15 minutes at 30 °C. Note : Prepare the solution fresh each time and use 20 or 40 ml glass vials for solution preparation.
4. Add 100 ml of 1 mM $HAuCl_4$ and stir for 90 minutes at 700 rpm. The solution should be initially yellowish and become colorless at the end of the 90 minutes.
5. Reduce stirring rate to 400 rpm and add 0.6 ml of HCl 37%. Continue stirring for 15 minutes.
6. Increase stirring rate to 1200 rpm, add 0.6 ml of 0.064 M ascorbic acid into growth solution and continue stirring for 30 seconds.
   Note1 : The ascorbic acid solution should be prepared fresh, prepare the solution during the previous waiting period.
   Note2 : Make sure to pipette the ascorbic acid directly into the solution. Due to the high concentration of CTAB, a dense foam layer can be formed inhibiting the diffusion of chemicals.
7. Add 80 μl of seed solution directly into the growth, stir at 1200 rpm for exactly for 30 seconds. Turn of stirring and leave undisturbed for approximately 12 h (overnight) at 30 °C.
   Note : The 12-hour reaction time is approximate and it can vary between 12 h – 15 h.
8. Remove the AuNR solution from heat and centrifuge at 4951rcf for 50 minutes (20 °C).
   Note : The solution should be an earthy red color and homogeneous looking without any precipitates.
9. Remove the supernatant by decantation and leave approximately 2 ml supernatant. Transfer the Au NR solution to an Erlenmeyer flask and add 90 ml of milli-Q-water. Leave undisturbed until ligand exchange (the afternoon of that day).
10. The CTAB coated Au NRs aren't stable for long periods of time. To increase stability and prepare the particles for polymer coating, the surface of the gold nanorods is treated with thiol groups. Dissolve 20 mg of N,N' -bis(acryloyl)cystamine in 10 ml ethanol (EtOH), set stirring rate to 700 rpm (3 cm stirring bar), and add this

solution to the 90 ml Au NR solution. Continue stirring at 700 rpm for 12 h. Note : Use sonication for a few minutes to dissolve the ligand. There can be some insoluble particles left which do not harm the process. These particles are probably some impurities.
Note : The 12-hour reaction time is approximate and it can vary between 12 h – 15 h.

11. Remove the thiolated Au NR solution and centrifuge at 13751rcf for 30 minutes (20 °C).
12. Remove the supernatant by decantation as much as possible and re-disperse in 15 ml milli-Q-water. This solution is stable and can be kept at 4 °C for a few months.

2.7.3 Polymer coating

This protocol was adapted from [32] to obtain a pNIPMAM coated with an average hydrodynamic diameter of 400nm.

1. Secure a 50 mL/ 250 mL/500mL 3-neck flask in an oil bath (see set-up in Figure 2.11). Add 15 mL/ 45mL/ 180mL of milli-Q-water and pre-purge with N2 for 15 minutes under continuous stirring (700 rpm). Use a Pasteur pipette for the N2 connection. Use a 2-cm oval stir bar for small flasks and a 4-cm one for the larger ones.
2. Insert a reflux column, secure with clamps, and start the cooling water during the pre-purging. This will give enough time for N2 to fill the column.
   Note : Make sure to reserve the third neck for gas exit. Close all necks with silicon caps and provide the gas exit at the top of the reflux column. Use a needle for this purpose.
3. Add 0.1 g/0.3g/1.2g N-isopropylmethacrylamide (monomer) and 0.01 g/ 0.03g/ 0.12g N,N'-methylenebisacrylamide (crosslinking agent) into the flask.
4. Heat the solution up to 70 °C under constant stirring (700 rpm) and constant N2 flow. Wait for 30 minutes when the temperature is reached to have a thermally homogeneous solution.
5. Increase stirring speed to 1200 rpm (2-cm oval stir bar) or to 1400 rpm (4-cm oval stir bar).
6. Inject 1 mL/ 3mL/12mL of thiolated AuNR solution directly into the reaction solution.
7. Continue stirring for exactly 1 minute and inject 80 μL/240 μL/960 μL of 0.1 M AAPH (free radical thermal initiator) into the reaction solution.
   Note : The AAPH solution should be prepared fresh.
8. Allow polymerization for 2 h at 70 °C.
   For polymer functionalization :
   a) For the amine functionalization, dilute 10μL/ 30μL/ 120 μL of allylamine in m-Qwater, for a final volume of 1mL, and add to the mixture after 30 min.
   b) For the alkyl group functionalization, dilute 90μL of propargyl methacrylate in 1mL of EtOH and add into your mixture after 100min. (for an initial solution of 45mL).
9. Remove the flask from heat and allow to cool to room temperature while stirring.

10. Centrifuge at 3500º relative centrifugal force (rcf) for 30 minutes at 10 °C.
11. Remove the supernatant and add fresh milli-Q-water. Repeat step 10 and 11 three times and concentrate the final solution to 1 ml or 3mL. Note that for a 180mL reaction, when resuspending in 3mL of mili-Qwater the gold suspension is 4 times more concentrated than resuspending the 14mL reaction in 1mL (This is very important for the magnetization calculations).

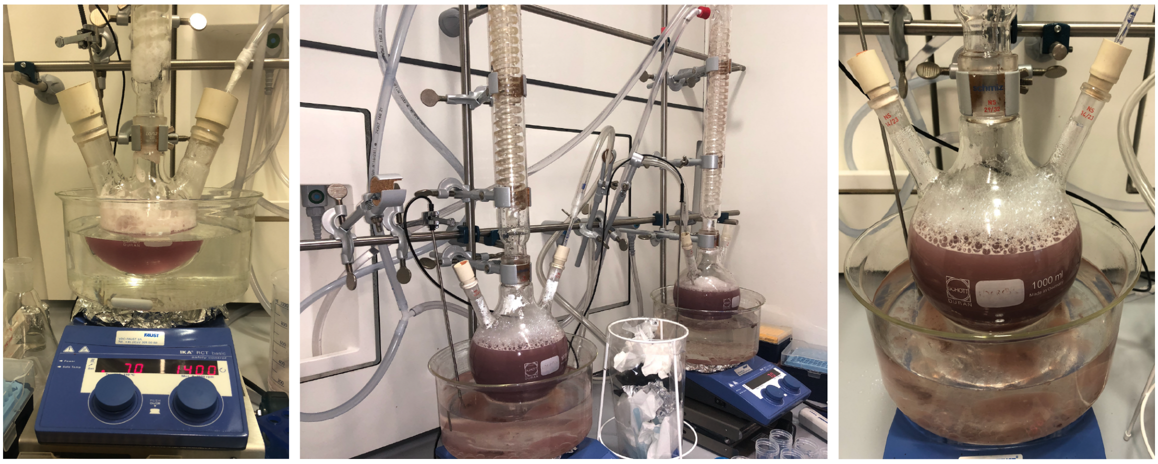

FIGURE 2.11 – pNIPMAM coating of AuNRs set-up. On the left, the polymerization is ongoing. In the first 30 min the suspension should change from transparent to this strawberry milkshake color. In the middle, a picture of 2 batches after polymerization. It is also possible to observe the reflux column in the middle neck, the N_2 flow connected with a Pasteur pipette on the right neck and on the left neck I connected a syringe tip through the silicon cap to allow the regulation of pressure. On the right, a zoom-in picture of the reaction suspension once the reaction is over.

2.7.4 Magnetization

This protocol was adapted from [62]. To calculate the AuNRs concentration obtained in the end of the synthesis, the suspension was dried and weighted. For a batch of 15mL, 20mg of AuNRs were synthesised. From this, the molar concentration was calculated using Equation 1, and it was estimated that with the protocol presented in this thesis one produces approximately 6.8×10^{-3}M. In the case of larger volume batch, where the gold is re suspended in 3 mL, the final concentration is 4 times higher (27.2×10^{-3}M)

$$C = \frac{m}{Mw.V} \tag{1}$$

where C is molar concentration in M (mol.L^{-1}, m the mass in g, Mw the molecular weight in g.mol^{-1} and V the volume in L.
As explained before, the magnetization is done in a 2 step reaction, where a Platinum is grown on the gold surface to promote Ni reduction and deposition in the presence of hydrazine and the molar ratios Au0/ PtII/ NiII are kept as unity.

The calculations presented next are for the highest concentration suspension (27.2×10^{-3}M). For 22.4 μmoles of AuNR :

Platinum coating

1. Prepare 40mL of a 0.1 M CTAB solution.
2. Add approximately 0.827 mL (22.4μmoles) of the coated AuNR suspension to the CTAB solution.
3. Add 22.4 µmoles of K_2PtCl_4. Prepare 0.071M of a K_2PtCl_4 solution and from this add 314 µL to the CTAB solution.
4. Sonicate for 30 minutes.
5. Add 628 µL of 0.1 M ascorbic acid mix it for 1-2 minutes.
6. Incubate in a hot oil bath at 40º C for 12h (overnight up to 15h). There should be a color change from clay-like red to dark purple-black.
7. Remove the solution from the heat and allow it to cool down at room temperature. Centrifuge at 5000rcf for 10 minutes at room temperature (20-25°C), three times.
8. Remove the supernatant and resuspend the particles in 24mL of 0.1M CTAB solution.

Nickel Coating

1. Prepare 34.8 mL of mili-Qwater.
2. Add 22.4 µmoles of Ni. Prepare a solution of 0.25 M $NiCl_2$ and add 89.6 µL form this solution to the mili-Q-water.
3. Add 716 µL of 2.5 M hydrazine to the solution.
4. Add the 24 mL of Pt coated AuNRs suspension.
5. Incubate the suspension in a hot oil bath at 40 ºC for 150 minutes. Once again, there should be a color change from dark purple-black to black.
6. remove the solution from the heat and allow it to cool down at room temperature. Centrifuge at 5000rcf for 10 minutes at room temperature (20-25°C), three times.
7. Remove the supernatant and resuspend the particles in 4mL of mili-Q-Water. Store in the fridge at 4ºC. Keep in mind the particles will oxidize over time and loose magnetization.
8. To test if the Ni coating was successful, held a magnet to the suspension and wait 10 to 30 min. The particles should agglomerate next to the magnet.

2.7.5 Particles characterization

Several techniques were used to characterize the morphology and structure as well as thermal and optical properties of the nOMAs. Transmission electron microscopy (TEM) and scanning TEM with EDX (STEM-EDX) were used to directly measure the overall size and do the elemental mapping of the nanoparticles, respectively. The TEM microscope Tecnai Osiris, FEI, was operated with a voltage of 200 kV. UV–vis measurements were performed with the V-670 UV–vis–NIR spectrophotometer (Jasco) to measure the absorption of the nanoactuators in a temperature range from 20-70ºC and wavelengths from 400 to 1000nm. Dynamic light scattering (DLS) measurements were performed using a Malvern Zetasizer Nano, to measure the hydrodynamic diameter of the polymer coated nanoparticles at different temperatures. Twelve measurements were taken for each temperature point from three different samples. [46]

2.7.6 Sample preparation for TEM imaging

For the visualization of the pNIPMAM coated particles (magnetic and non-magnetic) with TEM, a negative staining was performed with 2% of uracil acetate as follows :

1. Discharge the carbon grid with a Discharge glow for 30s to allow the grid to become hydrophilic. After treatment, we have 1h to work on the sample.
2. Dilute 50 times the AuNR suspension.
3. On a piece of parafilm put a 15µL droplet of the diluted suspension.
4. Put the TEM grid on the droplet with the carbon facing down, for 2 min.
5. Put the carbon gird on DI water (our buffer) to wash.
6. Put a 15µl drop of the uracil acetate on the parafilm.
7. Pick the grid and blot it in a filter paper. After put the grid on the top of the droplet for 15s.
8. Remove the grid gently and blot it in the filter paper to remove the excess of stain.
9. Let it evaporate at room temperature. You can out the grid under light to make the evaporation process faster.

3 Top-down and bottom-up assembly of microactuators from optomechanical nanoactuators

3.1 Introduction

One of the main objectives of this thesis is to develop techniques to fabricate cell-sized actuators. Increasing the size must scale up the forces provided by the nanoactuators, from pN to nN, without sacrificing their rapid response. Compared to bulk hydrogels, colloidal assembly of nanogels leads to faster transport of water during swelling and deswelling phases [59]. Furthermore, colloidal assembly ensures a homogeneous distribution of gold nanorods, which is important for uniform heating and contraction.

In this chapter, I describe a number of techniques that we developed for the assembly of optomechanical microactuators (μOMAs). Figure 3.1 shows a schematic overview. The first technique is based on the formation of droplet-based templates in which the nanoactuators self-assemble into spherical microactuators. The second technique is based on conventional printing where an actuatable ink is formed by mixing the nanoactuators with a nanoporous polymer solution. The third technique relies on thermocapillary forces and a chemical reaction that takes place at the surface of the nanoactuators. The first and third technique provide the optimal mechanical power as the assembled microactuator is composed purely of nanoactuators with a maximum packing ratio. The second technique, on the other hand, is more versatile in terms of controlling the geometry of the microactuator.

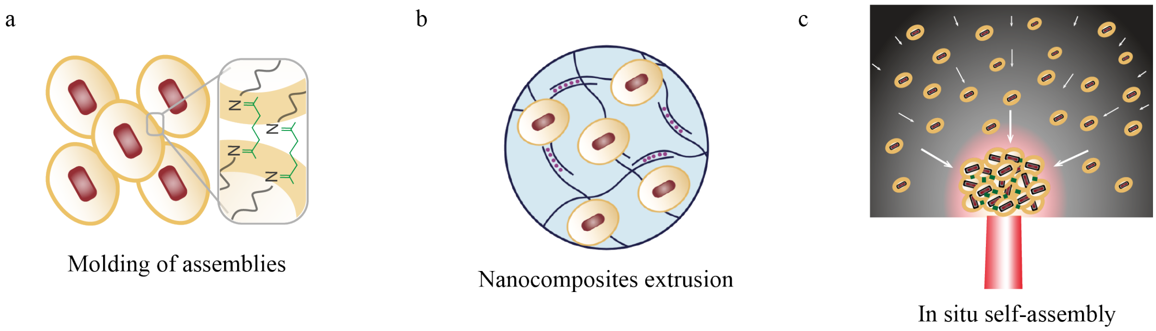

Molding of assemblies

Nanocomposites extrusion

In situ self-assembly

FIGURE 3.1 – Overview of the microacturators' assembly techniques explored in this work. a. Schematic representation of the molding process of nOMA. b. Casting and 3D printing of nanocomposites. c. Directed in situ self-assembly.

3.2 Template-assisted assembly of microactuators

The coupling between adjacent nOMAs must be strong enough to effectively transmit the force and sustain the connectivity during multiple deformation cycles. An amine–aldehyde condensation reaction was used to covalently link the nOMAs and assemble microactuators in the desired form. The molecule glutaraldehyde acts as a linker between amine groups by utilizing two available reaction sites (Figure 3.2a) [55, 59]. Mixing amine functionalized nOMAs with glutaraldehyde and heating the solution overnight at 65^{o}C led to the assembly of thin-film nOMAs with random shapes Figure 3.2b. The surface of these films was investigated using in-liquid atomic force microscopy and the topography images revealed close-packed layers of colloidal nanoactuators forming a porous network Figure 3.2c [45].

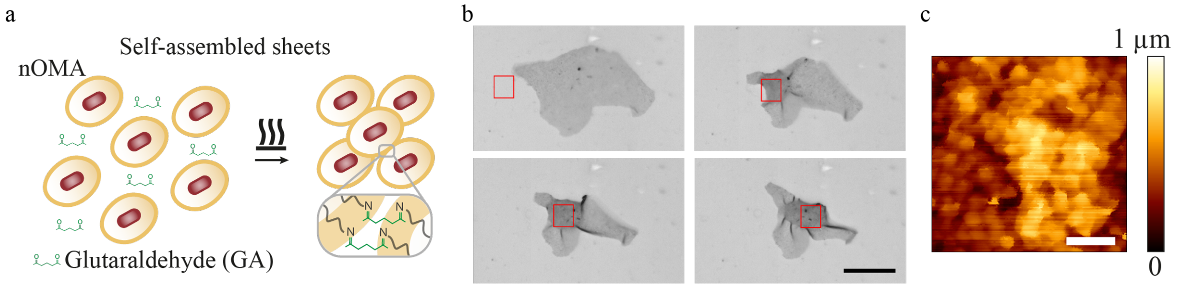

Figure 3.2 – Colloidal assembly. a. Schematic representation of the multifunctional nOMA and the assembly process. The nOMAs are crosslinked with glutaraldehyde through the amine groups, at 65^{o}C. b. Representative image of randomly shaped mOMAs, that formed a sheet. The red scare outlines the area of laser actuation. Scale bar, 50 μm c.Topography scan of a representative self-assembled sheet using in-liquid atomic force microscopy. Scale bar, 1 μm [45].

A systematic characterization of actuator performance and streamlined prototyping of micromachinery requires high throughput, monodisperse and repeatable synthesis of μOMAs with well defined properties. Spherical μOMAs were fabricated using a microfluidic approach based on the break-off process of droplets in two-phase flows at a T-junction.[64] An aqueous solution of nOMAs and glutaraldehyde forms the discontinuous phase while the continuous phase comprises the surfactant and oil mixture (Figure 3.3a.). The emulsion was collected and heated overnight to facilitate the crosslinking process. Colloidal suspensions are not very stable at high temperatures but our reaction requires an overnight incubation at 65^{o}C. After several trials, fluorinated oil and fluorinated surfactants were found to be the optimal choice. Consistent with the structure of the films, we observe a close-packed arrangement of nOMAs, while the interstices between the particles form a scaffold with uniform pores (Figure 3.3b). In-liquid AFM measurements on fully swollen samples showed that the elastic modulus of actuators was 4.8 ± 2.1 kPa (n = 15) at room temperature.[45]

For a microfluidic channel with width w, flow rates for the continuous Q_{cont} and discontinuous phase Q_{dis}, the size of the droplet l is given by [64] :

$$\frac{l}{w} = 2.3389\frac{Q_{dis}}{Q_{cont}} + 0.7843 \qquad (2)$$

The microfluidic process resulted in a monodisperse suspension with less than 10% variation in size. μOMAs with diameters ranging from 5 ± 0.4 µm to 50 ± 4.7 µm were fabricated by tuning the channel size and flow rates (Figure 3.3c).

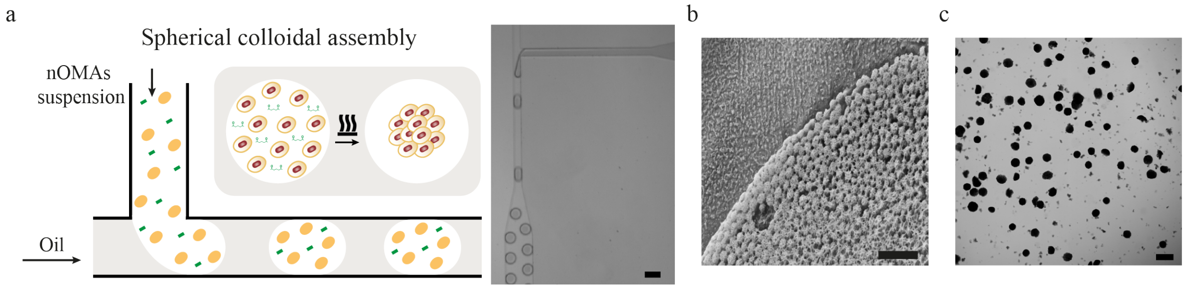

Figure 3.3 – Microfluidic assisted colloidal assembly. a. Right : Schematic illustration of the T-shaped microfluidic template-assisted self-assembly process of spherical microactuators. Left : Representative example of the T-junction microfluidic channel. Scale bar : 100μm. Continuous phase is composed of the fluorinated oil and fluorinated surfactant, and the discontinuous phase is the mOMAs aqueous suspension with the cross-linker glutaraldehyde. b. A cross-sectional cryo-SEM image of a representative microactuator. Scale bar, 2 μm. c. Monodisperse suspension of microspheres after overnight (ON) cross-linking and purification. Scale bar : 100μm [45].

In order to produce larger microactuators, a different microfluidic chip was used, This device works due to a hydrodynamic flow focusing phenomenon (Figure 3.4a). μOMAs with diameters ranging from 80 to 200 μm were fabricated by tuning the flow rates (Figure 3.4b).

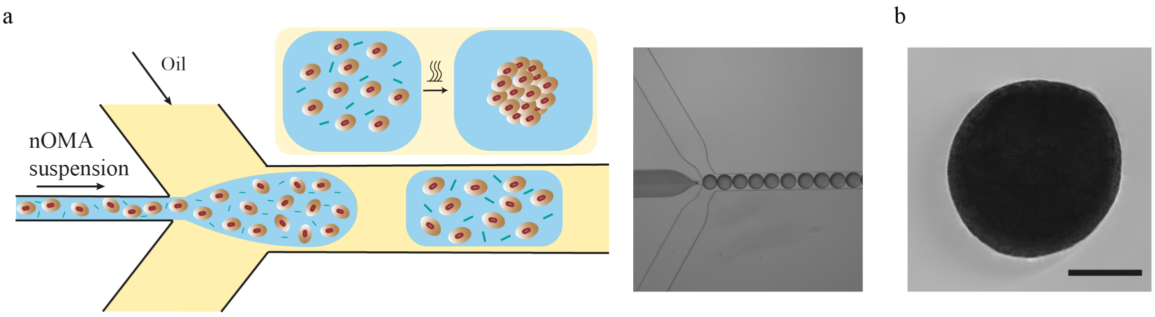

Figure 3.4 – Second version of Microfluidic assisted colloidal assembly. a. Right : Schematic illustration of the flow focusing microfluidic colloidal assembly process. An aqueous solution of nOMAs and crosslinker forms the discontinuous phase while the continuous phase comprises the surfactant and oil mixture. The emulsion was collected and heated overnight to facilitate the crosslinking process. Left : Representative example of the focused flow microfluidic channel. b. Representative example of a large microactuator (approximately 150 μm). Scale bar, 100 μm [65].

3.2.1 Characterization of contraction and relaxation kinetics

To study the dynamics of contraction and relaxation of the μOMAs, a NIR laser was coupled to an inverted fluorescence microscope. A LabView program modulates the frequency, duration, and intensity of the laser exposure through a digital to analog converter (DAC) board. A Matlab script was used to automatically calculate the area from each recorded frame.

The spherical μOMAs were highly responsive to NIR excitation and exhibited drastic deformation upon exposure, as shown in Figure 3.5a. Deformation was monitored by measuring the actuation strain, ε, which is defined as percentage change in radius, R, normalized with respect to the initial radius,R_0, (Figure 3.5b, equation 3). [45]

$$\varepsilon(\%) = \frac{R_0 - R}{R_0} \times 100 \tag{3}$$

The contraction phase can be divided into two periods, one representing the fast decrease in actuator size generating up to 20% strain in tens of milliseconds followed by a significantly slower period that would gradually stabilize the length within minutes. Pulse width modulation revealed that contraction was very fast as expected and predominantly completed within the first 60–80 ms of actuation at 1.4 mW of laser power (Figure 3.5c). Approximately 50% of the steady-state level was reached within the first 25 ms of actuation while exceeding 70% required another 25 ms of exposure.[45]

In conventional bulk hydrogel actuators, the time, t, to swell is determined by the polymer relaxation time, τ, which characterizes the increase of size in time.[66] The size of μOMAs followed a similar temporal evolution and increased exponentially with time during the relaxation phase until the polymer went back to its original state (Figure 3.5d, equation 4).

$$y = A \exp(-\frac{t}{\tau}) \tag{4}$$

From the data, we obtained τ values ranging from 0.4 to 2.6 seconds as a function of the original μOMAs size (Figure 3.5e). The linear relationship between the cross-sectional area of the actuator and the corresponding relaxation time suggests that relaxation was controlled by diffusion, D (equation 5).

$$\tau = \frac{R_0^2}{D} \tag{5}$$

The diffusion coefficient for our colloidal scaffold was estimated as 675 $\mu m^2 s^{-1}$ which is approximately two orders of magnitude higher than bulk pNIPMAM hydrogels. [67] Faster actuation kinetics can be achieved by sacrificing actuation strain. We modulated the frequency of 50 ms laser pulses and recorded the time varying response (Figure 3.5f). At low frequencies, the actuator could reach 65–70% of the maximum actuation strain and had time to relax back to the fully swollen state. The amplitude of the strain decreased with increasing frequency, which corresponds to 12% strain at 2 Hz and 8% strain at 4 Hz. At frequencies above 8 Hz, the strain shows less than 2% deviation with respect to the baseline over time. Compared to continuous exposure, driving the actuator at high frequencies would generate a comparable strain with higher power efficiency. The actuation strain can be directed to follow an arbitrarily shaped waveform provided that the duration of signal is slow enough not to interfere with the natural contraction and relaxation kinetics.

Regarding the larger μbeads, they also exhibited a significant deformation upon laser exposure, as shown in Figure 3.6a. The actuation was highly reversible and could be sustained for at least 10^4 cycles. Deformation was also monitored by measuring the actuation strain, ε (Figure 3.6b) and the maximum strain was recorded as 25±2.75 % (n = 50) for

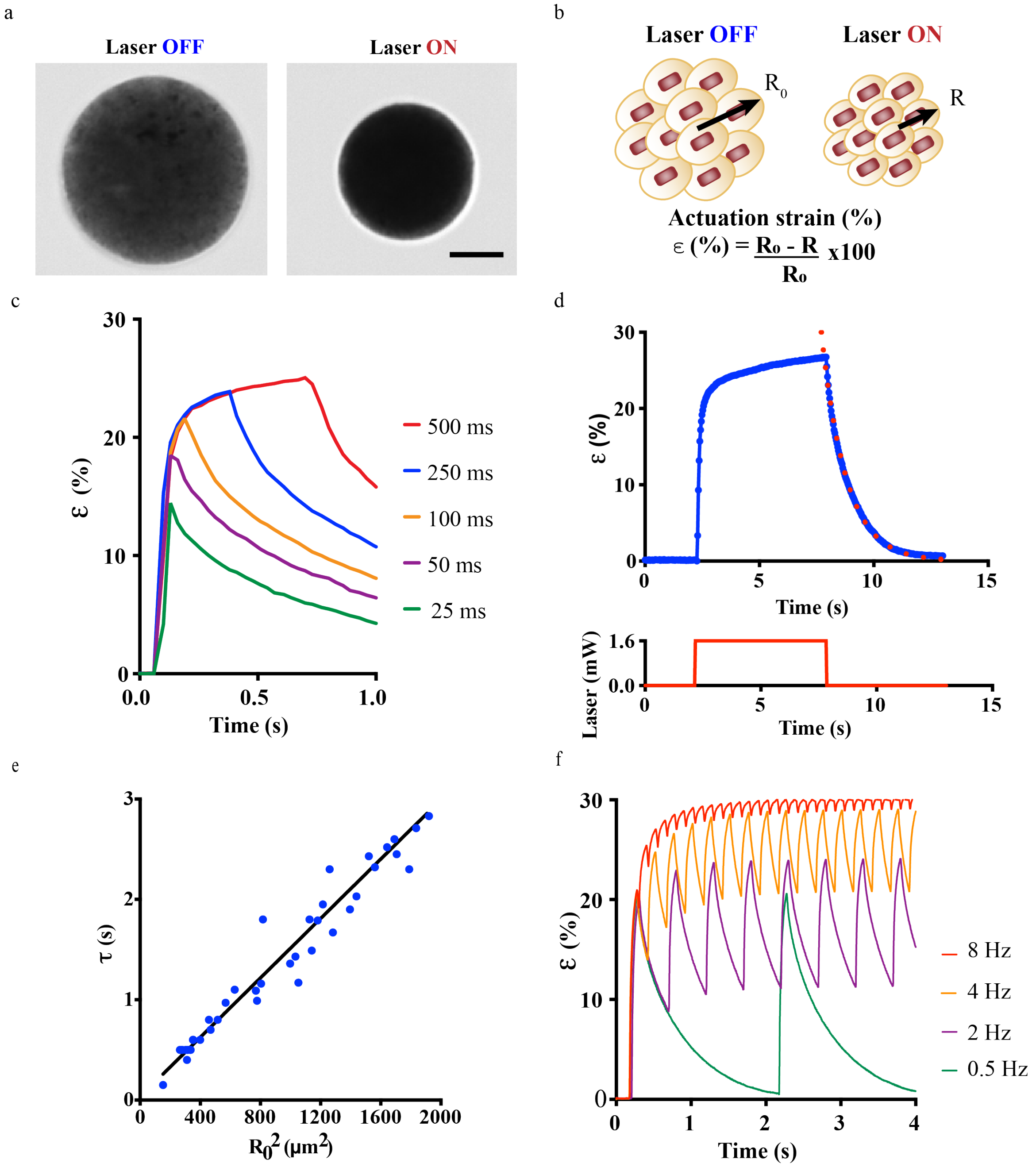

Figure 3.5 – Characterization of the contraction and relaxation kinetics. a. Representative example showing the fully contracted state of a microactuator upon NIR illumination. The laser power was set to 1.4 mW. Scale bar, 10 µm. b. Schematic description of actuation process and measurement of strain (ε). R_0 refers to the initial radius of the microactuator at the fully swollen state and R represents time-varying radius upon laser illumination. c. Actuation strain over time for varying pulse durations. All measurements were done at 1 Hz pulse frequency with 1.6 mW laser power. d. Actuation strain versus time plot for a single contraction–relaxation cycle. An exponential fit to the relaxation curve characterizes the relaxation constant. The lower graph shows the laser input over time. e. Relaxation time constant (τ) with respect to the square of radius in the fully swollen state. f. Microactuator performance is plotted over time for different actuation frequencies. All measurements were done at 100 ms pulse width with 1.6 mW laser power [45].

200 μm μOMAs at 15 mW laser power (measured on the microscope stage). When comparing larger with smaller beads we concluded that the duration of the relaxation phase changes depending on the size of the actuator. For example, nOMAs complete the full

actuation cycle at the maximum strain within 10 msec but the μOMAs that are 100-200 μm in diameter completed the full actuation cycle at the maximum strain within 8 to 15 sec.

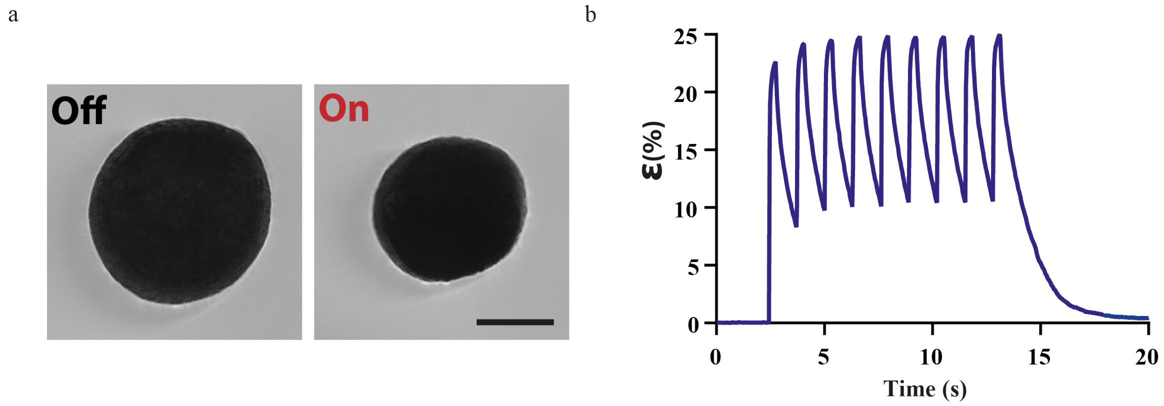

FIGURE 3.6 – Characterization of the contraction and relaxation kinetics of the larger μOMAs. a. A representative example showing the fully contracted state of a μOMA upon NIR illumination. The laser power on the sample was adjusted to 10 mW. Scale bar, 100 μm. b. Actuation strain versus time plot for a 15 mW NIR signal with 260 ms pulse duration at 0.4 Hz [65].

3.2.2 Fluorescent labelling of microactuators

As mentioned in Section 2.5, the pNIPMAM shell was decorated with amine and alkyne groups. Their presence in the surface of the nanoparticles and microassemblies opens up a wide range of possibilites for coupling them to ECM proteins, cells, and fluorescent molecules. It is possible to perform EDC or NHS-Ester chemistry in the presence of amine groups to obtain amide linkages, which allows us to connect the actuators to receptor proteins, fibronectin, and collagen type I (3.7b). The presence of alkyne groups on the polymer surface permits further functionalization through click chemistry in the presence of azide-functionalized molecules or peptides (Figure 3.7c). I labelled the microactuators with two different fluorescent dies using either the NHS-Ester or click chemistry. In Figure 3.7d a μOMA was labelled with the Alexa Fluor™647 NHS Ester (Succinimidyl Ester) and in Figure 3.7e another μOMA was labelled with FAM-Azide through click chemistry. Please see the detailed protocols in Section 3.2.4.5.

3.2.2.1 Formation of colloidosomes

Analogous to liposomes, which are aggregates of lipids that form a continuous shell, colloidosomes are agglomerates of colloids. As a consequence of their porosity, colloidosomes have been explored for biomedical, food and agricultural applications. Diffusion through pores, rupture due to shear stress and swelling-shrinking upon exposure to a chemical stimuli are potential ways of delivering compounds [69, 70, 71, 72]. Encapsulation of molecules inside such a capsule would deliver nutrients and drugs in a controllable manner. Colloidosomes have also been proposed to be used as microreactors [69, 70, 71, 73, 72].

Shah and co-workers reported the synthesis of colloidosomes from pNIPAM microgels with an average diameter of 750 nm via flow-focusing microfluidics [55]. The pNIPAM shells keep their thermoresponsive properties, which has been exploited for wirelessly

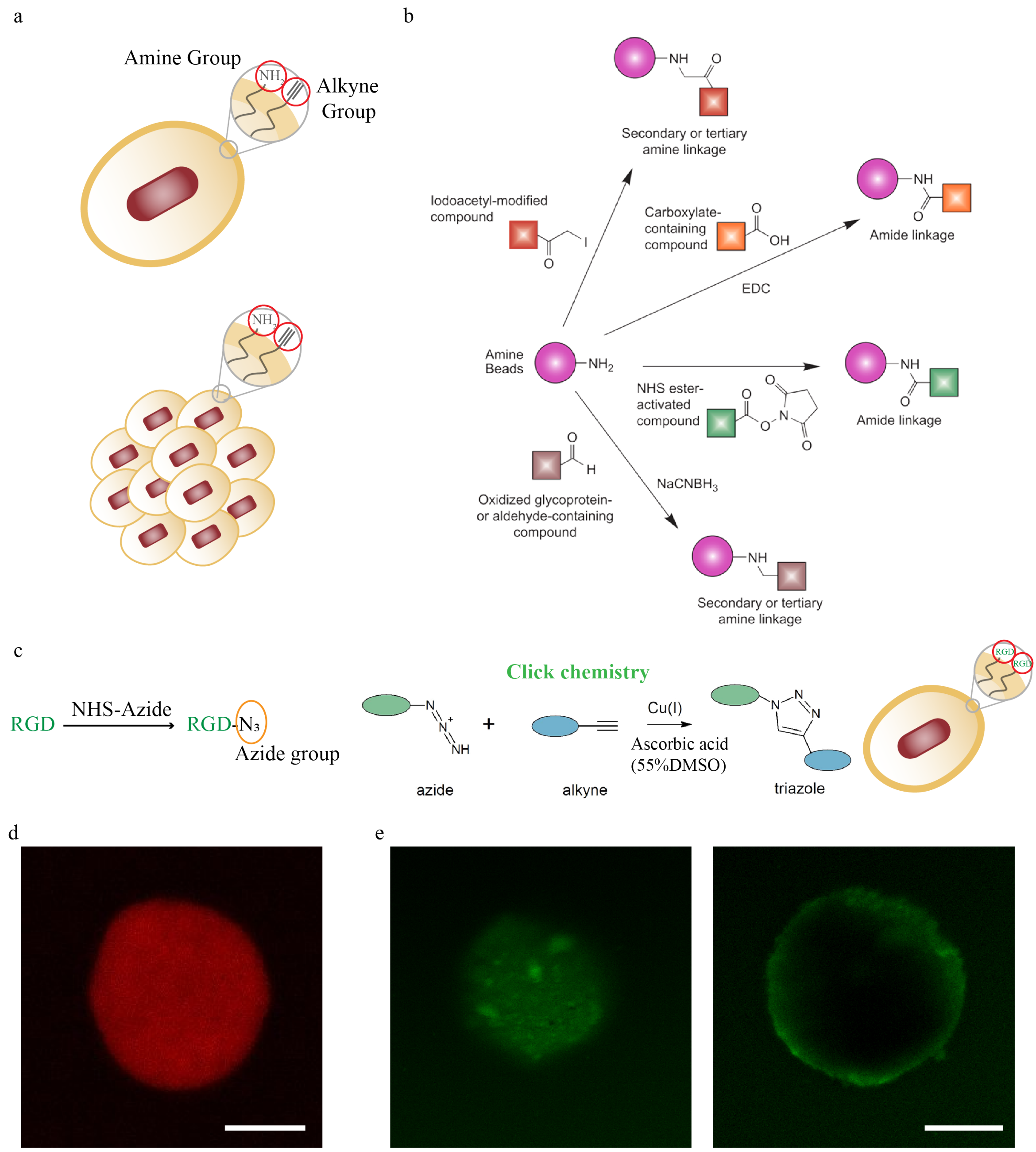
a
Amine Group
NH_2
Alkyne Group
NH_2
b
NH
O
Secondary or tertiary amine linkage
Iodoacetyl-modified compound
I
O
Carboxylate-containing compound
O
OH
NH
O
Amide linkage
EDC
Amine Beads
NH_2
NHS ester-activated compound
O
O
O
N
O
NH
O
Amide linkage
O
H
Oxidized glycoprotein- or aldehyde-containing compound
$NaCNBH_3$
NH
Secondary or tertiary amine linkage
c
RGD
NHS-Azide
RGD-N_3
Azide group
Click chemistry
N
N^+
NH
azide
+
alkyne
Cu(I)
Ascorbic acid (55%DMSO)
N
N
N
triazole
RGD
RGD
d
e

FIGURE 3.7 – Surface functionalization of the actuators with fluorophores. a. Schematic representation of the functional groups present on the surface of the nano and micro OMA. b. Schematic illustration of possible reactions with the amine groups for surface functionalization, resulting in secondary and tertiary amine linkages or amide bonds. c. Schematic illustration of click chemistry with the alkyne group. d. A representative example showing a microactuator labelled with Alexa Fluor ™647 NHS Ester. e. A representative example showing a colloidosome labelled with FAM-azide 488. On the left the bottom of the colloidosome and on the right a plane in the middle. Scale bars : 20 μm [68].

controlled drug delivery [74]. As a preliminary study, I formed microactuators from nOMAs with an average diameter of 965 nm and 760 nm using the T-junction microfluidic device. The nanoactuators assembled as colloidosomes, which was observable in brightfield images (Figure 3.8). While the preliminary results have shown the feasibility, further experiments are needed to optimize the fabrication process [47]. Due to time constraints, we could not move this work further.

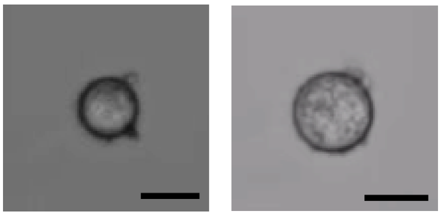

Figure 3.8 – **Colloidosomes.** Representative examples of two colloidosomes. Scale bar 10μm.

3.2.3 Conclusions

The μOMAs show outstanding performance with respect to the achievable maximum actuation strain (30%) and fast contraction–relaxation kinetics (in the order of milliseconds). The colloidal assembly of nOMAs into spherical μOMAs speeds the diffusion of fluid by forming a porous network with a diffusion coefficient of 675 $\mu m^2.s^{-1}$. Furthermore, the enhanced kinetics are achieved without significant loss in mechanical strength as the Young's modulus of μOMAs (4.8 ± 2.1 kPa) is comparable to the stiffness of bulk hydrogels.

3.2.4 Detailed protocols

3.2.4.1 Materials

All reagents were purchased from Sigma Aldrich and used as received, unless otherwise stated : glutaraldehyde solution (50% in water) ; 1H,1H,2H,2H-perfluoro- 1-octanol (PFO, 97%) ; 2-Hydroxy-2-methylpropiophenone (DAROCUR), and polydimethylsiloxane (PDMS) SYLGARD 184 kit. Novec 7500 engineered fluid, the fluorinated oil, was purchased from 3M. The surfactant Pico-Surf was acquired from Dolomite Microfluidics.

3.2.4.2 Fabrication of microfluidic channels

The devices were designed with the program Klayout. The wafers were prepared in the clean room by our colleague Murat Kaynak. The microfluidic devices are made of PDMS, using the Sylgard 184 Silicone Elastomer Kit as follows :

1. Mix for several minutes the elastomer and the curing agent with a ratio of 10 :1.
2. Desiccate as long as necessary until all bubbles are gone.
3. Pour the PDMS onto the wafers
4. Desiccate as long as necessary.
5. Bake the PDMS in the oven at 65°C for at least 3h.
6. Once the PDMS is cured, remove it very carefully. To help add a small volume of ethanol and use a tweezer, carefully, on the side of the mould.
7. With a biopsy punch (outer diameter 0.5mm), make the holes in the inlets and outlet of the device.
8. Clean the devices with compressed N_2 and with scotch tape.
9. Treat the surface of the glass slides and the microchannel with a High Frequency Generator (BD-10A High Frequency Generator from Electro-Technic Products). This will oxidase both surfaces and promote the bonding between the two surfaces (equivalent to plasma treatment).

10. Press the microfluidic channels on the glass for the bonding.
11. To improve the bonding it is advised to leave the channels over night at 120^{o}C.

3.2.4.3 Fabrication of microactuators

Self-assembled sheets and microactuators were fabricated by an amine–aldehyde condensation reaction based on a reported protocol [55]. The stock of nOMA solution was concentrated to 16 mg.ml^{-1} by centrifuging and re-dispersing in 20 % (v/v) glutaraldehyde in milli-Qwater. The nOMA solution concentration was calculated based on the dry mass of a batch of stock nOMA solution. This solution was heated overnight in an Eppendorf tube at 65 °C to synthesize self-assembled sheets.

The spherical microactuators were fabricated using a T-junction or flow focusing microfluidic device and the NEMESYS low pressure microfluidic pump. The discontinuous phase was the reaction solution described above while the continuous phase was a solution of 2% (or 3% for bigger droplets in the case of the flow focusing devices) surfactant in fluorinated oil. The resulting emulsion of spherical μOMAs was broken with 20 % (v/v) 1H,1H,2H,2H-perfluoro-1-octanol (PFO) in fluorinated oil and washed three times with ethanol to remove unreacted gluteraldehyde. The detailed protocol is as follows :

AuNRs suspension preparation (discontinuous phase) :

1. Centrifuge the coated AuNRs suspension at 15000 rpm, 4^{o}C for 5 min.
2. Remove the supernantant.
3. Suspend in mili-Qwater (80% of the final volume).
4. For a homogeneous suspension sonicate for a couple of minutes.
5. Add Gluteraldehyde (20%V/V).

Oil preparation (Continuous phase) :

1. Fluorinated Oil (3m NoveC 7500 Engineered Fluid)
2. 2% (or 3% for big droplets) of 5% fluorinated surfactant (Picosurf)

Transfer the solutions to the syringes (1mL). In case of the T shape microfluidic channels, the AuNRs suspension flows perpendicular to the oil inlet and the outlet. One side will be the inlet for the oil and the other the outlet for collecting the droplets. The droplets are collected to a glass vial containing a small volume of the continuous phase solution. After collection, seal the vials with parafilm and put them in the oven at 65^oC over night for the crosslinking reaction to occur.

After Over-Night reaction :

1. Add some mili-Qwater to the suspension ;
2. Then add an oil solution with 20% Perfluotooctanol (PFO) (total volume equal to the water volume)
3. Vortex ;
4. Wait 1 or 2 min for the phase separation to conclude ;
5. When there is phase separation try to remove as much oil as possible.

6. Transfer the suspension to an Amicon Ultra filter tube 30K ;
7. Spin down to clean 3 to 4 times, and ressuspend each time with Ethanol (10min at 20^oC, 14000 rcf)
8. Spin down to clean 3 to 4 times, and ressuspend each time with mili-QWater (5min at 20^C, 14000rcf)
9. Inverted filtration to collect the microspheres.

Important note : Before using the microfluidics, device pre-treat the channels with the continuous phase for 10 min approximately, so the AuNRs suspension will not get sticky to the walls.

3.2.4.4 Characterization of microactuators

The internal structure of the μOMAs was investigated using cryo-SEM (Nvision 40 Zeiss). Prior to imaging, an aqueous suspension of μOMAs was frozen in liquid N_2, fractured, etched, and sputter coated (Baltec MED 020) and transferred to the SEM with a cold chamber (Leica EM VCT100).

Imaging and force spectroscopy were all performed in liquid with NanoWizard 4a Bioscience AFM (JPK Instruments). Imaging was done using qp-BioAC-Cl-10 cantilevers (Nanosensors) and CB2 tip with a measured stiffness of 0.099 $N.m^{-1}$. Force spectroscopy measurements were done with custom colloidal tip cantilevers at room temperature and 50^oC with 15 minutes of settling time. Polystyrene microbeads (6 µm, Polysciences) were dispersed onto a glass slide, dried and bound to cantilevers (HQ :CSC37, MikroMasch) using a glue (M-Bond 610 adhesive Kit, SPI). The colloidal tip cantilever had a measured stiffness of 0.374 $N.m^{-1}$. Force curves were obtained on 16 microactuators and each indentation was performed three times. Prior to both imaging and force spectroscopy, samples were transferred to a sugar solution and pipetted on to poly-lysine pretreated plastic Petri dishes to facilitate immobilization onto the surface. Each indentation measurement was analyzed by JPK data processing software using the standard Young's modulus calculation approach offered.

3.2.4.5 Fluorescent labelling

Fluorescent labelling through NHS-Ester chemistry :

250μL of a microsphere suspension in mili-Qwater was mixed with 100μL of 1M sodium bicarbonate, $NaHCO_3$, and 1.25 μL of Alexa Fluor™647 NHS Ester (Succinimidyl Ester) (ThermoFisher Scientific) stock solution and incubated for 2h at room temperature. The reaction mixture was transferred to an Amicon Ultra 0.5 Centrifugal Filter Devices and 5 washing steps were done with the following washing solutions :

1. $375\mu L$ of 1M $NaHCO_3$ mixed with $125\mu L$ of PBS
2. $250\mu L$ of 1M $NaHCO_3$ mixed with $250\mu L$ of PBS
3. $125\mu L$ of 1M $NaHCO_3$ mixed with $375\mu L$ of PBS
4. $500\mu L$ of PBS

5. $500\mu L$ of PBS

Store the beads at 4^o.

Fluorescent labelling through Click-chemistry :

Protocol was adapted from [75]. Briefly, the microspheres were suspended in a 50μL reaction solution containing 2.5μL of 30mM FAM-azide (5-isomer, Prod. D4130, Lumniprobe) ; 2.5μL of 10mM ascorbic acid (SIGMA ALDRICH) ; 5μL of 10mM Copper (II)-TBTA complex (in 55%DMSO, Prod. 21050, Lubmiprobe) and 40 μL of 55%(v/v) DMSO (in water). The suspension was incubated for 3h at 50^oC. The microspheres were washed 3 times with ethanol by centrifugation for 2min and 14000rcf.

3.2.5 Experimental set-up and video processing

All experiments were performed using a Nikon Ti Eclipse motorized inverted microscope and phase-contrast images were captured with an ORCA-Flash4.0 CMOS camera (Hamamatsu). A 785 nm laser (Thorlabs) beam coupled through the FRAP unit provided NIR illumination. The laser beam was guided through 10X or 20X objectives (Nikon) and an NIR filter cube (Chroma). The videos were captured at full pixel resolution (2048 × 2048) with frame rates ranging from 33 fps to 200 fps depending on the requirement of the experiment. A program based on an edge-detection algorithm in Matlab (Mathworks, MA) was used to measure the size of μOMAs from time-lapse videos.

3.3 Casting and printing of nanocomposite microactuators

Bottom-up assembly provides powerful actuators but the design space is quite limited. We asked whether we could use conventional top-down additive manufacturing techniques to form μOMAs from nOMAs. Printing or casting relies on the synthesis of a polymerizable ink. Incorporating a non-actuated material into the mix surely decreases the mechanical force the actuator can generate but it may increase the actuation strain with rational design of architecture. Furthermore, using biopolymers with viscoelastic or shape-memory properties, more complex actuators can be developed. I explored two materials, alginate and polyacrylamide. Alginate is widely used for tissue engineering and drug delivery applications. It does interface very well with biological tissues. Polyacrylamide has linear elastic properties at small deformations, and therefore enable measurement of forces. I postulated that forces can be applied and measured simultaneously using a polyacrylamide-nanoactuator composite film.

3.3.1 Extrusion of fiber microactuators

In extrusion printing, pressurized nozzle pushes the ink to form continuous liquid filaments that are solidified immediately or shortly after being ejected from the nozzle [76]. This technique is favorable for printing nanocomposite polymer solutions for two reasons. First, extrusion is particularly suited for highly viscous inks and photopolymerization would be quite challenging in our case due to the opacity of gold nanorod suspension.

Alginate is a natural anionic polymer composed of β-D-mannuronate and α-L-guluronate residues [77, 78]. Alginate can be gelled using various co-monomers, therefore, the mechanical and chemical properties of the gel can be tuned. The two main methods to crosslink alginate gels are based on ionic or covalent bonding. Ionic crosslinking is done by the addition of a di-cation, most commonly Calcium (Ca^{2+}), in the form of calcium chloride ($CaCl_2$) salt. The high solubility of $CaCl_2$ in aqueous solutions results in a fast and inhomogeneous polymerization that can be poorly controlled. To slow down the process and increase homogeneity, calcium sulfate ($CaSO_4$) or calcium carbonate ($CaCO_3$) could be used. Alternatively, phosphate buffers could be added to the solution or ambient temperature could be decreased in order to reduce Ca^{2+} reactivity [78]. Ionic crosslinking brings two interesting properties. Calcium ions can be naturally replaced to dissolve alginate and degrade the gel. Ionically crosslinked alginate exhibits plastic deformation under stress. Upon mechanical loading, alginate gels relax as the ionic bonds dissociate and form elsewhere and at the same time the water is expelled. Covalently crosslinked alginate does not degrade in physiological solutions and does not display plastic deformation [78].

The fiber microactuator consists of nOMAs physically entrapped inside ionically-crosslinked nanoporous alginate gels (Figure 3.9). The nanocomposite was aspirated into a glass micropipette using capillary action and subsequently gelled upon exposure to calcium ions during extrusion.

3.3.1.1 Characterization of fiber microactuators

The extruded fibers were highly responsive to NIR excitation and exhibited large deformation (Figure 3.10a), comparable to the levels reached by spherical μOMAs even

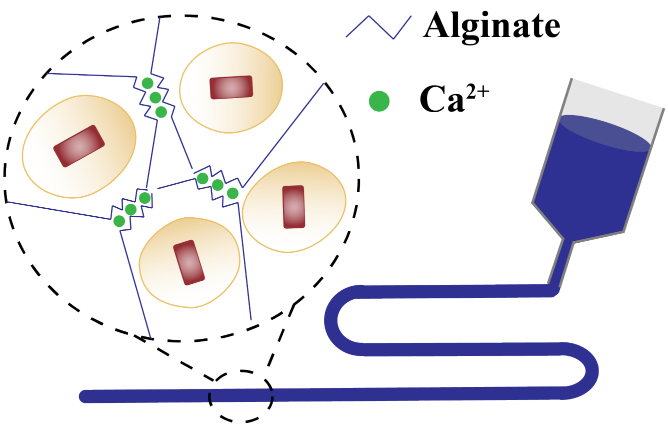

FIGURE 3.9 – Extrusion of alginate composite fibers. Schematic illustration of the extrusion process and content of the nanocomposite fiber μOMAs.

though the nOMA volume was significantly lower (~20%). The contraction kinetics also resembled the performance of the spherical μOMAs, 80% of the steady-state level was reached within the first 25 ms of actuation, as shown in Figure 3.10b. The actuation strain, ε, quantifies percent change in the thickness, T, normalized with respect to the initial thickness, T_0, of the fiber (equation 6).

$$\varepsilon(\%) = \frac{T_0 - T}{T_0} \times 100 \tag{6}$$

By tuning the laser power and alginate concentration, we could reach up to 45% strain with alginate-composite fibers. The relaxation, on the other hand, displayed a staged process where a fast relaxation phase due to release of elastic energy was followed by a slower diffusion process. The relaxation rate of the first stage during which the fiber regains 70% of its original size was 0.5 seconds for 50 μm thick fibers. With these specifications, the alginate-μOMAs composite fibers can deliver 10% strain at 2.5 Hz and 3% strain at 10 Hz [45].

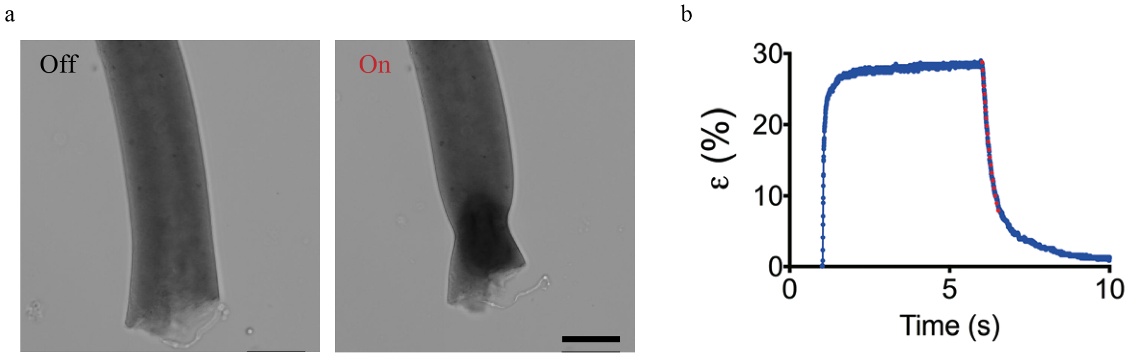

FIGURE 3.10 – Alginate fibers actuation. a. Optical actuation of ane alginate composite fiber. On the left a fiber on a relaxed state, and on the right a fiber contracted in the area of optical stimulation. b. Actuation strain versus time plot for a single contraction–relaxation cycle. An exponential fit to the first stage of the relaxation curve characterizes the relaxation constant [45].

3.3.2 Casting of actuated polymer substrates

As an alternative strategy, we explored casting of the composite hydrogel in the form of a thin film. The gel was polymerized between two solid surfaces, either between two glass coverslips or between an agarose slab and a glass coverslip. The thickness of the film was tuned with the volume of the suspension. Three different polymers were tested : polyacrylamide (pAAm), alginate, and a mixture of alginate and pAAm.

Polyacrylamide-based composite :

Polyacrylamide gels are synthetic hydrogels with high water content composed of acrylamide monomers and the cross-linker bis-acrylamide [79, 80]. The material has a constant storage modulus, therefore it is considered to be linearly elastic [81, 80]. The mechanical properties (i.e., Young's modulus) can be finely tuned by adjusting the composition. This tunability and optical transparency make this hydrogel a good choice for traction force microscopy [81, 77].

The nOMAs were physically entrapped in a pAAm gel by mixing them in the precursor solution prior to gel polymerization. The detailed protocol can be found in Section 3.3.4.3. Briefly, the nOMAs were concentrated through centrifugation and suspended in the precursor solution with rigorous mixing and vortexing. Fluoresccent micropraticles (1μm) were also added to the precursor solution for quantifying deformation. Polyacrylamide was formed by the copolymerization of acrylamide (AAm) and bis-acrylamide (BIS) while the polymerization reaction was initiated by ammonium persulfate (APS). The reaction generates free radicals that convert the acrylamide monomers into radicals. These radicals react with other monomers in a cascaded manner until two radicals meet and the reaction terminates. The radicalization of APS was accelerated by the addition of the catalyzer tetramethylenediamine, TEMED. The co-monomer BIS crosslinks randomly to the elongating polymer chains, forming a gel with porosity and mechanical properties dependent on the polymerization conditions and monomer concentrations [82].

As reported in several works [25, 27, 80, 82, 83], polyacrylamide stiffness can be finely tuned by playing with total concentration of monomers, C_T, cross-linker to monomer ratio concentration, $C_{cross-linker}$ and initiator concentration, C_{APS}, that are defined as

$$C_T(\%) = \frac{m_{AAm} + m_{BIS}}{V_T} \times 100\% \tag{7}$$

and

$$C_{cross-linker}(\%) = \frac{m_{BIS}}{m_{AAm} + m_{BIS}} \times 100\% \tag{8}$$

where m_{AAm} is the mass of acrylamide, m_{BIS} the mass of bis-acrylamide and V_T the total volume of the precursor solution.

In this work I kept $C_{cross-linker}$ constant at 3.25% and formed composites from a precursor solution with C_T of 7.9% in order to tune the stiffness of the gel to 1 kPa. The different initial conditions used in this study are summarized in Table 8. PBS was added to gels to avoid dehydration.

nOMAs concentration	Thickness	Polymerization conditions
1 mg/mL	50 μm	Room Temperature
2 mg/mL	100 μm	65^{o}C
4 mg/mL	150 μm	wait 20min
8 mg/mL	200 μm	wait 1h
	300 μm	

Table 8 – Summary of all the conditions tested for pAAM-based composites polymerization.

The maximum deformation of the gel under NIR illumination was quantified through the displacement of the fluorescent particles. The preliminary results showed that gels that contained 1 to 2 mg/mL nOMAs did not react to the laser. Notably, when the concentration was increased to 8 mg/mL, the deformation was quite small, which could be due to limited penetration of laser light. Gels with 4 mg/mL nOMAS showed the highest deformation (up to 10 μm).

Alginate-based composite :

We formed thin films of alginate nanocomposite on agarose by squeezing the suspension with a coverslip. Different concentrations of both alginate (0.1, 0.5, and 1%) and calcium chloride (1, 5, and 10 mM) were tested to determine the optimal parameters that would lead to largest actuation strain upon laser stimulation. As in the pAAm gels, performance was quantified by the displacement of the entrapped fluorescent particles. The nOMAs concentration was maintained at 4 mg/mL since this concentration worked best with the pAAm gels. Gels formed with 1 mM $CaCl_2$ and 0.5% alginate showed the greatest deformation under optical stimulation (up to 56μm).

Polyacrylamide + alginate composite :

Alginate gels deformed significantly more than polyacrylamide gels. However, they were brittle and cracked upon repeated actuation. To improve the mechanical properties, I decided to mix these two polymers. Previous work has shown that highly stretchable and tough hydrogels can be formed by mixing these two compounds [84, 85]. In the presence of alginate, in addition to covalent bonding between AAm monomers and BIS, the carboxylic group of alginate also binds to the amide groups of acrylamide. Once pAAm was crosslinked, $CaCl_2$ was added to promote the ionic cross-linking of alginate. Alginate concentration (0.5 and 1%), gel thickness (100, 150, and 300 μm) and nOMAs content (4, 8, and 16 mg/mL) were modulated. 1% alginate, 8 mg/mL nOMAs, and 150 m thick gels displayed the maximum displacement, up to 50.56 μm. The gel was quite tough and we did not observe cracks even if we transported the film to another substrate. Further experiments must be done to improve the composition and polymerization conditions. All deformation analysis was done on 2D due to the restrictions in imaging. Displacement of particles in the thickness direciton must be analyzed to better understand the mechanical response of the substrates.

3.3.3 Conclusions

The mechanical and geometric properties of the actuators became tunable with the incorporation of alginate. The performance can be further improved with the reinforcement of the architecture using fibrillar proteins such as collagen or cellulose. With proper physical or chemical coupling to nOMAs, any soft hydrogel can serve as the matrix. Preliminary results show that the reinforcement of alginate with pAAm made the gels tougher and easier to manipulate. This flexibility in polymer choice may facilitate mechanochemical interfacing of actuated matter with biological samples.

3.3.4 Detailed protocols

3.3.4.1 Materials

All reagents were purchased from Sigma Aldrich and used as received, unless otherwise stated : Sodium alginate from brown algae ; Calcium Chloride ($CaCl_2$, ≥93.0 %) ;10M Tris-buffer (supplied by EPFL) ; acrylamide (AAm), N'-N'-methylenebisacrylamide (Bis) ; ammonium persulfate (APS), N'-trytmethylethylenediamine (TEMED) and agarose.

3.3.4.2 Synthesis of alginate-composite fibers

The nanocomposite fiber actuators were fabricated by dispersing 40 $mg.mL^{-1}$ nOMAs in 1 % (v/v) sodium alginate in milli-Q water. The nanocomposite was transferred into a glass microcapillary by capillary forces and subsequently immersed in a 10 mM $CaCl_2$ solution for 12 h to allow Ca^{2+} to diffuse in. The crosslinked fiber was extruded from the capillary using a pressure dispenser.

3.3.4.3 Synthesis of Polyacrylamide-composite films

For polyacrylamide gels preparation, stock solutions were prepared in advanced. APS is prepared fresh before each use.

Stock solutions in 10mM Tris-buffer :
- [AAm]=0.5312g/mL (40%w/w)
- [BIS]= 0.02646g/mL (2%w/w)
- [APS]= 0.5mg/mL (0.05% w/v)

For 1kPa, 1mL (C_t=7.9% ; $C_{cross-linker}$=3.25%) :
- m_{BIS} =0.00257g -> V=0.0971mL=97.1μL
- m_{AAm}=0.07643g-> V=0.1438mL=143.8μL
- V_{APS} =0.6mL (0.03%w/v)
- $V_{Tris10mM}$=158μL

Gel preparation :

1. Centrifuge the coated nOMAs suspension at 15000 rpm, 4^{o}C for 5 min, to obtain the desired concentration.

2. Remove the supernatant.
3. Suspend in the precursor solution.
4. For a homogeneous suspension sonicate for a couple of minutes.
5. Add 0.6% w/v of fluorescent microparticles.
6. Sonicate again a couple of minutes.
7. Put the suspension on ice to slow down polymerization.
8. Add 0.4%v/v TEMED.
9. Add the desired volume in between to glass slides or cover-slips.
10. Wait 1h at room temperature and then add PBS.

If it is intended to attach the pAAm to the glass-bottom surface, the glass can be functionalized in advance with amine groups.

3.3.4.4 Synthesis of alginate-composite films

Alginate composites were prepared in a simillar manner as the fibers.

For the agarose gels, the calcium chloride was added to the agarose solution before polymerization, and then put in the oven to polymerize.

3.3.4.5 Synthesis of Polyacrylamide-alginate-composite films

For the 2-layer gels, first pAAM was polymerize with calcium chloride in the precursor solution, and then alginate was polymerized on top.

For pAAm-alginate mixture, sodium alginate was added to the pAAm precursor solution. pAAm was polymerized as described before and then a calcium chloride solution was added on the gel.

3.3.4.6 Experimental set-up

Same as in section 3.2.5.

3.4 In situ-self-assembly of microactuators

Controllable in situ assembly of microscopic machinery from nanoscale actuators capable of transducing electromagnetic radiation into mechanical work has potential to revolutionize microrobotics and minimally invasive medicine [86, 87]. With the realization of such technology, we can envision injection of a suspension of nanoactuators that are instructed to form devices with desired architecture and functionality at the target location. Previous work has shown that valves, mixers, [88, 89, 90] and mobile manipulators [63, 91, 92, 93] can be temporarily assembled within microfluidic environments from magnetic microparticles. Low-strength homogeneous magnetic fields simultaneously coordinate the assembly process and power the assembled microactuators [94, 95]. As a step forward, utilizing advanced additive manufacturing techniques and dielectrophoretic interactions between structures have recently enabled hierarchical shape-encoded assembly of more sophisticated mobile micromachines [96]. However, the performance of the machinery forged by bottom-up assembly methods is far from that of the engineering solutions brought by conventional top-down microfabrication techniques.

Animal muscle provides a great example for scalable hierarchical assembly of high performance actuators from nanoscale actomyosin units. Macroscale robotic artificial muscles already demonstrated the great potential in mimicking nature by providing large range of motions in a compact body without the use of complex mechanisms [97]. The presented actuators, ranging from shape memory alloys to soft pneumatic devices, cannot be miniaturized due to the reliance on electrical, mechanical, or fluidic tethers. Laser illumination provides a wireless alternative for powering microscale artificial muscle actuators [45, 98, 99, 100, 101, 102]. Notably, the combination of plasmonic photothermal effect of gold nanoparticles with chemomechanical potential of stimuli responsive hydrogels enables rapid, biocompatible, and efficient conversion of energy at nanoscale [45, 32, 60, 103]. These properties are instrumental for the development of remotely powered biomedical microrobotic systems. Previous work has also shown that gold nanoparticles generate thermocapillary convection and thermophoretic effects upon laser illumination, and the localized forces can be utilized for bringing particles together in a spatiotemporally controlled fashion [104, 105, 106, 107, 108, 109, 110]. Combining both magnetic and optical actuation methods is the next frontier in the development of multifunctional smart microrobotic systems [111]. We postulated that colloidal systems comprising nanoscale plasmon heat engines along with magnetic dipoles might simultaneously realize programmable self-assembly and dexterous wireless micromanipulation.

In this section I report the synthesis, power and control methodology for direct-write colloidal assembly of microactuators. The building block is a modified version of nOMA that has a gold nanorod coated with platinum and nickel layers at its core.

3.4.1 Photothermal and magnetic assembly of mNAs

The synthesis of nOMAs with catalytic and magnetic properties Figure 3.11a was reported in sections 2.6 and 2.7.4, where it was also shown their responsiveness to magnetic fields. The overall directed colloidal assembly process is shown in Figure 3.11b. Rotating magnetic fields program mNAs into transient clusters that discharge as soon as we turn off the magnetic field. In contrast, photothermal assembly process produces permanent assemblies that sustain physical attachment after the removal of the laser illumination. Localized nanoscale heating leads to ultrafast hydrogel volume-phase transition that is on the order of nanoseconds [112]. In our experiments, activation of mNAs at their LSPR frequency generated a strong and steep thermal gradient inside the solution that led to the formation of thermocapillary convection. Particles started to move with the flow from cold to hot regions as prescribed by the location of the laser beam. Physical and chemical interactions among agglomerating mNAs resulted in irreversible attachment and the formation of permanent microscale assemblies.

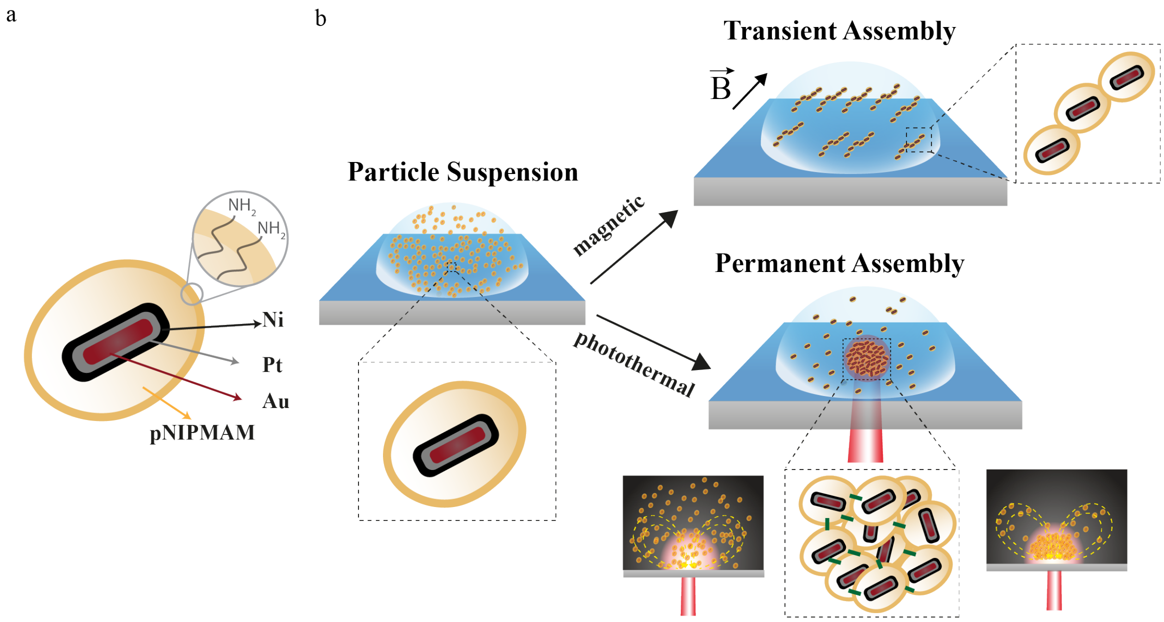

FIGURE 3.11 – Photothermal and magnetic assembly of mNAs. a. A schematic representation of the multifunctional mOMA (mNAs). b. Schematic representation of the programmable assembly process. Left : Nanoactuator suspension on a glass slide. While magnetic manipulation drives reversible assembly of mNAs into chains (top right), photothermal effects generated by NIR illumination form permanent assemblies of mNAs (bottom right) [46].

3.4.2 Controlled in situ self-assembly and characterization of mNAs

Figure 3.12a shows a sequence of time-lapse images taken from a representative movie recorded during the in situ colloidal assembly of the soft microrobotic artificial muscle (artificial μmuscle). Upon NIR exposure, mNAs that were inside the exposure area started to serve as nanoscale heaters and contributed to the generation of directed thermocapillary flows that brought more particles into the assembly site. The nucleation of the artificial µmuscle started as soon as mNAs came sufficiently close to each other, which could be detected from the phase change in the workspace. The delay between the activation of the laser and beginning of the nucleation process depended on the laser power density.

We observed a delay of about 2.5 s at a power density of 5.5 μWμm^{-2}, whereas increasing the power density to 7 μWμm^{-2} reduced the delay to less than a second.

The growth rate, measured as area versus time, was controlled by the laser power density, reaching as high as 93μm^{2}s^{-1} at 7 μWμm^{-2} (Figure 3.12b). Once the size of the assembly exceeds the illumination area, the part of the actuator that resides outside the illumination area stops generating heat. In addition, at microscale, heat transfer takes place quite rapidly. As a result, the temperature of the outer edge of the structure drops below LCST of the hydrogel, which leads to local swelling. The resultant nonlinear expansion along with asymmetry in the convective flow prescribed the printing of actuators in the form of filaments even though the laser beam was held stationary. The increase in the size of the assembly due to swelling must be considered during the design process. We generated streamlines by tracking 1 μm-diameter fluorescent polystyrene beads in consecutive measurements to visualize the fluid flow, as shown in Figure 3.12c. The thermal gradient was powerful enough to transport beads that were up to 360 μm away from the laser spot at a power density of 5.6 μWμm^{-2}. Particle image velocimetry (PIV) showed that the flow velocity was maximum around the laser spot and decreased in the radial direction (Figure 3.12d). The magnitude of instantaneous velocity was as high as 223 μm.s^{-1} at a power density of 7 μW.μm^{-2} and 70.7 μm.s^{-1} at 5.6 μWμm^{-2}.

After the completion of the assembly phase, structures were resuspended in water to study the actuation performance. They readily responded to low-intensity laser illumination ($<$4 μW.μm^{-2}) and low-strength magnetic fields ($<$30 mT). Each nanogel undergoes a volume-phase transition with plasmon heating that collectively led to rapid and controllable contraction of artificial μmuscle, as shown in Figure 3.12e. The amplitude, duration, repetition, and loading rate of mechanical output of the actuator can be effectively controlled by NIR pulse train. Deformation was monitored by measuring the actuation strain, which was defined as percentage change in radius normalized with respect to the initial radius (Figure 3.12f). To demonstrate frequency modulation, we applied optical signals with a fixed pulse width of 100 ms at varying frequencies and recorded the contraction–relaxation cycles of the microactuator (Figure 3.12g). At low frequencies, artificial μmuscle could reach 65–70% of the maximum actuation strain and had time to relax back to the fully swollen state. With increasing frequency, structures went into a tetanus-like state, where the gel did not have time to swell and stayed contracted. Likewise, adjusting the input laser power for a given pulse width and signal period provided control over actuator deformation through amplitude modulation (Figure 3.12h). The optical energy density absorbed by the artificial μmuscle was estimated to be 3.06 x 1011 kJm^{-3} (see section 3.4.6.6, equation 9).

Spatiotemporally controlled laser illumination can assemble mNAs into artificial µmuscle with arbitrary shapes. We instructed the mNAs to form a fiber-shaped artificial μmuscle to demonstrate multiple degrees of freedom (DOF) actuation. The fiber behaved as a bending actuator, and its curvature was actively and reversibly controlled by tuning the location and power of NIR illumination (Figure 3.12i). The actuator was continuously deformable without showing any signs of detachment or plastic deformation, presenting unlimited DOF for robotic manipulation tasks. Laser writing of actuators can be done sequentially by moving the laser beam as long as there are free mNAs in the workspace. As an experimental demonstration, we fabricated an actuator in the form of a square frame in four writing steps, as shown in Figure 3.12j. Controlling the thickness of the frame was challenging specifically at the joints because elongated or repeated laser expo-

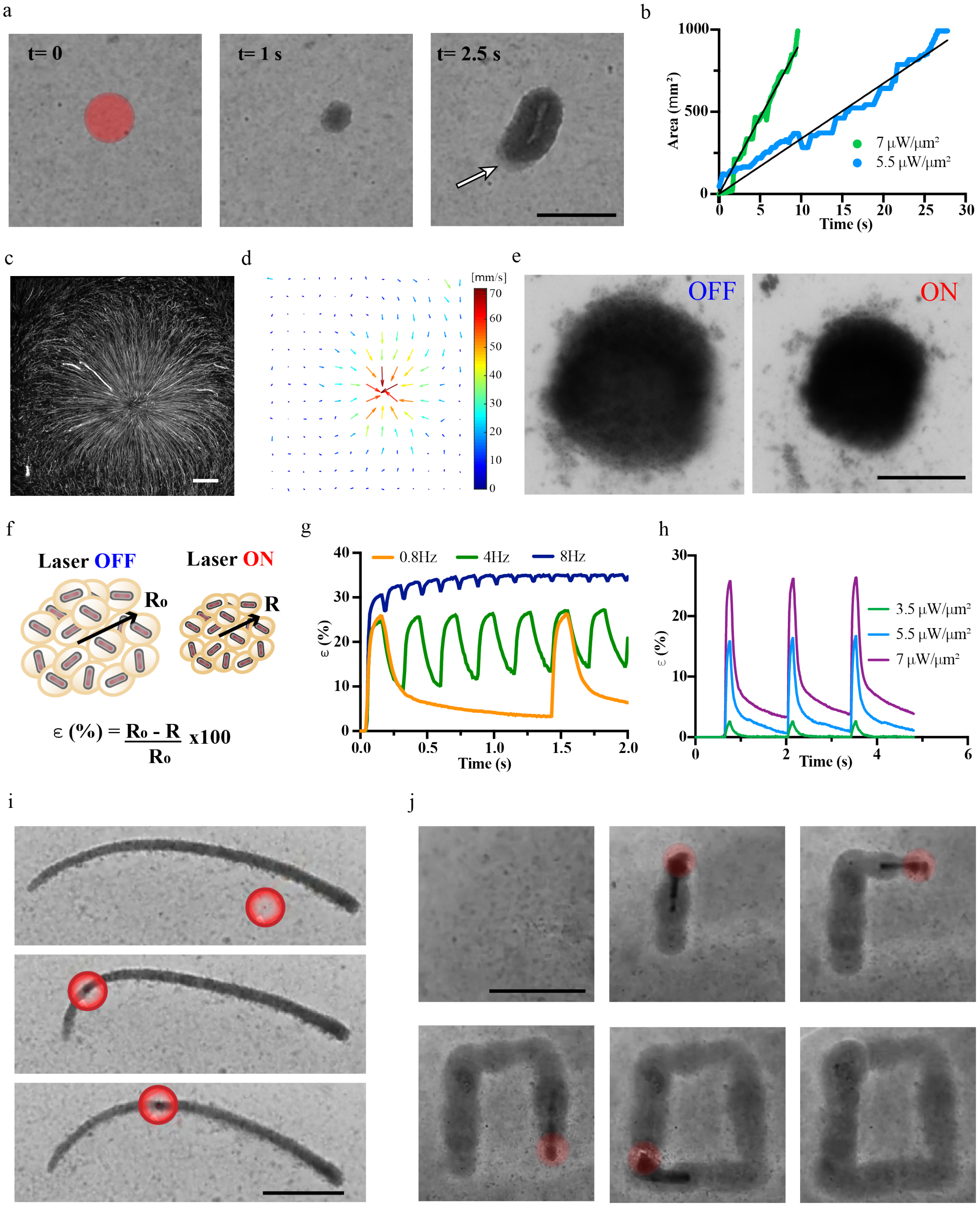

Figure 3.12 – **Controlled self-assembly and characterization of artificial μmuscle.** a. Snapshots from a time-lapse movie showing the nucleation and growth of the actuator under NIR illumination. Scale bar, 25μm. b. Growth in area with respect to time under continuous NIR illumination at two different power densities. The growth rate was calculated using a linear fit. The slopes of the curves are given by 92.949μm^2.s^{-1} (R^2=0.9761) and 33.637μm^2.s^{-1} (R^2=0.9539) for the optical power density of 7 and 5.5μWμm^{-2}, respectively. c. Streamlines showing thermocapillary flows generated around the laser spot. Scale bar, 100μm. d. PIV showing the direction and magnitude of particle velocity. e. Representative images showing optical actuation of a circular artificial μmuscle excited with 7μWμm^{-2} NIR exposure. Scale bar, 50μm. f. Actuation strain, $\varepsilon(\%)$, is measured as percent change in radius. R$_0$ denotes the initial radius of the actuator at its fully swollen state. g. Actuation strain over time for various actuation frequencies. Measurements were done at 100 ms pulse width with 7μWμm^{-2} laser power density. h. Actuation strain over time for different laser power densities. Measurements were done at 100ms pulse width and 0.8Hz frequency. i. Selective NIR exposure leads to continuous control over the curvature of the fiber-shaped artificial μmuscle. Scale bar, 25μm. j. Printing of actuators with arbitrary shapes. In the representative example, actuator with a square shape was formed by moving the laser beam. Scale bar, 50μm [46].

sure causes over-polymerization. As a result, printing parameters must be optimized for a given shape. We probed the magnetic response of the assemblies through application of magnetic torque. An artificial µmuscle with asymmetric shape was printed to be able to demonstrate magnetic control of orientation and translation. The μmuscle oriented along the direction of externally applied homogeneous magnetic field with field strength as low as 10mT, and followed the rotating field up to 10Hz at 40mT before reaching step-out frequency. In addition to orientation control, we demonstrated remote positioning of μmuscle using magnetic field gradients.

3.4.3 Understanding the mechanism of permanent colloidal assembly

We performed a series of experiments to gain insight on the mechanism of the assembly process. Surprisingly, nonmagnetic nanoactuators with only Au nanorod core did not attach to each other, although they generated strong thermocapillary convection. We hypothesized that the disappearance of permanent attachment may be explained by the following effects : 1) extra metallic layers somehow provide the activation energy for a chemical reaction or physical polymer entanglement ; and 2) magnetism plays an important role in the binding process. The absorbance spectra of particles with varying metallic coatings provided evidence for the first hypothesis (Figure 3.13a). With the deposition of Pt and Ni layers, the signal flattened and the LSPR peak shifted toward the red end of the spectrum by 23 and 72 nm, respectively [113]. The broadening and damping effects are expected to facilitate the generation of more heat at a given laser power density [114]. Not surprisingly, PIV reported lower flow velocity around the illuminated area in the absence of Pt–Ni coating. To probe the potential role of a chemical reaction, we checked whether the amine groups presented on the surfaces of the mNAs are required for the assembly. Notably, mNAs without amine groups did not attach to each other, while exchanging the amine group with alkyne group sustained connectivity but with reduced cohesion.

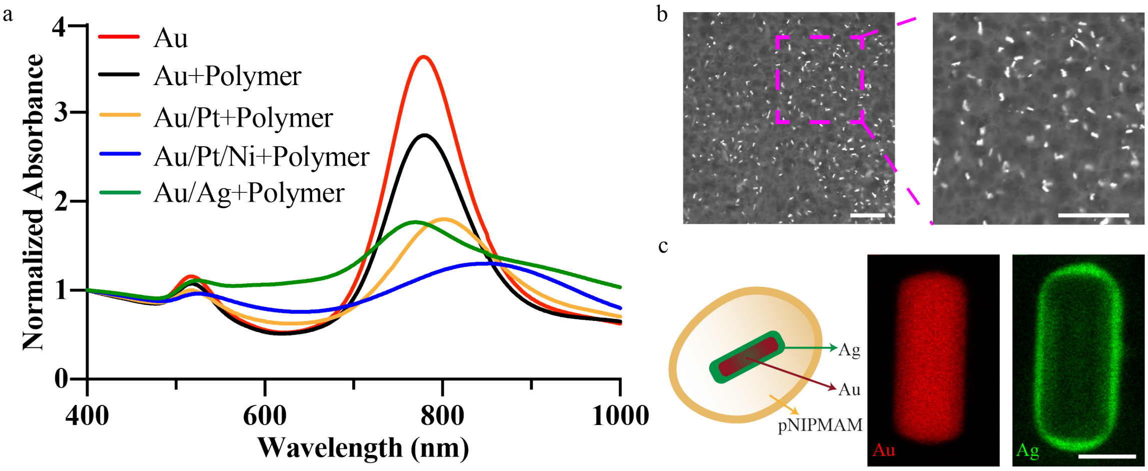

Figure 3.13 – Discovering the mechanism of permanent colloidal assembly. a. Normalized UV–vis–NIR absorbance spectra for gold nanoparticles with different metal coatings. b. Cryo-SEM image of the assembly. Nanorods show no indication of preferential alignment. Scale bar, 1μm. c. A schematic illustration of a nanoactuator (left) that consists of a gold nanorod coated with silver (Ag) and encapsulated inside pNIPMAM hydrogel. STEM-EDX images (right) show distribution of the different elements and verify the presence of Ag coating around the Au core. Scale bar, 30 nm [46].

We next explored whether magnetic interactions among mNAs led to attractive forces that held the particles together. Nonmagnetic nanoactuators with Au–Pt core (without Ni coating) also clicked to each other upon laser illumination. Furthermore, cryo-SEM images of magnetic assemblies showed no evidence of alignment among the nanorods (Figure 3.13b). We concluded that magnetism did not play a major role in the laser-induced assembly process. Finally, we checked whether Pt layer was indispensable for the catalysis of a specific reaction. We deposited a silver layer on Au nanorod by reducing Ag salt,[115] which was verified using microelemental EDX analysis (Figure 3.13c). Nanoactuators with Au–Ag core also formed permanent assemblies under NIR exposure. The UV–vis spectroscopy showed that Ag and Pt coating resulted in similar absorbance spectra ; thus, the heat losses are expected to be comparable (Figure 3.13a). As a final test, we resuspended assemblies into acetone and applied gentle pipetting to check whether the particles stayed together due to an unspecific adhesion process. The fact that they survived this treatment reinforced the theory that mNAs attached to each other due to the covalent cross-linking of amine groups, and this reaction required reaching a certain temperature and/or catalytic activity that was achieved by the additional metal coating.

3.4.4 Experimental set-up

All experiments were performed on a motorized inverted microscope (Nikon Ti-Eclipse) coupled with a 785 nm laser source (120mW, Thorlabs) that provided NIR illumination (Figure 3.14a). The laser illumination was controlled with a custom LabView program. For magnetic manipulation, a circular Halbach array, attached to a rotational stage and optimized for uniform magnetic field, 40mT, was mounted on the inverted microscope (Figure 3.14a and b). The rotation stage was controlled by a program written in MATLAB. Images and videos were captured using an ORCA-Flash4.0 CMOS camera (Hamamatsu). Videos were recorded with frame rates ranging from 33 to 100 fps depending on the experimental conditions.

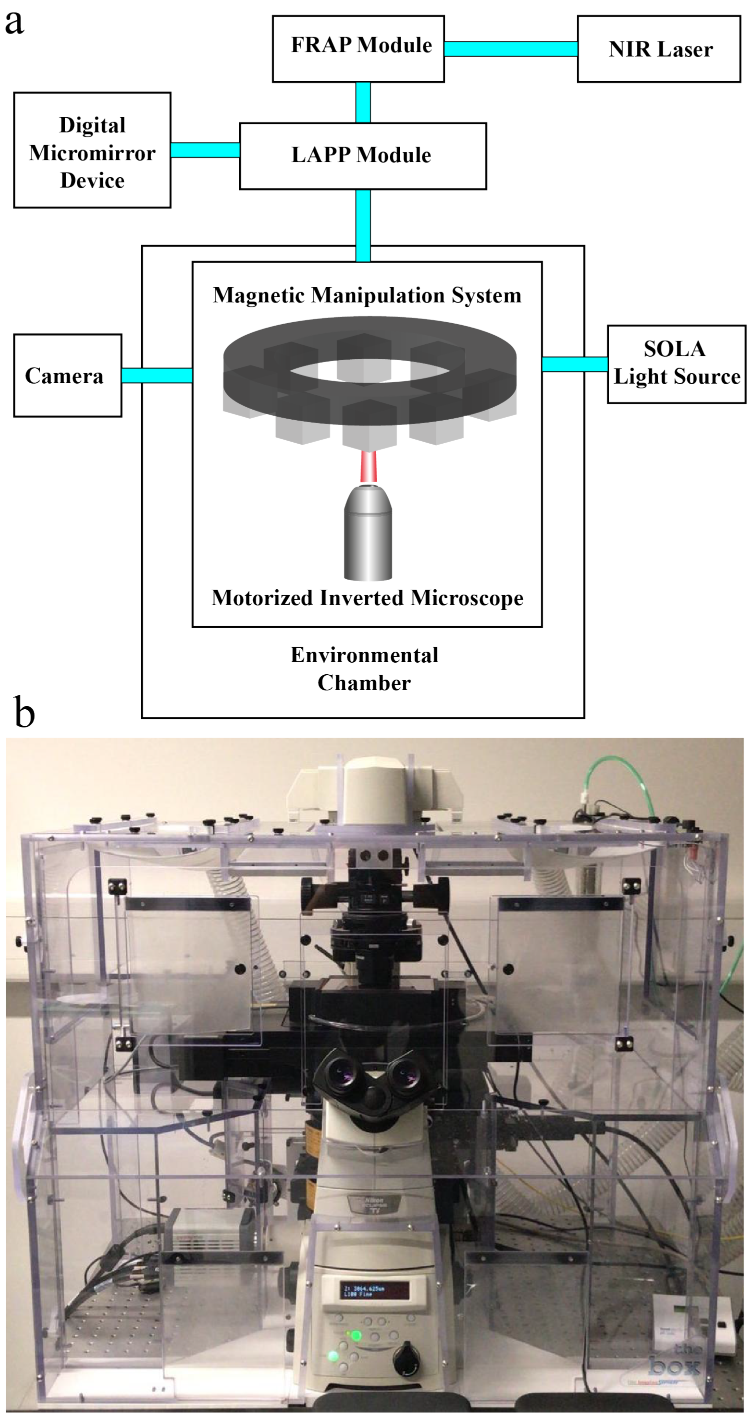
a
FRAP Module
NIR Laser
Digital Micromirror Device
LAPP Module
Magnetic Manipulation System
Camera
SOLA Light Source
Motorized Inverted Microscope
Environmental Chamber
b

Figure 3.14 – **Experimental set-up** a. A schematic illustration showing key components of the system. The NIR illumination is provided by a laser that is connected to the fluorescence recovery after photobleaching (FRAP) module of the microscope via fiber optic cable. A Digital Micromirror Device (DMD) projects UV light for the photopolymerization of the hydrogel structures. The motorized inverted microscope has two turrets stacked on top of each other to enable simultaneous laser illumination and fluorescence imaging. SOLA light source provides the illumination required for fluorescence imaging of tracer particles. The environmental chamber around the system provides controlled temperature and humidity during the experiments. The magnetic control system was mountedon top of the stage around the sample. Rectangles colored cyan show the optical path. b. A picture of the experimental platform [46].

3.4.5 Conclusions

We harnessed laser power to accomplish three distinct goals : optofluidic transport and manipulation of nanoactuators by thermocapillary convection, catalyzing a local reaction for phase transition and permanent assembly of agglomerating nanoactuators into artificial μmuscle, and localized heating for fast hydrogel volume-phase transition and actuation of the self-assembled artificial μmuscle. Methods that utilize hydrodynamic forces to manipulate particles offer several advantages such as favorable force scaling, low power requirement, and large workspace. Other optothermal effects such as thermophoresis have been reported in the literature in the context of particle assembly [105, 116]. Thermophoresis is not expected to play an important role in our manipulation protocol because, when we repeated the experiments in closed chambers where evaporation cannot take place, the particles showed very limited motion. Furthermore, both mNAs and fluorescent polystyrene beads moved from cold to hot regions in our experiments and we do not have charged surfactants in the solution. The colloidal assembly approach may be pushed to the next level if, instead of photopolymerization, we could self-assemble mechanisms from nanoscale building blocks. This concept may be realized by synthesizing thermally nonresponsive nanogels with gold nanorod core. Tuning the plasmon resonance frequency of the active and passive components using nanorods with different aspect ratios will enable coordinated assembly of mechanisms and actuators. Finally, the assembly process may become reversible by the initiation of covalent bonds that can be enzymatically removed or using DNA linkers [117].

Although the complexity of the shapes that can be achieved by laser writing is unprecedented, the technique may not be suitable for in vivo applications where penetration of NIR is an issue and Marangoni flows may not be generated effectively. In contrast, magnetic fields are suitable for particle manipulation and powering actuators under these conditions. The magnetic properties of the mNAs pave the way for the formation of dynamically stable morphologies using rotating and oscillating magnetic fields. The heat that is required for chemically crosslinking the particles and driving the sol–gel transition can be generated using radiofrequency (RF) oscillating magnetic fields. RF signals can also be used for powering the self-assembled artificial μmuscle. Previous work has shown that bulk thermoresponsive hydrogels fabricated from magnetic nanocomposites could be actuated using magnetic hyperthermia [74, 118]. However, this strategy will come with an important trade-off, the spatial resolution and frequency selective activation provided by plasmon resonance heating will be lost. Intuitively, the resolution of printing depends on the laser dose and the concentration of mNAs, and precise control over laser spot would enable printing of structures with arbitrary complexity.

3.4.6 Detailed protocols

3.4.6.1 Materials

All reagents were purchased from Sigma Aldrich and used as received, unless otherwise stated : hexadecyltrimethylammonium bromide (CTAB, 98%), silver nitrate ($AgNO_3$, 99.0%), L-ascorbic acid (99.9%) and sodium hydroxide (NaOH, 10 M in H2O).

3.4.6.2 Synthesis of nanoactuators

The synthesis of nonmagnetic and magnetic nanoactuators were described in section 2.7.

The protocol for silver coating was adapted from previously published reports and applies to pNIPMAM coated and non-coated AuNRs. [115, 119] Briefly, hydrogel coated nanorods were resuspended in a 5 mL solution of 0.01 M CTAB and 0.1mM AgNO3 to obtain a final gold concentration of $9.6\text{x}10^{-4}$ M. The reaction solution was left undisturbed at room temperature for 1 min, and subsequently 100 μL of 0.1 M ascorbic acid and 50 μL of 10 M NaOH solution were added. The solution was incubated for 3 h at room temperature with vigorous stirring. Finally, the product was purified by repeated centrifugation for 10 min at 3500 rcf at 10^{o}C and resuspended in mili-Qwater.

Note : after adding NaOH there should be a color change from red to yellow.

3.4.6.3 Characterization of Nanoactuators and microactuators

Several techniques were used to characterize the morphology and structure as well as thermal and optical properties of the materials. Transmission electron microscopy (TEM) and scanning TEM with EDX (STEM-EDX) were used to directly measure the overall size and elemental mapping of the nanoparticles, respectively. As described in section 2.7.6 the samples were prepared by depositing a 15 μL droplet of the nanoparticle suspension onto a carbon grid. The samples were dried at room temperature. TEM microscope (Tecnai Osiris, FEI) was operated with a voltage of 200 kV. UV–vis measurements were performed with V-670 UV–vis–NIR spectrophotometer (Jasco). The internal structure of the microscale assemblies was visualized using cryo-SEM (Zeiss Gemini 500) with an acceleration voltage of 5 kV, working distance of 9.6 nm, magnification of 14,260X, field of view (FOV) of 8.016 μm, and an imaging mode with variable pressure and a detection of electron backscatter diffraction (VP BSD).

3.4.6.4 Sample Preparation for Cryo-SEM imaging

The assemblies were encapsulated inside 10mM gelatin frozen -20^{o}C and cut into small cubes in the micrometer range. The gelatin cubes containing the samples were then transferred into 2M sucrose solution and kept chilled at 4^{o}C overnight. The following day, the cubes were placed on SEM holders and dipped into liquid nitrogen for rapid freezing. The frozen samples were prepared for imaging using Leica EM ACE600, where they were sublimated at -90^{o}C for 10 min to remove impurities and subsequently coated with a 5 nm layer of carbon at -150°C using sputtering. Focused ion beam (FIB) was used to remove remaining impurities. Leica EM vacuum cryo manipulation was used for holder mounting.

3.4.6.5 Image processing

Fiji from ImageJ [120] was used to analyze images and some videos. To study the deformation properties of the assemblies, videos with 100 fps were obtained and processed with a program based on edge-detection algorithm in MATLAB. [121] To study the flow rate generated in our experiments, 1 μm-diameter fluorescent particles were added to the colloidal suspension and fluorescent imaging was performed while the laser was on. Videos were recorded with high frame rate and processed in MATLAB with the PIV tool, [122] and plotted with the plugin quiverc [123].

3.4.6.6 Calculation of energy density absorbed by the artificial μmuscle

The energy density absorbed by an artificial μmuscle, $E_{\mu muscle}$, was estimated using the following equation. We assume that all the energy carried by the photons that reach the surface of the gold nanoparticle is converted into thermal energy. This formulation was deduced from Beer-Lambert's law [112].

$$E_{\mu muscle} = \frac{P_{laser}.(1-\xi)^2.(1-10^{\varepsilon_{AUNR}.l.c}).t}{\sigma.l} \tag{9}$$

where P_{laser} is the laser power measured on the glass slide, ξ is the scattering coefficient of IR window, ε_{AuNR} is the molar absorption coefficient of the AuNR, l is the optical pathlength, c is the molar concentration of the gold nanorods in the artificial µmuscle, t is the laser exposure time, and σ is the area of the laser beam.

Note that, for simplification, the contributions of the Pt and Ni layers were not considered. The molar concentration of particles in an artificial µmuscle was estimated with the following equation :

$$c = \frac{1}{V_{mNA}.N_A} \tag{10}$$

where V_{mNA}, is the volume of a single mNA and NA is the Avogadro number.

4 Development of soft robotic microdevices using projection lithography

4.1 Introduction

Microscopic soft devices that can actively interrogate and precisely perturb the biological microenvironment through physical and chemical interactions can revolutionize therapy and biomedical research [86, 124, 125]. Hydrogels have been serving as a platform to provide spatial and temporal control over the release of various therapeutic agents [126]. Through appropriately designed composition and structure, they can respond to various biochemical and physical stimuli by showing conformational or optical changes [127, 128]. High water content and tunable mechanical properties provide physical similarity to biological matter, giving the hydrogels excellent biocompatibility and stability [85]. A broad range of printing, folding, molding, and assembly methods are available for forming complex 3D hydrogel mesostructures [76]. Although hydrogel microsystems have shown the unique capability of operating autonomously as sensors and actuators inside microfluidic devices, [129, 130] existing prototypes cannot perform complex mechanical functions with high dexterity and performance. Magnetically and acoustically actuated hydrogel structures have shown great promise for utilizing mechanical power in regenerative medicine [131, 132, 133, 134, 135] and building miniaturized untethered machinery [136, 137, 138, 139, 140, 141]. However, these scaffolds cannot achieve coordination among multiple actuators, and the force and torque acting on the structures depend on their volume which does not scale down favorably. Optical manipulation methods offer high resolution [142] and enable biomimetic motions of photosensitive materials [101]. Yet, none of the existing formulations allow modular assembly and addressable actuation of untethered hydrogel MEMS devices within microfluidic platforms, a technological development that may become instrumental for mechanobiology [143, 144].

Skeletal muscle, the epitome of soft biological actuators, delivers tightly controlled actuation with unmatched power to weight ratio across vast size scales. The hierarchical architecture of muscle, from actomyosin motors to muscle bundles, provides scalability without sacrificing functionality. Fascicles consist of bundles of elongated muscle fibers surrounded by fibrous connective tissue, which together form a linear actuator optimized for force transmission. Artificial microactuators made out of nanoscale transducers that exhibit similar hierarchical architecture may fill this technological gap in terms of functionality and performance [145]. Although assembly methods are available to organize molecular motors based on nucleic acids, [146, 147] proteins, [148, 149] or synthetic molecules [150] into larger arrays, none of these constructs match physiologically relevant spatiotemporal force and deformation regimes. Another important feature underlying the spectacular performance of biological systems is the coordination among many specialized functional modules that are spatially arranged with the presence of a skeleton. The skeleton not only supports the structure of the organism, but also stores and releases energy in a controllable fashion. Inspired by these principles, we aim to physically couple hierarchical assemblies of nanoactuators with rationally-designed compliant mechanisms and develop modular soft robotic microdevices that can perform dexterous micromanipulation (Figures 4.1 and 4.2).

Here we present an experimental framework for the fabrication of soft robotic microdevices that seamlessly compliments conventional microfluidics technology. The key idea is to combine the rapid and efficient transduction of energy via the plasmonic photothermal effect at nanoscale [60, 109, 151, 152] with colloidal self-assembly [109] and spatially modulated optofluidic [153] additive manufacturing processes at microscale. Individual

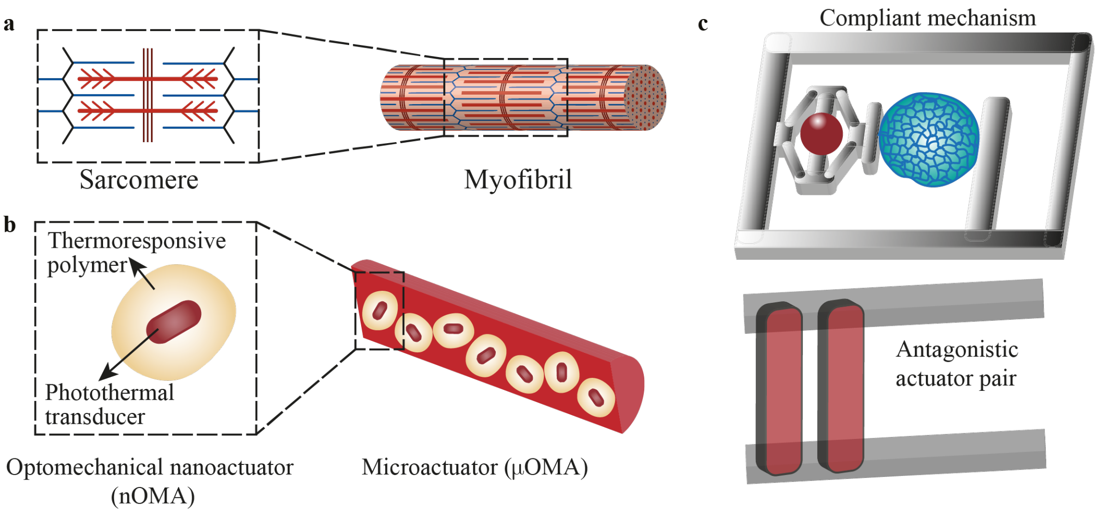
a
Sarcomere
Myofibril
b
Thermoresponsive polymer
Photothermal transducer
Optomechanical nanoactuator (nOMA)
Microactuator (µOMA)
c
Compliant mechanism
Antagonistic actuator pair

Figure 4.1 – Inspiration, concept, and realization of bioinspired soft robotic actuators and microdevices. a. The hierarchical sarcomere architecture within myofibrils is a great example from nature motivating the bottom up assembly of microactuators for powering larger scale machines. b. We utilized the superior efficiency of gold plasmonic nanotransducers by either directly linking nanoactuators together using colloidal self-assembly or embedding them into soft biopolymers. c. A variety of soft robotic microdevices are constructed by physically attaching microactuators to hydrogel mechanisms that are directly photopolymerized around the actuators without additional assembly procedures [45].

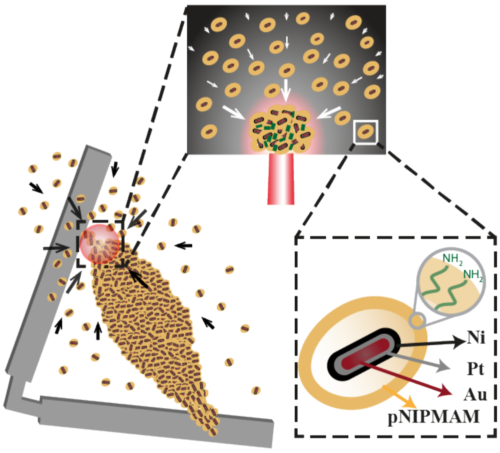
NH_2
NH_2
Ni
Pt
Au
pNIPMAM

Figure 4.2 – Concept of *in situ* development of bioinspired soft robotic actuators and microdevices. I took advantage of the eletromagnetic and catalytic properties of the mNAs to to build soft robotic devices wirelessly and *in situ*.

polymer coating around each gold nanorod ensures homogeneous distribution of nanoactuators (nOMAs), thus preserving the performance of the microactuators (μOMAs) at multiple scales. We built a maskless microscope projection photolithography system for in situ sequential polymerization of hydrogel structures constituting monolithic compliant mechanisms. Analytical models and finite element (FE) analysis provide effective rules for designing complex machine components. Actively modulated NIR illumination enables repeatable and precise operation for the machinery.

4.2 Design, production and characterization of compliant hydrogel mechanisms

Figure 4.3a shows a schematic representation of the fabrication of structures using in situ polymerization of a hydrogel monomer. We chose poly(ethylene glycol) diacrylate (PEGDA) as the hydrogel for manufacturing the skeleton due to its tunable stiffness, ease of polymerization, and temperature independent swelling properties. Rapid and controllable polymerization kinetics at the microscale permitted formation of structures with feature sizes ranging from 10 μm to 500 μm in less than 100 ms. We first utilized actuators as active hinges to control the rotation of a cantilever beam with respect to a fixed base (Figure 4.3b). The rotational motion can be precisely controlled by tuning the power and duration of NIR exposure. A 25% strain applied by the 40 μm actuator rotated the arm by 20^o. Next, we polymerized a cantilever beam that has several μOMAs on its side (Figure 4.3c). Prior to polymerization, we brought μOMAs together using a micromanipulator. μOMAs were located with 3 μm position error at their target locations within 20 s (depending on the initial and final locations) within a workspace of 400×400 m^2 using teleoperation. NIR illumination selectively activated μOMAs according to the pre-defined pattern. The longitudinal tensile strain generated by the contraction of μOMAs at each segment is converted to reversible bending of the hydrogel beam. The beam behaves as a bilayer bending actuator and the curvature can be actively controlled by tuning the location and power of NIR stimulation. Selective activation of μOMAs led to varying manipulator geometry that follows a continuous curvature kinematics, and the backbone pose can be successfully captured by the FEM analysis (Figure 4.3c). The PEGDA structures were modeled as an elastic material as strains were in the linear elastic range. We applied empirical μOMAs deformation values as boundary conditions in the model and the elastic modulus was measured as 550 ± 120 kPa using in-liquid AFM indentation tests.

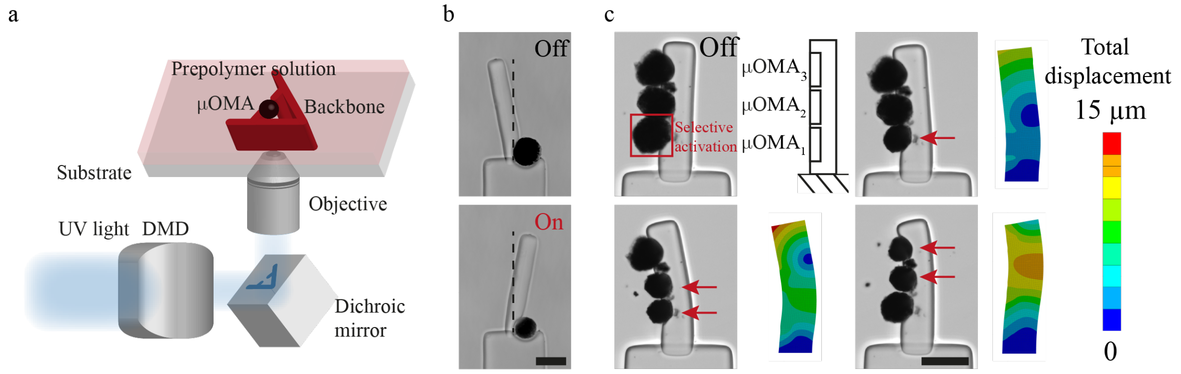

Figure 4.3 – *In situ* fabrication of hydrogel mechanisms a. Schematic of the fabrication methodology for building multibody microsystems. Digital maskless lithography inside microchannels drives the polymerization of compliant mechanisms physically coupled to the actuators. b. The rotation of a cantilever beam using a single μOMA serving as an active hinge. c. Demonstration of the control of deformation of a microscale bending actuator using structured illumination. FEM analysis predicts the deformation patterns. Scale bars, 50 μm [45].

We built and tested a series of mechanisms actuated by a single μOMA that would demonstrate the fundamental principles for the development of advanced machinery. We constructed lever systems to gain control over the displacement by polymerizing an elastic beam with distributed compliance around the μOMA (Figure 4.4a). The contraction of the μOMA moves the lever arms toward each other (flexion) while opening (extension) is achieved with the removal of the actuator force due to the stored energy. The angle of actuator insertion and the distance from the curved region to the point of force application determine the angular displacement according to the following trigonometric formula :

$$\theta_f = 2\sin^{-1}(\sin\frac{\theta_i}{2} - \frac{\Delta L}{2l}) \tag{11}$$

where ΔL is the deformation of the actuator, l is the distance from the hinge to the point of force application, θ_i is the initial angle and θ_f is the final angle between the arms (see Figure 4.4b). The final geometry of machines slightly deviates from the CAD drawings due to the swelling of μOMAs and the consequent extension of the associated flexible parts upon submerging in water. In the case of lever systems, the angle between the arms of the beam increases by $10^o \pm 2^o$ depending on the initial design and the size of the actuator. The experimental measurements were in accordance with the analytical calculations as shown in Figure 4.4c, and these results demonstrate that the transformation of actuator deformation into arm closure can be controlled by the geometric design of the lever system (see Figure 4.4a and c).

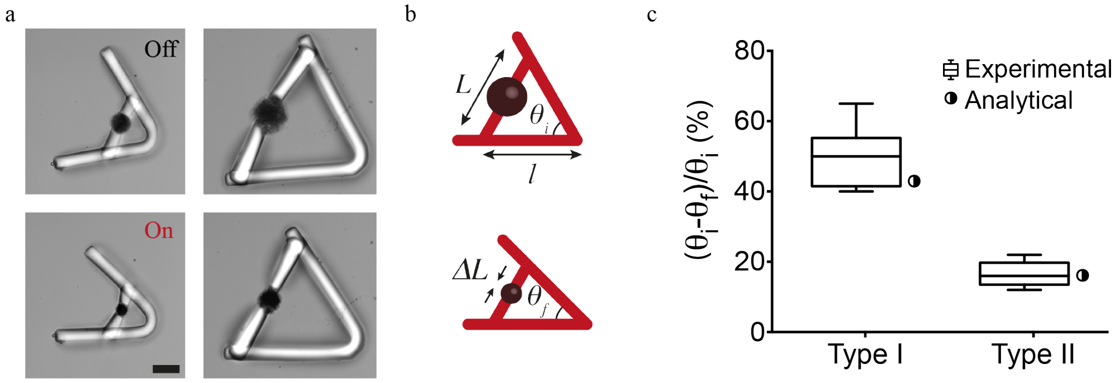

FIGURE 4.4 – *In situ* fabrication of hydrogel lever systems a. Lever system for controlling the transmission of stress and strain with a transmission angle of 60^o, with the artificial μmuscle in different positions. Scale bar, 50 μm. b. The schematic description of the geometrical design parameters in the lever system. c. The change in the transmission angle $\theta_f - \theta_i$ normalized with the initial value θ_i for two different lever arm designs. We compared two types of devices having the same transmission angle of 60^o and varying arm length l (type I : 100 µm and type II : 250 µm) (in a.). Experimental measurements (n = 8) are compared with the calculated values for the initial design parameters [45].

As an alternative approach, we fabricated levers with slender regions serving as single-axis flexure hinges. Complex deformation patterns can be generated by increasing the number of hinges and tuning the flexibility of connectors (Figure 4.5).

We next constructed a cantilever system where the deformation was applied from one side of the beam to characterize the force output of a single μOMA (Figure 4.6a). We used linear bending theory and experimental measurements to link the measured cantilever deflection to the amount of force generated by the actuators. The bending modulus of the beams was measured using a commercially available MEMS capacitive force sensor (Figure 4.6c). The modulus was found as 800 $\pm$ 85 kPa (n = 8) from the slope of the force-displacement curves (Figure 4.6g). The force applied by a 40 μm actuator at 20% strain was 10.3 μN, which corresponds to a uniaxial compressive stress of 8.1 kPa. The

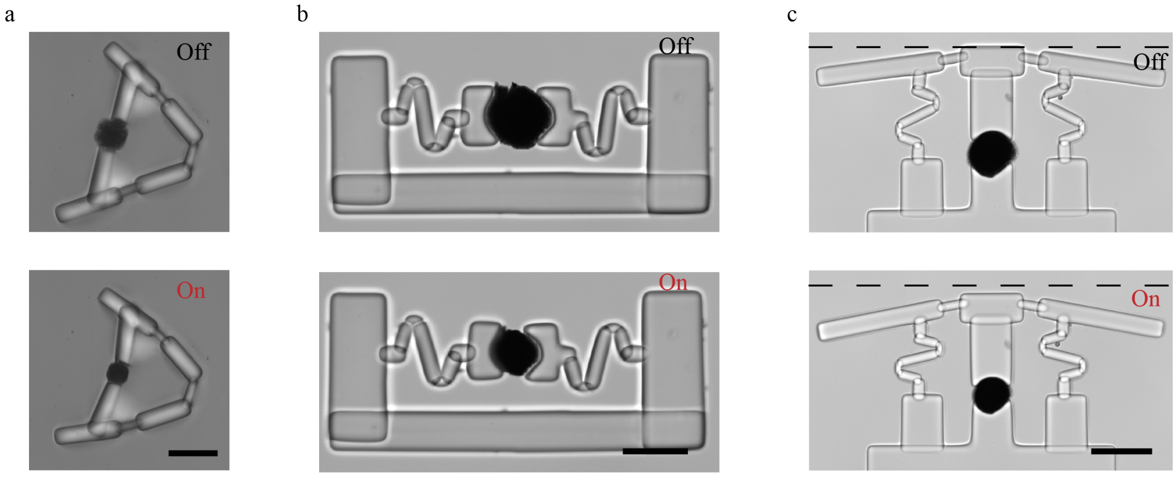

Figure 4.5 – *In situ* fabrication of hydrogel compliant mechanisms with multiple mechanical elements. a. The actuation of a lever arm with multiple flexure hinges. The position of the hinges determines the overall deformation profile. b. A serial double spring mechanism. The springs deform in response to actuator stress. c. A parallel spring arrangement. This configuration aids the deformation along the pre-defined axis by eliminating out-of-axis movement. Scale bars, 100 μm [45].

mass of a single μOMA is approximately 38.2 nanograms and the actuation speed is 500 μm.s^{-1} during the initial contraction phase, which together provides a power-to-mass ratio of 0.14 kW.kg^{-1}. The maximum stress and relative stroke of engineered skeletal muscle actuators were previously reported as 0.1–2 kPa and 0.01, respectively [154, 155, 156, 157]. Biohybrid actuators based on cardiomyocytes perform better with 10–30 kPa stress and 0.2–0.4 relative stroke [154]. Our results showed that the performance of optomechanical μOMAs is comparable to bioengineered actuators within a similar size range. Transmission of force and subsequent deformation can be concontrolled by installing passive elastic elements in series or parallel with the μOMAs (Figure 4.5). As a representative example, the actuation is completely decoupled from the cantilever displacement due to the extensibility of the engineered spring (Figures 4.5b and 4.6b).

This platform can be used not only to build soft microdevices for mechanobiology studies but also to study motion. In multicellular organisms, muscles are the source of force and motion. In musculoskeletal system, muscle tissues transmit force to the bones to generate movement. These mechanisms usually do not move in space but rotate around a joint axis, where the muscle provides torque. Being our spherical actuator our synthetic muscle, I tried to mimic the motion of spermatozoids, by playing with the size of the head and the tail and the configuration of the tail, as shown in Figure 4.7. The examples here are just proof of concept of the possible applications of our materials, since this was not the main goal of this thesis.

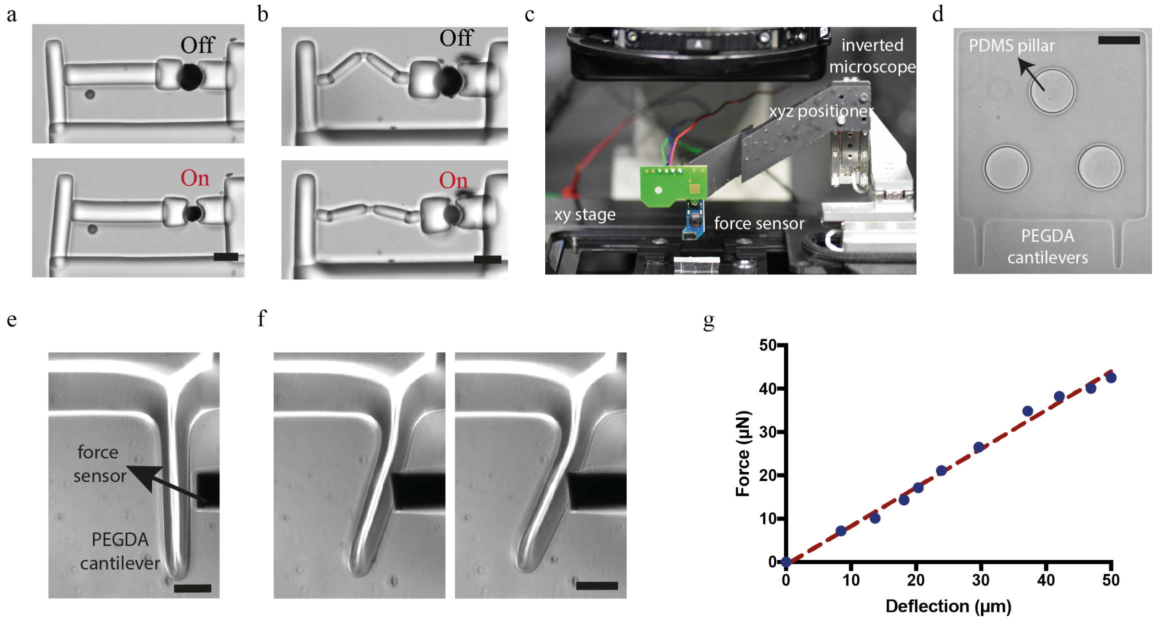
a
Off
On
b
Off
On
c
inverted microscope
xyz positioner
xy stage
force sensor
d
PDMS pillar
PEGDA cantilevers
e
force sensor
PEGDA cantilever
f
g
Force (µN)
0
10
20
30
40
50
Deflection (µm)
0
10
20
30
40
50

FIGURE 4.6 – Cantilever system and characterization of bending modulus a. A cantilever system for measuring the force generated by a single actuator. cale bar, 50 μm b. A cantilever system with a serial elastic spring connection. Spring deformation blocks force transmission to the cantilever. Scale bar, 50 μm. c. The position of the MEMS based capacitive force sensor is controlled by a motorized xyz micromanipulator while the position of the sample is controlled by the microscope stage. d. The base of the cantilever device is polymerized directly around the PDMS micropillars using the digital maskless lithography system. The pillars stabilize the base and keep it stationary during bending tests. Scale bar, 100 μm. e. Close-up of the cantilever beam and the tip of the sensor. Scale bar, 50 μm. f. Snapshots from a representative microindentation experiment. Scale bar, 50 μm. g. A representative force versus deflection curve. The slope of the linear fit is used for calculating the bending modulus [45].

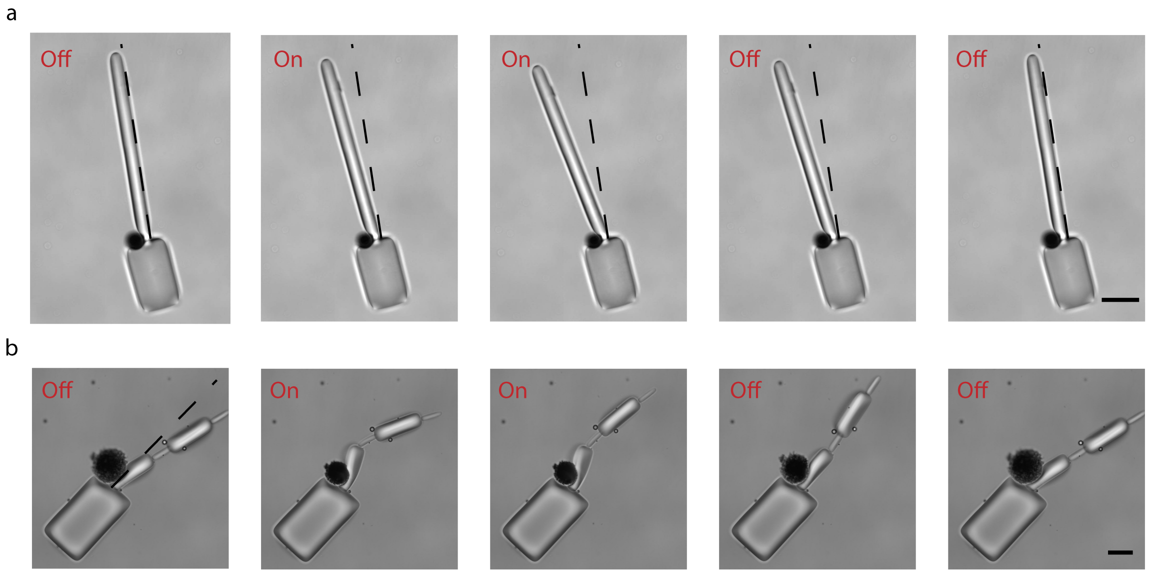
a
Off
On
On
Off
Off
b
Off
On
On
Off
Off

FIGURE 4.7 – Development of soft robotic microprototypes to study locomotion a. Representative example of a spermatozoid like microrobot. Scale bar, 100 μm. b. Representative example of a spermatozoid like microrobot with a tail with a flexible hinge that increases the its curvature when actuated. Scale bar, 50 μm.

4.3 Development and characterization of soft robotic microgrippers

We applied our material system to demonstrate the development of dexterous biomanipulation tools for microscopic samples. With a slight change in the blueprint, levers can be converted into an angular jaw microgripper that operates like a slider-rocker. In this configuration, the gripper jaws are synchronously opened and closed around a central pivot point, moving in an arching motion (Figure 4.8a and b). Next, we integrated an amplification mechanism by incorporating a second pair of cantilever beams connected to both the fingers and the actuator unit (Figure 4.8c). This arrangement constraints the fingers to follow a straight line, a feature that is known to improve accuracy of manipulation and at the same time improved the degree of displacement (Figure 4.8d). FEM analysis of the second generation microgrippers showed very good quantitative agreement for strain, as shown in Figure 4.9c. A 10% strain applied by the 40 μm actuator leads to full closure of the fingers with the aid of the amplification mechanism. The amplification ratio and stress distribution on the mechanism can be further improved by optimizing the design (Figure 4.9a). The grippers can be operated for minutes under continuous NIR exposure without showing any sign of fatigue (Figure 4.9b and c).

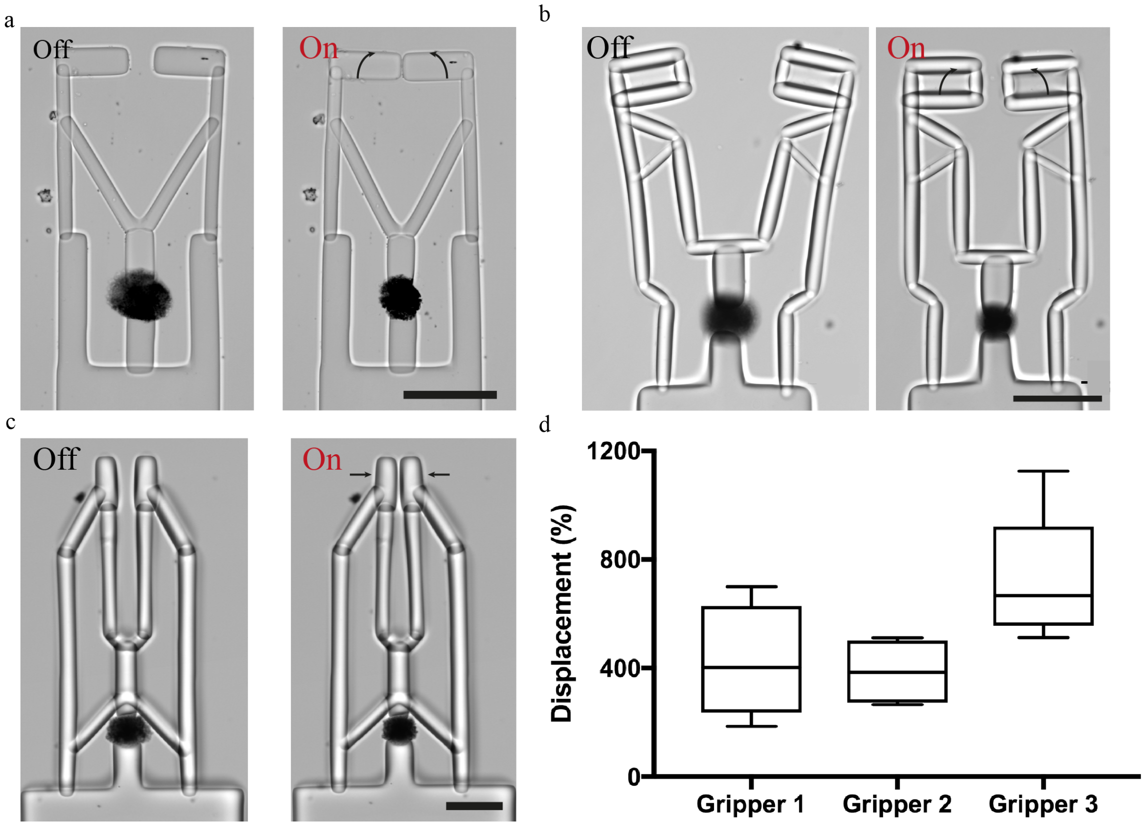

FIGURE 4.8 – Development of soft robotic microgrippers actuated by μOMAs a. An angular jaw gripper with rotating arms (Gripper 1). b. A more robust design for an angular jaw gripper (Gripper 2). c. The parallel jaw gripper (Gripper 3). d. Displacement for the different gripper designs. The parallel jaw gripper shows the best performance. Scale bars, 100 μm [45].

The mechanism shown in Figure 4.8c was combined with a bridge-type flextensional mechanism (Figure 4.10) to develop the microgrippers shown in Figure 4.11a that opened upon NIR exposure. Naturally closed configuration would allow holding samples and application of a constant compressive stress for extended periods in the absence of ex-

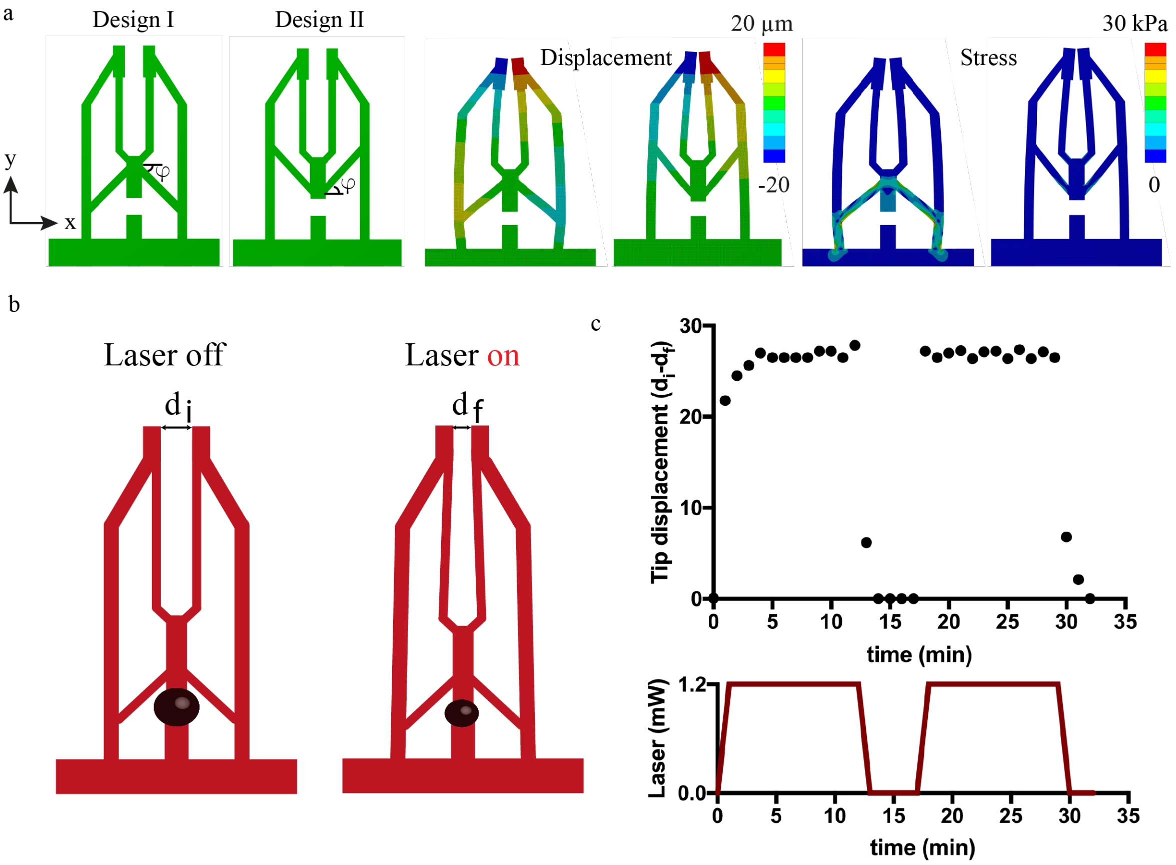

Figure 4.9 – FEM simulations and performance characterization of parallel jaw μgrippers. a. FEM simulations of two alternative gripper designs. Changes in the link angles result in significant variations in strain at the fingers and stress distribution in the skeleton. b. Long-term activation of a microgripper device with the illustrated design. c. The tip displacement of the gripper is plotted over time. The actuators can work robustly against the load for relatively long actuation periods. The results were replicated for six different microgrippers [45].

ternal actuation. On top of that, these models can be used for transporting microscale objects. Flextensional mechanisms provide control over the direction and amplitude of displacement. The output displacement Δx as a function of input displacement Δy is given by :

$$\Delta = \sqrt{l^2 \sin^2(\theta) - (\Delta y)^2 + 2l\cos(\theta)\Delta y} - l\sin(\theta) \tag{12}$$

An increase in the nominal linkage angle θ will decrease Δx. Another important parameter is the length of the linkage arms l, the longer the arm is the larger the output displacement. We fabricated four different prototypes by varying θ and l (Figure 4.10a-d). The measured displacement of the mechanism was found to reasonably match that predicted by the analytical equation and FE analysis (Figure 4.10e). It is also possible to provide linear displacement in opposite directions by combining two flextensional mechanisms in different orientations, hence providing full control over translational motion. (Figure 4.10f).

As a final step, I designed inverted grippers that open the arms upon contraction of the actuator (Figure 4.11). As mentioned, these models could be used for transporting mi-

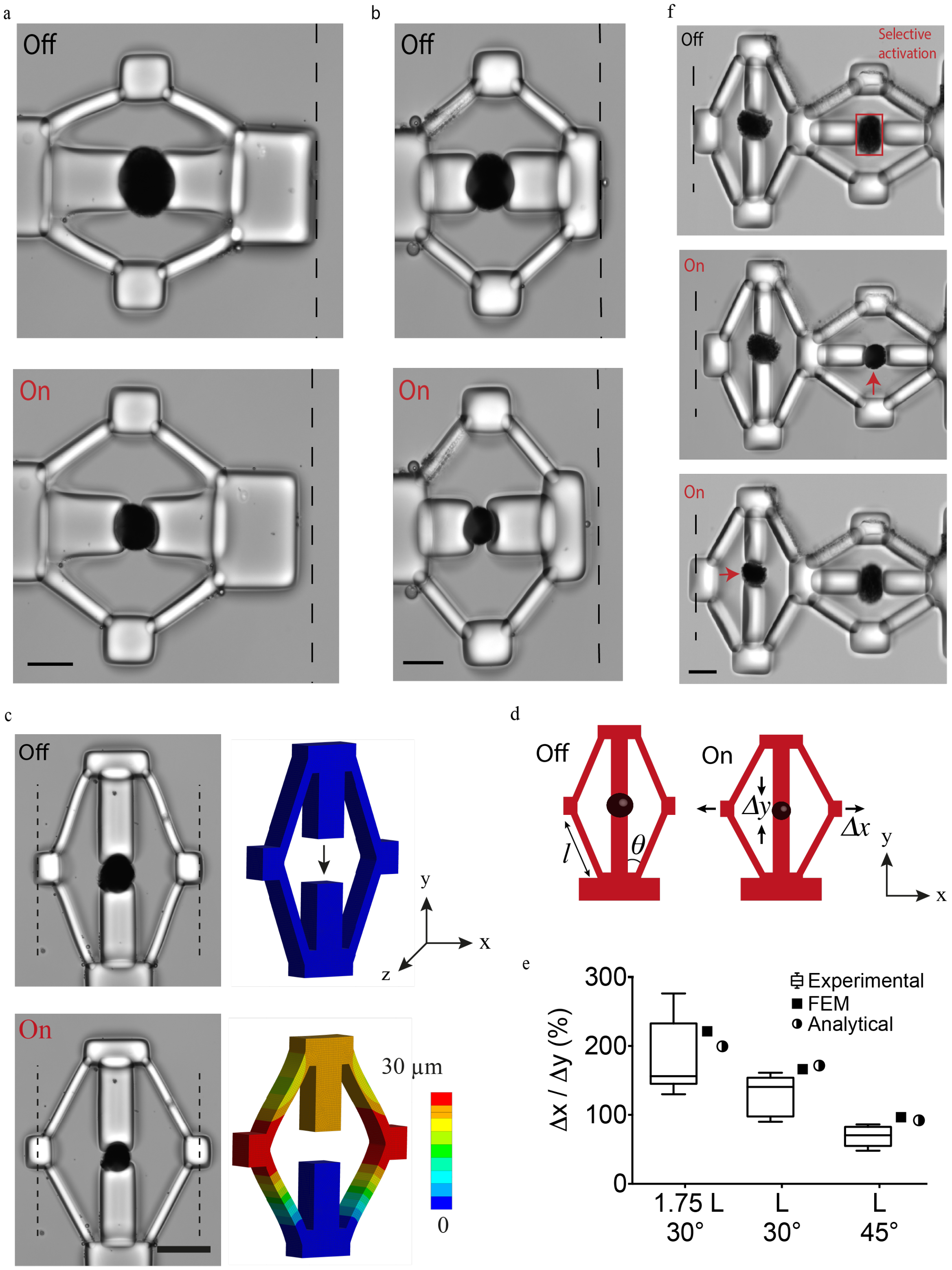
a
Off
On
b
Off
On
f
Off
Selective activation
On
On
c
Off
On
y
x
z
30 µm
0
d
Off
On
Δy
Δx
l
θ
y
x
e
Experimental
FEM
Analytical
Δx / Δy (%)
300
200
100
0
1.75 L 30°
L 30°
L 45°

Figure 4.10 – Development of flextensional mechanisms a-c. Flextensional mechanisms with different link angles (30^o or 45^o) and arm lengths (75 μm or 150 μm). c. The FEM analysis of a representative example for a flextensional mechanism. d. Schematic illustration of the flextensional mechanism denoting the input, output, and design parameters. e. The free displacement of the arm is plotted for the different geometrical mechanism designs along with the simulation results and solutions of the analytical equations. f. Optical images of a stacked flextensional mechanism during actuation. The selective activation of μOMAs results in forward and backward displacement at the tip. All scale bars, 50 μm [45].

croscale objects. If magnetic nanoparticles are added to the skeleton, it will be possible to wirelessly position the gripper, hence the object, to the final destination. The compliance of the skeleton allows manipulation of biological samples with minimal risk of damage. The dynamics of closure and opening of grippers can be controlled by modulating the laser input or by controlling the elasticity of the material.

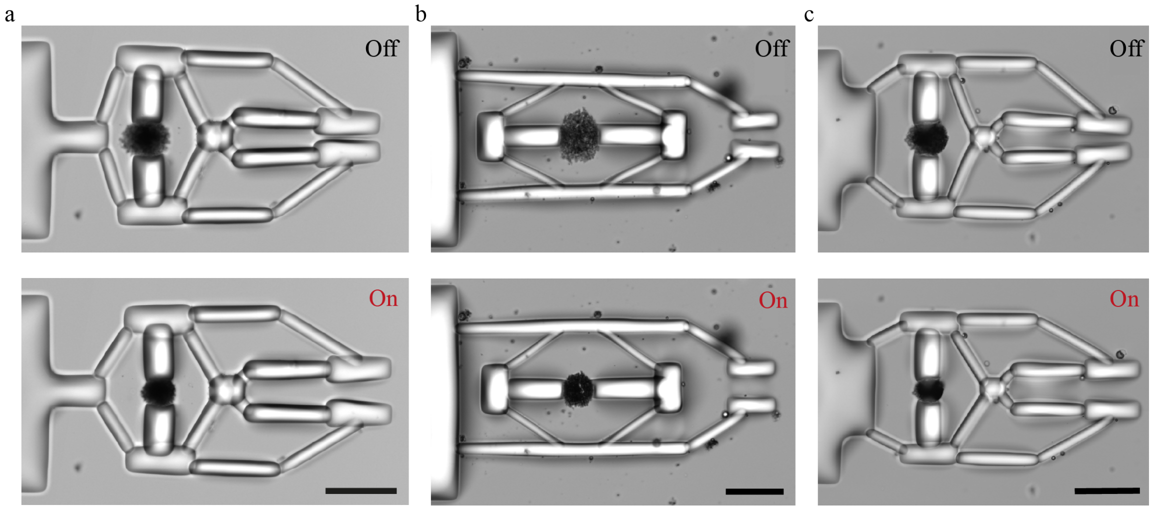

FIGURE 4.11 – Development of inverted soft robotic microgrippers actuated by μOMAs a-c. Flextensional mechanism integrated into different designs of the gripping mechanism to convert contraction of the actuator into extension of the arms. Scale bars, 100 μm [45].

4.4 Investigating tissue mechanics *in vitro* using untethered soft robotic microdevices

Recent advances in three-dimensional (3D) culture techniques revolutionized the biomimicry of engineered mammalian tissues. These models enable testing of novel therapeutic agents on human tissues, thus circumventing animal trials, and facilitate the discovery of fundamental biological principles [158, 159, 160, 161]. Microfluidic technology and genetic engineering have already become instrumental in revealing biochemical pathways that play important role in the physiology and disease of engineered tissues [162, 163, 164]. To match the precision and versatility of chemical and molecular manipulation techniques, novel mechanical manipulation tools are required. Our understanding of cell mechanics during homeostasis and disease has been garnered from techniques that work on monolayers [165]. These studies have shown that cellular state depends on sensing and transduction of mechanical signals (i.e. mechanotransduction), which involve proteins and associated pathways generating intracellular signaling that ultimately give rise to transcriptional programming and changes in cell phenotype [166]. The shaping of tissues and maintenance of their physiological activity involve the spatial and temporal regulation of mechanics at multiple scales. Lack of tools hinder the development of the field because applying the engineering methods that are optimized for planar substrates to 3D biological samples poses major challenges.

Mechanical loading of *in vitro* tissues must be performed in a way that is compatible with biochemical manipulation techniques and modern imaging modalities such as confocal and two-photon microscopy. That is to say, robotic micromanipulation tools must operate inside transparent chambers with well-defined chemical composition under physiological pH, temperature, and humidity. Another important specification is maintaining the natural microenvironment of the biological samples during testing as cells are exquisitely sensitive to substrate topography and stiffness, as well as the type and density of ligands presented on the surfaces. The end-effector that is in contact with the samples must be compliant (modulus in the kPa range) with tunable surface chemistry. Finally, considering the inevitable accumulation of proteins and other organics from the serum and cell secretion on the machine parts, the device must be disposable.

Robotic manipulation based on traditional MEMS (microelectromechanical systems) technology deliver fine control over deformation (nm to μm) while providing force measurements with high resolution (nN to μN) [167, 168, 169, 170]. Recently, robotic manipulation tools have been integrated with microfluidic chips for high-throughput automated testing of 3D biological samples [171, 172]. Although MEMS sensors are very sensitive and actuators are precise, the technology is too expensive to be disposable, the end-effectors do not interface well with biological tissues due to their relatively high stiffness and associated electronics, and the design framework cannot be dynamically adapted to the configuration of the specimen. From materials perspective, hydrogels are ideal for biomanipulation because their high water content and tunable chemistry provide excellent compatibility with living matter [126, 173, 174]. Stimuli-responsive hydrogels provide ample opportunities in the course of building soft microscale actuators and machines for biomedical applications [124, 130, 136, 175, 176, 177, 178]. Bulk hydrogel actuators, however, mostly suffer from low stress, poor resolution, and limited strain rate. One way to address these limitations is hierarchically structuring hydrogel nanocomposites using bottom-up manufacturing techniques based on self-assembly. This scalable approach provides means to harness efficient nanoscale energy transduction mechanisms at larger scales [60]. In section 3, I introduced the cell-sized optomechanical actuators that exhibit mechanical properties (4.8±2.1 kPa stiffness) and performance metrics (relative stroke up to 0.3 and stress up to 10 kPa) that are comparable to that of living muscle cells [45]. As mentioned, these microactuators have the capability to convert optical energy into heat by the gold core, which is transduced into mechanical work due to reversible collapse of the encapsulating nanogel. By modulating the laser input it is possible to have a fine control over actuation with sub-micron spatial resolution at millisecond temporal resolution. In the previous sections, it was demonstrated that a variety of microscopic artifacts can be constructed with the incorporation of passive hydrogel structures that are directly polymerized around the actuators using digital lithography without additional assembly procedures.

This section describes the design, fabrication, and operation of soft robotic devices for long-term dynamic mechanical loading and characterization of 3D biological samples. The robotic toolkit involves several modules ; (1) the actuated flextensional mechanism pushing a piston-like end-effector for spatiotemporally resolved compression, (2) a body frame that is used to position the device inside microfluidic channels or open chambers, and (3) a calibrated cantilever beam for the quantification of tissue stiffness. The fabrication method is based on additive manufacturing where the design of different modules can be adapted according to the specifications of each biological sample on the fly. Upon laser exposure, the soft actuator contracts and the mechanism transforms the contraction into displacement of the piston. The deformation of the cantilever reports the stiffness of the sample. We demonstrate the functionality of the prototype using hydrogel sensor beads with known stiffness and 3D cell aggregates.

As show in the previous subsections, we fabricated the mechanisms using a maskless projection photolithography method [153, 179]. Brielfy, The system consists of a programmable digital micromirror device (DMD) module that projects light coming from an ultraviolet LED source through microscope objective according to CAD drawings (Figure 4.12). The μOMAs were suspended in a solution of poly (ethylene glycol) diacrylate (PEGDA, 575 kDa) monomer solution supplemented with 20% (v/v) 2-Hydroxy-2-methylpropiophenone (DAROCUR) photoinitiator. UV exposure initiates the free-radical polymerization of structures in the desired form within milliseconds.

To develop the compressor devices, we utilized flextensional mechanisms for generating uniaxial compression of biological specimen (Section 4.3 Figure 4.10a). The purpose of the flextensional mechanism is to change the direction of motion (from contraction of the actuator to the extension of the piston) and amplify the displacement generated by the actuator while reducing mechanical advantage as a trade off.

4.4.1 Design and computational analysis of the compressor microdevice

We applied our material system to develop a versatile, remotely controlled biomanipulation platform. Figure 4.13a shows an image of the compression device, revealing the overall strategy for the simultaneous execution of mechanical loading and characterization operations. There are four major machine components : actuated flextensional mechanism as the driver, end-effector that acts like a piston, cantilever beam for quantifying stiffness, and outer frame. The outer frame is designed to minimize the bending of the actuated structures. The compression device utilized the same flextensional mechanism shown in

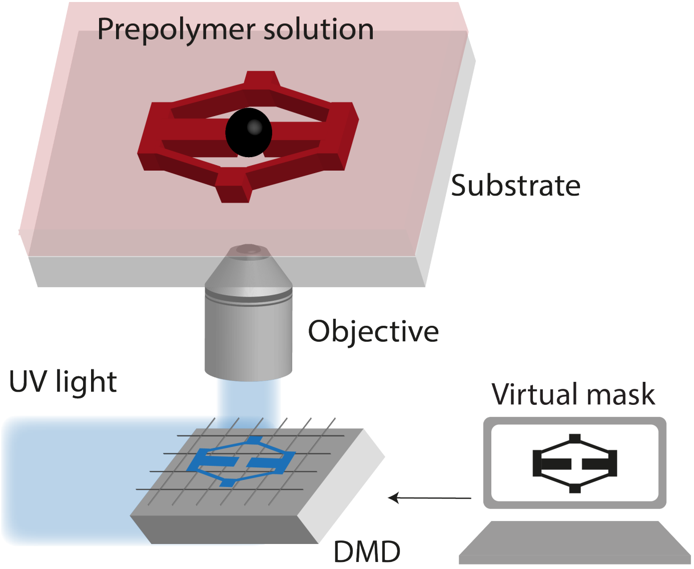

FIGURE 4.12 – *In situ* fabrication of the compressor components. The fabrication methodology for building compliant flextensional mechanisms. The projector defines the geometry of the structures polymerizing around the actuators [65].

Figure 4.10a to convert the contraction of a single μOMA into extension of the arm, which as a result moves the piston forward. The cantilever beam reports the mechanical properties of the compressed specimen. The characteristics of the measurement can be tuned by modulating beam geometry according to the sample properties. Figure 4.13b shows a prototype with a thicker beam, which enables the device to quantify higher stiffness but with lower sensitivity. The piston, which transmits the force to the sample, can be shaped according to the intended stress profile, as demonstrated by the incorporation of a pointy tip (Figure 4.13c). Multiple compressors with various different modules were fabricated *en masse* using the programmable features of the DMD module (Figure 4.14).

The displacement of the piston is defined by the actuator size and dynamically controlled by the duration of laser excitation (Figure 4.13d). In our experiments, the displacement was recorded as high as 170 μm. Figure 4.13e depicts the piston displacement under the laser illumination with 500 ms pulse duration at 0.1 Hz for two different power levels. We assessed the long-term performance under repeated actuation cycles and confirmed that the displacement did not change after 1000 cycles (Figure 4.15).

We built a finite element model of the device to facilitate the design process and report stresses on the beams. Structures were modeled as linear elastic substrates where the empirical value of the Young's modulus (see sections 4.2 and 4.4.3) was used. Experimentally measured actuator displacements were taken as prescribed displacement boundary conditions. Figure 4.13f consists of simulation results coming from layouts with different arm length and angles, highlighting the relation between geometry and maximum displacement. Moreover, numerical simulations reported the accumulated stress on the actuated beams, which further quantified the device performance.

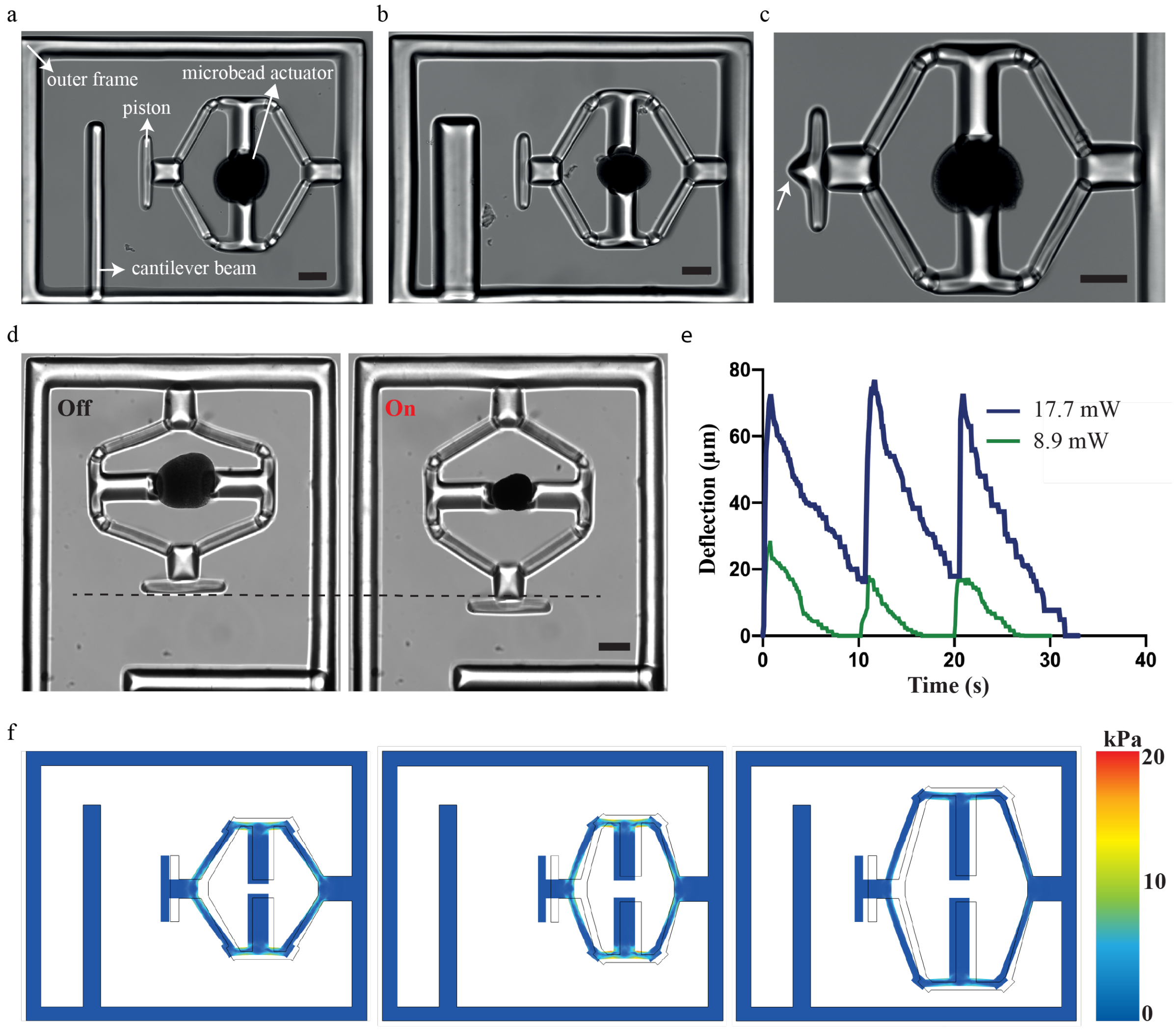

FIGURE 4.13 – Design, operation, and computational analysis of the compressors. a. A representative bright-field microscope image of the device showing the different modules. b. The cantilever beam geometry can be modified to tune the the sensitivity of the sensor. c. The design of the piston can be modified to tune the applied stress. White arrow points to the sharp tip engineered for localized indentation. d. Temporal sequence of micrographs from a representative actuation cycle. e. The displacement vs time plot for the piston at different NIR laser power. The signal duration is 100 ms and the actuation frequency is 0.1 Hz. f. Simulation results for different flextensional mechanism designs. The arm angle and length can be modified to tune the piston displacement and stress on the mechanism. Scale bars, 100 μm [65].

4.4.2 Heat transfer during device operation

Reliable device performance and long-term biocompatibility of the actuation strategy relies on the following assumption ; heating is transient and confined to the actuator. Previous work has shown that the temperature of nOMAs is inversely proportional to the distance from the gold nanorod and heat is dissipated within milliseconds, and thus particles undergo negligible surface heating [32, 180], Clustering hundreds of nanoheaters together is expected to trap heat inside the μOMA, essentially reducing the laser power required to reach the lower critical solution temperature at which the thermoresponsive polymer goes through a phase transition. On the other hand, negligible surface heating condition may not hold any more.

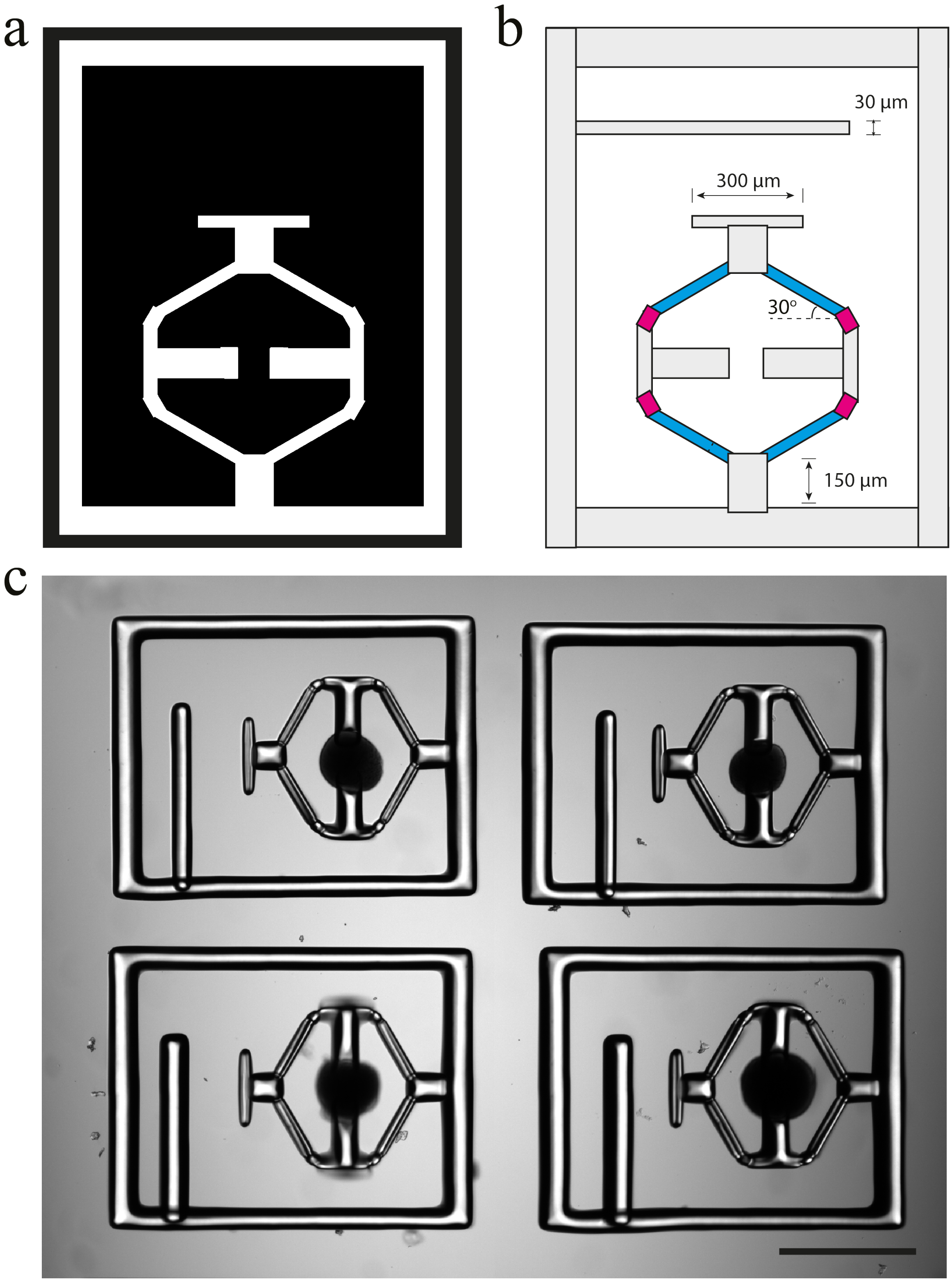

FIGURE 4.14 – Rapid prototyping of compression devices using projection lithography. a. A representative CAD drawing of the device. Single exposure using this digital mask polymerizes the mechanism as a whole. b. Alternatively, the mechanism is divided into different regions (shown with different colors) and flexible beams are fabricated with separate illumination to avoid over-polymerization. c. Devices are fabricated *en masse*. Sensing probes with two different sensitivities are shown on the top and bottom rows. Scale bar, 500 μm [65].

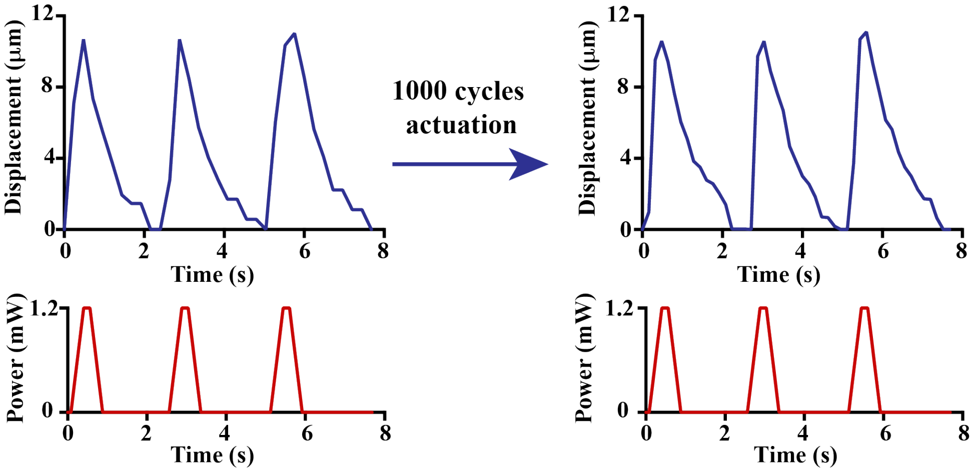

FIGURE 4.15 – Testing of the soft robotic compressor microdevice performance. The displacement of the piston over time under repetitive laser stimulation. There was no detectable change in the performance of the device after 1000 actuation cycles. The laser power was set to 1.2 mW and the results were replicated for six different microdevices [45].

We performed numerical simulations to assess whether heat transfer during the actuation of μOMA could compromise the viability of biological samples. We first calculated the number of nOMAs that would fit into a 400 nm thick cross-sectional cut in the middle of a 100 μm-diameter actuator, assuming close packing of equal particles. Figure 4.16a shows the geometric configuration of the computational model. Single rectangle shown in the inset of Figure 4.16a corresponds to a group of 400 nOMAs. Conduction in solids is used to assign the boundary heat source value to each nOMA, which is calculated using the following formula :

$$P = \frac{P_{laser}}{A_{laserbeam}} A_{absorption} \tag{13}$$

where P_{laser} is the measured laser power, $A_{laserbeam}$ is the area of the laser beam used to actuate the μOMA, $A_{absorption}$ is the absorption cross-section of one gold nanorod. In the reported simulation results, P_{laser}=14.22 mW, $A_{laserbeam}$=1.96·10^{-9} m^2, and $A_{absorption}$=6000 nm^2. μOMA was placed in a 1 mm^2 water bath, which was taken to be large so that we could eliminate potential issues associated with diffusion. Note that we assigned a fixed boundary temperature of 37 ^{o}C to the walls of the bath. The software solved the following equation :

$$d_z \rho C_p \frac{\partial T}{\partial t} + d_z \rho C_p \mathbf{u} \cdot \nabla T + \nabla \cdot \mathbf{q} = d_z Q + q_0 + d_z Q_{ted} \tag{14}$$

where Q_{ted} is the thermoelastic damping coefficient and d_z is the thickness of domain in the out-of-plane direction. We approximated the shape as a disk with thickness of 400 nm, which is the diameter of a single nOMA. Q_{ted} is the thermoelastic damping which represents the thermoelastic effects in solids. The conductive heat flux, $\mathbf{q}$, is given by $\mathbf{q} = -d_z k \nabla T$.

In our material system, plasmon heating phenomenon is expected to stabilize at a certain temperature for a given laser power. To experimentally demonstrate this property, we continuously actuated beads an hour at a given laser power and verified that the level of contraction stayed the same (Figure 4.17). Considering the transient response, the settling

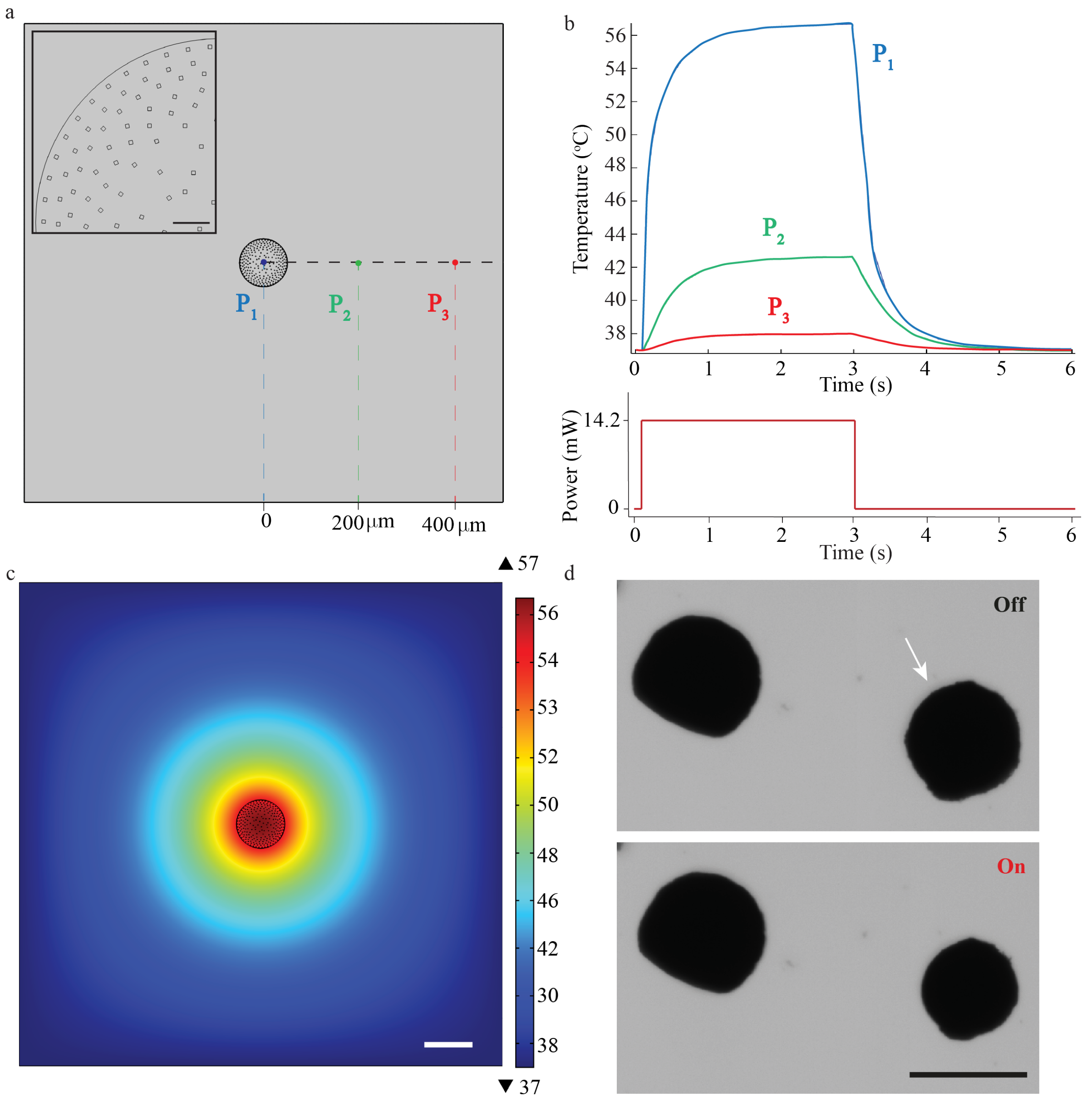

FIGURE 4.16 – Finite element simulations of the heat transfer during actuation. a. 2D drawing showing the boundary conditions. Inset is a close-up view of the actuator highlighting the nano-heater elements. Scale bar, 10μm. b. Temperature changes over a complete actuation cycle at the three different points shown in a. The input excitation signal is shown on the bottom plot. c. Temperature as a function of distance from the μOMA irradiated at 14.2 mW laser power at the steady state. Scale bar, 100 μm. d. Selective actuation of a μOMA (denoted with the white arrow) at 14.2 mW laser power in close proximity of another μOMA. Bottom image shows that only the illuminated actuator responds to the signal. Scale bar, 100 μm [65].

time for the temperature to reach its equilibrium value depends on the laser power as well as the boundary conditions. Taking this dynamics into account, in our simulations, we applied a laser pulse as an input to the simulation that was long enough for the system to reach steady state. Figure 4.16b shows the evolution of temperature at three different points that were denoted in Figure 4.16a. Figure 4.16c shows the temperature distribution around the actuator at the equilibrium. The highest temperature was reported as 56.7 ^{o}C at the core of the actuator for the given laser power (P_{laser}=14.2 mW), which dissipated with a relatively steep curve. The steady-state temperature at locations 200

μm and 400 μm away from the surface of the μOMA were 42.6 ^{o}C and 37.9 ^{o}C, respectively.

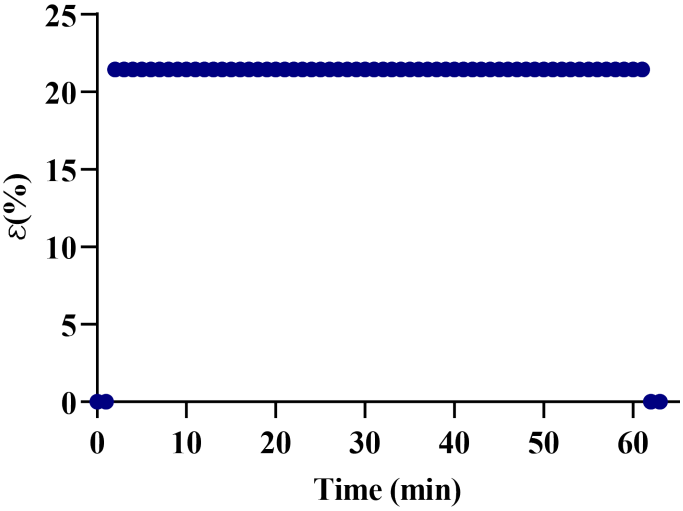

FIGURE 4.17 – Long-term actuation of a μOMA. The deformation of the microactuator does not change over time for a given laser power. The strain generated by a microactuator under continuous 15 mW laser illumination is measured every minute over an hour [65].

We experimentally validated the implications of this analysis by placing the actuators close to each other at various distances. Figure 4.16d shows the selective actuation of a μOMA in the vicinity of another muOMA. The actuator that was placed 150 μm away from the activated one did not show any response. We only observed reaction from the non-activated actuator once the distance between the actuators were less than 50 μm. These observations showed that numerical analysis was overestimating the temperature. Taken together, we have a framework to design the soft robotic device and tune the control parameters so that the temperature around the biological specimen never exceeds the tolerable levels. In the experiments presented in Section 4.4.4, the spheroids were placed 500 μm away from the actuator to protect the samples from overheating.

4.4.3 Calibration of poly-acrylamide sensing probes

The stiffness measurements rely on the calibration of the cantilever beam, which was performed using a commercially available capacitive MEMS force sensor. The force sensor was mounted on a three-axis motorized micromanipulator while the workspace was monitored using an optical microscope (Figure 4.6c). The base of the PEGDA cantilevers were polymerized around poly-(dimethylsiloxane) (PDMS) pillars that were microfabricated on the surface of a glass chamber to avoid motion during loading (Figure 4.6d). Force versus deflection curve shown in Figure 4.6g was obtained using the calibration settings (i.e. coefficient for voltage to force conversion) provided by the manufacturer. The sensor is capable of measuring forces perpendicular to the sensor's axis, which allows for the monitoring of both the sensing-probe tip and the sample under the microscope (Figure 4.6e). The beam was progressively deformed with a speed of 1 μm·s^{-1} (Figure 4.6f). We calculated the Young's modulus (E) of PEGDA structures as 800±85 kPa (6 different beams and 6 independent measurements from each beam) using the Euler-Bernoulli beam equation :

$$E = \frac{F(3l - x)x^2}{6I\delta_{max}} \tag{15}$$

where F is the force, l is the length and I is the second moment of inertia of the beam, x is the distance from the base of the beam to the location of loading, and δ_{max} is the maximum deformation of the beam.

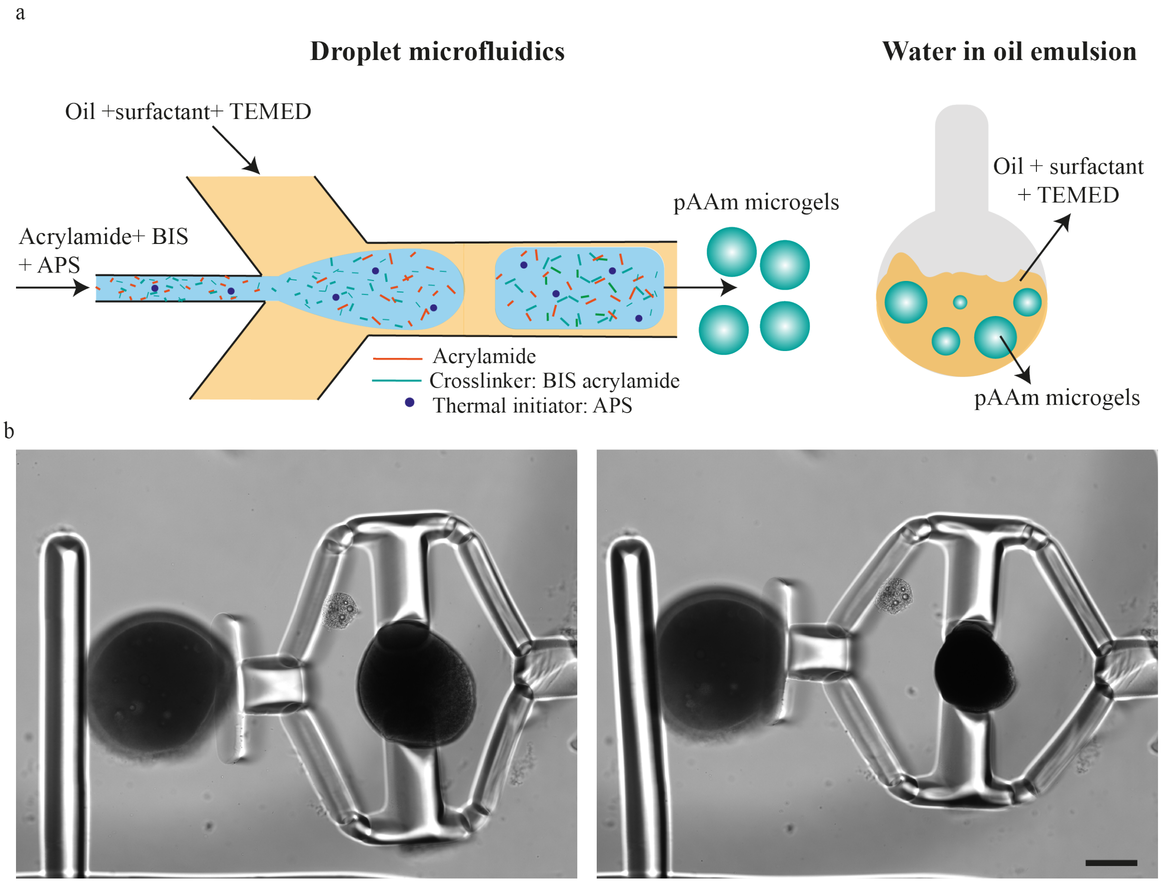
a
Droplet microfluidics
Water in oil emulsion
Oil +surfactant+ TEMED
Acrylamide+ BIS
+ APS
pAAm microgels
Acrylamide
Crosslinker: BIS acrylamide
Thermal initiator: APS
Oil + surfactant
+ TEMED
pAAm microgels
b

FIGURE 4.18 – Fabrication of pAAm beads and calibration of the sensing probe. a. Representative schematic of 2 different methodologies to fabricate pAAm microbeads. On the left through microfluidics and on the right a simple water in oil emulsion. b. Representative images from a compression test for PAAm beads. Scale bar, 100 μm [65].

We next tested the accuracy of our measurements using polyacrylamide (PAAm) microgel beads. Previous work has shown that PAAm microgel beads can be used as standardized calibration samples for mechanical measurements [25, 83]. Beads with controlled size and elasticity can be fabricated by tuning the pre-gel composition [25]. Importantly, using this protocol, microgels with elasticity in the range of tissue relevant mechanical properties can be fabricated. We fabricated microgels with elasticity ranging from 1.92±0.46 kPa (n = 10) to 9.19±3.82 kPa (n = 10) by varying the monomer (PAAm) and crosslinker (BIS) concentrations. Young's modulus was measured using the same force sensor and these values are in accordance with AFM characterization data [25].

PAAm beads were placed into the compression device using a micromanipulator and the laser power was increased with 0.8 mW increments. The deformation of the cantilever probe along with the displacement of the piston were measured from the microscope images, which together quantify the deformation of the PAAm bead (Figure 4.19). Force acting on the cantilever beam were calculated using Euler-Bernoulli beam theory and experimentally measured Young's modulus. The calculated force is assumed to be the same as the one applied on the PAAm bead. The Young's modulus of the beads were then calculated using Hertzian half space contact mechanics model :

$$\begin{aligned} \delta &= \frac{3(1-\nu^2)F}{4Ea} - \frac{f(a)F}{\pi E}, \\ f(a) &= \frac{2(1+\nu)R^2}{(a^2+4R^2)^{3/2}} + \frac{1-\nu^2}{(a^2+4R^2)^{1/2}}. \end{aligned} \tag{16}$$

where R is the radius of the sphere, ν is Poisson's ratio (taken as 0.49), δ is the compressive displacement, f is the force, and a is the radius of contact area. Young's modulus can be extracted from the relationship between δ and f for values satisfying the condition $\delta/R \leq 0.2$. This model accommodates for large deformations [181].

In this work, we only made measurement for one material composition. The Young's modulus of the PAAm beads with 40% (w/w) PAAm, 2% (w/w) BIS was measured as 5.75±1.63 kPa (n = 6). At this composition, the Young's modulus was measured as 7±2.15 kPa (n = 8) by the force sensor shown in Figure 4.6c. Preliminary results demonstrate the feasibility of making quantitative measurements using an all-hydrogel, remotely actuated compliant mechanism. However, further characterization with many samples is required to provide a comprehensive calibration data. The material of choice is not limited to soft hydrogels that swells and adsorbs proteins. We fabricated devices from another polymer, Trimethylolpropane ethoxylate triacrylate (TPETA, 692kDa), that is elastic and protein repellent (Figure 4.19). Depending on the application, different modules can be fabricated from different photopolymerizable polymers.

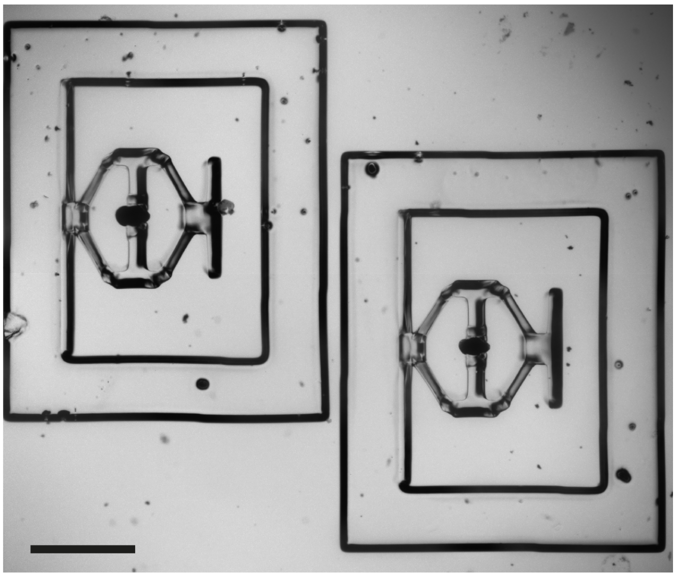

FIGURE 4.19 – Compressor microdevices fabricated from TPETA polymer. Representative images from a compressor microdevices made out of TPETA. Scale bar, 500 μm [65].

4.4.4 Biomechanical characterization

As a proof-of-concept demonstration, we tested the feasibility of compressing cell clusters (spheroids). The overall simultaneous mechanical loading and characterization concept is illustrated in Figure 4.20a. We verified the biocompatibility of the materials by performing cell viability assays with a first generation compressor microdevice (see Figure 4.21). Spheroids were self-assembled from human embryonic kidney (HEK) cells using a high-throughput microengineered cell culture device (Figure 4.20b). Cells adhere to each other and form a compact 3D tissue with a spherical shape over two days of culture (Figure 4.20c). They were then transferred to the chamber where the devices were operated.

Figure 4.20d shows a representative example for the compression of the spheroids. A single spheroid was placed between the piston and the cantilever beam using a micromanipulator. We recorded a compressive strain up to 40% with a device that had a cantilever with 70 μm thickness and an μOMA with 160 μm diameter. We observed a slight deflection on the cantilever, corresponding to a few μm displacement. The beam was too stiff for making a reliable measurement but this experiment showed how much a spheroid could be compressed using the current prototype as the force was primarily harnessed to load the sample. We fabricated a compressor device with a thinner cantilever, having a thickness of 20 μm. This time the deflection of the beam was obvious (Figure 4.20e). The Young's modulus of the sample was measured as 2.45±0.46 kPa (n = 6). The geometry and stiffness of the cantilever beam must be tuned carefully according to the characteristics of the sample, which may require prior measurements done with an electronic probe or high-throughput screening using various cantilever designs.

4.4.5 Integration with microfluidic systems

Microfluidic cell culture devices push the biomimicry of engineered tissues to the next level by providing long-term perfusion, introduction of chemicals and cells in a dynamic fashion, and notably, improving the reproducibility and throughput via automation [182, 183, 184]. We developed an integrated microfluidic solution to showcase that our fabrication and actuation paradigm is compatible with these devices. We fabricated an open PDMS chamber with docking stations on its walls for assembling the compressors (Figure 4.22). The actuation modules were transferred to this chamber in the same hydrogel prepolymer solution, positioned at target docking stations using a micromanipulator, and anchored to the walls with an additional projection photolithography step. This final step ensured that the compressors did not rotate or detach during sample loading and actuation. The sensing module was fabricated on the other side of the chamber during the manufacturing of the base. The chamber was closed once the biological samples were placed in position. As an alternative to the docking site approach, the base could be polymerized around pillars as shown in Figure 4.6d, which would reduce the area of the blueprint.

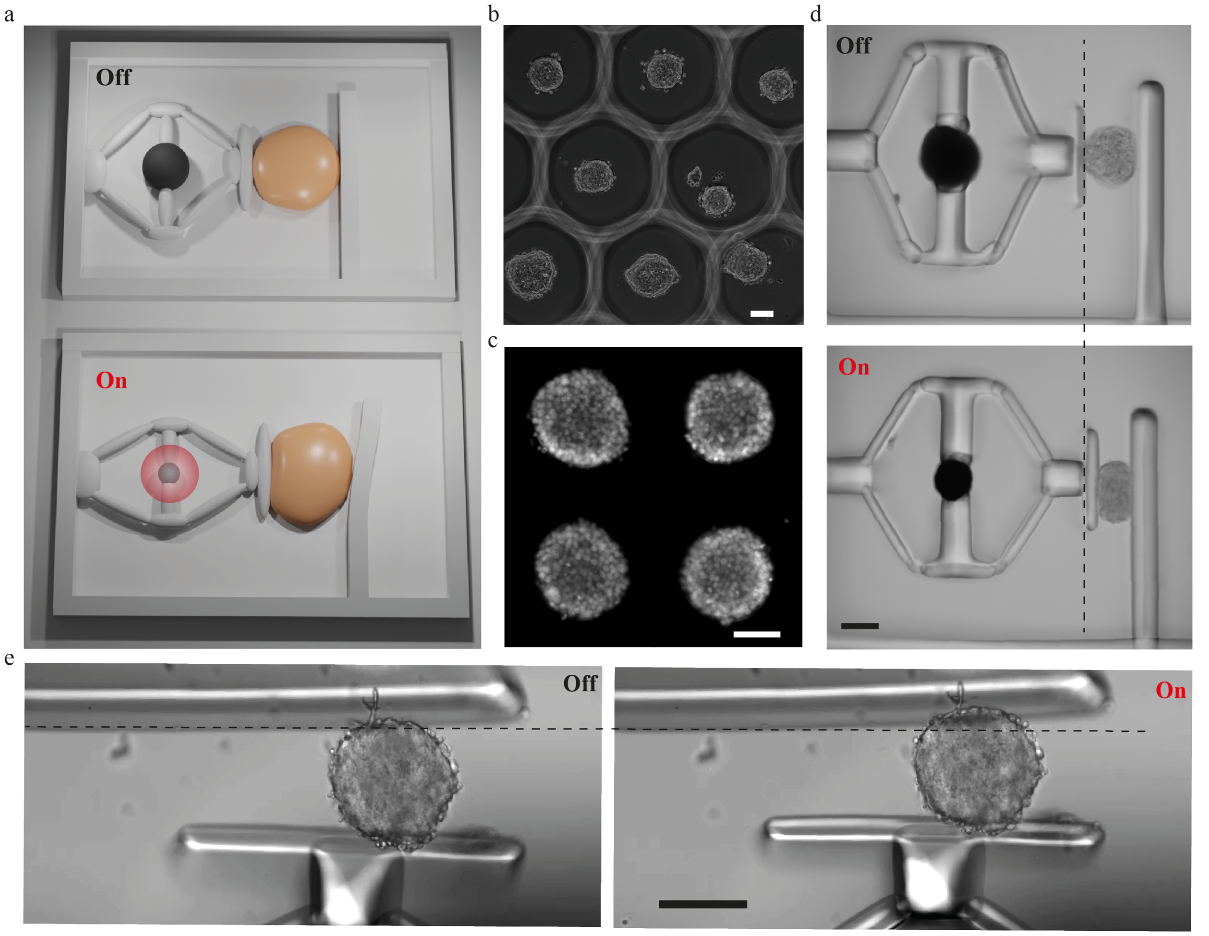

FIGURE 4.20 – Biomechanical characterization of 3D tissue samples. a Schematic depiction of the working principle (not to the scale). Upon application of NIR illumination, the monolithic compliant mechanism deforms and the piston compresses the sample. The cantilever beam reports the sample stiffness. b. Phase-contrast image shows high-throughput fabrication of spheroids using hydrogel wells. c. Fluorescent image of an array of self-assembled spheroids labeled with a DNA dye. d. Snapshots from a representative compression experiment where the deflection of the beam is not obvious. e. A compression device with a more sensitive cantilever beam. The beam deflects during the loading of the sample, reporting its stiffness. Scale bars, 100μm [65].

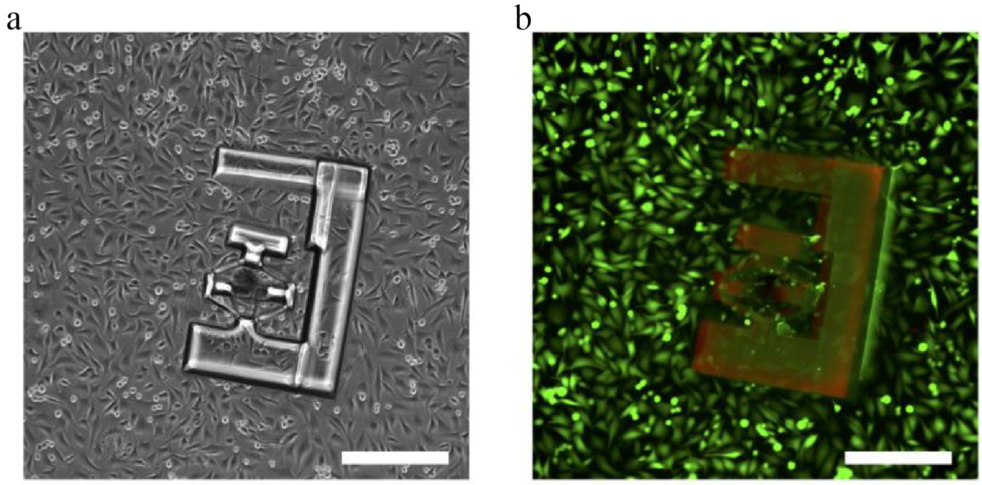

FIGURE 4.21 – Live/dead assay on the cell-seeded compression microdevice. a Phase contrast imaging of single cells seeded on the 1stgeneration of compression microdevice. b. Fluorescent imaging. Green color indicates live cells (calcein-AM) and red color indicates dead cells (ethidium homodimer-1). Scale bars, 200μm [45].

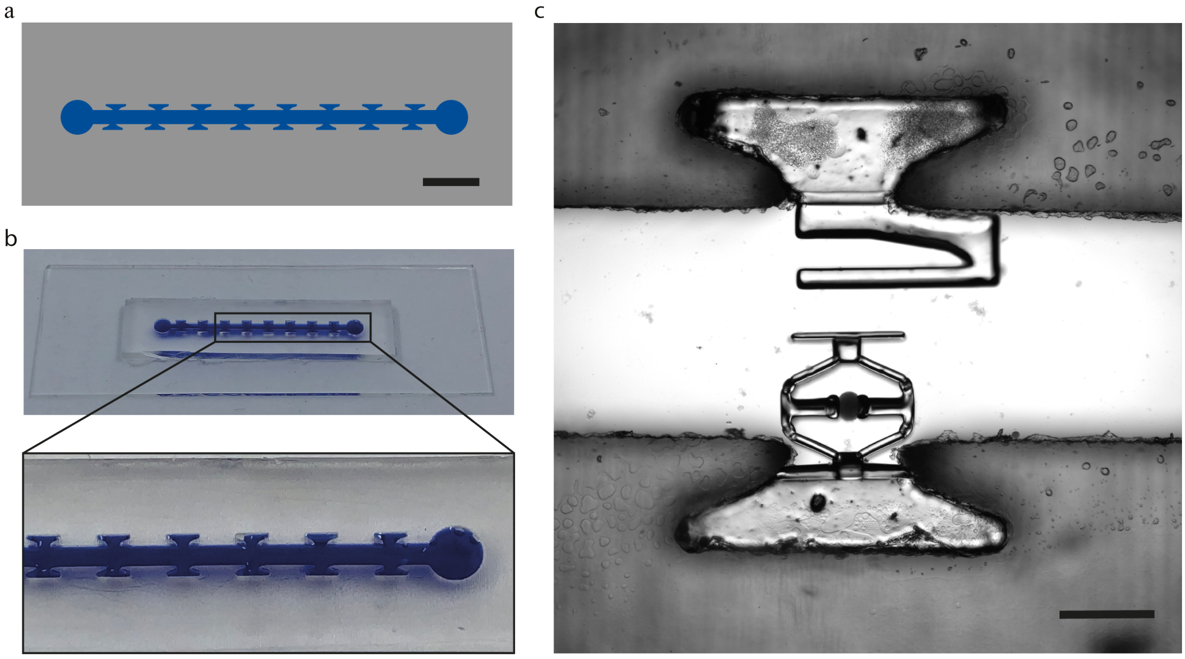

FIGURE 4.22 – Assembly of devices inside microfluidic systems. a CAD design of the microfluidic device. Scale bar, 5 mm. b. Photographs of the microfluidic chip. The engraved docking stations are highlighted with blue ink. c. Representative example of a soft robotic device assembled inside the channel. The compression module was fabricated elsewhere and transported to the channel while the sensing module and the base were polymerized inside the channel. Scale bar, 500 μm [65].

4.5 Design and in-situ production of antagonistic mechanism

The pneumatic extrusion method presented in Section 3.3 allows us to print fibers at specified locations inside the monomer solution prior to polymerization of the PEGDA structures. We built two proof-of-concept devices actuated by multiple μOMA fiber. The first device is in the class of continuum robots; continuously bending, infinite-degree-of-freedom robots with elastic structures. The device consists of two μOMA fiber connected through a discrete backbone, as shown in Figure 4.23a. The tip position of the robot was freely and precisely controlled within the 2D configuration space by modulating the optical power and spatial distribution of NIR exposure (Figure 4.23b). We mapped the configuration space for the tip of the robot by simulating the deformation at the geometric extremes using FEM analysis (Figure 4.23c). We used thermal expansion to model the strain response of the actuators. μOMAs were assigned an experimentally derived modulus and a negative thermal expansion coefficient according to experimentally derived strains. In-liquid AFM measurements on fully swollen samples showed that the elastic modulus of the fiber μOMAs was 3.5 ± 1.9 kPa ($n = 15$) at room temperature. The PEGDA structures were again modeled as an elastic material and assigned a thermal expansion coefficient of zero. FEM analysis successfully captured the morphological changes upon selective NIR exposure, as shown in Figure 4.23d.

The second system developed is an advanced microgripper actuated by an antagonistic pair of fiber μOMAs, as shown in Figure 4.23e. The robot achieves large reversible deformation in opening and closing modes by selective activation of the actuators. While the agonist contracts, the antagonist extends thanks to the flexibility provided by the biopolymer. FE simulations of displacement matched the experimental results, as shown in Figure 4.23f. This arrangement paves the way to adjust the stiffness of the actuation machinery to achieve sophisticated motion trajectories and precise control of interaction forces when handling soft and sensitive biological samples [185].

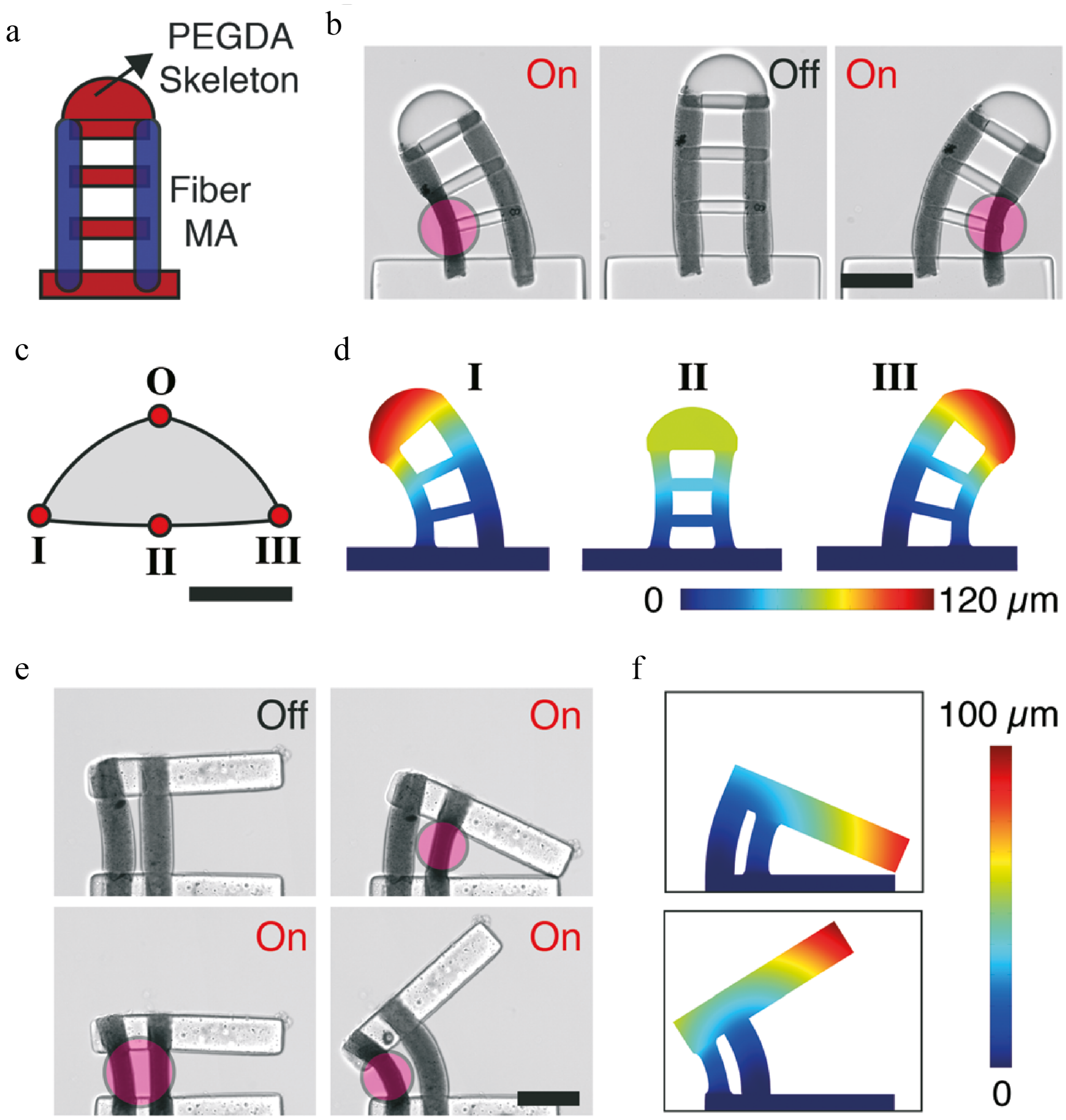

FIGURE 4.23 – Development of soft robotic microdevices actuated by μOMA fibers a. The PEGDA skeleton is polymerized around the printed fiber μOMAs while forming physical encapsulation of fibers within the structure. b. Selective NIR exposure leads to continuous control over the curvature of the manipulator. c. The 2D configuration space of the device plotted by generating a polynomial fit passing through the extreme positions provided by the FEM simulations shown in d. The nonactuated original location of the tip position is denoted by O. e. Soft robotic microgripper controlled by an antagonistic μOMA fiber pair. f. Displacement contour plot showing the displacement of the arm corresponding to the two extreme cases, fully open and fully closed. All scale bars, 100 μm [45].

4.6 Controlled *in-situ* self-assembly and characterization of soft micromachines

As shown in Section 3, artificial μmuscle can also be synthesized *in-situ* via photothermal or electromagnetic forces. Like the microspheres and the fibers, their isotropic contraction an also be converted to linear or rotary motion with desired mechanical advantage using compliant mechanisms. We chose poly(ethylene glycol) diacrylate (PEGDA) as the hydrogel for manufacturing the mechanisms due to its tunable stiffness, ease of polymerization, and temperature-independent swelling properties. Upon laser exposure, the mNAs accumulated between the arms of a lever mechanism that was designed to amplify the deformation (Figure 4.24a). Figure 4.24b shows time-lapse images from an experimental assembly process. The particles not only attached to each other but also firmly adhered to the surface of the PEGDA structure. The contraction of the *in situ* assembled artificial μmuscle moved the arms toward each other (flexion), whereas opening (extension) was achieved with the removal of the actuator force due to the stored energy (Figure 4.24c). Contraction of the actuator that gives 20% closing of the lever was completed in 750 ms, whereas relaxation took seconds due to the diffusion process (Figure 4.24d). The contraction–relaxation curves were identical for several actuation cycles (Figure 4.24e).

Long-term performance of the micromachines was tested with the application of 1000 actuation cycles, each consisted of laser pulses with 0.5 Hz frequency, 50% duty cycle, and 7 μWμm^{-2} power density. The angular displacement was recorded as $9.8^o \pm 0.7^o$ for the first 5 cycles and $9.7^o \pm 1.3^o$ for the last 5 cycles. This test verified the robustness of the actuator. The strong adhesion of nanoactuators to the PEGDA structures also provides a versatile route to form layered actuators. By depositing an actuation layer at the base of an elastic beam, we engineered an active hinge that could rotate the beam in both clockwise and counterclockwise directions in an antagonistic fashion (Figure 4.24f). Figure 4.24g shows snapshots from an experimental assembly process. By simply changing the location (Figure 4.24h) and intensity (Figure 4.24i) of laser exposure, we precisely controlled the angular displacement of the beam. Finally, we asked whether the actuators would heat or show signs of fatigue during elongated exposure. The rotating beam device was excited continuously at various power densities for 10 min during which deformation angle remained the same (Figure 4.24j).

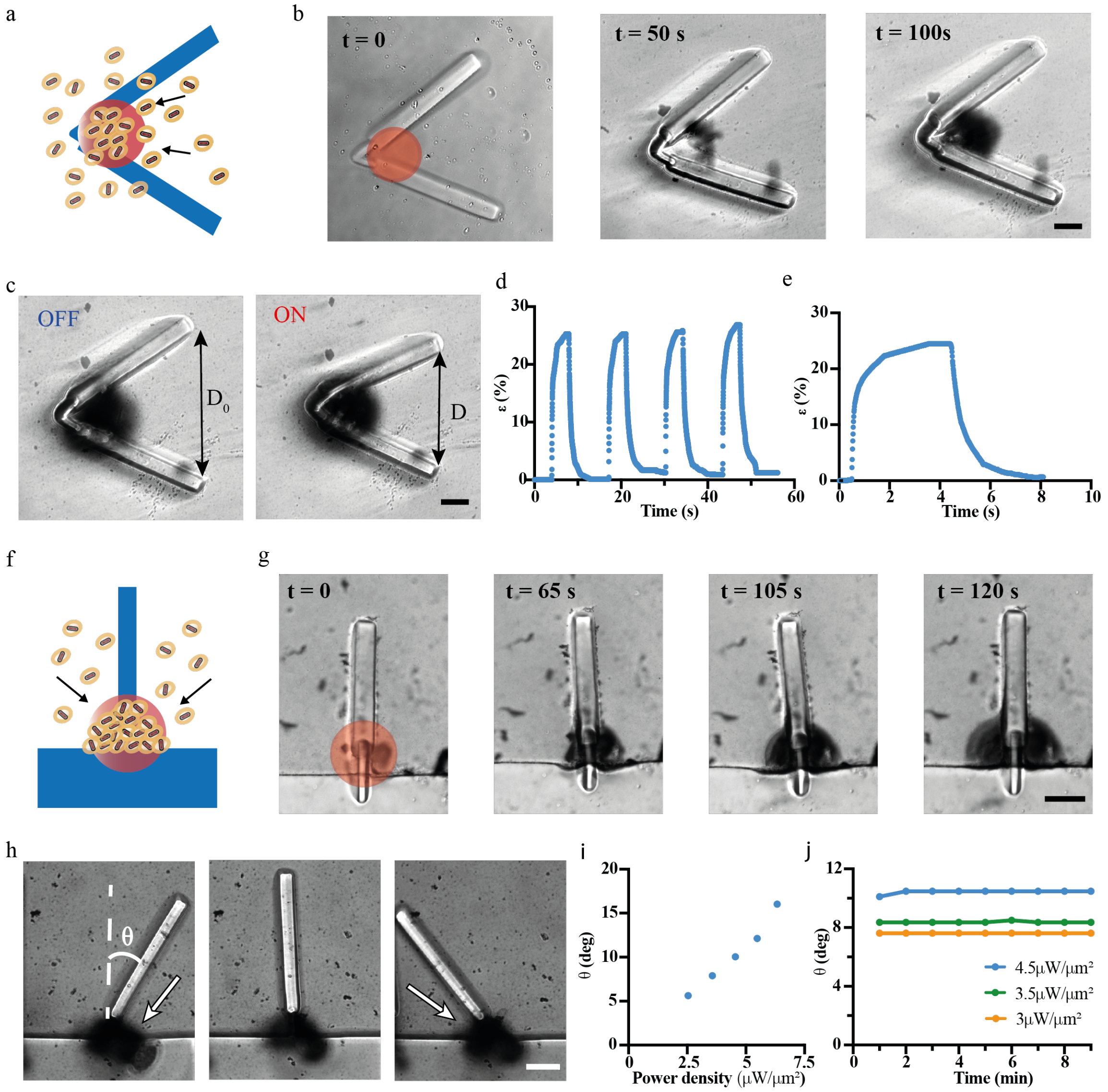

FIGURE 4.24 – Controlled self-assembly and characterization of soft micromachines actuated by artificial μmuscle. a. Schematic representation of *in situ* assembly of artificial μmuscle between the arms of a lever mechanism. b. Snapshots from a time-lapse movie showing the growing actuator at the designated location. The compliant lever mechanism was fabricated from a hydrogel that does not respond to changes in temperature. c. Optical actuation with 7 μWμm^{-2} laser power density. D_0 denotes the reference distance between the arms at the fully swollen state of the actuator. d. Actuation strain over time graph for a single actuation cycle at a laser power density of 7 μWμm^{-2}. e. Actuation strain over time under NIR illumination with 3s pulse width and 0.1 Hz frequency at 7 μWμm^{-2} laser power density. f. Schematic representation of the self-assembly of antagonistic actuators with bidirectional rotation. g. Time-lapse images showing the self-assembly of the actuators on both sides of the beam. h. Optical actuation upon NIR illumination with 7 μWμm^{-2} laser power density. Images show the relaxed and fully contracted states of the machine. The angular displacement, θ, is measured with respect to the reference state. i. The change in θ as a function of laser power density. The trend is linear for the given power density values. j. Angular displacement of the beam over time at different laser power densities. The angular displacement stays the same for minutes under continuous NIR illumination. All scale bars, 50 μm [46].

4.7 Conclusions

Maskless optofluidic photopolymerization process enables the manufacturing of custom shaped functional microparts that are physically connected to the actuation units. By varying the number and distribution of actuators or playing with the design of the compliant mechanisms, we can generate a repertoire of complex micromachines. Furthermore, combination of longitudinal, transverse, and/or oblique actuator arrangements can lead to the development of highly adaptive continuum microrobots providing remotely controlled 3D motion. The class of programmable, soft actuated hydrogel microdevices presented has potential for a wide range of applications including generation of physiologically or pathologically relevant mechanical stimuli for in vitro mechanobiology studies. The hydrogel materials employed in the development of our microdevices have moduli in the order of tens of kPa which is comparable to that of biological tissues, providing an inherently safer alternative for biomedical interfacing compared to other robotic approaches.

With the presented methodology, we can *in situ* fabricate arrays of devices inside microfluidic chips. By taking advantage of laminar flow and pneumatic valves, the microfluidic chip can be programmed to place biological samples at designated compartments. This way, we can build a fully automated, high-throughput mechanochemical testing platform. The blueprint for the chassis and machine components are highly re-configurable, which allows rapid design and prototyping of a variety of different soft robotic systems.

Forces applied by the device are within physiological levels (on the order of μN). The deformation and stress profiles can be further modulated by changing the design of the flextensional mechanism and the shape of the piston. This methodology allows real-time monitoring of changes in gene expression and protein signaling in response to controlled mechanical loading. Cantilever beam simultaneously provides real-time measurements of elasticity. Together, we can monitor and perturb both physical and biochemical properties of the tissues. While the cantilever based measurements are not as sensitive as electrostatic comb drives, the sensitivity is acceptable for capturing major changes in tissue mechanics.

Projection lithography is convenient and versatile yet the design of the mechanisms are limited to extruded shapes. The polymers that we used, on the other hand, have already been adapted to 3D nanoprinting using two-photon polymerization [186, 187, 188]. Printing mechanisms around the actuators is one interesting avenue. An alternative solution is to push the printing concept to the next level. As shown, multifunctinal nOMAs can be assembled on-demand by harnessing thermocapillary flows [46]. Thus, it is conceivable that the whole machine can be manufactured *in situ* using direct laser writing. With the resolution provided by printing, machines can perform dexterous manipulation of biological samples.

4.8 Detailed protocols

4.8.1 Materials

All chemicals were purchased from Sigma Aldrich unless stated otherwise : poly(ethylene glycol) diacrylate (PEGDA, 700 kDa and 525kDA), 2-Hydroxy-2-methylpropiophenone (DAROCUR), polydimethylsiloxane (PDMS) SYLGARD 184 kit, Trimethylopropane ethoxylate triacrylate (TPETA, 692kDa), ammonium persulfate (APS), acrylamide (AAm), bisacrylamide (BIS), surfactant Tween 80, mineral oil, tetramethylethylenediamine (TEMED). Tris Buffer 10M was provided by EPFL facility.

Supplies for cell culture were purchased from ThermoFischer Scientific : Dulbecco's modified Eagle medium (DMEM/F-12), fetal bovine serum (FBS), Penicillin/Streptomycin, 0.25%Trypsin-EDTA and Hoechst 33342 nucleic acid stain. HEPES solutionn was purchased from SIGMA Aldrich

4.8.2 Synthesis of microactuators

See section 3. For the compliant mechanisms, the spherical μOMAs produced with t-shape microfluidic device were used. For the compressor microdevices the larger spherical μOMAs produced with the flow focusing microfluidic device were use.

4.8.3 Fabrication of hydrogel mechanisms : Digital maslkless lithography

Maskless projection photolithography is performed with a programmable digital micromirror device module (Andor Technology) connected to the microscope. The digital projector contains an 800 x 600 micromirror array and operated with a minimum exposure time of 50 μs at a maximum frame rate of 5000 fps. The platform projects light provided by an ultraviolet LED source (365 nm) using a computer-aided design (CAD)-based digital blueprint, which initiates subsequent free-radical polymerization of photosensitive materials. 2D drawings defined the planar shape of the structures, whereas the height was simply controlled by the channel size. Overlapping regions between the mechanism and the actuators were created in the polymerization process to ensure a mechanically stable connection and efficient transmission of forces. The modulated beam was projected through a 10 or 20X microscope objective, depending on the resolution desired, onto the substrate where we had actuators suspended in the hydrogel prepolymer solution composed of PEGDA and 20% DAROCUR. The microfluidic devices were fabricated from poly-(dimethylsiloxane) (PDMS) using soft lithography.

4.8.4 Laser actuation

All experiments were performed using a motorized inverted microscope (Nikon Ti-E) and images were captured with an ORCA-Flash4.0 CMOS camera (Hamamatsu). A 785 nm laser (110 mW, Thorlabs) beam coupled to the microscope provided NIR illumination. The laser illumination was modulated using a custom LabView program. During biological manipulation, the devices were submerged in culture medium supplemented with HEPES solution and the chamber was kept at physiological conditions using an environmental chamber (Life Imaging Services). The videos were captured at full pixel resolution (2048 × 2048) with frame rates ranging from 33 fps to 200 fps depending on the requirement of the experiment. A program based on an edge-detection algorithm in Matlab (Mathworks, MA) was used to measure the deformation from time-lapse videos.

4.8.5 Mechanical characterization of hydrogel mechanisms : MEMs force sensor measurements

A commercial MEMS force sensor (FT-S1000-LAT, FemtoTools) with a resolution of 0.05 μN was mounted on a motorized XYZ micromanipulator (SLC-2040, SmarAct GmbH) using a 3D printed adapter. The force sensor was positioned manually using the corresponding controller while being visually monitored using the microscope. The force sensor was powered by a programmable linear power supply (Keysight E3631A), and output was measured using a precision multimeter (Keysight 34465A).

4.8.6 Synthesis of polyacrylamide beads

The polyacrylamide (PAAm) beads were synthesized following a protocol from the literature [25] with some modifications. The reaction solution was obtained by mixing 0.3% (w/v) ammonium persulfate (APS) with different amounts of acrylamide (AAm) and bis-acrylamide (BIS) in 10mM Tris buffer. This solution was added to the continuous phase composed of mineral oil with 5% (v/v) surfactant Tween 80. The emulsion was stirred at 800 rpm and purged with N_2 for a minimum of 15 min. Subsequently, 300 μL of the catalyzer Tetramethylethylenediamine (TEMED) was added drop-wise. The obtained beads were cleaned through centrifugation with ethanol and Milli-Q water.

4.8.7 Formation of spheroids

HEK293T cells were cultured in Dulbecco's modified Eagle medium (DMEM/F-12) supplemented with 10% fetal bovine serum and 1% penicillin/streptomycin. Cells were passaged upon achieving confluency at a 1 :4 ratio using 0.25% Trypsin-EDTA and discarded after 20 passages. All experiments were done using cells tested for mycoplasma negative. A high-throughput device with microengineered hydrogel films on the bottom of conventional multiwell plates was used to initiate spheroid formation [189]. The size of spheroids was controlled with the initial cell number. In this work, to produce spheroids with 150 μm in average, 1000 cells were used. The spheroids were transferred to the device after 32 h of culture. The nuclei were labeled using Hoechst 33342 stain.

4.8.8 Viability assay

Madin–Darby canine kidney (MDCK) cells were cultured in T-flasks in Dulbecco's modified Eagle medium (DMEM/F-12) 5% FBS and 1% penicillin–streptomycin. MDCK cells were seeded on a well-plate containing several microdevices and cultured overnight. The cells were stained using a viability/cytotoxicity assay kit from Biotium according to the manufacturer recommendations. The kit contains the cytoplasmic dyes Calcein AM for staining the living cells (green) and ethidium homodimer III for staining the dead cells (red). Briefly, 2 µM Calcein AM and 4 µM ethidium homodimer III were mixed in PBS solution. Cells were incubated inside this solution for 30 minutes at 37 °C. The solution was then replaced with complemented medium. Cells were visualized using a Nikon Ti Eclipse motorized inverted fluorescence microscope.

4.8.9 Simulations : Finite element models

Microstructures solid mechanics simulations :

The numerical simulations were performed in COMSOL Multiphysics finite element analysis software. The models simulate the solid mechanics of the microstructures and do not take into account the hydrodynamic response of the surroundings. PEGDA structures were modeled as linear elastic substrates with a Young's modulus of 500 kPa and Poisson's ratio of 0.33. 3D CAD drawings were created in CATIA (Dassault Systemes) and imported to FEM software for further analysis. We either applied experimentally measured actuator displacements as boundary conditions or recapitulated the contraction of soft actuator with heating of materials in the simulations. See Table 9 for the list of input parameters. Accuracy of the mesh was ascertained through a mesh refinement study based on the experimental strain values.

Simulated body	Mesh Size	Physics	Applied displacement	Young's modulus	Poisson's ratio
Flextensional mechanism	4μm	Static structural	23.5μm	500kPa	0.33
Microgripper	3μm	Static structural	7μm	500kPa	0.33
Continuum manipulator	2μm	Static structural	10-15μm	500kPa	0.33

Table 9 – Parameters used in the FEM analysis of solid deformation [45].

Heat transfer simulations :

Structural analysis and calculations of the temperature distribution were performed by finite element simulation (Comsol Multiphysics, Burlington MA). The heat capacity and thermal conductivity of the polymer hydrogel is assumed to be equivalent to that of water [32]. Smallest mesh element size is used as 0.125 μm and biggest element size is chosen as 37 μm with maximum element growth rate of 1.25. Accuracy of the mesh was ascertained through a mesh refinement study.

5 Tensile loading transmitted through collagen matrix drives mammary acini toward invasive phenotype

5.1 Introduction

We defined the final goal of the project as using μOMAs to generate forces within living tissues and study mechanobiology. To this end, we chose a model system that has been extensively studied, mammary acini organoids. Notably, several articles provided empirical evidence on the mechanical interactions among mammary acini embedded inside collagen gels, and theoretical work speculated on the underlying physical mechanisms. We thought it would be ideal to prove that the reported interactions were indeed driven by cell-mediated forces by using an untethered actuator that serves as a mechanical cell. We successfully built an in vitro bioengineered platform where acini could be formed and cultured inside collagen gels. Integration of the microactuators with the ECM also worked seamlessly. However, the parameter space for mechanical excitation is too large, i.e. various factors may play an important role in mechanotransduction and signal transmission. For example, the distance between the actuator and the target acini, the magnitude/duration/frequency of deformation, and the timing of excitation are important. Preliminary trials did not generate any significant change on the phenotype of the cells that constituted the target acini. We decided to start with a relatively simple assay to determine the excitation parameters. In this chapter, I introduce a more traditional robotic micromanipulation system that allowed us to apply sustained local mechanical stretch to acini. In the conclusion chapter, I will elaborate on how the material system introduced in the previous chapters could be adapted to push this platform to the next level.

5.2 Background on 3D mammary organoids

The mammary gland is composed of several branched ducts, connecting the lobules to the nipples [190]. It is a highly polarized structured composed of luminal epithelial cells surrounding a hollow lumen and myoepithelial and basal cells on the outer layer [190, 191]. The luminal epithelial cells are responsible for secretion of milk into the lumen of ducts and lobules [192]. During lactation phase, milk is expelled from the lobules with the help of myoepithelial cells, that have contractility properties and are present in the basal surface of the epithelial cells. These cells have a crucial role in suppressing tumor growth, invasion and angiogenesis. The mammary glands are surrounded by a basement membrane (BM) composed mainly of laminin, collagen IV and proteoglycans. It is responsible for maintaining epithelial polarity and differentiation, hence preventing luminal epithelial and myoepithelial cells from migrating out to the interstitial stroma. Malignant breast tissue is typically characterized by the absence of myoepithelium and/or epithelial basement membrane. When the tissue lacks these two components, we are in the presence of an invasive carcinoma, where cells can disrupt the basal membrane to infiltrate the stroma. Luminal epithelial cells are anchored to the BM through transmembrane integrins, that can sense the microenvironment and trigger intracellular signaling pathways [190]. The breast epithelium is unique because it is constantly being remodelled through cycles of branching, especially during puberty, pregnancy and lactation. The study of these morphogenic processes is crucial, particularly to understand breast cancer.

3D culture models recapitulate the in vivo architecture including the hollow lumen, apico-basal polarity of cells, deposition of a BM, and even production of milk proteins [191]. As a result, 3D culture of mammary gland is regularly used for cancer research and the study of branching morphogenesis [190]. The organoids show several different phenotypes depending on the culture conditions. The cells may form 3D branches, as in the course of morphogenesis, or they may have an invasive phenotype, as in the metastatic tumors [191, 193, 194, 195, 196, 197, 198]. The most relevant work to our investigation involves transferring MCF10A acini into collagen matrix to study the mechanical interactions among acini [199, 193, 200]. Those interactions happen through collagen I alignment, among acini that are up to 1.2 mm apart from each other.

Specifics of the culture conditions matter for our mechanical actuation experiments. As the most widely accepted approach, mammary organoids have been grown on Matrigel or embedded in Matrigel. In this configuration they form growth arrested acini, and they branch out with the addition of growth factors [191, 193, 194, 195, 196, 197]. Inside a mixture of collagen I and Matrigel, acini show a similar behavior but form longer branches [196, 197]. When the organoids have been grown only in collagen I, they showed an invasive behavior [196, 197, 198]. The branches were no longer polar and round at the tips, but protrusive. Interestingly, if the organoids were grown in Matrigel and then transferred to collagen I, they dissociated and started to interact with each other through fiber alignment [193]. A drawback of this culture system is that the organoids are subjected to mechanical stresses during isolation and transport. Unless completely cleaned, a thin layer of Matrigel remains on the surface of the acini. Lastly, Guo et.al. [194] developed a sandwich method, where acini were grown on Matrigel and then overlaid with collagen I. We chose this method for our culture system because of several reasons (see Figure 5.1a). First, growing the acini on the same plane is advantageous for time-lapse imaging and for the application of well-calibrated forces. Second, as there is no transfer step, the risk of mechanically damaging the acini is minimized. Lastly, this ECM arrangement mimics the in vivo interface between the basal membrane and fibrilar ECM.

Here, we ask the following question. Can we artificially stimulate the acini to invade the collagen gel that cover the top surface? We distributed acini at a relatively low density on Matrigel so that they are positioned far away from each other to interact with one another. Our results showed that a simple tensile loading is sufficient to change their phenotype. Furthermore, combined with the inhibition of myosin contractility, mechanical loading induces a massive branching behavior that led to formation of highly branched networks.

5.3 The in vitro culture system

MCF10A cells were seeded on Matrigel. They formed spherical cell clusters with a lumen inside, representing the acini morphology, within 5 days of culture [191, 193, 194, 195]. Immunofluoresence imaging showed a characteristic laminin-rich basement membrane at the interface of the acini with the Matrigel (Figure 5.1b) ,as a manifestation of apical polarity [191, 198]. Organoids were cultured in a medium that contained growth factors, and, as a result, they kept growing over time [196, 197]. Acini cultured longer on Matrigel formed buds (Figure 5.1c), resembling branching morphogenesis of the mammary gland [196]. A similar morphogenic outcome was detected when we covered the top part of the acini with collagen I at day 5 (Figure 5.1d). The expression of vimentin on the periphery of the acini and their branches was an indication of the presence of myoepithelial cells, known to be found on the outer layer of the mammary gland lobules [191, 196, 201, 202, 203]. In the presence of collagen I, organoids developed more branches with larger sizes, consistent with previous work [197].

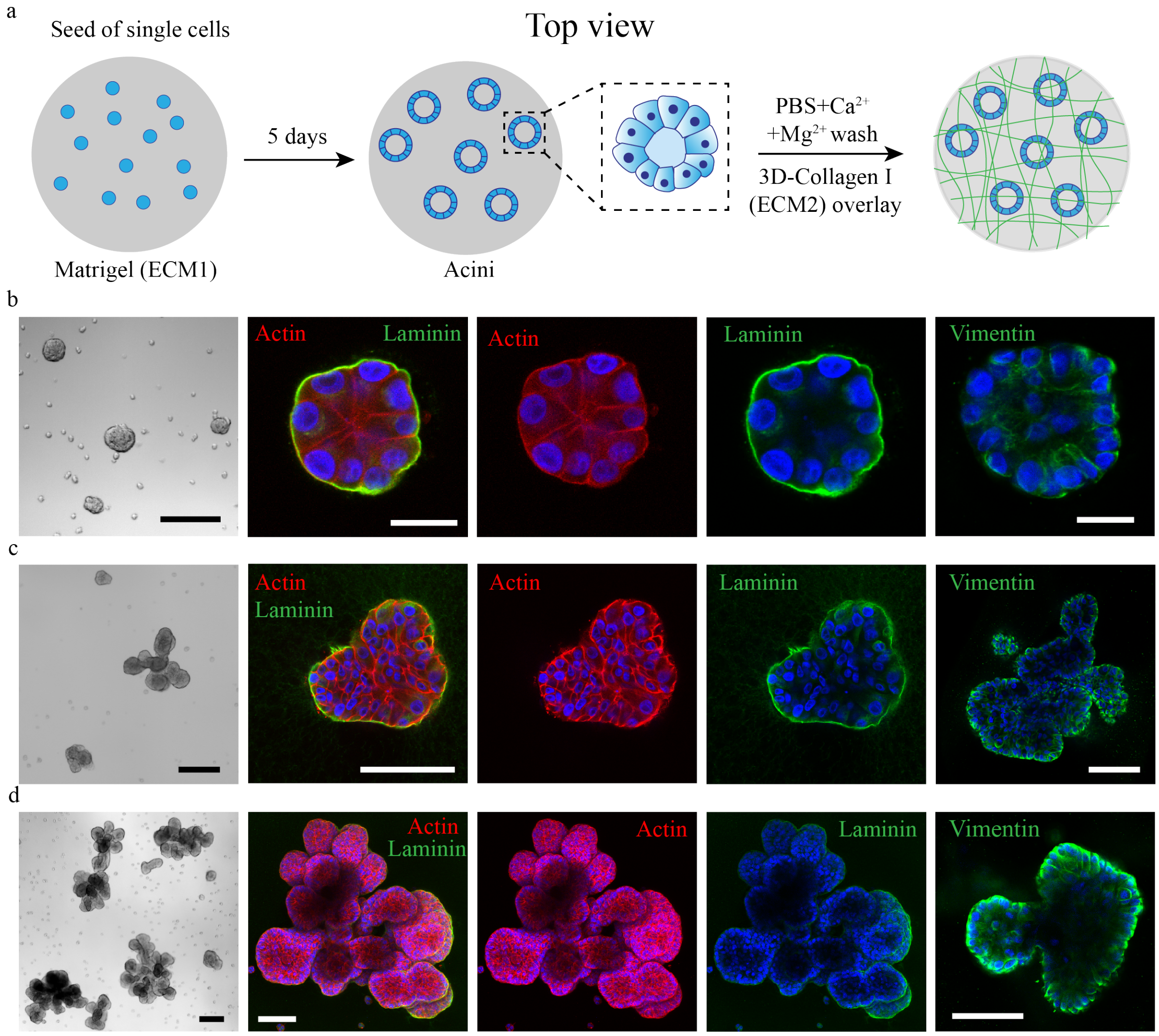
a
Seed of single cells
Top view
5 days
PBS+Ca^{2+}
+Mg^{2+} wash
3D-Collagen I
(ECM2) overlay
Matrigel (ECM1)
Acini
b
Actin
Laminin
Actin
Laminin
Vimentin
c
Actin
Laminin
Actin
Laminin
Vimentin
d
Actin
Laminin
Actin
Laminin
Vimentin

FIGURE 5.1 – MCF10A epithelial organoids growth methodology and characterization. a. Schematic of MCF10A acini growth (Top view). Single cells are seeded on Matrigel with 3D-growth medium. After 5 days, most of cellular spheroids formed have a lumen, a characteristic of the MCF10A acini. The culture devices are washed with PBS supplemented with Ca^{+2} and Mg^{+2} and 3D-collagen I is added on top and incubated for 1h at 37^{o}C. As control, the acini are left growing without the collagen layer. b,c. Representative brightfield (BF) and confocal images of MCF-10A epithelial organoids after b. 4 days and c. 12 days of growth on Matrigel. Scale bars, b. BF :100μm ; Confocal :25μm ; c. BF :250μm ; confocal :100μm. d. Representative brightfield (BF) and confocal images of MCF-10A epithelial organoids after 12 days (grown for 5 days on Matrigel plus 7 days sandwiched with collagen I). Scale bars, 250 ; 250 and 100μm.

5.4 Optomechanical actuation to stimulate cells

Spherical microactuators functionalized with a photoactivable heterobifunctional cross-linker, sulfo-SANPAH (Pierce$^{\mathrm{TM}}$). The functional group of sulfo-SANPAH, a N-hydroxy-succinimide (NHS) Ester, reacts with the amine groups present on the collagen fibers (Figure5.2). The μOMAs were suspended in the collagen precursor solution, which was added on top of the Matrigel and incubated for 1h. Almost all actuators sank and stayed on the Matrigel-collagen interface, where the organoids rest. Actuators were dynamically and continuously activated with the NIR laser. Majority of the μOMAs remained attached to the matrix and maintained their strain over time.

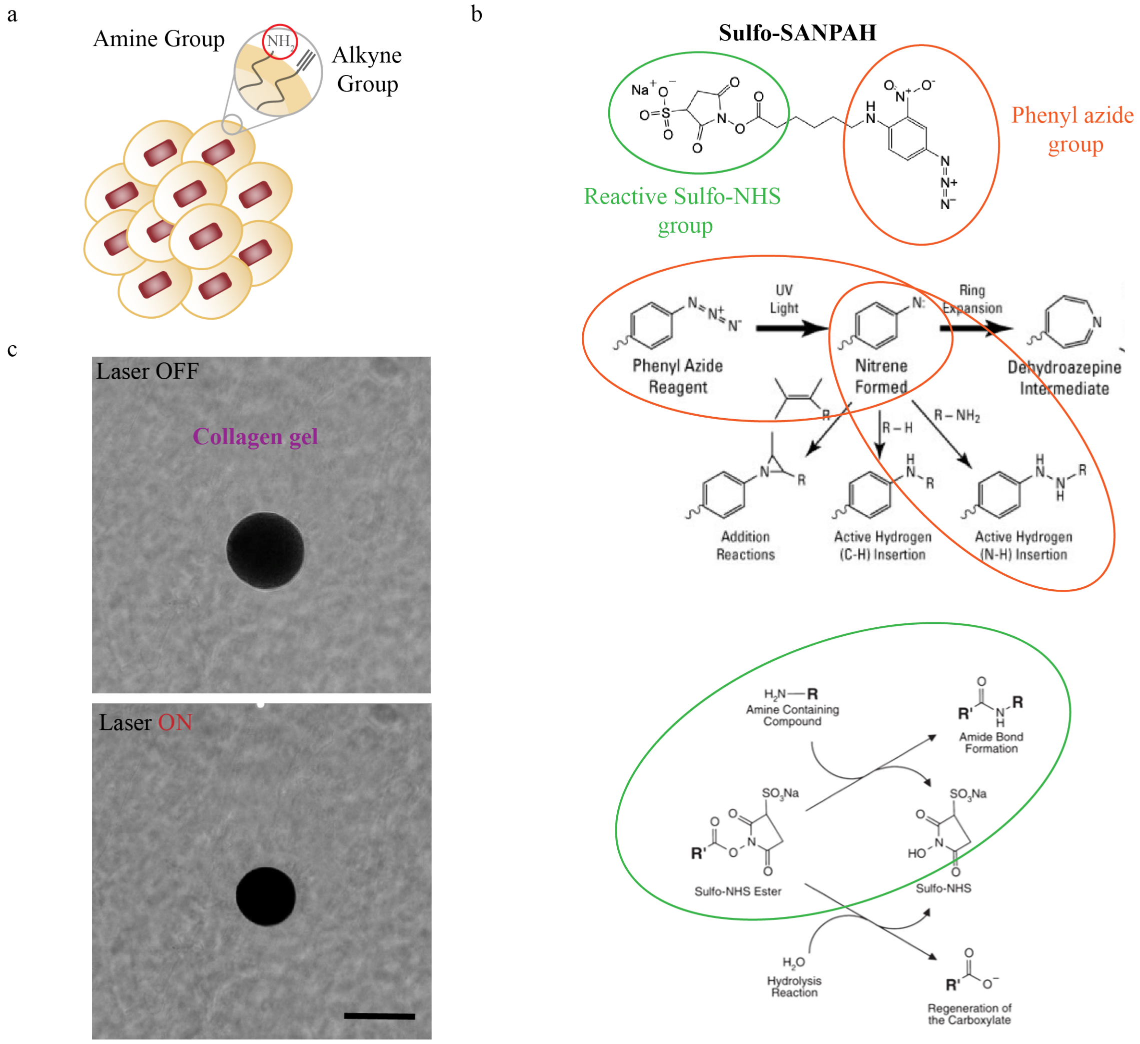
a
Amine Group
NH2
Alkyne Group
b
Sulfo-SANPAH
Reactive Sulfo-NHS group
Phenyl azide group
UV Light
Ring Expansion
Phenyl Azide Reagent
Nitrene Formed
Dehydroazepine Intermediate
R – H
R – NH2
Addition Reactions
Active Hydrogen (C-H) Insertion
Active Hydrogen (N-H) Insertion
H2N—R Amine Containing Compound
Amide Bond Formation
Sulfo-NHS Ester
Sulfo-NHS
H2O Hydrolysis Reaction
Regeneration of the Carboxylate
c
Laser OFF
Collagen gel
Laser ON

FIGURE 5.2 – mOMAs fucntionalization for collagen integration. a. Schematic representation of the microactuator with amine groups on the surface. b. Schematic representation of the functionalization reaction with the heterobifunctional molecule Sulfo-SANPAH. c. Representative example of a microactuator embedded in a collagen I matrix, in its relaxed state and fully contracted under NIR illumination. Scale bar 100μm.[68]

Next, μOMAs were activated in the presence of the acini to test whether we could induce the formation of any protrusions into the collagen matrix (Figure 5.3). The actuators were operated overnight either continuously or in a cyclic manner at different frequencies ranging from 0.1 Hz to 1 Hz (data not shown). We observed that the acini that were located within 200 μm distance to an actuator visibly deformed upon NIR illumination

(Figure 5.3). Further experiments should be done to characterize the collagen deformation and the forces applied to the cells using particle tracking, rheology, and stress/strain sensors. Due to time constraints, we decided to move to a different platform where we can generate very high deformation and push the limits of mechanical loading.

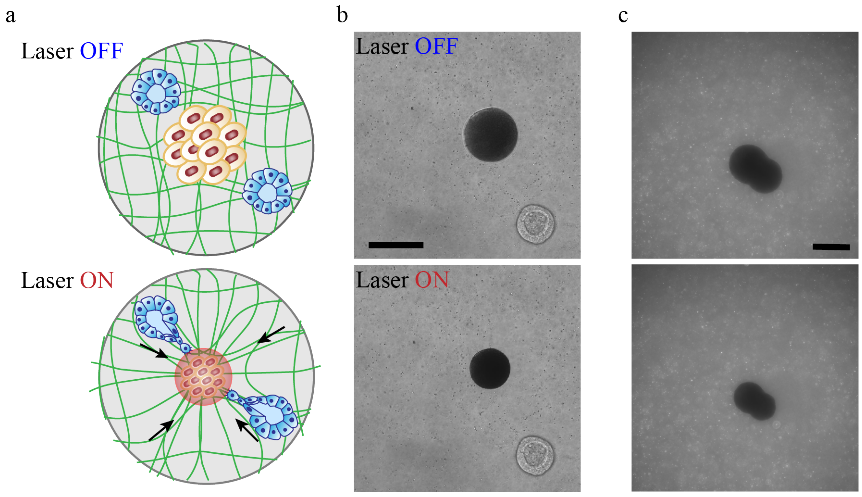

FIGURE 5.3 – mOMAs factuation in 3D-collagen I. a. Schematic representation of the mechanical actuation set-up with the MCF10A acini and the microactuators. b. Representative example of a spherical actuator deforming a MDCK cyst. c. Actuation of the spherical microactuator in a 3D-Collagen I labelled with fluorescent 1μm beads. Scale bars 100 μm.

5.5 Micromanipulation platform

Tensile stresses were applied to acini by embedding a stainless steel pin (4cm long and 30 μm in diameter) inside the collagen gel. The pin was pulled using a micromanipulator with 4 degrees of freedom (Figure 5.4b). The micromanipulator was assembled on a 3D-printed base that fit our microscope stage. The design of the base could be easily adapted according to the size of the dish and the specifications of the microscope. We moved the base along with the manipulator and the sample from the incubator to the microscope to enable long term culture without blocking the microscope.

After 5 days of culture on Matrigel, the samples were washed with PBS. The pin was positioned about 100μm above the Matrigel surface (Figure 5.4a). Reconstitued collagen I was then added on top and polymerized at 37^{o}C for 1 h. Once the collagen was gelled, culture medium was added and the sample was mechanically loaded by moving the pin in x axis, parallel to the base of the dish. We systematically varied the duration of the loading, and decided to set the duration to 2 days. After 2 days, the pin was returned to its original position. We varied the displacement from 50 to 600 μm. It was found that the maximum pull that can be done is 300 μm before the gel started to detach from the pin. We pulled the pin by 300 μm in the rest of the experiments.

5.5.1 Characterization of the invasive phenotype

Mechanical loading resulted in several changes in the acini and their microenvironment. We used the percentage of acini that had protrusions 7 days after forming the collagen matrix as our primary metric for the evaluation of invasiveness (Figure 5.4d). The results showed that pulling the pin by 300 μm had a significantly higher impact on the phenotypic change compared to the control where the samples were not mechanically loaded or pulling the pin by 150 μm (Figure 5.4e).

Next, we checked the distribution of several important protein markers using immunostaining. Vimentin was specifically expressed by cells residing along the protrusions (Figure 5.5a), which could be linked to the migration of myoepithelial cells during tumor formation [201]. In agreement with the published results [198], fibronectin deposition was visible around the branches invading the collagen, whereas we did not see fibronectin around non-invasive part of the acini (Figure 5.5b). Finally, collagen was aligned at the tip of the branches, while fibers remained unorganized around the rest of the acini. Laminin was visible inside the cells that formed the protrusions, as an indication of loss of polarity (Figure 5.5c).

In the next sections, I explored the mechanism behind the emergence of the invasive phenotype.

5.5.2 Tensile loading and matrix remodelling

Fiber alignment could guide the cell migration into the collagen matrix. We checked the state of the collagen matrix before and after mechanical loading to determine whether there was plastic deformation. The results showed that collagen alignment only occured in the vicinity of the pin (within 200 μm diameter), and the rest of the collagen matrix appeared to be unstructured (Figure 5.6a). Furthermore, fibers returned to their original state upon removal of the mechanical loading, ruling out the possibility of plastic deformation.

Fiber deformation was quantified from particle displacements (Figure 5.6b). The particles were displaced up to 100μm, and this maximum level of displacement was recorded around the pin. There was no bead displacement at location more than 1 mm away from the pin. The phenotypic change was not triggered by strain, therefore, stress induced signaling remained as the sole explanation.

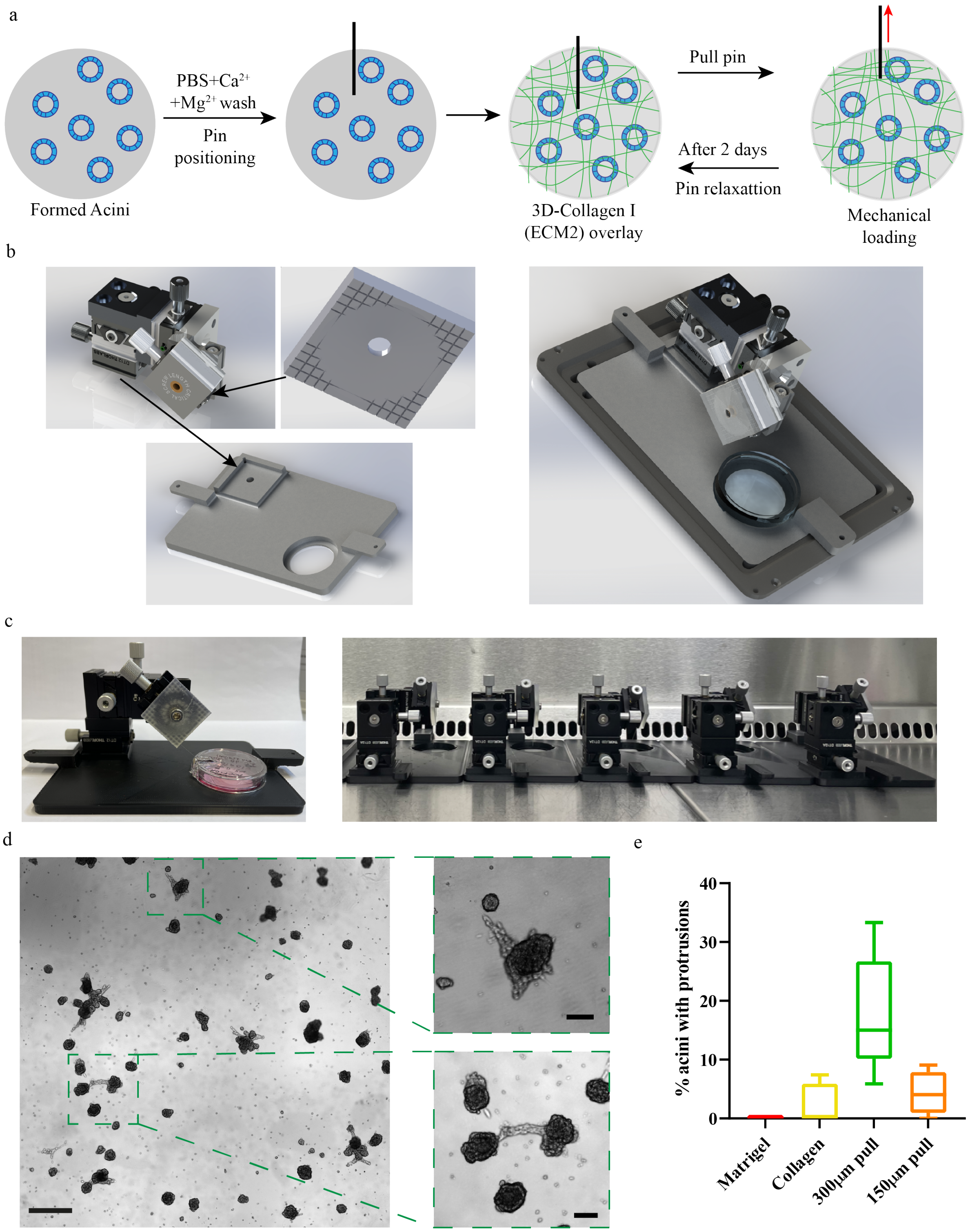
a
PBS+Ca^{2+}
+Mg^{2+} wash
Pin
positioning
Formed Acini
Pull pin
After 2 days
Pin relaxattion
3D-Collagen I
(ECM2) overlay
Mechanical
loading
b
c
d
e
% acini with protrusions
40
30
20
10
0
Matrigel
Collagen
300µm pull
150µm pull

FIGURE 5.4 – Platform development for mechanical manipulation of MCF10A acini. a. Schematic of MCF10A acini mechanical manipulation (Top view). Once the acini are formed, they are washed with PBS supplemented with calcium and magnesium and then, under the microscope, a stainless steel pin is positioned approximately at 100 μm of the surface focus. After, 3D-collagen is added and incubated for 1h. Once gelled, medium is added and, under the microscope, the pin is pulled for 300μm for 2 days and then pull back to its initial position. b. Set-up designs in SolidWorks. The micromanipulator, purchased form Thorlabs, is assembled in a 3D printed customized support for the microscope. The pin holder, also 3D printed in-house, is assembled on the rotational part of the manipulator. c. Left : Picture of the assembled device with a sample. Right : For high-throughput, several devices are used at the same time. d. Representative BF images of the resulting phenotype, 7 days after the initial pull (5 days after pin relaxation). Scale bars, 100 μm. e. Quantification of % of acini with protrusions for n>200 organoids per condition from 4-7 independent experiments.

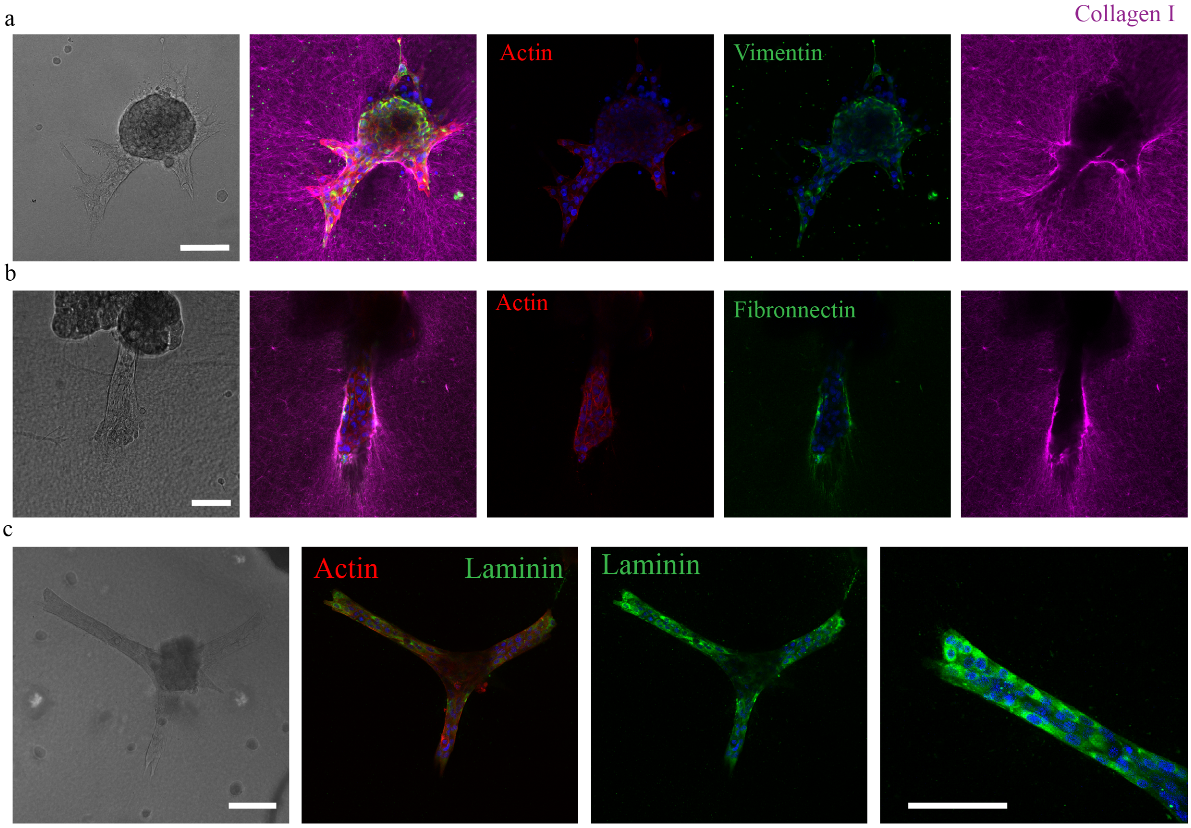
a
Collagen I
Actin
Vimentin
b
Actin
Fibronnectin
c
Actin
Laminin
Laminin

Figure 5.5 – Mechanically stress-induced invasive cell phenotype. Representative confocal images of actin, vimentin (a),fibronectin (b) and laminin (c), staining on 12 day-old organoids subjected to stress, induced by the 300 μm pull. Collagen type I was also labeled. It is possible to observe collagen I alignment around the acini's protrusions. On the left are bright-field images. Scale bars, 100 μm.

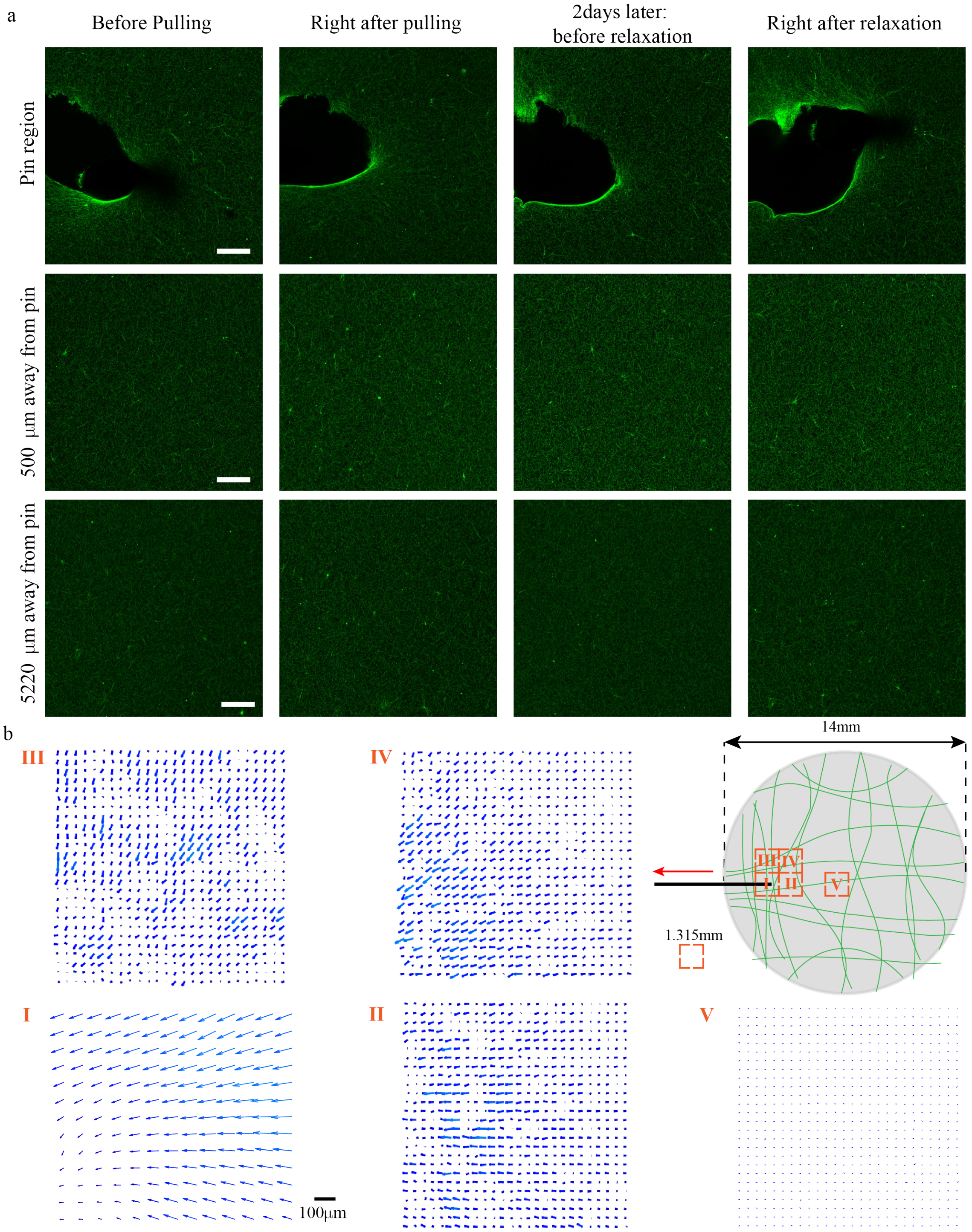
a
Before Pulling
Right after pulling
2days later:
before relaxation
Right after relaxation
Pin region
500 μm away from pin
5220 μm away from pin
b
III
IV
14mm
1.315mm
I
II
V
100μm

FIGURE 5.6 – Collagen deformation characterization a. Representative images of fluorescently labelled 3D-collagen at different distances from the pin before, during and after pulling. Scale bar, 100μm. b. Vectorial displacement maps at different regions of the collagen Matrix (preliminary data). Up and right from the areas highlighted there is no displacement, as shown in region V.

5.5.3 Tensile loading and intracellular mechanics

The response of the acini to mechanical loading depends on the state of the constituent cells. First, the force must be transmitted to the cells, therefore, the level of attachment to the surrounding collagen matrix is important. Second, cell mechanics that entails the cortical tension, actin cytoskeleton, and actomyosin contractility is involved in the mechanotransduction process. We first investigated the role of contractility. To this end, non-muscle myosin II activity was suppressed with a cell-permeable small molecule, Blebbistatin. Low concentrations of Blebbistatin are known to induce migration of epithelial cells due to a decrease in cortical tension [204, 205]. Blebbistatin was added at two key time points, either during the 2 days the acini were stimulated or right after returning the pin to its original position (Figure 5.7a). Inhibiting myosin activity during mechanical loading resulted in a very invasive phenotype. Almost all acini branched out and they were already connected to each other at the end of 5 days of culture post-stimulation (Figure 5.7c). The protrusions were significantly longer and collagen fibers were aligned in between acini (Figure 5.7d). Blebbistatin treatment also increased the invasiveness in the control samples that were not mechanically stimulated (Figure 5.7b). Notably, when Blebbistatin was added after mechanical loading, the drug did not make the same impact. The cells were more invasive compared to the chemically non-treated samples, yet we did not observe network formation.

Several studies have shown the role of RhoA/Rock/MLC pathway on the invasive and carcinogenic phenotype of tumors, including the mammary cancer [20, 201, 206, 207, 208]. RhoA is the key regulator of the activity of myosin II [209]. The pathway involves several proteins, and the protein directly involved in the regulation of myosin II activity is Rho Kinase (ROCK). Both ROCKI and ROCKII upregulate myosin II activity by augmenting the level of phosphorilation of the regulatory myosin light chain (MLC), which in return will promote the assembly and ATPase activity of myosin II. We tested whether the whole pathway is involved in the phenotypic transition.

Inhibiting RhoA activity during pulling almost completely eliminated the effect of mechanical loading (Figure 5.8a). We tried to rescue the invasive phenotype by adding Blebbistatin after inhibition of RhoA signaling during pulling. There was an increase in the number of acini with protrusions, reaching the levels of samples that are not chemically treated. Swithching the order of administration of drugs, i.e. first Blebbistatin during pulling and then RhoA inhibitor resulted in a similar outcome. Rho signaling is required for both mechanotransduction and invading the collagen gel. Inhibition of myosin II results in a decrease of cell stiffness and cortical tension, which is correlated to metastatic behavior [192, 210]. RhoA activity is also related to myosin contractility. However, the downstream signaling pathway has more extended implications, including the inhibition of cell migration.

Rho/Rock mediated actomyosin contractility is responsible for collagen remodelling, specifically fiber alignment during migration [192, 206]. Previous work has shown that within aligned matrices the Rho/Rock/MLC pathway is not necessary for cell invasion [20, 206]. Since the collagen characterization studies excluded the influence of matrix-alignment on the invasive phenotype, we checked whether ROCK was coordinating the matrix invasion of cells and acini-acini interactions through matrix alignment. Inhibiton of ROCK decreased the invasive phenotype (Figure 5.8c). When added to the media after

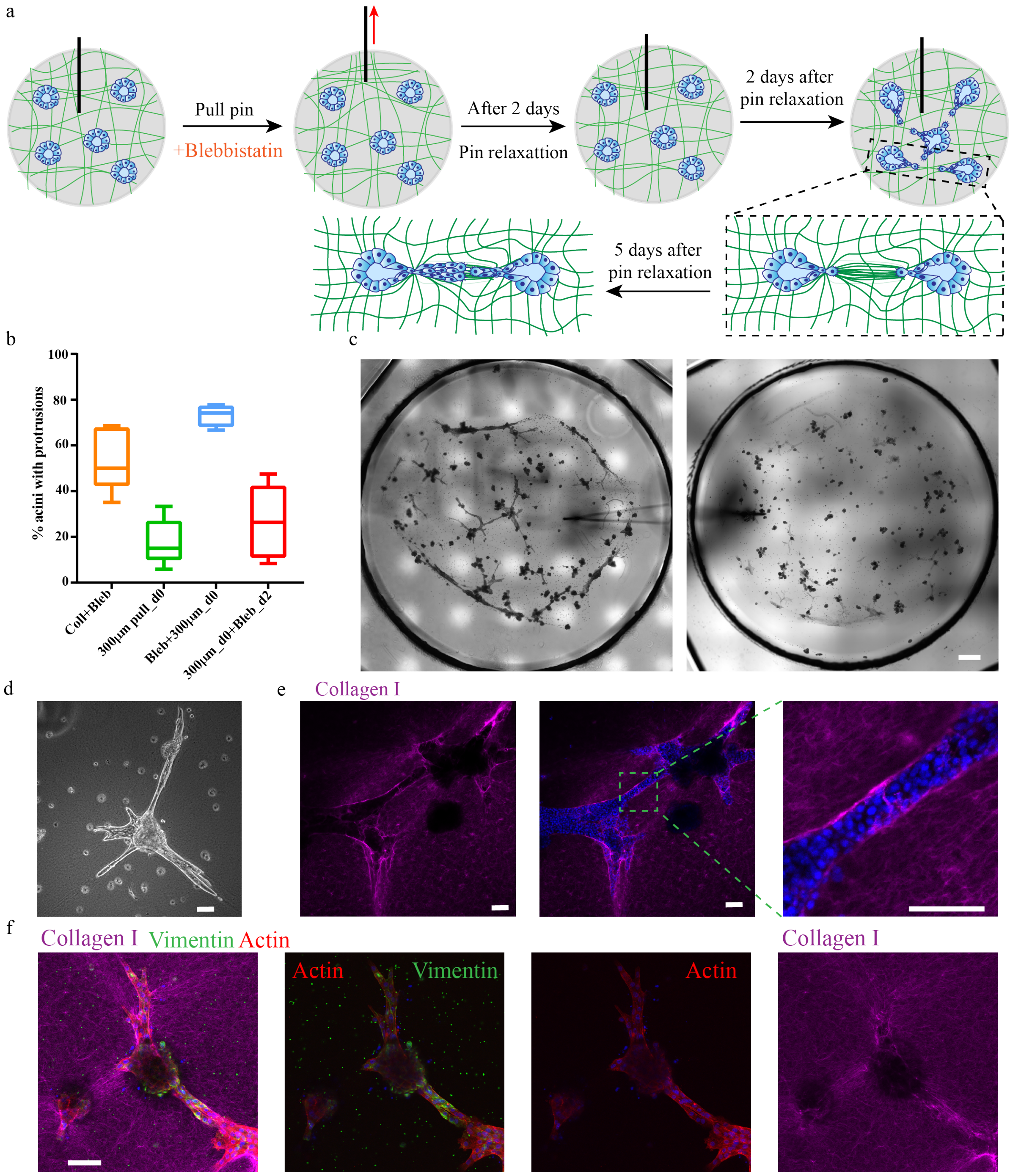
a
Pull pin
+Blebbistatin
After 2 days
Pin relaxattion
2 days after
pin relaxation
5 days after
pin relaxation
b
100
80
60
40
20
0
% acini with protrusions
Coll+Bleb
300μm pull_d0
Bleb+300μm_d0
300μm_d0+Bleb_d2
c
d
e
Collagen I
f
Collagen I
Vimentin
Actin
Actin
Vimentin
Actin
Collagen I

Figure 5.7 – Investigating the role of myosin II in the invasive phenotype. a. Schematic of mechanical manipulation and suppression of myosin II with Blebbistatin. Blebbistatin is added during the mechanical manipualtion (Bleb+300μm_d0) or after pin relaxation (300μm_d0_Bleb_d2) for 2days. Two days after pin relaxation, it is possible to observe already the formation of some invadopodia and some collagen alignment around them. 5 days after pin relaxation it is possible to observe long protrusions and some connections between the organoids. b. Quantification of % of invasive acini for n>200 organoids per condition from 4-7 independent experiments. c. Representative brightfield images of the epithelial organoids 5 days after of pin relaxation. Left : Bleb+300μm_d0. Right : 300μm_d0_Bleb_d2. Scale bar, 1mm. d. Representative phase-contrast image of acini with invasive phenotype connecting with each other. e-f. Representative confocal image of invasive acini connecting with each other. Collagen I alignment can also be seen. d,e,f. Scale bars, 100μm.

pulling combined with myosin inhibition, cells branched out but had difficulty to remodel the ECM, which resulted in shorter protrusions.

Treating the samples with $\beta 1$ integrin blocking antibody (AIIB2) completely eliminated the effects of mechanical loading. We did not observe any protrusions (data not shown). Cells must be connected to the collagen fibers during and after mechanical loading to be able invade the matrix.

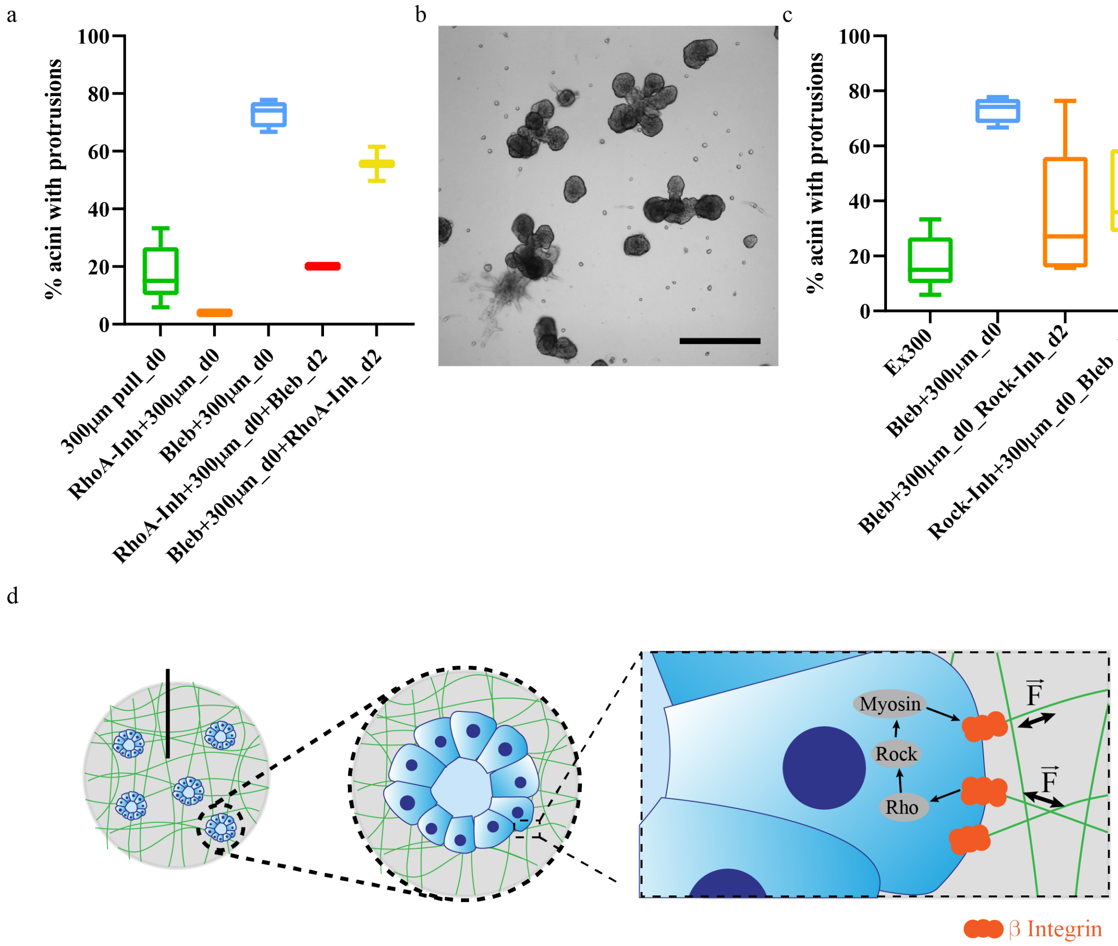

FIGURE 5.8 – Investigating cellular processes involved in the epithelial invasive phenotype. a. Quantification of % of acini with protrusions for n>150 organoids per condition from 1-7 independent experiments. Several conditions were tested : RhoA inhibitor is added during the mechanical manipulation (RhoA-Inh+300μm_d0) ; the combination of Blebbistatin and RhoA inhibitor was also tested, first adding RhoA inhibitor while pulling and then Blebbistatin after relaxation (RhoA-Inh+300μm_d0+Bleb_d2) or vice-versa (Bleb+300μm_d0+RhoA-Inh_d2). b. Representative brightfield images of the epithelial organoids after 5days of pin relaxation. RhoA inhibitor was added while pulling and blebbistating was added after pin relaxation. Scale bar, 500 μm. c. Quantification of % of acini with protrusions for n>250 organoids per condition from 4-7 independent experiments. The combination of Blebbistatin and Rock inhibitor (Y27632) was tested. First adding Rock inhibitor while pulling and then Blebbistatin after relaxation (Rock-Inh+300μm_d0+Bleb_d2) or vice-versa (Bleb+300μm_d0+Rock-Inh_d2). d. Schematic representation of the mechanotransduction mechanism. The integrins sense the mechanical properties of the environment and the forces propagating through the ECM, inducing a cascade-response signalling via Rho/Rock/MLC pathway. Blockage of this cascade inhibits carcinogenic-cellular responses.

5.6 Discussion

The work presented in this chapter was motivated by the recent reports on the involvement of mechanical forces in branching morphogenesis and carcinogenesis of mammary gland organoids [193, 194]. These processes involve long-distance mechanical interactions through fibrous ECM. We have shown that application of tensile forces induce an invasive phenotype on the mammary organoids. This effect is more emphasized when the cell contractility was reduced through myosin II inhibition. Imaging of collagen fibers and embedded tracer particles during mechanical loading excluded the possibility that matrix remodeling initiated or guided the invasion process. Pharmacological experiments showed that Rho/Rock/MLC pathway was involved in the mechanotranduction and matrix invasion.

This simple platform opens up several opportunities to study mechanobiology of cell clusters embedded inside matrices. Now that we have a basis to plan on manipulation experiments, we will use the wireless optomechanical actuators to generate localized stresses.

5.7 Detailed Protocols

5.7.1 2D cell culture

MCF10A cells (ATTCC® CRL-10317^{TM}) were culture in Dulbecco's modiefied Eagle's medium/Nutrient Mixture F-12 with Glutamax (DMEM/F-12, GlutaMAX™ supplement) supplemented with 20ng/mL of EGF (PrepoTech) ; 5%(v/v) horse serum (HS, ThermoFischer Scientific) ; 0.5μg/mL of Hydrocortisone (SIGMA Aldrich) ; 100ng/mL of Cholera Toxin (SIGMA Aldrich) ; 10μg/mL of insulin (SIGMA Aldrich) and 1%(v/v) penicilin/streptomycin (ThermoFischer Scientific). The cells were passed every 2/3 days up to 5 passages, following the protocol published elsewhere [191]. Briefly, or 2 days culture seed 1x10^{4}cells/cm^2 and for 3 days culture (over-weekend) seed 2.67x10^{3}cells/cm^2. For a T75 culture flask :

1. Aspirate the medium and add 10mL of PBS for washing.
2. Aspirate, add 3mL of 0.05%Trypsin-0.48mM EDTA (ThermoFischer Scientific) and incubate in a 5%CO$_2$ humidified incubator at 37^o for 15 min.
3. Neutralize the cell suspension by adding complete growth medium (CGM). Add at least double of the volume of Trypsin. Pipette up and down gently do dissociate cell clumps.
4. Aliquot cells into 15mL falcon tubes and centrifuge at 120g for 5min at room temperature.
5. Ressuspend the cell pellet in CGM.
6. With a hemocytometer count cells. Plate 8x10^5 cells for 2 days or 2x10^{5}cells for 3 days culture.
7. Incubate.

Note : To avoid thermal shock put the T-flask in the incubator with the medium while you trypsinize the cells. It warms up the medium and stabilizes the pH.

5.7.2 3D cell culture : MCF10A acini formation

MCF10A acini were cultured on Matrigel in a 3D culture medium (3D-CM) composed by DMEM/F-12, GlutaMAX™ supplement, 10ng/mL of EGF ; 2%(v/v) HS ; 0.5μg/mL of Hydrocortisone ; 100ng/mL of Cholera Toxin ; 10μg/mL of insulin and 1%(v/v) penicilin/streptomycin supplemented with 2% (v/v) Matrigel (BD Biosciences Growth Factor Reduced (GFR) Matrigel Matrix). They were formed on glass-bottom petri-dishes, prepared in-house or bought from Mattek, for imaging purposes. MCF10A acini were formed following several reported protocols [191, 194, 195] as follows :

1. Spread 80μL.cm^{-2} of 8mg/mL Matrigel on the coverslip and incubate at 37^{o}C for 30 min. (It is important to do it in a humidified incubator to avoid dehydration.)
2. In the mean time, prepare the 3D-CM with 2%(v/v) Matrigel. (Note : The 3D-CM can be kept in the fridge at 4^o but the Matrigel should be added fresh each time. When handling Matrigel it should be kept on ice to prevent it from thawing.)
3. Trypsinize the cells as mentioned for 2D cell culture.

4. Ressuspend the cells in the right volume (see next step).
5. Once the gels are formed, add the single cells on the Matrigel with a seeding density of $3.14\text{x}10^3$cells/cm^2. (The seeding density should be adapted to the cell passage and acini density desired.)
6. Incubate for 30 min to 1h.
7. Cover with 3D-CM complemented with 2%(v/v) Matrigel, prepared on step 2.
8. Incubate and replace the medium every 2-3 days.

In this work the acini formed within 5 days, age at which the acini were used for mechanobiology studies.

5.7.3 Experimental set-up : MCF10A acini sandwich and pin set-up

After 5 days, acini were formed and sandwiched between the Matrigel bottom layer and a 1mg/mL 3D-Collagen I (5mg/mL, Cultrex^{TM} 3-D Culture Matrix Rat Collagen I from R&D Systems) layer, added on top for mechanobiology studies. Like Matrigel, collagen must be handled on ice. Collagen I was prepared according to the manufacturer specifications. Collagen I was labelled either with Alexa Fluor NHS-Ester 647 or 488 either with Dylight 650 (ThermoFischer Scientific). Aliquots of collagen I were prepared with the fluorescent die at a ratio of 1 :1000 and stored at 4^{o}C. The labelled collagen is added to the non-labeled collagen solution in a ratio of 1 :7.

The acini were washed 3 times for 5 min with chill PBS supplemented with Ca^{2+} and Mg^{2+} (DPBS, SIGMA Aldrich). To avoid avoid collagen detachment, the petri-dishes were well dried around the Matrigel area with the help of a pipette tip connected to the aspirator. Then, a hole was made on the petri-dishes with a soldering machine followed by the positioning of the pin (Stainless insect pin ; size 000 ; tip diameter 0.03mm ; 4cm length ; Fine Science Tools) under the inverted microscope. Once the set-up was ready, the collagen was added carefully on top of the acini and Matrigel layer and incubated for 1h at 37^{o}C. When gelled, add 3D-CM without Matrigel. For experiments with inhibitors, 10μM Blebbistatin (SIGMA Aldrich), 10μM Rho inhibitor I (Cytoskeleton) and 10μM Rock inhibitor (Y-27632 dihydrochloride, STEMCELL^{TM} Technologies) were added on day 5 (while pulling) or day 7 (after pin release) for a 48h treatment. For experiments blocking integrins, the Anti-Integrin Beta1, clone AIIB2 (Azide Free) antibody (Merck Milipore) was used.

5.7.4 Immunohistology

The immunostaining was based on the protocols reported elsewhere [191, 198]. Briefly, samples were fixed with 2% paraformaldehyde (PFA, SIGMA Aldrich) for 20 min at room temperature and then washed 3 times 5min with PBS 1X. The acini were then permeabilized with 0.5% Triton X-100 (SIGMA Aldrich) in PBS for 10 min at 4^{o}C followed by 3 washes of 15 min at room temperature with 100mM glycine solution (100mM glycine, 130mM NaCl, 7mM Na_2HPO_4 and 3.5mM NaH_2PO_4 in mili-Qwater). After they were blocked for 1.5h with IF buffer (130mM NaCl, 7mM Na_2HPO_4, 3.5mM NaH_2PO_4, 7.7 mM NaN_3, 0.1% bovine serum albumin (BSA), 0.2% Triton X-100, 0.05%Tween-20 in mili-Qwater) and 10%(v/v) goat serum. The acini were incubated over night at 4^{o}C with primary antibody [Vimentin (D21H3) XP®Rabbit mAb 5741, from Cell Signalling

Technology® ; E-cadherin (24E10) Rabbit mAb 3195, from Cell Signalling Technology® ; Fibronectin : Anti-Fibronectin antibody (ab2413), from abcam ; Laminin : Anti-Laminin 5 antibody (ab14509), from abcam] diluted in the blocking solution with a dilution of 1 :50 and washed 3 times for 20 min with IF buffer at room temperature with gentle rocking. After, the acini were incubated over night at 4^{o}C with the fluorescent conjugated antibody in block solution with a dilution of 1 :100 (IgG (H+L) Cross-Adsorbed Goat anti-Rabbit, Alexa Fluor™647 or 488, Invitrogen). Once again, the samples were washed 3 times for 20 min with IF buffer at room temperature with gentle rocking followed by actin cytoskeleton staining with Phalloidin (Texas Red or 488, 3 :1000) for 15 min and 2 times 5min washing with PBS 10x, and nucleus staining with Hoesch (2 :1000) for 15min and 2 times 5min washing with PBS 10x. Samples were then sandwiched with fluorescent mounting media and a coverslip, and stored at 4^{o}C.

5.7.5 Image acquisition and data analysis

All live-experiments were performed using a Nikon Ti Eclipse motorized inverted microscope. Bright-field (BF), differential interference contrast (DIC) and phase-contrast (PH) images were captured with an ORCA-Flash4.0 CMOS camera (Hamamatsu). The acini were imaged every 2/3 days, to track their morphological changes. The organoid morphologies were quantified manually. Fiji from ImageJ [120] was used to analyze images.

The acini and collagen matrix immunofluorescence characterization was done using a Leica SP8 multipurpose point scanning inverted confocal microscope.

For particle displacement quantification, 1 μm-diameter fluorescent particles were added to the collagen matrix. Videos were recorded with high frame rate and processed in MATLAB with the PIV tool, [122] and plotted with the plugin quiverc [123].

5.7.6 mOMAs integration in collagen

The spherical microactuators were embedded in the 3D-collagen matrix by functionalizing them with a heterobifunctional crosslinker, sulfo-SANPAH (Pierce^{TM}). Briefly, the microactuators are spun down for 2 min at 14000rcf and the supernatant is removed. Then, 0.5mg/mL of sulfo-SANPAH in PBS are added in a ratio of 1 :2 (v/v) beads :SANPAH, and mixed for a proper homogenization. The suspension is exposed to UV light (300-460nm) for 7 minutes to activate the cross-linker and initiate the functionalization reaction. After, the suspension is washed 2 times with PBS 1X and 1 time with ethanol, to remove unreacted sulfo-SANPAH. The supernatant is removed and the rest of the ethanol is evaporated in the hood while the collagen gel mixture is prepared. Once both are ready, the collagen is added to the functionalized microactuators, then added on the experimental set-up and incubated for 1 hour. Once the collagen is polymerized, add PBS or culture medium.

6 Conclusions and outlook

6.1 Actuators and mechanical systems

Mammalian cells are surrounded by other cells and matrix proteins that provide various mechanical signals. Advances in materials science and microengineering brought 3D cell culture models that mimic the conditions within living organs. While the mechanical properties and architecture of the ECM can be tuned using engineered materials, existing techniques do not allow the application of spatiotemporally resolved forces within bioengineered platforms in a minimally invasive fashion. In this thesis, I described one such technique that involves the use of optically addressable soft microactuators.

I presented a repertoire of actuators and devices with different layouts and functions. Nevertheless, the building actuator block is always a nanogel that can transduce light into heat and, subsequently, mechanical work. Gold nanorods coated with pNIPMAM harvest light and generate heat at the LSPR of gold. This thermal energy is then converted into mechanical work with the contraction of the thermoresponsive polymer, as a consequence of the breakage of hydrogen bonds. This process is fast, powerful, and reversible. To scale up the forces provided by the nanoactuators, the particles were agglomerated and crosslinked. Spherical optomechanical microacuators composed only of nanoactuators were synthesized using a template-assisted microfluidic approach. The resulting microactuators exhibit mechanical properties (4.8 ± 2.1 kPa stiffness) and performance metrics (actuation strain up to 0.3 and stress up to 10 kPa) that are comparable to mammalian cells. NIR laser illumination provides effective spatiotemporal control over actuation (sub-micron spatial resolution at millisecond temporal resolution). As a second strategy, an ink in the form of a hydrogel-nanoactuator composite was prepared. This ink was casted and printed to form actuators with various forms and structures, such as thin films and fibers. The last strategy involves laser directed assembly of nanoactuators.

I showed that the morphology of the gold core and the polymer coating could be finely tuned by changing the synthesis conditions. Notably, I demonstrated that these nanoactuators could be upgraded to become multifunctional by adding other metal layers to the core. In our application, Pt coating provided catalytic activity and Ni coating provided magnetization. Together, these two extra layers realized on-demand self-assembly of microactuators. It would be interesting to explore other functionalities such as controlling the electric charge of the particles. Charged nanoparticles respond to electrophoretic forces. Optoelectronic manipulation is a versatile technique to simultaneously transport hundreds of particles on a plane [211]. This way, we may increase the complexity of devices assembled from the colloidal suspension. The colloidal assembly approach may be pushed to the next level if, instead of photopolymerization, we could self-assemble mechanisms from nanoscale building blocks. This concept may be realized by synthesizing thermally nonresponsive nanogels with gold nanorod core. Tuning the plasmon resonance frequency of the active and passive components using nanorods with different aspect ratios will enable coordinated assembly of mechanisms and actuators. Finally, the assembly process may become reversible by the initiation of covalent bonds that can be enzymatically removed or using DNA linkers [117].

Although the complexity of the shapes that can be achieved by laser writing is unprecedented, the technique may not be suitable for in vivo applications where penetration of NIR is an issue and Marangoni flows may not be generated effectively. In contrast, magnetic fields are suitable for particle manipulation and powering actuators under these conditions. The magnetic properties of the mNAs pave the way for the formation of dynamically stable morphologies using rotating and oscillating magnetic fields. The heat that is required for chemically crosslinking the particles and driving the sol–gel transition can be generated using radiofrequency (RF) oscillating magnetic fields. RF signals can also be used for powering the self-assembled artificial μmuscle. Previous work has shown that bulk thermoresponsive hydrogels fabricated from magnetic nanocomposites could be actuated using magnetic hyperthermia [74, 118]. However, this strategy will come with an important trade-off, the spatial resolution and frequency selective activation provided by plasmon resonance heating will be lost. Intuitively, the resolution of printing depends on the laser dose and the concentration of mNAs, and precise control over laser spot would enable printing of structures with arbitrary complexity.

From the device side, compliant mechanisms were fabricated from a biocompatible hydrogel, PEGDA, using projection lithography. A programmable Digital Micromirror Device (DMD) that was connected to an inverted microscope projected the UV light to predetermined regions and polymerized the hydrogel in situ around the actuators. A variety of microdevices were presented ranging from lever arms, continuum microrobots, flextensional mechanisms, and microgrippers. The design space is only limited by the imagination of the researcher. The mechanisms could be printed using direct laser writing for creating more sophisticated 3D machines. Any polymer that can be photopolymerized and deformed by the actuators can be used for building the mechanisms.

6.2 Mechanobiology

We introduced a soft robotic compression device for mechanical characterization and stimulation of organoids. A cantilever beam was incorporated for real-time monitoring of mechanical properties of 3D cell clusters. I showed that the compression device could be fabricated inside microfluidic channels, which opens up the door to a wide range of combinatorial biomechanical studies with high-throughput. Combination of pharmacological studies with real-time biomechanical characterization of organoids will bring new perspectives to the crosstalk between biochemical signaling and cell mechanics. There is work to be done to provide a complete solution. The samples were loaded manually, which is sub-optimal. Organoids can be guided with fluid flow inside channels with structured compartments or integrated valves. Once the samples are located in place, a programmed laser system will apply the predefined loading regimen on each device in an automated fashion.

As final contribution, it was demonstrated that externally applied tensile stresses initiate biomechanical interactions among organgoids inside a fibrillar matrix. A 3D model of the human mammary gland was developed following a sandwich configuration where the acini were grown on matrigel, and later covered by collagen I. External forces were applied using a micromanipulated stainless steel pin. Combination of mechanical forces and chemical inhibition presented an invasive phenotype. The results also showed that the Rho/Rock pathway is involved in the mechanotransduction process. Blocking β1-integrin isolated the acini from mechanical stimulation. The work done here, regarding biomechanical characterization and manipulation, is far from completed. The pin set-up was expected to provide us the excitation parameter so that we could plan experiments with the wireless microactuators. A detailed characterization of the forces exerted on the

ECM is on the way. This characterization is going to be performed using polyacrylamide (pAAm) or alginate sensor beads [24, 25, 26, 27].

6.3 Bioinspired programmable active matter

Gottfried Wilhelm Leibniz once said “I define the Organism, or natural Machine, a machine in which each part is a machine [. . .], whereas the parts of our artificial machines are not machines”. Although both natural and synthetic machines require an input of energy to perform work, living organisms possess a self-organized hierarchy from the nano- to the macroscale. Every unit of a biological system is active, and interacts with other units through integrated feedback loops as if machines are made from smaller machines. In other words, organisms are non-equilibrium self-organized hierarchical dynamical systems, which is a manifestation of oscillatory patterns of interactions among building blocks. On the other hand, man-made machines are assembled from inactive building blocks. This construction and operation framework gives limited ability to mimic lifelike properties to 1) study fundamental principles that govern the adaptive behavior of self-organizing structures and 2) engineer machines that operate away from equilibrium. There is an emerging field called active matter, a sub-class of soft matter physics and chemistry that focuses on the study of self-driven systems, in which energy is directly supplied to the building blocks [212].

An impactful contribution to the field of active soft matter would be the development of autonomous micromechanical hydrogel systems from self-driven hierarchically assembled nanoscale machines. These autonomous micromachines can serve as a platform to study fundamental biological processes driven by mechanical work such as self-organization in the embryo, driven by growth, differential adhesion, and cortical tension. An important contribution of such work would be the introduction of mechanosensing into artificial systems with the objective of coupling the local oscillations of individual machines to generate self-organized collective deformations. Autonomous micromachines with time-varying actuation would also allow the study of biological locomotion, which is primarily based on coordinated oscillations or undulations of musculoskeletal components interacting mechanically with the surrounding environment.

Multicellular organisms are complex biological systems that grow from a single cell during embryogenesis through spatiotemporally controlled proliferation, differentiation, migration, and apoptosis. Each cell operates like a microscale factory self-assembled from nanoscale proteins and other biochemical molecules. Embryonic research has decisively shown that disordered and distributed biological systems can spontaneously form patterns and organized structures via selective and specific interactions that lead to rearrangement of the relative positions of the units within the embryo in the absence of external control inputs[213, 214]. Recapitulating this self-organization in synthetic systems may open up completely new avenues for building adaptive soft micromachinery.

The first step to implement biological construction principles in synthetic system is to understand the governing physical and chemical rules. To explain self-sorting, scientists made analogies with immiscible liquids such as oil and water, where the multicellular aggregates are represented as oil droplets in water. In a liquid system, molecules of different properties phase-segregate (cohesion) in order to minimize the surface tension. Steinberg proposed the Differential Adhesion Hypothesis (DAH) based on this liquid-tissue analogy, where he stated that random motility allows cells to reorganize and differences in cell adhesion generate mechanical forces that drive segregation. It is proposed that cell segregation is driven by mechanical forces of affinity and tension, analogous to surface tension that occurs at the molecular level for oil and water. A difference in affinity between two cell populations leads to tension at their interface because cells of one or both populations experience stronger cohesive forces from homologous cells than from heterologous cells. In principle, this imbalance in forces will drive segregation to generate and maintain a flat interface that minimizes contact between the two cell populations and interfacial tension will drive the segregation of the more cohesive population to the center. An alternative hypothesis called Differential Interfacial Tension (DITH) proposes that segregation can be driven by tension and cell-surface contraction generated independently of differential adhesion. In fundamental contrast to inanimate liquids, tension at the cell surface is maintained by the permanent expenditure of metabolic energy to support contraction of the cortex. Signaling from one cell population induces assembly and contraction of cell-surface-associated actomyosin in the adjacent cells. This cortical tension sharpens the borders and restrains movement of cells across the interface [215, 216, 217].

Random sorting of different cell populations cannot lead to complex patterns. Patterning requires spatial regulation of cell–cell adhesion, actin dynamics, and actomyosin-based contractility. Reaction–diffusion systems are feasible and attractive models for how repeating spatial patterns emerge from an initially homogeneous group of cells. As an alternative theory, the concept of positional information has been proposed as the major driver of tissue patterning. The mechanism involves cells differentiating according to their position within a chemical or mechanical gradient. Recent work has shown that patterning of vertebrate digits is a result of both mechanisms. In theory, mechanical rather than chemical instabilities may underlie tissue patterns, an idea largely explored in the context of mesenchymal condensation [215, 216, 217]. Whether chemically or mechanically controlled, the differential mechanical state such as adhesiveness, viscosity, contractility, and elasticity of spatially compartmentalized cells lead to morphogenesis, which is basically the establishment of a functional multicellular form and structure [215, 216, 217].

Once the biological system is constructed, hierarchically-organized muscle and connective tissue units together drive various types of spatiotemporally coordinated motion. One of the most elegant examples of coupled mechanical oscillators is the beating heart. Cells beating in unison can exert a much stronger force, required for regular pumping of blood through the body. When the beating is not coherent, arrhythmia can occur, which impairs proper function. Recent work has shown that mechanical coupling between cells facilitated by X-ROS signaling, ensures that the final outcome of action potential pacing is synchronized beating [129, 218]. Another example to the generation of motion via coupled oscillators is locomotion, which is primarily produced by appendages that oscillate or by bodies that undulate, pulse, or undergo peristaltic waves [219]. Application of coordinated, time-varying forces to the surrounding fluid or substrate is the key for successful movement. Although the activation of skeletal muscle units is generally controlled by motor neurons, mechanical coupling among muscle units and between the body and the environment can passively tune the gait, which allows the animals to spontaneously adapt their motion or preserve stability during maneuvers.

The key for developing experimental platforms that can reveal biological construction and operation principles is engineering of structures from materials that allow sensing, actuation, and computation on the same system. Artificial cells have been engineered from biological components, such as protein motors and filamentous polymers that are present in the cytoskeleton or DNA-binding enzymes that act as motors. However, none of these systems are regulated spontaneously by internal feedback mechanisms. Furthermore, apart from simple shape deformations, these droplet-based systems cannot perform useful mechanical work and they are far from self-organizing into functional machinery [219, 220]. Hydrogels have been serving as a platform to provide spatial and temporal control over the release of various therapeutic agents. Through appropriately designed composition and structure, they can respond to various biochemical and physical stimuli by showing conformational or optical changes. High water content and tunable mechanical properties provide physical similarity to biological matter, giving the hydrogels excellent biocompatibility and stability. A broad range of printing, folding, molding, and assembly methods are available for forming complex 3D hydrogel mesostructures [221, 222, 223].

Although hydrogel microsystems have shown the unique capability of operating simultaneously as sensors and delivery vehicles, existing prototypes cannot perform complex autonomous mechanical functions with high efficiency. One promising approach to introduce self-regulatory behavior to hydrogels is utilizing exothermic catalytic inorganic or biochemical reactions that undergo reversible and repeatable cycles. Pioneering work has already shown the feasibility of building self-sustained homeostatic systems that couple the chemical reaction with mechanical transduction, which in turn triggers the chemical reaction in a cyclic manner [129]. Self-oscillating gels based on the integration of thermal oscillatory Belousov-Zhabotinsky (BZ) reaction into the polymer backbone have been developed. BZ is a cyclic redox reaction with thermal bistability, that, when coupled to a thermoresponsive polymer induces a periodic conformational change [220, 221, 222, 223, 224, 225, 226, 227, 228, 229, 230]. BZ gels oscillate periodically without the need for external stimuli as the rhythmic pulsations are fueled by the reaction occurring within the hydrogel network. Although proof-of-concept examples of coupled oscillating micromechanical systems have been already introduced, [230] the field is still in its infancy from engineering point of view. Furthermore, BZ reaction has to be replaced with a more generic catalytic reaction that allows better control over oscillation dynamics and incorporation of a wide range of hydrogels.

The last missing piece in this puzzle is engineering a connection between self-sustained agents to build higher order artificial tissues and organisms. Recent efforts in polymer mechanochemistry introduced ways to design functional materials with the ability to rearrange molecularly in response to mechanical input or to transduce mechanical loading into chemical reactions. For example, mechanical stress can be lead to fluorescence as a result of a spatial separation between the quencher and the fluorophore molecules. Alternatively, loading can induce variations in the optomechanical properties of the material due to translocations in molecular assemblies. Thus, the path to engineering mechanosensing in hydrogel systems goes through integration of a motif called “mechanophore” capable of transducing mechanical forces to catalyze a chemical reaction [231, 232, 233, 234]. More recently, it has been shown that macroscopic isotropic hydrodynamic pressure can be translated into molecular level anisotropic strain with the aid of soft mechanophores coupled to hard ligands [235].

In this thesis, I brought together functional active materials with hydrogels to build more complex machinery (section 4) and I showed proof of concept of functional materials that could be used for drug delivery, termed as colloidosomes (section 3). To reach a more cell-like unit, an autonomous system, this work should be continued by integrating mechanosensing and/or self-regulatory properties as suggested.

References

[1] Yuri M. Efremov, Irina M. Zurina, Viktoria S. Presniakova, Nastasia V. Kosheleva, Denis V. Butnaru, Andrey A. Svistunov, Yury A. Rochev, and Peter S. Timashev. Mechanical properties of cell sheets and spheroids : the link between single cells and complex tissues. *Biophysical Reviews 2021*, pages 1–21, 7 2021.

[2] Dan Liu, Sixun Chen, and May Win Naing. A review of manufacturing capabilities of cell spheroid generation technologies and future development. *Biotechnology and Bioengineering*, 118(2) :542–554, 2 2021.

[3] Adam J. Engler, Shamik Sen, H. Lee Sweeney, and Dennis E. Discher. Matrix Elasticity Directs Stem Cell Lineage Specification. *Cell*, 126(4) :677–689, 2006.

[4] Nikolce Gjorevski, Norman Sachs, Andrea Manfrin, Sonja Giger, Maiia E. Bragina, Paloma Ordóñez-Morán, Hans Clevers, and Matthias P. Lutolf. Designer matrices for intestinal stem cell and organoid culture. *Nature 2016 539 :7630*, 539(7630) :560–564, 11 2016.

[5] Kim S, Uroz M, Bays JL, and Chen CS. Harnessing Mechanobiology for Tissue Engineering. *Developmental cell*, 56(2) :180–191, 1 2021.

[6] Ella A. Hushka, F. Max Yavitt, Tobin E. Brown, Peter J. Dempsey, and Kristi S. Anseth. Relaxation of Extracellular Matrix Forces Directs Crypt Formation and Architecture in Intestinal Organoids. *Advanced Healthcare Materials*, 9(8) :1901214, 4 2020.

[7] Tadanori Mammoto, Akiko Mammoto, and Donald E. Ingber. Mechanobiology and developmental control. *Annual Review of Cell and Developmental Biology*, 29 :27–61, 2013.

[8] Parthiv Kant Chaudhuri, Boon Chuan Low, and Chwee Teck Lim. Mechanobiology of Tumor Growth. *Chemical Reviews*, 118(14) :6499–6515, 2018.

[9] Donald Ingber. Mechanobiology and diseases of mechanotransduction. *https ://doi.org/10.1080/07853890310016333*, 35(8) :564–577, 2009.

[10] Karin A. Jansen, Dominique M. Donato, Hayri E. Balcioglu, Thomas Schmidt, Erik H.J. Danen, and Gijsje H. Koenderink. A guide to mechanobiology : Where biology and physics meet. *Biochimica et Biophysica Acta (BBA) - Molecular Cell Research*, 1853(11) :3043–3052, 11 2015.

[11] Joanna Y. Lee, Jessica K. Chang, Antonia A. Dominguez, Hong pyo Lee, Sungmin Nam, Julie Chang, Sushama Varma, Lei S. Qi, Robert B. West, and Ovijit Chaudhuri. YAP-independent mechanotransduction drives breast cancer progression. *Nature Communications*, 10(1) :1–9, 2019.

[12] Alberto Elosegui-Artola, Ion Andreu, Amy E.M. Beedle, Ainhoa Lezamiz, Marina Uroz, Anita J. Kosmalska, Roger Oria, Jenny Z. Kechagia, Palma Rico-Lastres, Anabel Lise Le Roux, Catherine M. Shanahan, Xavier Trepat, Daniel Navajas, Sergi Garcia-Manyes, and Pere Roca-Cusachs. Force Triggers YAP Nuclear Entry by Regulating Transport across Nuclear Pores. *Cell*, 171(6) :1397–1410, 2017.

[13] Alexis Hubaud, Ido Regev, L. Mahadevan, and Olivier Pourquié. Excitable Dynamics and Yap-Dependent Mechanical Cues Drive the Segmentation Clock. *Cell*, 171(3) :668–682, 2017.

[14] Panciera T, Azzolin L, Cordenonsi M, and Piccolo S. Mechanobiology of YAP and TAZ in physiology and disease. *Nature reviews. Molecular cell biology*, 18(12) :758–770, 12 2017.

[15] Allison N. Ramey-Ward, Hanquan Su, and Khalid Salaita. Mechanical Stimulation of Adhesion Receptors Using Light-Responsive Nanoparticle Actuators Enhances Myogenesis. *ACS Applied Materials & Interfaces*, 12(32) :35903–35917, 8 2020.

[16] Sarah T. Boyle, Jasreen Kular, Max Nobis, Andrew Ruszkiewicz, Paul Timpson, and Michael S. Samuel. Acute compressive stress activates RHO/ROCK-mediated cellular processes. *Small GTPases*, 11(5) :354–370, 2020.

[17] Brandon D. Riehl, Eunju Kim, Tasneem Bouzid, and Jung Yul Lim. The Role of Microenvironmental Cues and Mechanical Loading Milieus in Breast Cancer Cell Progression and Metastasis. *Frontiers in Bioengineering and Biotechnology*, 0 :1571, 1 2021.

[18] Janet M. Tse, Gang Cheng, James A. Tyrrell, Sarah A. Wilcox-Adelman, Yves Boucher, Rakesh K. Jain, and Lance L. Munn. Mechanical compression drives cancer cells toward invasive phenotype. *Proceedings of the National Academy of Sciences of the United States of America*, 109(3) :911–916, 2012.

[19] Benjamin L. Ricca, Gautham Venugopalan, Saori Furuta, Kandice Tanner, Walter A. Orellana, Clay D. Reber, Douglas G. Brownfield, Mina J. Bissell, and Daniel A. Fletcher. Transient external force induces phenotypic reversion of malignant epithelial structures via nitric oxide signaling. *eLife*, 7 :1–19, 2018.

[20] Douglas G. Brownfield, Gautham Venugopalan, Alvin Lo, Hidetoshi Mori, Kandice Tanner, Daniel A. Fletcher, and Mina J. Bissell. Patterned collagen fibers orient branching mammary epithelium through distinct signaling modules. *Current Biology*, 23(8) :703–709, 4 2013.

[21] Saeid Ansaryan, Mohammad Ali Khayamian, Mohammad Saghafi, Shahriar Shalileh, Mohammad Saied Nikshoar, Fereshteh Abbasvandi, Morteza Mahmoudi, Farideh Bahrami, and Mohammad Abdolahad. Stretch Induces Invasive Phenotypes in Breast Cells Due to Activation of Aerobic-Glycolysis-Related Pathways. *Advanced Biosystems*, 3(7) :1800294, 7 2019.

[22] Kabilan Sakthivel, Hitendra Kumar, Mohamed G. A. Mohamed, Bahram Talebjedi, Justin Shim, Homayoun Najjaran, Mina Hoorfar, and Keekyoung Kim. High Throughput Screening of Cell Mechanical Response Using a Stretchable 3D Cellular Microarray Platform. *Small*, 16(30) :2000941, 7 2020.

[23] Friedhelm Serwane, Alessandro Mongera, Payam Rowghanian, David A Kealhofer, Adam A Lucio, Zachary M Hockenbery, and Otger Campàs. In vivo quantification of spatially varying mechanical properties in developing tissues. *Nature Methods*, 1, 2016.

[24] Erfan Mohagheghian, Junyu Luo, Junjian Chen, Gaurav Chaudhary, Junwei Chen, Jian Sun, Randy H. Ewoldt, and Ning Wang. Quantifying compressive forces between living cell layers and within tissues using elastic round microgels. *Nature Communications*, 9(1), 2018.

[25] S. Girardo, N. Träber, K. Wagner, G. Cojoc, C. Herold, R. Goswami, R. Schlüßler, S. Abuhattum, A. Taubenberger, F. Reichel, D. Mokbel, M. Herbig, M. Schürmann, P. Müller, T. Heida, A. Jacobi, E. Ulbricht, J. Thiele, C. Werner, and J. Guck. Standardized microgel beads as elastic cell mechanical probes. *Journal of Materials Chemistry B*, 6(39) :6245–6261, 10 2018.

[26] N. Träber, K. Uhlmann, S. Girardo, G. Kesavan, K. Wagner, J. Friedrichs, R. Goswami, K. Bai, M. Brand, C. Werner, D. Balzani, and J. Guck. Polyacrylamide Bead Sensors for in vivo Quantification of Cell-Scale Stress in Zebrafish Development. *Scientific Reports*, 9(1) :1–14, 2019.

[27] Wontae Lee, Nikita Kalashnikov, Stephanie Mok, Ruba Halaoui, Elena Kuzmin, Andrew J. Putnam, Shuichi Takayama, Morag Park, Luke McCaffrey, Ruogang Zhao, Richard L. Leask, and Christopher Moraes. Dispersible hydrogel force sensors reveal patterns of solid mechanical stress in multicellular spheroid cultures. *Nature Communications*, 10(1) :1–14, 2019.

[28] Nicolas Desprat, Willy Supatto, Philippe Alexandre Pouille, Emmanuel Beaurepaire, and Emmanuel Farge. Tissue Deformation Modulates Twist Expression to Determine Anterior Midgut Differentiation in Drosophila Embryos. *Developmental Cell*, 15(3) :470–477, 9 2008.

[29] Xian Wang, Zhuoran Zhang, Hirotaka Tao, Jun Liu, Sevan Hopyan, and Yu Sun. Characterizing Inner Pressure and Stiffness of Trophoblast and Inner Cell Mass of Blastocysts. *Biophysical Journal*, 115(12) :2443–2450, 12 2018.

[30] Min Zhu, Hirotaka Tao, Mohammad Samani, Mengxi Luo, Xian Wang, Sevan Hopyan, and Yu Sun. Spatial mapping of tissue properties in vivo reveals a 3D stiffness gradient in the mouse limb bud. *Proceedings of the National Academy of Sciences*, 117(9) :4781–4791, 3 2020.

[31] Stephanie Mok, Sara Al Habyan, Charles Ledoux, Wontae Lee, Katherine N. MacDonald, Luke McCaffrey, and Christopher Moraes. Mapping cellular-scale internal mechanics in 3D tissues with thermally responsive hydrogel probes. *Nature Communications 2020 11 :1*, 11(1) :1–11, 9 2020.

[32] Zheng Liu, Yang Liu, Yuan Chang, Hamid Reza Seyf, Asegun Henry, Alexa L. Mattheyses, Kevin Yehl, Yun Zhang, Zhuangqun Huang, and Khalid Salaita. Nanoscale optomechanical actuators for controlling mechanotransduction in living cells. *Nature Methods*, 13(2) :143–146, 2016.

[33] Ludovic Cademartiri and Geoffrey A.Ozin. *Concepts of Nanochemistry*. Wiley-VCH, 2016.

[34] Jani Hämäläinen, Mikko Ritala, and Markku Leskelä. Atomic layer deposition of noble metals and their oxides, 1 2014.

[35] C. Frank Shaw. Gold-Based Therapeutic Agents. *Chemical Reviews*, 99(9) :2589–2600, 1999.

[36] Xiaohu Xia Younan Xia and Hsin-Chieh Peng. Shape-controlled synthesis of colloidal metal nanocrystals : Thermodynamic versus kinetic products. *Journal of the American Chemical Society*, 137(25) :7947–7966, 2015.

[37] Faraday Michael. The bakerian lecture.- experimental relations of gold (and other metals) to light. *Phil. Trans. R. Soc.*, 147 :145–181, 1857.

[38] Paul Mulvaney. Surface plasmon spectroscopy of nanosized metal particles paul mulvaney. *Langmuir*, 12 :788–800, 1996.

[39] Alaaldin M. Alkilany, Lucas B. Thompson, Stefano P. Boulos, Patrick N. Sisco, and Catherine J. Murphy. Gold nanorods : Their potential for photothermal therapeutics and drug delivery, tempered by the complexity of their biological interactions, 2 2012.

[40] Babak Nikoobakht and Mostafa A El-Sayed. Preparation and Growth Mechanism of Gold Nanorods (NRs) Using Seed-Mediated Growth Method. *Chemistry of Materials*, 15(10) :1957–1962, 2003.

[41] Leonardo Scarabelli, Ana Sánchez-Iglesias, Jorge Pérez-Juste, and Luis M. Liz-Marzán. A "Tips and Tricks" Practical Guide to the Synthesis of Gold Nanorods. *Journal of Physical Chemistry Letters*, 6(21) :4270–4279, 2015.

[42] Marek Grzelczak, Jorge Pérez-Juste, Paul Mulvaney, and Luis M. Liz-Marzán. Shape control in gold nanoparticle synthesis. *Chem. Soc. Rev.*, 37(9) :1783–1791, 2008.

[43] Xingchen Ye, Chen Zheng, Jun Chen, Yuzhi Gao, and Christopher B Murray. Using Binary Surfactant Mixtures to Simultaneously Improve Dimensional Tunability and Monodispersity in the Seeded-Growth of Gold Nanorods Using Binary Surfactant Mixtures to Simultaneously Improve Dimensional Tunability and Monodispersity in the Seeded-G. *Nano letters*, 13 :765–771, 2013.

[44] Leonardo Scarabelli, Ana Sánchez-Iglesias, Jorge Pérez-Juste, and Luis M. Liz-Marzán. A "Tips and Tricks" Practical Guide to the Synthesis of Gold Nanorods. *Journal of Physical Chemistry Letters*, 6(21) :4270–4279, 2015.

[45] Berna Özkale, Raquel Parreira, Ahmet Bekdemir, Lucio Pancaldi, Ece Özelçi, Claire Amadio, Murat Kaynak, Francesco Stellacci, David J. Mooney, and Mahmut Selman Sakar. Modular soft robotic microdevices for dexterous biomanipulation. *Lab on a Chip*, 19(5) :778–788, 2019.

[46] Raquel Parreira, Ece Özelçi, and Mahmut Selman Sakar. Remotely Controlled Colloidal Assembly of Soft Microrobotic Artificial Muscle. *Advanced Intelligent Systems*, 2(7) :2000062, 2020.

[47] Selma Attia. Synthesis and surface functionalization of optomechanical polymer nanocomposites. (June), 2019.

[48] Samuel E Lohse, Jonathan R Eller, Sean T Sivapalan, Michael R Plews, and Catherine J Murphy. A Simple Millifluidic Benchtop Reactor System for the High-Throughput Synthesis and Functionalization of Gold Nanoparticles with Different Sizes and Shapes. *ACS Nano*, 7(5) :4135–4150, 2013.

[49] Mettler Toledo. Particletrack with fbrm technology.

[50] Syrris. Syrris atlas hd.

[51] Mettler Toledo. Optimax 1001 termostat.

[52] SYSTAG. Flexycube.

[53] radleys. Mya 4 reaction.

[54] Ivan Gorelikov, Lora M Field, Eugenia Kumacheva, Ivan Gorelikov, Lora M Field, and Eugenia Kumacheva. Hybrid Microgels Photoresponsive in the Near-Infrared Spectral Range Hybrid Microgels Photoresponsive in the Near-Infrared Spectral Range. 126(49) :15938–15939, 2004.

[55] Rhutesh K. Shah, Jin Woong Kim, and David A. Weitz. Monodisperse stimuli-responsive colloidosomes by self-assembly of microgels in droplets. *Langmuir*, 26(3) :1561–1565, 2010.

[56] Mallika Das, Nicolas Sanson, Dnniele Fava, and Eugenia Kumacheva. Microgels loaded with gold nanorods : Photothermally triggered volume transitions under physiological conditions. *Langmuir*, 23(1) :196–201, 2007.

[57] Rafael Contreras-Cáceres, Ana Sánchez-Iglesias, Matthias Karg, Isabel Pastoriza-Santos, Jorge Pérez-Juste, Jessica Pacifico, Thomas Hellweg, Antonio Fernández-Barbero, and Luis M. Liz-Marzán. Encapsulation and growth of gold nanoparticles in thermoresponsive microgels. *Advanced Materials*, 20(9) :1666–1670, 2008.

[58] Matthias Karg, Isabel Pastoriza-Santos, Jorge Pérez-Juste, Thomas Hellweg, and Luis M. Liz-Marzán. Nanorod-coated PNIPAM microgels : Thermoresponsive optical properties. *Small*, 3(7) :1222–1229, 2007.

[59] Eun Chul Cho, Jin-Woong Kim, Alberto Fernandez-Nieves, and David A Weitz. Highly Responsive Hydrogel Scaffolds Formed by Three-Dimensional Organization of Microgel Nanoparticles. *Nano Letters*, 8(1) :1172–1678, 2008.

[60] Tao Ding, Ventsislav K Valev, Andrew R Salmon, Chris J Forman, Stoyan K Smoukov, Oren A Scherman, Daan Frenkel, and Jeremy J. Baumberg. Light-induced actuating nanotransducers. *Proceedings of the National Academy of Sciences*, pages 3–7, 2016.

[61] Rafael Contreras-Cáceres, Jessica Pacifico, Isabel Pastoriza-Santos, Jorge Pérez-Juste, Antonio Fernández-Barbero, and Luis M Liz-Marzán. Au@pNIPAM Thermosensitive Nanostructures : Control over Shell Cross-linking, Overall Dimensions, and Core Growth. *Advanced Functional Materials*, 19(19) :3070–3076, 2009.

[62] Ana Sánchez-Iglesias, Marek Grzelczak, Benito Rodríguez-González, Pablo Guardia-Girós, Isabel Pastoriza-Santos, Jorge Pérez-Juste, Maurizio Prato, and Luis M. Liz-Marzán. Synthesis of multifunctional composite microgels via in situ Ni growth on pNIPAM-coated au nanoparticles. *ACS Nano*, 3(10) :3184–3190, 2009.

[63] Hui Xie, Mengmeng Sun, Xinjian Fan, Zhihua Lin, Weinan Chen, Lei Wang, Lixin Dong, and Qiang He. Reconfigurable magnetic microrobot swarm : Multimode transformation, locomotion, and manipulation. *Science Robotics*, 4(28) :1–15, 2019.

[64] Piotr Garstecki, Michael J. Fuerstman, Howard A. Stone, and George M. Whitesides. Formation of droplets and bubbles in a microfluidic T-junction—scaling and mechanism of break-up. *Lab on a Chip*, 6(3) :437, 2006.

[65] Raquel Parreira, Ece Özelçi, and Mahmut Selman Sakar. Investigating Tissue Mechanics in vitro Using Untethered Soft Robotic Microdevices. *Frontiers in Robotics and AI*, 8(March) :1–12, 2021.

[66] Toyoichi Tanaka, Eriko Sato, Yoshitsugu Hirokawa, Shunsuke Hirotsu, and Joyce Peetermans. Critical kinetics of volume phase transition of gels. *Physical Review Letters*, 55(22) :2455–2458, 1985.

[67] Kenji Kubota, Kenzi Hamano, Nobuhiro Kuwahara, Shouei Fujishige, and Isao Ando. Characterization of Poly(N-isopropylmethacrylamide) in Water. *Polymer Journal*, 22(12) :1051–1057, 1990.

[68] Greg T. Hermanson. *Bioconjugate techniques*. Academic Press, third edition.

[69] A D Dinsmore, Ming F Hsu, M G Nikolaides, Manuel Marquez, A R Bausch, and D A Weitz. Colloidosomes : selectively permeable capsules composed of colloidal particles. *Science*, 298(5595) :1006–9, 2002.

[70] F. J. Rossier-Miranda, C. G P H Schroën, and R. M. Boom. Colloidosomes : Versatile microcapsules in perspective. *Colloids and Surfaces A : Physicochemical and Engineering Aspects*, 343(1-3) :43–49, 2009.

[71] Tobias Bollhorst, Tim Grieb, Andreas Rosenauer, Gerald Fuller, Michael Maas, and Kurosch Rezwan. Synthesis Route for the Self-Assembly of Submicrometer-Sized Colloidosomes with Tailorable Nanopores.

[72] Daeyeon Lee and David A. Weitz. Double emulsion-templated nanoparticle colloidosomes with selective permeability. *Advanced Materials*, 20(18) :3498–3503, 2008.

[73] J S Sander and A R Studart. Monodisperse Functional Colloidosomes with Tailored Nanoparticle Shells. 2011.

[74] Brian P. Timko, Tal Dvir, and Daniel S. Kohane. Remotely triggerable drug delivery systems. *Advanced Materials*, 22(44) :4925–4943, 2010.

[75] Zheng Liu, Yang Liu, Yuan Chang, Hamid Reza Seyf, Asegun Henry, Alexa L Mattheyses, Kevin Yehl, Yun Zhang, Zhuangqun Huang, and Khalid Salaita. Nanoscale optomechanical actuators for controlling mechanotransduction in living cells. *Nature Methods*, (december) :1–8, 2015.

[76] Yihui Zhang, Fan Zhang, Zheng Yan, Qiang Ma, Xiuling Li, Yonggang Huang, and John A Rogers. Printing, folding and assembly methods for forming 3D mesostructures in advanced materials. 2017.

[77] Steven R. Caliari and Jason A. Burdick. A practical guide to hydrogels for cell culture, 5 2016.

[78] Kuen Yong Lee and David J. Mooney. Alginate : Properties and biomedical applications, 1 2012.

[79] Pere Roca-Cusachs, Vito Conte, and Xavier Trepat. Quantifying forces in cell biology. *Nature Cell Biology*, 19(7) :742–751, 2017.

[80] Aleksandra K. Denisin and Beth L. Pruitt. Tuning the Range of Polyacrylamide Gel Stiffness for Mechanobiology Applications. *ACS Applied Materials and Interfaces*, 8(34) :21893–21902, 2016.

[81] Pere Roca-Cusachs, Vito Conte, and Xavier Trepat. Quantifying forces in cell biology. *Nature Cell Biology*, 19(7) :742–751, 2017.

[82] Paul Menter. Acrylamide polymerization.

[83] M. E. Dolega, M. Delarue, F. Ingremeau, J. Prost, A. Delon, and G. Cappello. Cell-like pressure sensors reveal increase of mechanical stress towards the core of multicellular spheroids under compression. *Nature Communications*, 8(1) :1–9, 1 2017.

[84] Yu Shrike Zhang and Ali Khademhosseini. Advances in engineering hydrogels, 5 2017.

[85] Jeong-Yun Sun, Xuanhe Zhao, Widusha R K Illeperuma, Ovijit Chaudhuri, Kyu Hwan Oh, David J Mooney, Joost J Vlassak, Zhigang Suo, and South Korea. Highly stretchable and tough hydrogels. 2012.

[86] Stefano Palagi and Peer Fischer. Bioinspired microrobots. *Nature Reviews Materials*, 3(6) :113–124, 2018.

[87] Metin Sitti, Ieee] Fellow, Hakan Ceylan, Wenqi Hu, Joshua Giltinan, Mehmet Turan, Sehyuk Yim, and Eric Diller. Biomedical Applications of Untethered Mobile Milli/Microrobots HHS Public Access. *Proceedings of the IEEE*, 103(2) :205–224, 2015.

[88] Alex Terray, John Oakey, and David W M Marr. Microfluidic Control Using Colloidal Devices. *Science*, 296(5574) :1841 LP – 1844, 6 2002.

[89] T. Sawetzki, S. Rahmouni, C. Bechinger, and D. W.M. Marr. In situ assembly of linked geometrically coupled microdevices. *Proceedings of the National Academy of Sciences of the United States of America*, 105(51) :20141–20145, 2008.

[90] Charles E. Sing, Lothar Schmid, Matthias F. Schneider, Thomas Franke, and Alfredo Alexander-Katz. Controlled surface-induced flows from the motion of self-assembled colloidal walkers. *Proceedings of the National Academy of Sciences of the United States of America*, 107(2) :535–540, 2010.

[91] Alexey Snezhko and Igor S. Aranson. Magnetic manipulation of self-assembled colloidal asters. *Nature Materials*, 10(9) :698–703, 2011.

[92] T. O. Tasci, P. S. Herson, K. B. Neeves, and D. W.M. Marr. Surface-enabled propulsion and control of colloidal microwheels. *Nature Communications*, 7, 2016.

[93] Jiangfan Yu, Ben Wang, Xingzhou Du, Qianqian Wang, and Li Zhang. Ultra-extensible ribbon-like magnetic microswarm. *Nature Communications*, 9(1) :3260, 2018.

[94] Randall M. Erb, Joshua J. Martin, Rasam Soheilian, Chunzhou Pan, and Jabulani R. Barber. Actuating Soft Matter with Magnetic Torque. *Advanced Functional Materials*, 26(22) :3859–3880, 2016.

[95] Mingsheng Wang, Le He, and Yadong Yin. Magnetic field guided colloidal assembly. *Materials Today*, 16(4) :110–116, 2013.

[96] Yunus Alapan, Berk Yigit, Onur Beker, Ahmet F. Demirörs, and Metin Sitti. Shape-encoded dynamic assembly of mobile micromachines. *Nature Materials*, 18(11) :1244–1251, 2019.

[97] Jun Zhang, Jun Sheng, Ciarán T. O'Neill, Conor J. Walsh, Robert J. Wood, Jee Hwan Ryu, Jaydev P. Desai, and Michael C. Yip. Robotic Artificial Muscles : Current Progress and Future Perspectives. *IEEE Transactions on Robotics*, 35(3) :761–781, 2019.

[98] Haiyan Jia, Erik Mailand, Jiangtao Zhou, Zhangjun Huang, Giovanni Dietler, John M. Kolinski, Xinling Wang, and Mahmut Selman Sakar. Universal Soft Robotic Microgripper. *Small*, 15(4) :1803870, 2019.

[99] Hyun Taek Lee, Min Soo Kim, Gil Yong Lee, Chung Soo Kim, and Sung Hoon Ahn. Shape Memory Alloy (SMA)-Based Microscale Actuators with 60% Deformation Rate and 1.6 kHz Actuation Speed. *Small*, 14(23) :1–7, 2018.

[100] Ahmed Mourran, Hang Zhang, Rostislav Vinokur, and Martin Möller. Soft Microrobots Employing Nonequilibrium Actuation via Plasmonic Heating. *Advanced Materials*, 29(2) :1604825, 1 2017.

[101] Stefano Palagi, Andrew G. Mark, Shang Yik Reigh, Kai Melde, Tian Qiu, Hao Zeng, Camilla Parmeggiani, Daniele Martella, Alberto Sanchez-Castillo, Nadia Kapernaum, Frank Giesselmann, Diederik S. Wiersma, Eric Lauga, and Peer Fischer. Structured light enables biomimetic swimming and versatile locomotion of photoresponsive soft microrobots. *Nature Materials*, 15(6) :647–653, 2016.

[102] Stefano Fusco, Mahmut Selman Sakar, Stephen Kennedy, Christian Peters, Rocco Bottani, Fabian Starsich, Angelo Mao, Georgios A. Sotiriou, Salvador Pané, Sotiris E. Pratsinis, David Mooney, and Bradley J. Nelson. An integrated microrobotic platform for on-demand, targeted therapeutic interventions. *Advanced Materials*, 26(6) :952–957, 2014.

[103] Marek Grzelczak, Luis M. Liz-Marzán, and Rafal Klajn. Stimuli-responsive self-assembly of nanoparticles. *Chemical Society Reviews*, 48(5) :1342–1361, 2019.

[104] Linhan Lin, Xiaolei Peng, Mingsong Wang, Leonardo Scarabelli, Zhangming Mao, Luis M. Liz-Marzán, Michael F. Becker, and Yuebing Zheng. Light-Directed Reversible Assembly of Plasmonic Nanoparticles Using Plasmon-Enhanced Thermophoresis. *ACS Nano*, 10(10) :9659–9668, 2016.

[105] Linhan Lin, Jianli Zhang, Xiaolei Peng, Zilong Wu, Anna C.H. Coughlan, Zhangming Mao, Michael A. Bevan, and Yuebing Zheng. Opto-thermophoretic assembly of colloidal matter. *Science Advances*, 3(9) :1–10, 2017.

[106] Jiajie Chen, Jacky Fong-Chuen Loo, Dongping Wang, Yu Zhang, Siu-Kai Kong, and Ho-Pui Ho. Thermal Optofluidics : Principles and Applications. *Advanced Optical Materials*, 8(1) :1–17, 2020.

[107] Felix Winterer, Christoph M. Maier, Carla Pernpeintner, and Theobald Lohmüller. Optofluidic transport and manipulation of plasmonic nanoparticles by thermocapillary convection. *Soft Matter*, 14(4) :628–634, 2018.

[108] Jun Ichi Chikazawa, Takayuki Uwada, Akihiro Furube, and Shuichi Hashimoto. Flow-induced transport via optical heating of a single gold nanoparticle. *Journal of Physical Chemistry C*, 123(7) :4512–4522, 2019.

[109] Hongbao Xin, Bumseok Namgung, and Luke P. Lee. Nanoplasmonic optical antennas for life sciences and medicine. *Nature Reviews Materials*, 3(8) :228–243, 2018.

[110] Ronald Terrazas Mallea, Aude Bolopion, Jean Charles Beugnot, Pierre Lambert, and Michael Gauthier. Laser-Induced thermocapillary convective flows : A new approach for noncontact actuation at microscale at the fluid/gas interface. *IEEE/ASME Transactions on Mechatronics*, 22(2) :693–704, 2017.

[111] Metin Sitti and Diederik S. Wiersma. Pros and Cons : Magnetic versus Optical Microrobots. *Advanced Materials*, 1906766 :1–9, 2020.

[112] Jing Zhao, Hanquan Su, Gregory E. Vansuch, Zheng Liu, Khalid Salaita, and R. Brian Dyer. Localized Nanoscale Heating Leads to Ultrafast Hydrogel Volume-Phase Transition. *ACS Nano*, 13(1) :515–525, 2019.

[113] Marek Grzelczak, Jorge Pérez-Juste, F. Javier García De Abajo, and Luis M. Liz-Marzán. Optical Properties of Platinum-Coated Gold Nanorods. *Journal of Physical Chemistry C*, 111(17) :6183–6188, 2007.

[114] Svetlana V. Boriskina, Thomas Alan Cooper, Lingping Zeng, George Ni, Jonathan K. Tong, Yoichiro Tsurimaki, Yi Huang, Laureen Meroueh, Gerald Mahan, and Gang Chen. Losses in plasmonics : from mitigating energy dissipation to embracing loss-enabled functionalities. *Advances in Optics and Photonics*, 9(4) :775, 2017.

[115] Kyoungweon Park, Lawrence F. Drummy, and Richard A. Vaia. Ag shell morphology on Au nanorod core : Role of Ag precursor complex. *Journal of Materials Chemistry*, 21(39) :15608–15618, 2011.

[116] Stefan Duhr and Dieter Braun. Why molecules move along a temperature gradient. *Proceedings of the National Academy of Sciences of the United States of America*, 103(52) :19678–19682, 2006.

[117] W. Benjamin Rogers, William M. Shih, and Vinothan N. Manoharan. Using DNA to program the self-assembly of colloidal nanoparticles and microparticles. *Nature Reviews Materials*, 1(3) :16008, 2016.

[118] Yuhui Li, Guoyou Huang, Xiaohui Zhang, Baoqiang Li, Yongmei Chen, Tingli Lu, Tian Jian Lu, and Feng Xu. Magnetic hydrogels and their potential biomedical applications. *Advanced Functional Materials*, 23(6) :660–672, 2013.

[119] Benito Rodríguez-González, Andrew Burrows, Masashi Watanabe, Christopher J. Kiely, and Luis M.Liz Marzán. Multishell bimetallic AuAg nanoparticles : Synthesis, structure and optical properties. *Journal of Materials Chemistry*, 15(17) :1755–1759, 2005.

[120] Johannes Schindelin, Ignacio Arganda-Carreras, Erwin Frise, Verena Kaynig, Mark Longair, Tobias Pietzsch, Stephan Preibisch, Curtis Rueden, Stephan Saalfeld, Benjamin Schmid, Jean-Yves Tinevez, Daniel James White, Volker Hartenstein, Kevin Eliceiri, Pavel Tomancak, and Albert Cardona. Fiji : An open-source platform for biological-image analysis. *Nature Methods*, 9(7) :676–682, 2012.

[121] Shawn Lankton and Allen Tannenbaum. Localizing Region-Based Active Contours. *IEEE Transactions on Image processing*, 17(11) :2029–2039, 2008.

[122] William Thielicke and Eize J. Stamhuis. PIVlab – Towards User-friendly, Affordable and Accurate Digital Particle Image Velocimetry in MATLAB. *Journal of Open Research Software*, 2, 10 2014.

[123] Bertrand Dano. Quiverc - File Exchange - MATLAB Central.

[124] Chengzhi Hu, Salvador Pané, and Bradley J Nelson. Soft Micro- and Nanorobotics. *Annual Review of Control, Robotics, and Autonomous Systems*, 1(1) :53–75, 5 2018.

[125] Sara Nocentini, Camilla Parmeggiani, Daniele Martella, and Diederik S Wiersma. Review 1800207 (1 of 17) Optically Driven Soft Micro Robotics. 2018.

[126] Jianyu Li and David J Mooney. Designing hydrogels for controlled drug delivery. *Nature Reviews Materials*, 1(12) :16071, 2016.

[127] Leonid Ionov. Biomimetic hydrogel-based actuating systems. *Advanced Functional Materials*, 23(36) :4555–4570, 2013.

[128] Martien A Cohen Stuart, Wilhelm T S Huck, Jan Genzer, Marcus Müller, Christopher Ober, Manfred Stamm, Gleb B Sukhorukov, Igal Szleifer, Vladimir V Tsukruk, Marek Urban, Françoise Winnik, Stefan Zauscher, Igor Luzinov, and Sergiy Minko. Emerging applications of stimuli-responsive polymer materials. *Nature Materials*, 9(2) :101–113, 2010.

[129] Ximin He, Michael Aizenberg, Olga Kuksenok, Lauren D. Zarzar, Ankita Shastri, Anna C. Balazs, and Joanna Aizenberg. Synthetic homeostatic materials with chemo-mechano-chemical self-regulation. *Nature*, 487(7406) :214–218, 2012.

[130] David J Beebe, Jeffrey S Moore, Joseph M Bauer, Qing Yu, Robin H Liu, Chelladurai Devadoss, and Byung-Ho Jo. Functional hydrogel structures for autonomous flow control inside microfluidic channels. *Nature*, 404(6778) :588–590, 2000.

[131] Xuanhe Zhao, Jaeyun Kim, Christine a Cezar, Nathaniel Huebsch, Kangwon Lee, Kamal Bouhadir, David J Mooney, Citable Link, Xuanhe Zhao, Jaeyun Kim, Christine a Cezar, Nathaniel Huebsch, and Kangwon Lee. Active scaffolds for on-demand drug and cell delivery. *Proceedings of the National Academy of Sciences of the United States of America*, 108(1) :67–72, 2011.

[132] Nathaniel Huebsch, Cathal J. Kearney, Xuanhe Zhao, Jaeyun Kim, Christine A. Cezar, Zhigang Suo, and David J. Mooney. Ultrasound-triggered disruption and

self-healing of reversibly cross-linked hydrogels for drug delivery and enhanced chemotherapy. *Proceedings of the National Academy of Sciences*, 111(27) :9762–9767, 7 2014.

[133] Christine A Cezar, Ellen T Roche, Herman H Vandenburgh, Georg N Duda, Conor J Walsh, and David J Mooney. Biologic-free mechanically induced muscle regeneration. *Proceedings of the National Academy of Sciences of the United States of America*, 113(6) :1534–9, 2 2016.

[134] Sau Yin Chin, Yukkee Cheung Poh, Anne-Céline Kohler, Jocelyn T Compton, Lauren L Hsu, Kathryn M Lau, Sohyun Kim, Benjamin W Lee, Francis Y Lee, and Samuel K Sia. Additive manufacturing of hydrogel-based materials for next-generation implantable medical devices. *Science Robotics*, 2(2) :eaah6451, 1 2017.

[135] Pingqiang Cai, Benhui Hu, Wan Ru Leow, Xiaoyuan Wang, Xian Jun Loh, Yun-Long Wu, and Xiaodong Chen. Biomechano-Interactive Materials and Interfaces. *Advanced Materials*, 30(31) :1800572, 8 2018.

[136] Hen-Wei Huang, Mahmut Selman Sakar, Andrew J Petruska, Salvador Pane, and Bradley J Nelson. Soft micromachines with programmable motility and morphology. *Nat Commun*, 7 :1–10, 2016.

[137] Jiyun Kim, Su Eun Chung, Sung-Eun Choi, Howon Lee, Junhoi Kim, and Sunghoon Kwon. Programming magnetic anisotropy in polymeric microactuators. *Nature Materials*, 10(10) :747–752, 2011.

[138] Daniel Ahmed, Mengqian Lu, Amir Nourhani, Paul E Lammert, Zak Stratton, Hari S Muddana, Vincent H Crespi, and Tony Jun Huang. Selectively manipulable acoustic-powered microswimmers. *Scientific Reports*, 5(1) :9744, 2015.

[139] Daniel Ahmed, Cornel Dillinger, Ayoung Hong, and Bradley J Nelson. Artificial Acousto-Magnetic Soft Microswimmers. *Advanced Materials Technologies*, 2(7) :1700050, 7 2017.

[140] Murat Kaynak, Adem Ozcelik, Amir Nourhani, Paul E Lammert, Vincent H Crespi, and Tony Jun Huang. Acoustic actuation of bioinspired microswimmers. *Lab on a Chip*, 17(3) :395–400, 2017.

[141] Ugur Bozuyuk, Oncay Yasa, I Ceren Yasa, Hakan Ceylan, Seda Kizilel, and Metin Sitti. Light-Triggered Drug Release from 3D-Printed Magnetic Chitosan Microswimmers. *ACS Nano*, 12(9) :9617–9625, 9 2018.

[142] Wenqi Hu, Kelly S Ishii, Qihui Fan, and Aaron T Ohta. Hydrogel microrobots actuated by optically generated vapour bubbles. *Lab Chip*, 12(19) :3821–3826, 2012.

[143] Deok-Ho Kim, Pak Kin Wong, Jungyul Park, Andre Levchenko, and Yu Sun. Microengineered Platforms for Cell Mechanobiology. *Annual Review of Biomedical Engineering*, 11(1) :203–233, 7 2009.

[144] William J Polacheck, Ran Li, Sebastien G M Uzel, and Roger D Kamm. Microfluidic platforms for mechanobiology. *Lab Chip*, 13(12) :2252–2267, 2013.

[145] Wilhelm T S Huck. Responsive polymers for nanoscale actuation. *Materials Today*, 11(7) :24–32, 2008.

[146] Alexander E. Marras, Lifeng Zhou, Hai Jun Su, and Carlos E. Castro. Programmable motion of DNA origami mechanisms. *Proceedings of the National Academy of Sciences of the United States of America*, 112(3) :713–718, 1 2015.

[147] Enzo Kopperger, Jonathan List, Sushi Madhira, Florian Rothfischer, Don C. Lamb, and Friedrich C. Simmel. A self-assembled nanoscale robotic arm controlled by electric fields. *Science*, 359(6373) :296–301, 1 2018.

[148] Henry Hess. Engineering applications of biomolecular motors. *Annual Review of Biomedical Engineering*, 13 :429–450, 8 2011.

[149] Yusuke Sato, Yuichi Hiratsuka, Ibuki Kawamata, Satoshi Murata, and Shin Ichiro M. Nomura. Micrometer-sized molecular robot changes its shape in response to signal molecules. *Science Robotics*, 2(4), 3 2017.

[150] Jiawen Chen, Franco King Chi Leung, Marc C.A. Stuart, Takashi Kajitani, Takanori Fukushima, Erik Van Der Giessen, and Ben L. Feringa. Artificial muscle-like function from hierarchical supramolecular assembly of photoresponsive molecular motors. *Nature Chemistry*, 10(2) :132–138, 2 2018.

[151] Ahmed Mourran, Hang Zhang, Rostislav Vinokur, and Martin Möller. Soft Microrobots Employing Nonequilibrium Actuation via Plasmonic Heating. *Advanced Materials*, 29(2), 2017.

[152] Isabel Pastoriza-Santos, Calum Kinnear, Jorge Pérez-Juste, Paul Mulvaney, and Luis M. Liz-Marzán. Plasmonic polymer nanocomposites, 10 2018.

[153] Su Eun Chung, Wook Park, Hyunsung Park, Kyoungsik Yu, Namkyoo Park, and Sunghoon Kwon. Optofluidic maskless lithography system for real-time synthesis of photopolymerized microstructures in microfluidic channels. *Applied Physics Letters*, 91(4) :41106, 7 2007.

[154] Leonardo Ricotti, Barry Trimmer, Adam W. Feinberg, Ritu Raman, Kevin K. Parker, Rashid Bashir, Metin Sitti, Sylvain Martel, Paolo Dario, and Arianna Menciassi. Biohybrid actuators for robotics : A review of devices actuated by living cells. *Science Robotics*, 2(12) :eaaq0495, 2017.

[155] Mahmut Selman Sakar, Devin Neal, Thomas Boudou, Michael A Borochin, Yinqing Li, Ron Weiss, Roger D Kamm, Christopher S Chen, and H Harry Asada. Formation and optogenetic control of engineered 3D skeletal muscle bioactuators. *Lab Chip*, 12(23) :4976–4985, 2012.

[156] Caroline Cvetkovic, Ritu Raman, Vincent Chan, Brian J. Williams, Madeline Tolish, Piyush Bajaj, Mahmut Selman Sakar, H. Harry Asada, M. Taher A. Saif, and Rashid Bashir. Three-dimensionally printed biological machines powered by skeletal muscle. *Proceedings of the National Academy of Sciences of the United States of America*, 111(28) :10125–10130, 7 2014.

[157] Adam W Feinberg. Biological Soft Robotics. *Annual Review of Biomedical Engineering*, 17(1) :243–265, 12 2015.

[158] Kenneth M. Yamada and Edna Cukierman. Modeling Tissue Morphogenesis and Cancer in 3D, 8 2007.

[159] Alessia Deglincerti, Gist F. Croft, Lauren N. Pietila, Magdalena Zernicka-Goetz, Eric D. Siggia, and Ali H. Brivanlou. Self-organization of the in vitro attached human embryo. *Nature*, 533(7602) :251–254, 5 2016.

[160] Devanjali Dutta, Inha Heo, and Hans Clevers. Disease Modeling in Stem Cell-Derived 3D Organoid Systems, 5 2017.

[161] Lucie A. Low, Christine Mummery, Brian R. Berridge, Christopher P. Austin, and Danilo A. Tagle. Organs-on-chips : into the next decade, 5 2021.

[162] Sangeeta N. Bhatia and Donald E. Ingber. Microfluidic organs-on-chips, 8 2014.

[163] Eric W. Esch, Anthony Bahinski, and Dongeun Huh. Organs-on-chips at the frontiers of drug discovery, 4 2015.

[164] Mami Matano, Shoichi Date, Mariko Shimokawa, Ai Takano, Masayuki Fujii, Yuki Ohta, Toshiaki Watanabe, Takanori Kanai, and Toshiro Sato. Modeling colorectal cancer using CRISPR-Cas9-mediated engineering of human intestinal organoids. *Nature Medicine*, 21(3) :256–262, 2 2015.

[165] William J. Polacheck and Christopher S. Chen. Measuring cell-generated forces : A guide to the available tools, 5 2016.

[166] Diana E. Jaalouk and Jan Lammerding. Mechanotransduction gone awry, 1 2009.

[167] Yu Sun, Kai Tak Wan, Kenneth P. Roberts, John C. Bischof, and Bradley J. Nelson. Mechanical property characterization of mouse zona pellucida. *IEEE Transactions on Nanobioscience*, 2(4) :279–286, 12 2003.

[168] Felix Beyeler, Adrian Neild, Stefano Oberti, Dominik J. Bell, Yu Sun, Jürg Dual, and Bradley J. Nelson. Monolithically fabricated microgripper with integrated force sensor for manipulating microobjects and biological cells aligned in an ultrasonic field. *Journal of Microelectromechanical Systems*, 16(1) :7–15, 2 2007.

[169] Adam J. Engler, Florian Rehfeldt, Shamik Sen, and Dennis E. Discher. Microtissue Elasticity : Measurements by Atomic Force Microscopy and Its Influence on Cell Differentiation, 1 2007.

[170] Keekyoung Kim, Xinyu Liu, Yong Zhang, and Yu Sun. Nanonewton force-controlled manipulation of biological cells using a monolithic MEMS microgripper with two-axis force feedback. *Journal of Micromechanics and Microengineering*, 18(5) :8, 5 2008.

[171] Keitaro Ito, Shinya Sakuma, Masaki Kimura, Takanori Takebe, Makoto Kaneko, and Fumihito Arai. Temporal transition of mechanical characteristics of HUVEC/MSC spheroids using a microfluidic chip with force sensor probes. *Micromachines*, 7(12) :221, 12 2016.

[172] Shinya Sakuma, Ko Nakahara, and Fumihito Arai. Continuous Mechanical Indexing of Single-Cell Spheroids Using a Robot-Integrated Microfluidic Chip. *IEEE Robotics and Automation Letters*, 4(3) :2973–2980, 7 2019.

[173] Allan S. Hoffman. Hydrogels for biomedical applications, 12 2012.

[174] Berna Özkale, Mahmut Selman Sakar, and David J. Mooney. Active biomaterials for mechanobiology, 1 2021.

[175] Leonid Ionov. Hydrogel-based actuators : Possibilities and limitations, 12 2014.

[176] Ozan Erol, Aishwarya Pantula, Wangqu Liu, and David H. Gracias. Transformer Hydrogels : A Review, 4 2019.

[177] Yuha Koike, Yoshiyuki Yokoyama, and Takeshi Hayakawa. Light-Driven Hydrogel Microactuators for On-Chip Cell Manipulations. *Frontiers in Mechanical Engineering*, 6(2) :2, 1 2020.

[178] Liyuan Tan, Aaron C. Davis, and David J. Cappelleri. Smart Polymers for Microscale Machines, 2 2021.

[179] Murat Kaynak, Furkan Ayhan, and Mahmut Selman Sakar. Compound micromachines powered by acoustic streaming. In *Proceedings - IEEE International Conference on Robotics and Automation*, volume 2019-May, pages 225–230. Institute of Electrical and Electronics Engineers Inc., 5 2019.

[180] Kenji Setoura, Yudai Okada, Daniel Werner, and Shuichi Hashimoto. Observation of nanoscale cooling effects by substrates and the surrounding media for single gold nanoparticles under CW-laser illumination. *ACS Nano*, 7(9) :7874–7885, 9 2013.

[181] Keekyoung Kim, Ji Cheng, Qun Liu, Xiao Yu Wu, and Yu Sun. Investigation of mechanical properties of soft hydrogel microcapsules in relation to protein delivery using a MEMS force sensor. *Journal of Biomedical Materials Research - Part A*, 92(1) :103–113, 1 2010.

[182] Brooke Schuster, Michael Junkin, Sara Saheb Kashaf, Isabel Romero-Calvo, Kori Kirby, Jonathan Matthews, Christopher R. Weber, Andrey Rzhetsky, Kevin P. White, and Savaş Tay. Automated microfluidic platform for dynamic and combinatorial drug screening of tumor organoids. *Nature Communications*, 11(1) :1–12, 12 2020.

[183] Mikhail Nikolaev, Olga Mitrofanova, Nicolas Broguiere, Sara Geraldo, Devanjali Dutta, Yoji Tabata, Bilge Elci, Nathalie Brandenberg, Irina Kolotuev, Nikolce Gjorevski, Hans Clevers, and Matthias P Lutolf. Homeostatic mini-intestines through scaffold-guided organoid morphogenesis. *Nature*, 585(7826) :574–578, 2020.

[184] Richard Novak, Miles Ingram, Susan Marquez, Debarun Das, Aaron Delahanty, Anna Herland, Ben M. Maoz, Sauveur S.F. Jeanty, Mahadevabharath R. Somayaji, Morgan Burt, Elizabeth Calamari, Angeliki Chalkiadaki, Alexander Cho, Youngjae Choe, David Benson Chou, Michael Cronce, Stephanie Dauth, Toni Divic, Jose Fernandez-Alcon, Thomas Ferrante, John Ferrier, Edward A. FitzGerald, Rachel Fleming, Sasan Jalili-Firoozinezhad, Thomas Grevesse, Josue A. Goss, Tiama Hamkins-Indik, Olivier Henry, Chris Hinojosa, Tessa Huffstater, Kyung Jin Jang, Ville Kujala, Lian Leng, Robert Mannix, Yuka Milton, Janna Nawroth, Bret A. Nestor, Carlos F. Ng, Blakely O'Connor, Tae Eun Park, Henry Sanchez, Josiah Sliz, Alexandra Sontheimer-Phelps, Ben Swenor, Guy Thompson, George J. Touloumes, Zachary Tranchemontagne, Norman Wen, Moran Yadid, Anthony Bahinski, Geraldine A. Hamilton, Daniel Levner, Oren Levy, Andrzej Przekwas, Rachelle Prantil-Baun, Kevin K. Parker, and Donald E. Ingber. Robotic fluidic coupling and interrogation of multiple vascularized organ chips. *Nature Biomedical Engineering*, 4(4) :407–420, 4 2020.

[185] Kaspar Althoefer. Antagonistic actuation and stiffness control in soft inflatable robots. *Nature Reviews Materials*, 3(6) :76–77, 2018.

[186] Marc Hippler, Eva Blasco, Jingyuan Qu, Motomu Tanaka, Christopher Barner-Kowollik, Martin Wegener, and Martin Bastmeyer. Controlling the shape of 3D microstructures by temperature and light. *Nature Communications*, 10(1) :1–8, 12 2019.

[187] Marc Hippler, Kai Weißenbruch, Kai Richler, Enrico D. Lemma, Masaki Nakahata, Benjamin Richter, Christopher Barner-Kowollik, Yoshinori Takashima, Akira Harada, Eva Blasco, Martin Wegener, Motomu Tanaka, and Martin Bastmeyer. Mechanical stimulation of single cells by reversible host-guest interactions in 3D microscaffolds. *Science Advances*, 6(39) :eabc2648, 9 2020.

[188] Murat Kaynak, Pietro Dirix, and Mahmut Selman Sakar. Addressable Acoustic Actuation of 3D Printed Soft Robotic Microsystems. *Advanced Science*, 7(20) :2001120, 10 2020.

[189] Nathalie Brandenberg, Sylke Hoehnel, Fabien Kuttler, Krisztian Homicsko, Camilla Ceroni, Till Ringel, Nikolce Gjorevski, Gerald Schwank, George Coukos, Gerardo

Turcatti, and Matthias P Lutolf. High-throughput automated organoid culture via stem-cell aggregation in microcavity arrays. *Nature Biomedical Engineering*, 4(9) :863–874, 2020.

[190] Pierre-Alexandre Vidi, Mina J. Bissell, and Sophie A. Lelièvre. Three-Dimensional Culture of Human Breast Epithelial Cells : The How and the Why. *Methods in Molecular Biology*, 945 :193–219, 2012.

[191] Jayanta Debnath, Senthil K. Muthuswamy, and Joan S. Brugge. Morphogenesis and oncogenesis of MCF-10A mammary epithelial acini grown in three-dimensional basement membrane cultures. *Methods*, 30(3) :256–268, 2003.

[192] Shawn P. Carey, Timothy M. D'Alfonso, Sandra J. Shin, and Cynthia A. Reinhart-King. Mechanobiology of tumor invasion : Engineering meets oncology. *Critical Reviews in Oncology/Hematology*, 83(2) :170–183, 2012.

[193] Quanming Shi, Rajarshi P. Ghosh, Hanna Engelke, Chris H. Rycroft, Luke Cassereau, James A. Sethian, Valerie M. Weaver, and Jan T. Liphardt. Rapid disorganization of mechanically interacting systems of mammary acini. *Proceedings of the National Academy of Sciences of the United States of America*, 111(2) :658–663, 2014.

[194] Chin Lin Guo, Mingxing Ouyang, Jiun Yann Yu, Jordan Maslov, Andrew Price, and Chih Yu Shen. Long-range mechanical force enables self-assembly of epithelial tubular patterns. *Proceedings of the National Academy of Sciences of the United States of America*, 109(15) :5576–5582, 2012.

[195] Genee Y Lee, Paraic A Kenny, Eva H Lee, and Mina J Bissell. Three-dimensional culture models of normal and malignant breast epithelial cells. *Nature Methods 2007 4 :4*, 4(4) :359–365, 3 2007.

[196] Kim-Vy Nguyen-Ngoc, Eliah R. Shamir, Robert J. Huebner, Jennifer N. Beck, Kevin J. Cheung, and Andrew J. Ewald. 3D Culture Assays of Murine Mammary Branching Morphogenesis and Epithelial Invasion. *Tissue Morphogenesis : Methods and Protocols*, pages 135–162, 9 2015.

[197] K.-V. NGUYEN-NGOC and A.J. EWALD. Mammary ductal elongation and myoepithelial migration are regulated by the composition of the extracellular matrix. *Journal of Microscopy*, 251(3) :212–223, 9 2013.

[198] Shawn P. Carey, Karen E. Martin, and Cynthia A. Reinhart-King. Three-dimensional collagen matrix induces a mechanosensitive invasive epithelial phenotype. *Scientific Reports*, 7(August 2016) :1–14, 2017.

[199] Ehsan Ban, J. Matthew Franklin, Sungmin Nam, Lucas R. Smith, Hailong Wang, Rebecca G. Wells, Ovijit Chaudhuri, Jan T. Liphardt, and Vivek B. Shenoy. Mechanisms of Plastic Deformation in Collagen Networks Induced by Cellular Forces. *Biophysical Journal*, 114(2) :450–461, 2018.

[200] Anirudha Banerjee and Todd M. Squires. Long-range, selective, on-demand suspension interactions : Combining and triggering soluto-inertial beacons. *Science Advances*, 5(8), 2019.

[201] Andrew J. Ewald, Audrey Brenot, Myhanh Duong, Bianca S. Chan, and Zena Werb. Collective Epithelial Migration and Cell Rearrangements Drive Mammary Branching Morphogenesis. *Developmental Cell*, 14(4) :570–581, 4 2008.

[202] Michael J. Warburton, Christine M. Hughes, Sharon A. Ferns, and Philip S. Rudland. Localization of vimentin in myoepithelial cells of the rat mammary gland. *The Histochemical Journal 1989 21 :11*, 21(11) :679–685, 11 1989.

[203] Werner Böcker, Bert Bier, Götz Freytag, Bettina Brömmelkamp, Ernst-Dieter Jarasch, Georg Edel, Barbara Dockhorn-Dworniczak, and Kurt W Schmid. An immunohistochemical study of the breast using antibodies to basal and luminal keratins, alpha-smooth muscle actin, vimentin, collagen IV and laminin. *Virchows Archiv A*, 421(4) :315–322, 1992.

[204] Mark S. Duxbury, Stanley W. Ashley, and Edward E. Whang. Inhibition of pancreatic adenocarcinoma cellular invasiveness by blebbistatin : a novel myosin II inhibitor. *Biochemical and Biophysical Research Communications*, 313(4) :992–997, 1 2004.

[205] Zhenan Liu, Leo A. van Grunsven, Elke Van Rossen, Ben Schroyen, Jean-Pierre Timmermans, Albert Geerts, and Hendrik Reynaert. Blebbistatin inhibits contraction and accelerates migration in mouse hepatic stellate cells. *British Journal of Pharmacology*, 159(2) :304–315, 1 2010.

[206] Paolo P. Provenzano, David R. Inman, Kevin W. Eliceiri, Steven M. Trier, and Patricia J. Keely. Contact Guidance Mediated Three-Dimensional Cell Migration is Regulated by Rho/ROCK-Dependent Matrix Reorganization. *Biophysical Journal*, 95(11) :5374–5384, 12 2008.

[207] Anna V Taubenberger, Salvatore Girardo, Nicole Träber, Elisabeth Fischer-Friedrich, Martin Kräter, Katrin Wagner, Thomas Kurth, Isabel Richter, Barbara Haller, Marcus Binner, Dominik Hahn, Uwe Freudenberg, Carsten Werner, and Jochen Guck. 3D Microenvironment Stiffness Regulates Tumor Spheroid Growth and Mechanics via p21 and ROCK. 2019.

[208] Brandon C. Jones, Laura C. Kelley, Yuriy V. Loskutov, Kristina M. Marinak, Varvara K. Kozyreva, Matthew B. Smolkin, and Elena N. Pugacheva. Dual Targeting of Mesenchymal and Amoeboid Motility Hinders Metastatic Behavior. *Molecular Cancer Research*, 15(6) :670–682, 6 2017.

[209] Elizabeth C. Lessey, Christophe Guilluy, and Keith Burridge. From mechanical force to RhoA activation. *Biochemistry*, 51(38) :7420, 9 2012.

[210] Ramin Omidvar, Mohammad Tafazzoli-shadpour, Mohammad Ali Shokrgozar, and Mostafa Rostami. Atomic force microscope-based single cell force spectroscopy of breast cancer cell lines : An approach for evaluating cellular invasion. *Journal of Biomechanics*, 47(13) :3373–3379, 2014.

[211] Pei Yu Chiou, Aaron T Ohta, and Ming C Wu. Massively parallel manipulation of single cells and microparticles using optical images. *Nature*, 436(7049) :370–372, 2005.

[212] Daniel Needleman and Zvonimir Dogic. Active matter at the interface between. 2017.

[213] L. (Lewis) Wolpert. *Principles of development.*

[214] Stanford University. and Center for the Study of Language and Information (U.S.). *Stanford encyclopedia of philosophy.* Stanford University, 1997.

[215] Yoshiki Sasai. Cytosystems dynamics in self-organization of tissue architecture. *Nature*, 493(7432) :318–326, 2013.

[216] G. Forga´cs and Stuart (Stuart A.) Newman. *Biological physics of the developing embryo.* Cambridge University Press, 2005.

[217] Thomas Lecuit and Pierre François Lenne. Cell surface mechanics and the control of cell shape, tissue patterns and morphogenesis. *Nature Reviews Molecular Cell Biology*, 8(8) :633–644, 2007.

[218] Ido Nitsan, Stavit Drori, Yair E. Lewis, Shlomi Cohen, and Shelly Tzlil. Mechanical communication in cardiac cell synchronized beating. *Nature Physics*, 12(5) :472–477, 2016.

[219] M H Dickinson, C T Farley, R J Full, M a R Koehl, R Kram, and S Lehman. How animals move : An integrative view [Review]. *Science*, 288(5463) :100–106, 2000.

[220] Randy D. Mehlenbacher, Rea Kolbl, Alice Lay, and Jennifer A. Dionne. Nanomaterials for in vivo imaging of mechanical forces and electrical fields. *Nature Reviews Materials*, 3 :1–17, 2017.

[221] William H Blackburn and L Andrew Lyon. NIH Public Access. *Particle Characterization*, 286(5) :563–569, 2008.

[222] João F. Mano. Stimuli-responsive polymeric systems for biomedical applications. *Advanced Engineering Materials*, 10(6) :515–527, 2008.

[223] Young-Jin Kim and Yukiko T. Matsunaga. Thermo-responsive polymers and their application as smart biomaterials. *J. Mater. Chem. B*, 2017.

[224] Sergey N. Semenov, Lewis J. Kraft, Alar Ainla, Mengxia Zhao, Mostafa Baghbanzadeh, Victoria E. Campbell, Kyungtae Kang, Jerome M. Fox, and George M. Whitesides. Autocatalytic, bistable, oscillatory networks of biologically relevant organic reactions. *Nature*, 537(7622) :656–660, 2016.

[225] Ryota Tamate, Takeshi Ueki, and Ryo Yoshida. Evolved Colloidosomes Undergoing Cell-like Autonomous Shape Oscillations with Buckling. *Angewandte Chemie - International Edition*, 55(17) :5179–5183, 2016.

[226] Youn Soo Kim, Ryota Tamate, Aya Mizutani Akimoto, and Ryo Yoshida. Recent developments in self-oscillating polymeric systems as smart materials : from polymers to bulk hydrogels. *Mater. Horiz.*, 2016.

[227] Takeshi Ueki, Michika Onoda, Ryota Tamate, Mitsuhiro Shibayama, and Ryo Yoshida. Self-oscillating AB diblock copolymer developed by post modification strategy. *Chaos*, 25(6), 2015.

[228] Ryo Yoshida and Takeshi Ueki. Evolution of self-oscillating polymer gels as autonomous polymer systems p. *NPG Asia Materials*, 6(6) :107–14, 2014.

[229] Daisuke Suzuki, Takeshi Kobayashi, Ryo Yoshida, and Toshihiro Hirai. Soft actuators of organized self-oscillating microgels. *Soft Matter*, 8(45) :11447–11449, 2012.

[230] Y. Fang, V. V. Yashin, S. P. Levitan, and A. C. Balazs. Pattern recognition with "materials that compute". *Science Advances*, 2(9) :e1601114–e1601114, 2016.

[231] Yoshimitsu Sagara, Marc Karman, Ester Verde-Sesto, Kazuya Matsuo, Yuna Kim, Nobuyuki Tamaoki, and Christoph Weder. Rotaxanes As Mechanochromic Fluorescent Force Transducers in Polymers. *Journal of the American Chemical Society*, page jacs.7b12405, 2018.

[232] Anna Lavrenova, Diederik W.R. Balkenende, Yoshimitsu Sagara, Stephen Schrettl, Yoan C. Simon, and Christoph Weder. Mechano- and Thermoresponsive Photoluminescent Supramolecular Polymer. *Journal of the American Chemical Society*, 139(12) :4302–4305, 2017.

[233] Yoshimitsu Sagara, Shogo Yamane, Masato Mitani, Christoph Weder, and Takashi Kato. Mechanoresponsive Luminescent Molecular Assemblies : An Emerging Class of Materials. *Advanced Materials*, 28(6) :1073–1095, 2016.

[234] Yang Liu, Kevin Yehl, Yoshie Narui, and Khalid Salaita. Tension Sensing Nanoparticles for Mechano-Imaging at the Living/Nonliving Interface. *Journal of the American Chemical Society*, 135(14) :5320–5323, 4 2013.

[235] Hao Yan, Fan Yang, Ding Pan, Yu Lin, J. Nathan Hohman, Diego Solis-Ibarra, Fei Hua Li, Jeremy E. P. Dahl, Robert M. K. Carlson, Boryslav A. Tkachenko, Andrey A. Fokin, Peter R. Schreiner, Giulia Galli, Wendy L. Mao, Zhi-Xun Shen, and Nicholas A. Melosh. Sterically controlled mechanochemistry under hydrostatic pressure. *Nature*, 554(7693) :505–510, 2018.

Raquel Filipa Penacho Parreira

Vaud, Switzerland

Skype: rparreira1 ✉ raquelfparreira@hotmail.com 📱 +41(0)789646531
www.linkedin.com/in/raquel-parreira-b9329a94

STRENGTHS

- GMP/GLP
- Project Manager
- 2D and 3D mammalian cell culture
- Responsible for chemistry lab organization and safety
- Multidisciplinary background
- Languages

EDUCATION

PhD in Bioengineering and Biotechnology **2017-2021**
École Polytechnique Fédérale de Lausanne, EPFL, Switzerland

Integrated Master in Biological Engineering **2011-2016**
Instituto Superior Técnico, IST, at University of Lisbon *17/20*

CORE EXPERIENCE

MicroBioRobotics Systems Laboratory (MICROBS) **2017-2021**
Doctoral thesis in Bioengineering and Biotechnology. *EPFL, Switzerland*

- “Soft Robotic Microdevices for Dexterous Biomanipulation and Mechanobiology”
- Developed technologies and methodologies for biomechanical research. Established protocols for polymer synthesis and gold nanoparticles coating. Developed soft actuatable materials and soft robots for biocompatible mechanical stimulation and characterization of biological samples in ex-vivo. Implemented and established protocols for cell culture and manipulation of human mammary gland cells (MCF10A) in 2D and 3D. I was in charge of the safety and maintenance of the chemical laboratory.

Laboratory of Stem Cell Dynamics (LDCS) **2016**
Master thesis in Biological Engineering *EPFL, Switzerland*

- “Corneal epithelium maintenance of the murine eyes”
- Worked with an organotypic culture for murine eyes to investigate if the cornea has stem cells. During this project, I had the opportunity to practice qPCRs; Immunohistology and Fluorescence microscopy.

Instituto Superior Técnico de Lisboa (IST) **2015**
Master project in Biological Engineering. *IST, Portugal*

- “Production of −Carotene in Photobioreactors”
- In a team of 6 we designed a project for the production of −Carotene, where we selected and designed the main equipment for upstream and downstream processing, developed mass and energy diagrams with SuperPro design and we evaluated economic viability and sensibility of the project.

ADDITIONAL EXPERIENCE

Teaching assistant for Master thesis and semester projects, EPFL *2017-2021*

- I trained and mentored students from Microtechnique; Chemical Engineering; Mechanical Engineering and Bioengineering throughout my PhD.

Innosuisse Start-up Training: Business Concept *2019 (1 semester)*

- Business training with Innosuisse-Swiss Innovation Agency at EPFL Innovation Park. I got the chance of practicing during the semester what we were learning with a real case Start-up idea.

MicroBioRobotics Systems Laboratory (MICROBS), EPFL *2016 (6 months)*

- Internship at EPFL, where I learned how to do photolithography and synthetizing gold nanoparticles.

LANGUAGES

- **English:** Fluent spoken and written (C1)
- **Portuguese:** Native language **Material Sciences and Chemistry:** Wet-lab; GLP/GMP; Gold nanoparticles synthesis; Transmission electron microscopy (TEM); Scanning electron microscopy (SEM); Dynamic Light scattering (DLS); Photo and Thermal polymerization; UV/Vis Spectroscopy
- **French:** Fluent spoken (C1) and Intermediate level written (B2)
- **German:** Goethe Institute Deutch Diploma on B2 in 2016
- **Spanish:**Intermediate level spoken and written (B1)
- **Italian:**Understood (B1)

CONFERENCES

- **Workshop IGNITION/SMYLE** in Besançon, France, 2017: Soft microactuators for mechanobiology; Poster and **Oral presentation**
- **SCS Fall meeting 2018**, EPFL, Switzerland: Reverse Engineering of Simple Life Forms in Fully Synthetic Hydrogel Microsystems; **Oral presentation**
- **Sixth International conference on Multifunctional, Hybrid and Nanomaterials**, Stiges, Spain, 2019: Biomimetic models from mechanically active nanocomposite materials; Poster
- **Annual meeting of BMES (Biomedical Engineering Society)** in Philadelphia, USA, 2019: Soft robotic microdevices for in vitro mechanochemical testing of 3D biological samples; **Oral presentation**
- **IBI-EDBB Mini Symposium**, EPFL, Switzerland, 2019: Soft Robotic Microdevices for Dexterous Biomanipulation and Mechanobiology; **Oral Presentation**

PUBLICATIONS

- Özkale, B.; **Parreira, R**.; Bekdemir, A.; Pancaldi, L.; Özelçi,E.; Amadio, C.; Kaynak, M.; Stellacci, F.; Mooney. D.J. and Selman, M.S., Modular soft robotic microdevices for dexterous biomanipulation, Lab on a Chip, 2019, doi: 10.1039/C8LC01200H
- **Parreira, R**.; Özelçi, E.; Selman, M.S., Remotely controlled colloidal assembly of soft microrobotic artificial muscle, Advanced Intelligent Systems, 2020, doi:10.1002/aisy.202000062
- **Parreira, R.**; Özelçi, E.; Selman, M.S., Investigating tissue mechanics in vitro using untethered soft robotic microdevices, Frontiers in Robotics and AI, 2021, doi: 10.3389/frobt.2021.649765

Extracurricular activities

Triathlon; Self-Defense (Instructor certificate); Hiking; Motorcycling; Beer Brewing; Piano.